Understanding the mechanics of lava dome collapse

Claire Ellen Harnett

Submitted in accordance with the requirements for the degree of
Doctor of Philosophy

The University of Leeds
School of Earth and Environment

March 2019

The candidate confirms that the work submitted is her own, except where work has been included which has formed part of jointly authored publications. The contribution of the candidate and the other authors to this work has been explicitly indicated below. The candidate confirms that appropriate credit has been given within the thesis where reference has been made to work of others.

This thesis is submitted as an alternative style of doctoral thesis including published material. This format is appropriate as the work of this thesis aligns into three distinct strands, each taking a unique approach in tackling the topic of lava dome collapse. These are preceded by an introductory chapter to place the publications within the context of relevant literature. The final chapter provides discussion of how the three publications can be considered together to further our knowledge of the intricacies of lava dome collapse processes.

The work in **Section 1.4** of the thesis has appeared as part of the following publication:

Walter, T. W., **Harnett, C. E.**, Varley, N., Bracamontes, D. V., Salzer, J., Zorn, E. U., Bretón, Arámbula, R., and Thomas, M. E. (2019). *Imaging the 2013 explosive crater excavation and new dome formation at Volcán de Colima with TerraSAR-X, time-lapse cameras and modelling.* Journal of Volcanology and Geothermal Research, 369, pp. 224-237, doi:10.1016/j.jvolgeores.2018.11.016.

TW supplied observational data from Colima and I conducted all modelling and associated data processing. I wrote the section of the manuscript which is adapted for inclusion here, and this was improved following comments from MT, NV, TW and EZ. The relevant supplementary material for this article is included in Appendix A.4.

The work in **Chapter 2** of the thesis has been published under the following title:

Harnett, C. E., Thomas, M. E., Calder, E. S., Ebmeier, S. K., Telford, A., Murphy, W., and Neuberg, J. (2019). *Presentation and analysis for a worldwide database of lava dome collapse events: the Global Archive of Dome Instabilities (GLADIS).* Bulletin of Volcanology, doi: 10.1007/s00445-019-1276-y.

The idea of compiling a database was initially developed by MT. I conducted all data collection, assimilation, statistical analysis and figure production, and wrote the manuscript. ES and MT provided useful discussions, refined the questions for analysis, and improved the manuscript. SE and AT assisted with statistical

analysis, and improved the manuscript. WM and JN helped to improve the manuscript. The manuscript also benefitted from peer review comments from Sarah Ogburn and an anonymous reviewer, as well as the editorial comments of Lucia Capra, Josef Dufek and Andrew Harris.

The work in **Chapter 3** of the thesis has been published under the following title:

Harnett, C. E., Thomas, M. E., Purvance, M., and Neuberg, J. (2018), *Using a discrete element approach to model lava dome emplacement and collapse*, Journal of Volcanology and Geothermal Research, 359, pp.68-77, doi:10.1016/j.jvolgeores.2018.06.017.

I wrote and ran all model codes. I processed all model outputs, created all figures, and wrote the manuscript, which was improved following comments from MT and JN. MP assisted with code implementation and edited the source code of Particle Flow Code. The ideas for model runs were conceptualised following discussions with MP, MT and JN. The manuscript also benefitted from peer review comments from Mike Heap and an anonymous reviewer, as well as the editorial comments of Kelly Russell. The supplementary material for this article is included in Appendix B.

The work in **Chapter 4** of the thesis has been published under the following title:

Harnett, C. E., Kendrick, J. E., Lamur, A. H., Stinton, A., Wallace, P. A., Utley, J. E. P., Murphy, W., Neuberg, J., and Lavallée, Y. (2019). *Evolution of mechanical properties of lava dome rocks across the 1995-2010 eruption of Soufrière Hills volcano, Montserrat.* Frontiers in Earth Science, 7 (7), doi: 10.3389/feart.2019.00007.

I conducted all fieldwork with MT and AS, conducted all laboratory experiments with JK and AL, processed the data, wrote the manuscript and produced all figures. PW and JU carried out the QEMSCAN analysis. The manuscript was improved following comments from all co-authors. The manuscript also benefitted from peer review comments from Micol Todesco and Oleg Melnik, as well as the editorial comments of Luis Lara. The supplementary material for this article is included in Appendix C.

Acknowledgements

Firstly, a huge thanks to NERC for funding this project, and to the various funders (VMSG, IAVCEI) who have supported me in conference attendance during my PhD.

This PhD has been more challenging and also more rewarding than I could have imagined when I set upon this path three and a half years ago. Here's to the people who came along for the ride.

Thanks to my supervisors Mark, Locko and Bill. Thanks to Mark for being engaged and approachable from the start, and always thinking my science was cool and exciting, even when I wasn't sure! There have been many highs (drinking beer in the Caribbean sea) and lows (ripped trousers whilst climbing a volcano...), so thanks for sticking with it. Thanks too go to Bill and Locko for useful discussions over the last few years.

I was lucky enough to get a place on the Itasca Educational Partnership for the whole duration of my PhD, without which I would have been lost. Not only did they generously provide me with the license to PFC5.0, but I was also mentored by Matt Purvance who rescued many coding nightmares. Thanks for the ongoing support and the ever calm replies to many a frustrated email, especially with material calibration. And Richard Rigby deserves an honourable mention for fixing all of the other IT queries over the years - you were the hero of the department, and you're sorely missed.

Thanks also to the Liverpool gang. An extra big thankyou to Jackie for answering my SOS with more commitment and enthusiasm than I could have asked for. Your long hours in the lab (and occasionally the hot tub!) were so appreciated, and happened at just the right time to propel me through to the end of my project. Thanks to Anthony for his patience in the lab, and for spending so much time helping with experiments. And thanks to Yan, Paul and Becky for fruitful discussions, and for a great trip to Japan.

I also spent time at Montserrat Volcano Observatory during this project, for which I owe thanks to Mark and Locko for helping to orchestrate it, and to Rod Stewart and the staff for making me feel so welcome whilst I was there. Thanks to Adam for the field assistance, Paddy for the glorious apartment, and Karen for the bush rum! Thanks too to Rob and Barbara for their friendship and weekend hikes.

I've had a very happy home in the Institute of Geophysics and Tectonics at Leeds, so a big thankyou to everyone who has helped along the way. Particular thanks to Susi for hot cider when I needed it, and for taking the time to help both my science and my wellbeing, and to Tim for helping with applications and being truly dedicated to IGT coffee. Studying at Leeds wouldn't have been the same without a lot of lovely people: Ruth, for endless cups of tea and theatre trips, and for always wanting a walk to get Fudge bars; Jennie, for cocktails, starters, and surprise desk bakes; Tom, for your endless patience with coding questions; Josh, for stupid dances and always being able to make me laugh; Sam, for debugging my MATLAB scripts and magically producing Python scripts in no time at all; James for helping with nasty FISH code and sharing the trials of the PhD experience; and Eduardo for the paper check-ins (and the nickname!). Everybody in Office 8.152 has helped this thesis in one way or another, and I am eternally grateful that you all eat my baking and ooh and aah in the right places.

Thanks too to the academic friends I wasn't lucky enough to share an office with. Thanks Phil for turning up at the times academia felt a bit lonely, and reminding me why science is cool, normally with a cocktail or two in hand. To Becky for being a reliable supplier of conference Nutella, and to Amelia, Jazmin, Janine, Dan and Sam for helping with science, but also for the friendship throughout.

A special thanks to Ben, for your proof-reading and debugging skills, but more importantly for being on my team and believing in me (even that time I was accidentally 12 orders of magnitude out). The write up process would have been a lot harder without you.

And finally, thanks to Mum and Dan. It's been a long slog, but I am so grateful to you both for always being interested, and listening to me be excited/distraught over dinner, but always encouraging me to keep going. Through every paper rejection, and every tiny triumph, your unwavering faith in me let me create a thesis that I'm really proud of, and I hope you both will be too.

Abstract

A lava dome collapse can lead to the generation of pyroclastic flows and debris avalanches, both of which are hazardous to areas surrounding the volcanic edifice. Although the understanding of lava dome emplacement and pyroclastic flows has improved in recent years, knowledge of the mechanisms that trigger collapse is still limited. In this project, I investigate lava dome collapse in three ways: (1) the implementation of a global, historical database of lava dome collapse events and its statistical analysis; (2) the development of a new numerical model simulating lava dome emplacement, evolution and collapse in the context of volcanic activity; and (3) exploration of temporal changes in geomechanical rock properties across the Soufrière Hills lava dome eruption.

First, a numerical model using the discrete element software *Particle Flow Code* is implemented and validated by showing how observed dome growth at Volcán de Colima can be reproduced. Next, the database analysis of the Global Archive of Dome Instabilities (*GLADIS*) highlights the most common mechanisms of lava dome collapse, and clearly links collapse volume to dome emplacement style. The identified collapse mechanisms (e.g. gravitational failure, switch in extrusion direction, internal gas overpressures, and topography) are incorporated into a new suite of numerical models. Simulations show that dome collapse resulting from gravitational failure and internal gas pressurisation leads to deep-seated rotational failures of large dome volume fractions, whereas topography-controlled collapses involve only superficial rockfalls. Lastly, an investigation into physical and mechanical rock properties of products from the 1995-2010 eruption of Soufrière Hills shows a clear correlation between high porosity (found in later eruptive products) and low compressive and tensile strengths. Laboratory investigations are used to define "strong" and "weak" scenarios which are incorporated in order to calibrate the numerical models, as well as scaling these rock properties to investigate dome stability when rock-mass properties are used.

By combining the analysis of a global database, laboratory work, and numerical modelling techniques, this project is a comprehensive study of the mechanisms that initiate lava dome collapse, and shows for the first time the links that exist between collapse volumes and modes, and conditions during lava dome emplacement.

Contents

List of Figures

List of Tables

Nomenclature

List of acronyms

ANOVA	Analysis of Variance
ASTM	American Society for Testing and Materials
BPM	Bonded Particle Method
BRV	Belham River Valley
DEM	Discrete Element Method
DRE	Dense Rock Equivalent
FEM	Finite Element Method
FJM	Flat-jointed contact model
GLADIS	Global Archive of Dome Instabilities
GSI	Geological Strength Index
GVP	Global Volcanism Program
ISRM	International Society for Rock Mechanics and Rock Engineering
MSH	Mount St. Helens
MVO	Montserrat Volcano Observatory
PBM	Parallel-bonded contact model
PFC	Particle Flow Code

QEMSCAN	Quantitative Evaluation of Minerals by Scanning electron microscopy
RMR	Rock Mass Rating
SHV	Soufrière Hills volcano
UCS	Uniaxial Compressive Strength
UTS	Uniaxial Tensile Strength
VEI	Volcanic Explosivity Index

List of symbols

ΔV	Absolute dome collapse volume	[10^6 m^3]
ϕ	Angle of internal friction	[°]
σ	Principal stress	[MPa]
ε	Strain	
E	Young's modulus	[GPa]
k_n	Normal stiffness	[MPa]
k_s	Shear stiffness	[MPa]
R_L	Schmidt hammer rebound value	
V	Original dome volume	[10^6 m^3]

Chapter 1

Introduction

Lava domes form when highly viscous lava is extruded from a volcanic vent and cannot flow far away so piles up, often in pre-existing calderas. Dome-building eruptions account for approximately 6% of volcanic eruptions around the world (*Calder et al.*, 2015) and are often linked with highly explosive activity (*Ogburn et al.*, 2015). Lava domes can collapse, forming pyroclastic flows and debris avalanches; these products can be very hazardous to populations surrounding the volcano, and yet there is still a limited understanding of what initiates these processes. Despite various modelling efforts examining the emplacement of a lava dome (e.g. *Buisson and Merle*, 2002; *Hale and Wadge*, 2003, 2005; *Hale*, 2008) and the flow-paths of resultant products (e.g. *Wadge et al.*, 1998; *Roche et al.*, 2004; *Saucedo et al.*, 2005; *Smith et al.*, 2018), there are still very few studies that examine the processes that trigger the collapse.

This project addresses this gap in knowledge by investigating the process of collapse initiation, and how the collapse process is affected by the condition of a lava dome prior to its failure. I address this using three main methods: (1) compilation and statistical analysis of a global and historical database of lava dome collapse events, as presented in Chapter 2; (2) creation of a new discrete element model and investigation of the effect of triggering mechanisms on the stability of a modelled dome, as presented in Chapter 3; and (3) determination of the heterogeneous nature of lava dome rock properties at Soufrière Hills volcano, as shown in Chapter 4. In Chapter 5, I incorporate rock properties characterised in Chapter 4 into models presented in Chapter 3 to assess the effect of rock strength on overall dome stability, and to discuss how this influences the current state of knowledge on lava dome collapse.

In this opening Chapter, I present background information on lava domes and

their structure. I review previous modelling studies (analogue, finite element, and discrete element), primarily simulating lava dome emplacement, but also those that examine collapse processes. I show why discrete element modelling techniques are used in this project, and explain how I calibrated the model using realistic rock properties. This highlights the need for the rock property characterisation presented in Chapter 4 and is pertinent to the models presented in Chapter 5. In this first Chapter, I also show how I have used observational data from Volcán de Colima to validate the modelling techniques that are used throughout this project. I will end this introductory Chapter by setting out my principle aim, my objectives, and describing the layout of this thesis.

1.1 Lava domes

1.1.1 Lava dome structure

There is still not a comprehensive understanding of the internal structure of a lava dome; this is primarily due to the difficulty in observing the dome interior. Dome collapse is the most likely method of exposing a cross section of a lava dome, but this process is often highly destructive and therefore leaves little evidence. A study at Volcán de Colima (*James and Varley*, 2012) found that the complexities of internal dome morphology played a vital role in the June 2011 explosion, and therefore in brittle failure of the dome. This confirms that understanding internal structure, and its evolution during emplacement, is important in developing overall understanding of a dome's structural stability.

The internal structure of the exposed submarine Showa Iwo-jima dome (*Maeno and Taniguchi*, 2006) was described as onion-like, but this is a rare example of direct observations of a lava dome's interior. Further ideas about the internal structure come from analogue and numerical modelling of lava dome emplacement, rather than from field observations.

The widely accepted model for lava dome structure comprises an internal fluid core, and an outer region that is solid and more frictionally controlled (Figure 1.1). The hypothesis that lava domes are a two-component system was first introduced by *Iverson* (1990), whereby a lava dome was characterised by an external shell of brittle rock. We now broadly understand that a transitional region exists between the core and talus, termed the carapace (Figure 1.1), although the relative proportions of each of these units are unknown. The term talus is twofold: it can be used to refer both to the solid outer region of the dome, and to

the slopes of loose material that aggregate during dome growth and small-scale instability. Although the term talus is used to describe both of these regions, it is important to note that any external shell will have a direct effect on the growth and morphology of the dome, whereas the effect of mechanically detached talus slopes will be indirect, through the application of confining pressure and the topographical effect of steep slopes of disaggregated rocks. The region termed talus in Figure 1.1 includes both the intact shell and the mechanically detached slopes, although the modelling approaches presented later in this project primarily consider the intact shell (discussed further in Section 3.2.2 and Section 5.4.5).

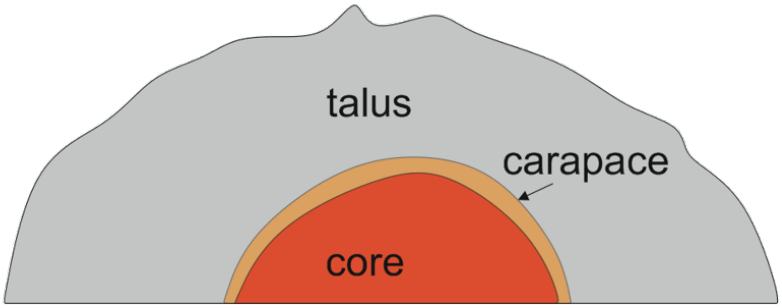

Figure 1.1: Conceptual diagram to show internal lava dome structure.

Wadge et al. (2009) described lava domes as comprising four distinct units: a lava core; an upper carapace; talus slopes (accumulated through dome disaggregation and rockfall generation); and more distal pyroclastic flow deposits. Relative volume fraction estimates were made for the Soufrière Hills volcano (SHV) between 1999 and 2007 (*Wadge et al.*, 2009). Core volume fraction ranged from 11-35% and talus volume ranged from 30-58%, although there were large uncertainties (∼25%) associated with these values due to the lack of knowledge regarding shape of the core within the dome. *Wadge et al.* (2009) concluded that a lava dome that already has a large portion of its material in the form of disaggregated talus slopes may be less hazardous.

1.1.2 Growth styles

Lava dome growth is primarily split into two growth styles: endogenous and exogenous (Figure 1.2). Endogenous growth is defined as new magma intruding into the dome, e.g. injection into the base of the dome causing expansion, whereas exogenous growth occurs when magma can reach the surface and extrude as new lobes or spines. The latter generally requires lava to be able to force itself through

a pre-existing solid carapace in order to reach the surface (*Calder et al.*, 2015). A dome often does not grow purely endogenously or exogenously, but can also grow through intermittent pulses of each growth style, or by switching from one style to the other. This can happen over longer day to month timescales (e.g *Nakada et al.*, 1995), or short term fluctuations in growth style can occur daily (e.g. *Watts et al.*, 2002).

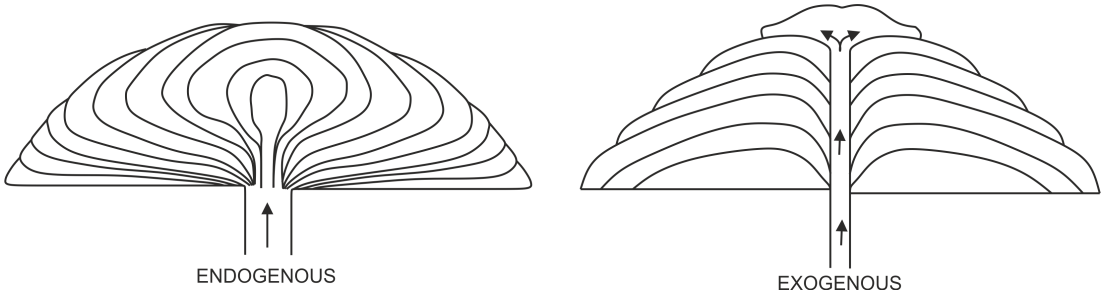

Figure 1.2: Sketch to show endogenous vs. exogenous lava dome growth. Reproduced from *Kilburn and Luongo* (1993).

Understanding the evolution of lava dome growth is of particular importance as a transition in growth style often occurs following collapse events, probably due to changes in magma supply (*Hale and Wadge*, 2008). The growth style also significantly impacts dome morphology (e.g. spine generation only occurs during exogenous growth), and this can have an impact on likely collapse modes and volumes.

1.1.3 Dome morphology

The morphology of a lava dome depends on factors such as composition, extrusion rate, and eruption temperature, all of which determine the rheology of the erupted material. *Blake* (1990) categorised dome morphology into four groups: upheaved plugs, Peléean domes, low lava domes, and coulées (Figure 1.3). Upheaved plugs occur when the extruded material is viscous enough that it does not deform upon exiting the conduit, and therefore the width of the plug is equal to the radius of the conduit. Peléean domes are characterised by steep talus slopes, and often have spines that extrude from the surface (a process similar to that of upheaved plugs). Low lava domes, however, are not characterised by steep slopes but instead are rounded in shape due to less viscous magma. Coulées are similar to low lava domes, but form on a gently inclined surface so that the flow dynamics are determined not only by the magma rheology, but also by the nature of the topography.

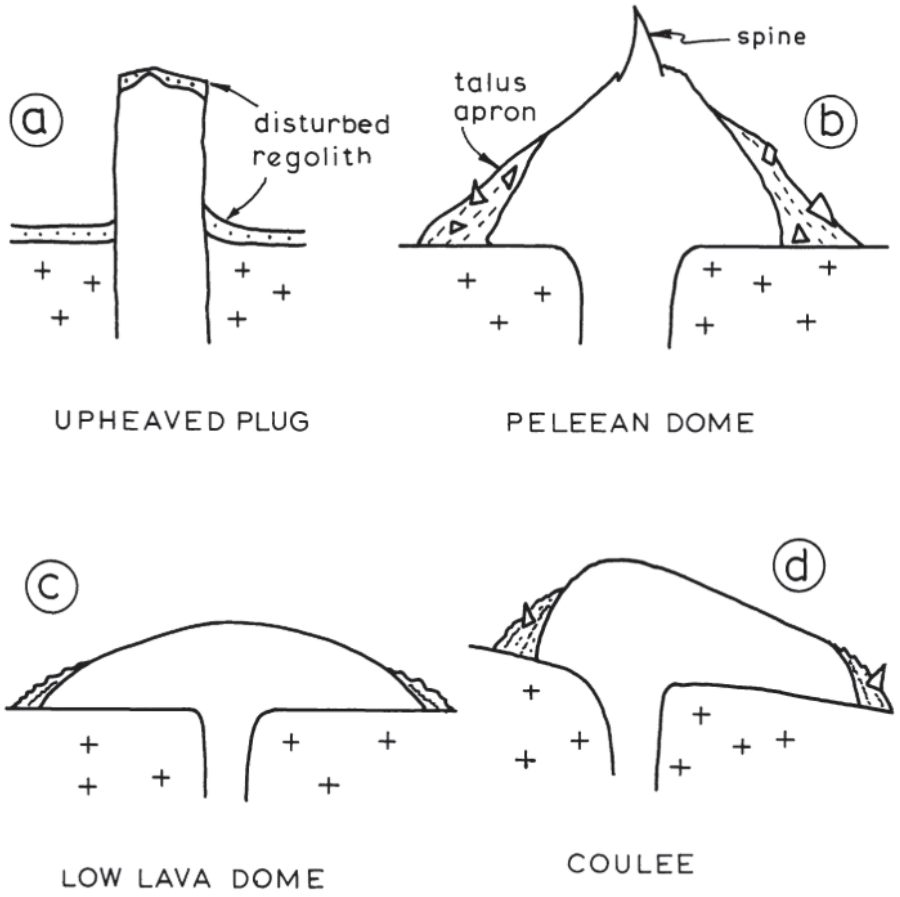

Figure 1.3: Sketches showing the distinguishing features, seen in cross-section, of the four types of domes determined by *Blake* (1990). Figure adopted from *Blake* (1990).

Blake (1990) suggested that the morphology of Peléean domes is determined by the mechanical properties of the talus material, whereas low lava dome and coulée morphology is governed by the mechanical and rheological properties of the magma. Of these four dome groups, Peléean domes are most likely to undergo collapse due to the steep slopes (generally with a height to radius ratio of 0.6-0.9). Any collapse experienced at a coulée-style dome is a flow-front type collapse, and is shallow so involves a limited volume of dome material.

Further work was undertaken on dome morphology following the early eruption of SHV (*Watts et al.*, 2002), where dome morphologies were defined as a function of degassing-induced crystallisation during ascent. Dome morphologies were classified as near-vertical spines, whaleback structures, megaspines, shear lobes and pancake lobes. In this classification, pancake lobes are similar to Blake's definition of low lava domes, but are less rounded and have low, steep sides.

1.1.4 Lava dome collapse

Lava domes often grow slowly, within a crater or previous collapse scar, giving the impression that they are stable landforms. Lava domes are, however, frequently unstable and undergo collapse, including events that destroy the entire dome. A big dome collapse can form pyroclastic flows which are one of the most hazardous products of a volcano as they are fast-moving, turbulent mixtures of rock fragments, gas and ash (*Branney and Kokelaar*, 2002). Collapses occur in multiple forms, ranging from small-scale rockfalls to large, deep-seated rotational failures. At an actively growing lava dome, it is common for small-scale rockfalls to occur almost continuously, while larger collapses occur less frequently and are often harder to forecast. The spectrum of individual events that are referred to by the term collapse are defined further in Section 2.3.1.

The first mention of a dome collapse in the literature was following the destruction of a lava spine during the 1902-1905 eruption of Mt. Pelée, Martinique (*Tanguy*, 2004). Despite further lava dome collapses occurring in the early 20th century (e.g. at Merapi, Indonesia (*Voight et al.*, 2000) and Volcán de Colima, Mexico (*Gonzalez et al.*, 2002)), the hazards associated with lava dome instability were really brought to the forefront of media attention in 1980 with the lateral blast at Mount St. Helens. The hazard at Mount St. Helens was underestimated due to the explosive nature of the event, which occurred due to the exposure of the cryptodome core following a landslide, and led to 57 fatalities. This tragedy sparked a wealth of research into volcanology in general, and more specifically volcanic instability.

This avenue of research was further broadened by the dome-forming 1995-2010 eruption of Soufrière Hills volcano, Montserrat. This is one of the most intensely-studied eruptions, and the quantity and quality of observations greatly furthered knowledge regarding lava dome collapse. A comprehensive review of this eruption, and other historical collapse events, enabled common triggers of collapse to be determined as part of this project, shown by the compilation and analysis of a collapse event database in Chapter 2. These include but are not limited to: over-steepening leading to gravitational failure; seismicity; weathering; a change in growth direction; over-pressurisation of the dome interior; and heavy rainfall. These triggering mechanisms and the conditions of a lava dome prior to its collapse are more thoroughly explored in Chapter 2.

1.2 Previous modelling studies

Modelling lava dome growth and collapse is challenging due to the number of different complex processes that are involved. To fully model emplacement, an understanding of rheology, temperature profile, cooling rate, and extrusion dynamics is required. It is important to note that dome emplacement and dome collapse have traditionally been approached using separate modelling techniques (*Hale and Wadge*, 2005), but collapse most commonly occurs during active dome growth, and so it is perhaps questionable to model these processes using separate methods. Most lava dome models to date focus on the emplacement of the lava dome, and so these are also discussed here for completeness.

1.2.1 Analogue emplacement modelling

Analogue lava dome emplacement models can be broadly split into two categories: those that use a simple Newtonian fluid, and those that incorporate non-Newtonian rheologies by introducing Bingham fluid dynamics. A Newtonian fluid is one in which the relationship between shear stress and shear rate is linear, e.g. water, whereas the constant viscosity in a non-Newtonian fluid is independent of stress. There are various types of non-Newtonian fluids, including shear-thickening, shear-thinning, and Bingham plastic materials. Shear-thickening fluids experience an increase in apparent viscosity with increased stress (e.g. oobleck), whilst shear-thinning fluid viscosity decreases with stress (e.g. nail polish). In a Bingham material, a finite yield stress must be applied before the material can flow, e.g. toothpaste or mayonnaise (Figure 1.4).

Huppert et al. (1982) presented a theoretical approach to lava dome growth considering a Newtonian fluid with constant viscosity, spreading on a rigid horizontal surface. The theoretical calculations were followed by a laboratory study using a viscous fluid that was released and allowed to spread, recording the morphology evolution as a function of time.

The study modelled the temporal evolution in dome height and width, as well as the actual profile of the dome, which they fitted to observational data from La Soufrière (Figures 1.5a, b). The model was found to fit observational data well during early extrusion, but diverged progressively over time (i.e. the model predicted that spreading should continue indefinitely which does not occur in observations). The study concluded that this was due to the Newtonian fluid not representing the retaining strength of the flow front, which can be interpreted

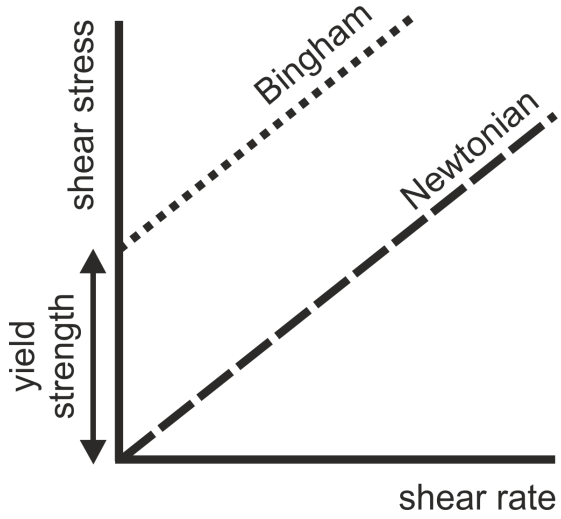

Figure 1.4: Sketch to show behaviour of Newtonian vs. Bingham materials.

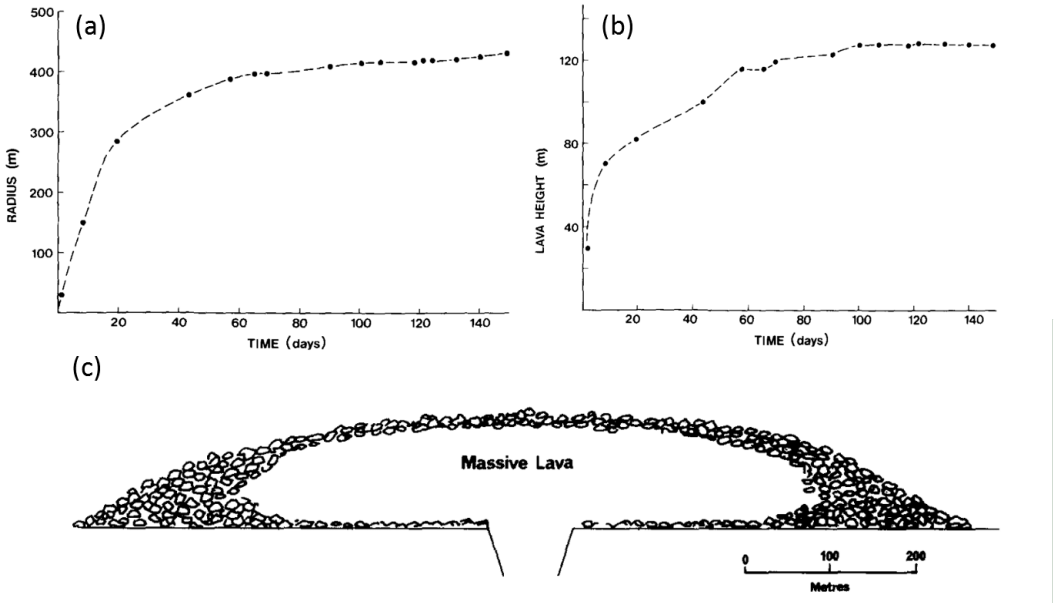

Figure 1.5: **(a)** Radius of the 1979 La Soufrière dome as a function of time; **(b)** height of the centre of the 1979 lava above the crater floor; and **(c)** schematic section through the flow front of 1979 lava. All figures adapted from *Huppert et al.* (1982).

to more broadly refer to the development of mechanical yield strength in lava as it cools, shown by the outer blockier region in Figure 1.5c. This flow front schematic is very similar to the current understanding of internal dome structure (Figure 1.1).

Later, *Blake* (1990) performed laboratory experiments using a kaolin slurry (which acts as a Bingham material) to emplace domes onto a horizontal base plane of cartridge paper and track the height/radius evolution and the advance

of surface markers. These analogue models showed approximately parabolic dome profiles, suggesting they best simulated low lava domes (see Section 1.1.3). *Blake* (1990) also found that low lava domes could be distinguished from Peléean lava domes by the ratio of dome height to lava yield strength, whereby Peléean domes typically have high yield strengths (at least 1-10 MPa) which create a talus collar and leave Peléean domes prone to explosions.

These early experiments neglected to fully consider the role of cooling in dome growth, as noted by *Griffiths and Fink* (1993). This study observed that spreading of lava above a vent will at some point cease, whereas if the fluid was purely viscous, the strain rate should never vanish. This allowed *Griffiths and Fink* (1993) to distinguish two types of flow: volume limited and cooling limited. In a volume limited flow the yield strength of the magma at the erupted temperature is able to oppose spreading, whereas in a cooling limited flow the spreading is stopped by the material strength that is obtained through heat loss. The study uses a temperature-controlled wax to enable a stiffer crust that still behaves dynamically (i.e. is not fixed) and assumes that this crust is: (a) rheologically distinct; (b) thin in comparison to the flow depth; and (c) not continually re-encompassed by the magma interior. *Griffiths and Fink* (1993) conclude that an outer crust with thickness of 10 m is sufficient to control the spreading of a dome that is 1 km wide; that is to say that in order to control material spreading, the ratio of the thickness of the crust to the thickness of the flow must be proportional to the ratio of the yield strength of the solid carapace to the shear strength of the magma. The inferred recommendation from this study was that future models should include an outer crust in order to model lava dome evolution more accurately.

Fink and Griffiths (1998) undertook analogue modelling using polyethylene glycol wax as it acts as a Newtonian fluid when molten, and can act both in a brittle and ductile manner when solid, dependent on stress application and temperature. These analogue experiments result in the proposal of a new dome classification scheme that is dependent upon the volume of lava erupted and the interior yield strength of the erupted material; these domes were classified into: spiny domes, lobate domes, platy domes and axisymmetric domes.

Buisson and Merle (2002) then conducted experiments vertically injecting a viscous (isothermal Newtonian) fluid onto a non-deformable horizontal base, and investigated the internal strains that occurred in the growing dome (Figure 1.6a), as these are otherwise unobservable. They compared the height-radius evolution to the analytical model derived by *Huppert et al.* (1982, Figure 1.6b), and found

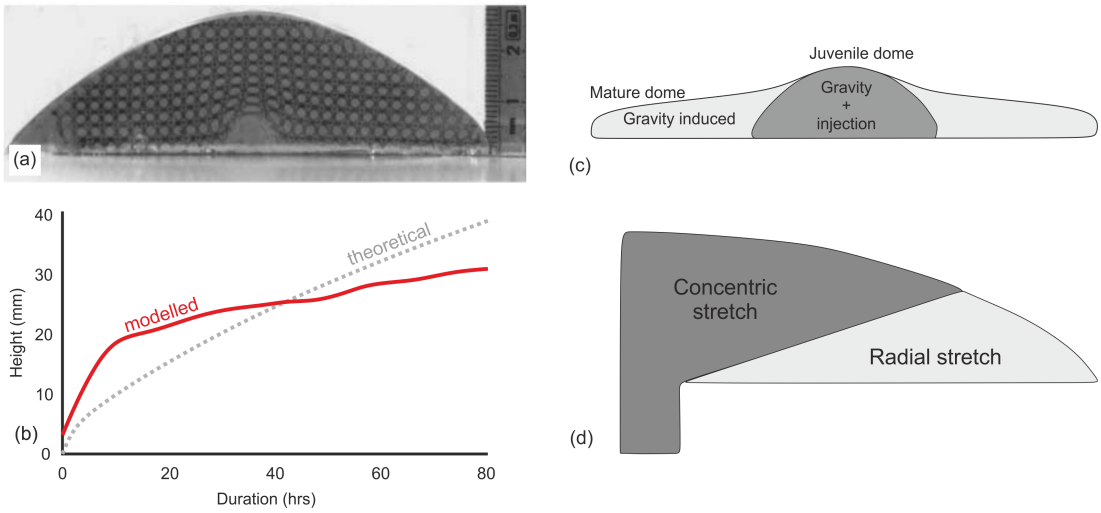

Figure 1.6: **(a)** Photograph of 2D experiment showing deformation of square and circle elements after injection of silicone; **(b)** Dome height evolution from analogue experimental model, and according to the theoretical equation from *Huppert et al.* (1982); **(c)** Conceptual sketch showing shape evolution from juvenile to mature dome; **(d)** Spatial distribution of radial and concentric stretching fields within a vertical section of a lava dome. Figures (a) - (c) adapted from *Buisson and Merle* (2002), and Figure (d) adapted from *Buisson and Merle* (2004).

a reasonably good match. The height evolution in the model had a steep initial increase, and then at a critical height, the vertical growth slowed. This is very similar to the observational data at La Soufrière in 1979, recorded by *Huppert et al.* (1982) and shown in Figure 1.5b.

Buisson and Merle (2002) showed that a lava dome comprises a central region where strain results from both gravity and vertical injection of material, and lateral zones where the strain domain is entirely gravity-induced (Figure 1.6c). Temporal analysis of the experiments showed that once the lateral regions existed, the shape of the central region did not evolve further. *Buisson and Merle* (2004) followed their analogue visualisation of strain within lava domes with a numerical approach to the same phenomenon. This study determined that the dome could be split into two areas: a central region of concentric stretch and a more lateral region of radial stretch (Figure 1.6d).

The combined efforts of various analogue modellers showed that a Newtonian fluid was insufficient to model lava dome growth, and more appropriate results were obtained by the use of a Bingham material, or an isothermal Newtonian fluid.

1.2.2 Numerical modelling studies

Numerical modelling efforts have taken the form of two main modelling methodologies: (1) finite element method and (2) discrete element method (Figure 1.7).

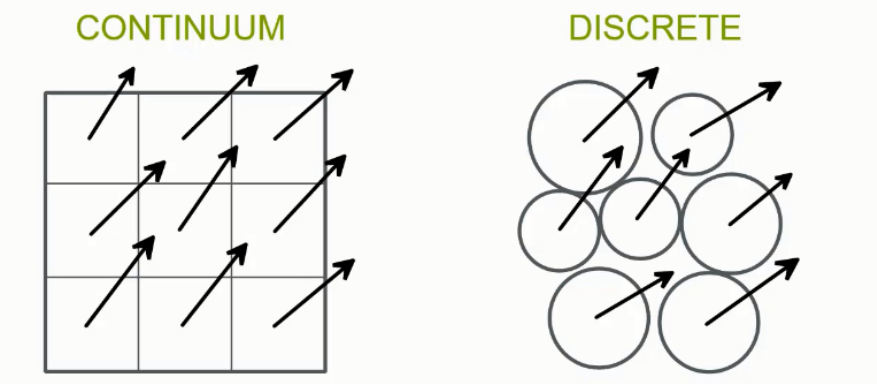

Figure 1.7: Conceptual representation of finite and discrete element modelling methodology. Credit: Mariana Sousani.

The finite element method (FEM) is generally used to calculate the solution to boundary value problems by solving partial differential equations. FEM subdivides the model domain into sections, normally termed zones, and each sub-domain solves a set of equations. These equations are then systematically recombined into a global set of equations. The modelled material is treated as a *continuum*, but an advantage of this method is that different zones can be assigned different mechanical properties. A disadvantage, however, is that the nature of the continuum requires the functions to be continuous across neighbouring zones, and as such, large displacements and strains are difficult to compute and make an FEM model computationally and numerically unstable. The movement of individual zones is used only to derive the bulk material response.

The discrete element method (DEM) was designed to address some of the limitations of FEM, and comprises a material made from individual particles. The DEM numerically calculates finite particle displacements and rotations, hence treating the material as a *discontinuum*. Each particle is a unique quantity and macroscopic behaviour results from individual particle interactions. This is useful for systems that are dependent on particle level behaviour, for example in the context of this project, large-scale dome stability can be affected by small-scale rockfalls and talus readjustment. DEM can also result in more accurate micro-mechanics due to the introduction of particle contact models.

Finite Element Method

In more recent years, there have been increased efforts to model lava dome growth numerically. A series of papers was published from 2003 onwards, led by Alina Hale, which used the finite element method (FEM) to model the growth dynamics of lava domes. These models revisited the idea first posed by *Iverson* (1990) that a dome must include both a malleable interior and a brittle carapace. The main findings from the initial study (*Hale and Wadge*, 2003) agreed with the analogue models, and found that the use of a purely Newtonian fluid was inadequate, and the inclusion of a solid carapace was essential in order to reproduce lava dome behaviour, using the example of the 1980 Mt St. Helens dome. *Hale et al.* (2007) used the level set method, a numerical technique first introduced by (*Sussman et al.*, 1994), to track the free surface of the dome without altering the finite element mesh. One benefit of this technique was that it did not require an initial condition of material above the surface, and so overcame the finding from the earlier study (2003) that the initial free surface shape could influence the final dome morphology. The 2007 study also concluded that a lava dome model requires both gravity and lava injection forces to be calculated, thus rendering a purely analytical solution insufficient. This study advanced the state of knowledge regarding computational modelling of lava domes but still did not include any resisting force within the talus material.

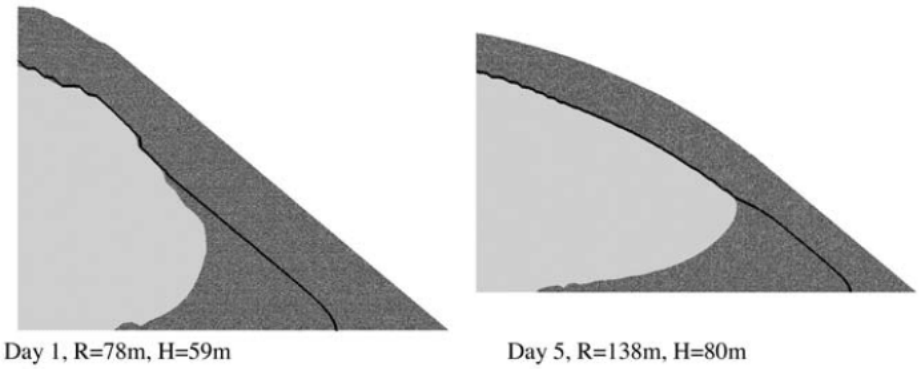

Figure 1.8: Evolution of 2D slices from a FEM model showing how height and radius vary over time, and using the level-set method to track the rheological interface. Core material shown to override talus substrate. Figure from *Hale* (2008).

Hale (2008) built a new FEM lava dome model that included an independently deformable talus region for the first time (Figure 1.8). The study described lava dome growth as occurring on two timescales: (1) continuous expansion

due to magma addition, and (2) readjustment of the talus material that has become detached from the main body of the dome. This study implemented the so-called solidus pressure for the first time to track the rheological interface between the core and the talus, where the solidus pressure marked the transition of magma from liquid to a crystallised solid state, discussed further in Section 3.2.2. By using the solidus pressure, the model incorporated pressure as a proxy for temperature (with the assumption that every thermal state has an equal pressure state; described further in Figure 3.2). One of the most significant findings of this study was that the core material was not strong enough to horizontally displace the talus, but rather core material was able to override the talus material and laterally spread (Figure 1.8). This was the first time that this complex morphology of the rheological interface had been shown in a numerical lava dome emplacement model. This morphology was perhaps not surprising considering the similarity between this and the schematic flow front section from *Huppert et al.* (1982) (Figure 1.5c).

The final two-part study by *Hale et al.* (2009a,b) approximated the readjustment of the talus slope as a critical-angle problem, in that the model could not simulate small-scale toppling or disaggregation of material, but the angle of the free surface of the dome could be interpreted as replicating these larger scale processes. This study also followed on from previous work (*Hale and Wadge*, 2008) by examining the evolution of shear bands as a marker of the transition from endogenous to exogenous behaviour. The paper discussed the difficulties of conducting field observations of potential lateral spreading of the core: surface deformation measurements would likely be masked by the disaggregation and addition of talus material, and so deformation deeper within the dome would be undetectable. Rockfalls were proposed as an alternative method of detecting the nature of spreading of the core material; if deformation of the talus is localised, it suggests core spreading in one direction (e.g. lobe dominated growth) whereas if rockfall occurrence is evenly distributed across the dome, it suggests that the core is growing equally in all directions, as occurs in endogenous growth. Rockfalls were further investigated in the second part of the study (*Hale et al.*, 2009b), but the model was limited in its exploration of discontinuous or non-equilibrium behaviour, and therefore was unable to accurately model the short term, non-equilibrium, asymmetric nature of rockfalls.

Discrete Element Method modelling

The discrete element method (DEM) is used to compute the motion of a large number of particles, as opposed to the solution of boundary value problems in the finite element method. *Husain et al.* (2014) used the DEM with the aim of understanding more about the internal structure of a lava dome. Using the software *Particle Flow Code* (PFC) from Itasca Consulting Group Inc., a model was designed whereby material was extruded on to a rigid horizontal substrate, fed by a vertical conduit. The magma in this model is most analogous to a Bingham plastic material, as it possesses a yield strength (represented by the bond strength that exists at the contacts between each particle in PFC). *Husain et al.* (2014) used the magma's solidus pressure to define a unidirectional transition from core to talus material. The talus material was given higher values of material stiffness and strength to ensure a constricting force was exerted on the ductile core by the outer shell. The study focused particularly on the sensitivity of the dome morphology to:

1. **Material stiffness**
   Material stiffness was analogous to viscosity in this study (discussed further in Section 3.2.2), and the models showed increased dome height with increased stiffness. Growth of the dome core was concentrated above the conduit exit with higher stiffness values, while lower stiffness values promoted more lateral spreading of the dome core.

2. **Friction**
   The friction coefficient controls the way in which the talus material forms a volcanic pile, and as such indirectly impacts the magnitude of force exerted on the core by the talus. Again the model showed more lateral spreading with lower friction. Angle of repose was also affected, but overall, there was very little influence of the coefficient of friction on the final dome morphology.

3. **Cohesion**
   The strength of the bonds within the model were equated to the overall material strength by *Husain et al.* (2014). A greater bond strength exhibited more spine-like features during dome evolution.

4. **Extrusion rate**
   The study claimed a significant effect of extrusion rate on dome geometry.

Core growth was concentrated towards the central conduit of the dome with lower extrusion rates, and there was a lower relative proportion of core to talus.

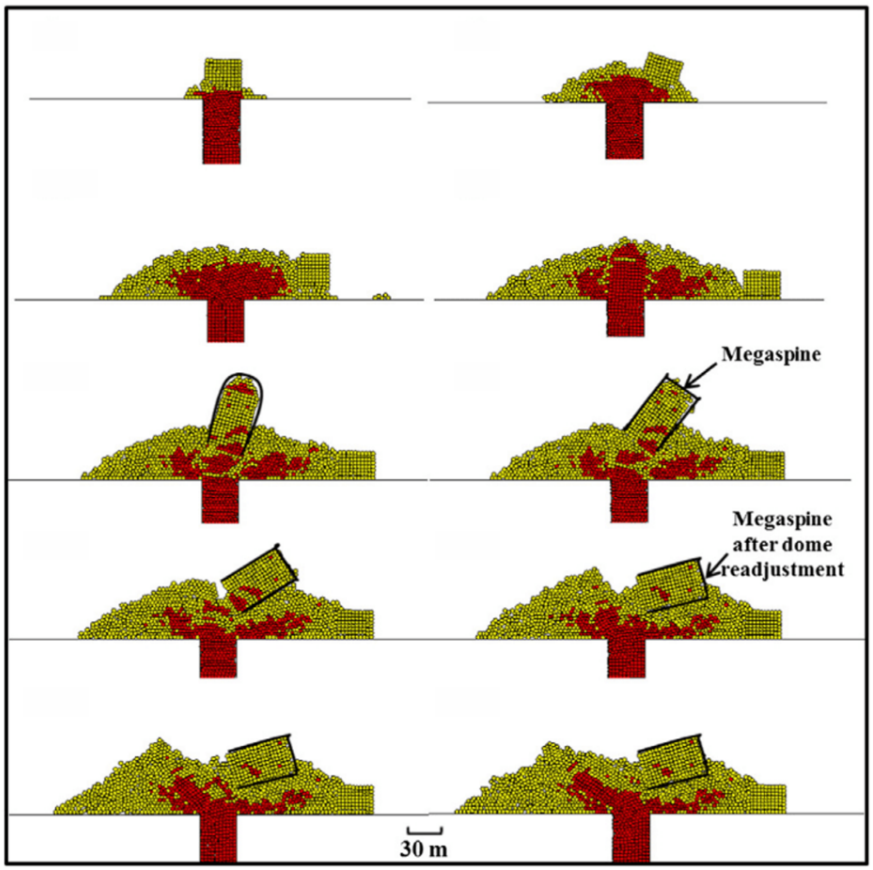

Figure 1.9: Lava dome morphology variation, from a model designed to replicate the lava dome evolution from June to July, 1996 at SHV, from *Husain et al.* (2014). Red particles are fluid core material, whilst yellow particles are solid talus material.

In addition to a parametric sensitivity analysis, *Husain et al.* (2014) focused on growth of the SHV dome from June to July 1996 (Figure 1.9). They mimicked the flow rate history and showed the following behaviour, designed to replicate the structure observed on 13 July 1996: (a) initial vertical extrusion due to lack of overlying material to provide resistance; (b) extruded lava began to collapse under weight of overlying column of material; (c) flow pattern changed to endogenous growth as material strength was insufficient to push through the stronger outer carapace; (d) pause in extrusion and further solidification of lava modelled by increasing stiffness and strength of conduit material, showing the development of a viscous plug; (e) extrusion was resumed and degassed plug extrudes upwards.

The study concluded that the strength and stiffness of the core magma exerted more control over dome morphology than frictional strength of the evolving talus. Spine growth only occurred at low extrusion rates and higher stiffness/strength combinations, whilst lower stiffness/strength and higher flow rates led to endogenous growth and no spine development.

This study was followed by *Husain et al.* (2018), where the authors focused on modelling pulsation sequences and the associated rheological changes at both SHV and Mount St. Helens. In pauses between extrusive activity, the model material experienced rheological stiffening (i.e. increase in bond strength). This study also found sagging and spreading of the domes between extrusion pulses.

The most recent publication from this series of discrete element models (*Husain et al.*, 2019) presented a suite of simulations, in which magma possessed a yield strength (as in Figure 1.4). This means that the models considered material stiffening and strengthening prior to solidification thus creating a non-Newtonian rheology, i.e. the material behaved as a stiffer liquid before it fully transitioned into the solid state. The models presented by *Husain et al.* (2019) correlated well with the analytical models from *Blake* (1990), and showed how the apparent viscosity of the magma was able to influence the magma rheology and growth style.

The numerical modelling undertaken by *Husain et al.* (2014, 2018, 2019) provides a promising new avenue for lava dome collapse research. These studies demonstrated that PFC could successfully be used to model large scale rock masses in volcanology, and showed morphologies that are qualitatively similar to those observed in the field. One of the main benefits of using discrete element modelling is the complexity in morphology that can be simulated (i.e. on a particle scale, rather than deformation of a fixed boundary in FEM). FEM becomes computationally expensive when the modelled problem involves large strains, and these often result in numerical instabilities. Although computational expense also increases in a DEM with large strains, DEM is specifically designed to avoid the need for such extensive re-meshing. Using the discrete element method also allows investigation of small scale rockfall-type collapses, whereas this detail would be hard to discern from an FEM model.

In this project, I use the same software (PFC) as *Husain et al.* (2014) to create a new DEM model to examine the process of lava dome collapse. Unlike the previous studies, the models presented in this project will maintain a constant viscosity, vary the solidus pressure, and be designed to focus more on the collapse process rather than dome emplacement and morphology. The models presented

in Chapter 3 incorporate new particle bonding capabilities introduced in PFC5.0, as outlined in Appendix A.2.1. This new particle bonding better simulates the behaviour of rock (*Potyondy*, 2012), and so is a more appropriate representation of talus material.

DEM still requires an initial free surface to be defined but in the model presented here, this occurs within the conduit rather than above the surface, and therefore the morphology of this free surface does not dictate overall dome morphology, as seen in previous FEM models (*Hale and Wadge*, 2003). I use the same concept as previous models (*Hale et al.*, 2009a,b; *Husain et al.*, 2014) in defining a transition point between core and talus material using a solidus pressure. The modelling method implemented in PFC is outlined in more detail in Appendix A.1, followed by validation of the dome emplacement model using observational data from Volcán de Colima in Section 1.4. Further methodology and details of model setup are provided in the published paper (*Harnett et al.*, 2018) presented in Chapter 3.

1.3 Improving PFC models using calibration

PFC, the modelling software used by *Husain et al.* (2014, 2018, 2019) and incorporated here, is a commercial software from the Itasca Consulting Group Inc. and employs the discrete element method proposed by *Cundall and Strack* (1979). Particles interact via contacts, which are installed at all particle-particle boundaries, and material behaviour is controlled by the micro-properties that exist at these contacts. These micro-properties are not equivalent to the macro-properties of the material as a whole. Therefore, a calibration procedure is required to determine the micro-properties that result in the same macro-behaviour of the solid model material to the real material in the laboratory. This calibration procedure is documented by various authors (e.g. *Holt et al.*, 2005; *Cho et al.*, 2007; *Wang and Tonon*, 2009; *Zhang et al.*, 2011; *Kazerani et al.*, 2012; *Potyondy*, 2015), and has been used in volcano-related deformation models by *Schöpfer et al.* (2007) and *Holohan et al.* (2011, 2017).

In order to determine the micro-properties required to match the macro-behaviour of a rock in the laboratory, I simulated uniaxial compression testing and Brazilian disk testing in PFC. I then compared the unconfined strength, indirect tensile strength, and Young's modulus between the real and synthetic samples. Although *Wu and Xu* (2016) and *Potyondy and Cundall*

(2004) suggested calibration procedures, the procedures involved iteratively changing various parameters and do not provide a streamlined approach to material calibration. I have adopted an iterative approach here to define the correct input parameters in PFC.

This iterative approach generally follows three steps:

1. Adjust contact stiffness to obtain correct macro Young's modulus
2. Adjust cohesion to obtain correct macro uniaxial compressive strength (UCS)
3. Adjust tensile strength to obtain correct macro uniaxial tensile strength (UTS), and therefore correct UCS/UTS ratio

The uniaxial compression test in PFC first required generation of a material of equal size to the samples tested in the laboratory. I followed the specific material genesis procedure outlined in Appendix A.2.2 to ensure that the material had low locked-in stresses and was isotropic and homogeneous. Once the material genesis was complete, uniaxial compression testing was carried out in PFC by applying a velocity to the two walls at the top and bottom of the sample (simulating loading platens in the laboratory) until the stress fell below 90% of the peak stress. The loading rate applied to the walls in PFC was 0.05 m/s. Although this was much faster than the rate of 0.1 mm/s (1×10^{-4} m/s) that was applied in the laboratory, the actual time step in each calculation cycle was chosen to be small enough that this loading rate still allowed sufficient time for micro-structural readjustment (*Potyondy and Cundall*, 2004; *Diederichs*, 1999; *Cho*, 2008).

For model calibration in PFC, I used rock samples collected from Montserrat during a field campaign in January 2016 (Figure 1.10). These samples were collected from Phase 1 deposits of the eruption of Soufrière Hills volcano (see Chapter 4 for eruptive history at Soufrière Hills volcano), and were collected at the Phase 1 site shown in Figure 4.1; these tests are not included in the results later shown in Chapter 4. I conducted compressive rock testing (both uniaxial and triaxial) at the Rock Mechanics, Engineering Geology and Hydrology laboratory at the University of Leeds. I carried out this testing on 37 mm samples after coring the rock samples and grinding the ends to be parallel; these methodologies are the same as outlined in Sections 4.3.2 and 4.3.6.

Figure 1.11 compares the behaviour of the material both in the laboratory and in the synthetic PFC experiment. The PFC material exhibited more linear behaviour because no pore spaces or initial fracture networks were explicitly built

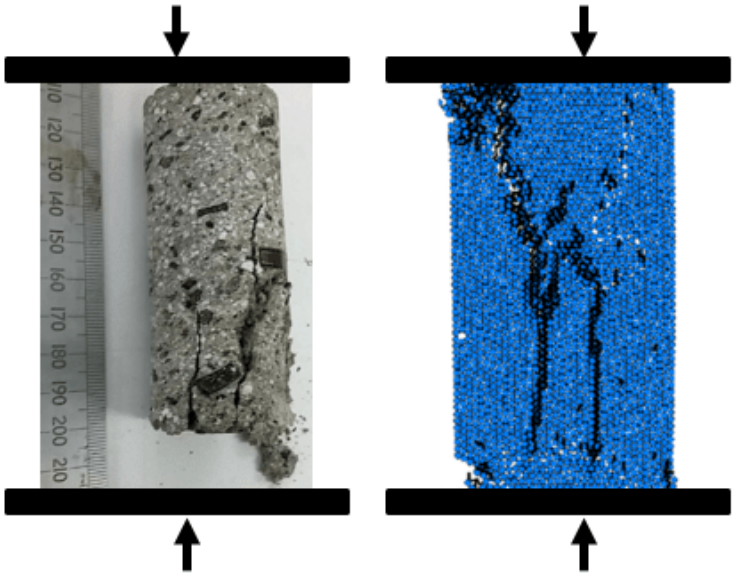

Figure 1.10: Example of comparison of a real rock after failure, and a PFC synthetic rock after failure, where black shows damage accumulation via bond breakage.

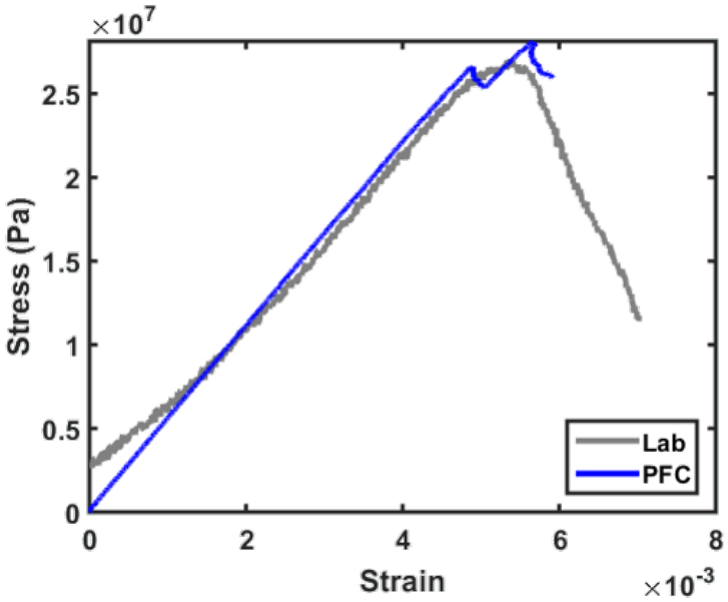

Figure 1.11: A comparison of the stress-strain response of the macro-scale behaviour of real rock in the laboratory (from Phase 1 of the eruption of SHV) and a synthetic PFC sample.

into the sample. As a result of this there was no initial pore or crack closure and therefore D' (the point at which compaction becomes dilation; Figure A.5) was not reached, but rather dilation occurred from the beginning of the test. Aside from this difference the two materials had a very similar stress-strain response, as exhibited by the similar macro-responses in each case (Table 1.1). The PFC experiment is programmed to cease when the stress reaches 90% of the modelled peak stress and the post peak behaviour is not considered in this calibration. Both the laboratory rock and synthetic rock are shown post-failure in Figure 1.10.

I then used these micro-properties to run a suite of laboratory-style tests in PFC to simulate material behaviour at increased confining pressures. This demonstrated that PFC is able to accurately represent the behaviour of a real rock both at ambient conditions and at depth. If the failure envelope of the PFC material matches that of the laboratory samples, calibration is complete and modelling of larger-scale scenarios can be conducted.

I therefore conducted triaxial laboratory tests on 37 mm cores of the same material as uniaxially tested. Confining pressures tests (at 3.5 MPa, 7.5 MPa, 10 MPa, and 15 MPa) showed the behaviour of the rock at increased depths. The results of these are shown in Figure 1.12. I fitted the data with a Mohr-Coulomb failure criterion and show this here in principal stress space using

$$\sigma_1 = \frac{2\cos\phi}{1-\sin\phi} + \frac{1+\sin\phi}{1-\sin\phi}\sigma_3, \tag{1.1}$$

where ϕ is the material's angle of internal friction.

Parameter	Experimental (Lab)	Numerical (PFC)
Porosity	16.5%	15.9%
Young's modulus	5.5 GPa	5.5 GPa
Uniaxial compressive strength	27.1 MPa	26.9 MPa
Tensile strength	3.2 MPa	3.1 MPa
UTS/UCS ratio	0.1	0.1

Table 1.1: Macro-properties of Phase 1 from laboratory experiments, compared to the equivalent calibrated synthetic material in PFC.

By calibrating the modelled material, it is possible to incorporate a more realistic solid material behaviour into the numerical model. This is a key advance presented in this project compared to previous studies, as calibration has not previously been undertaken in DEM models of lava domes.

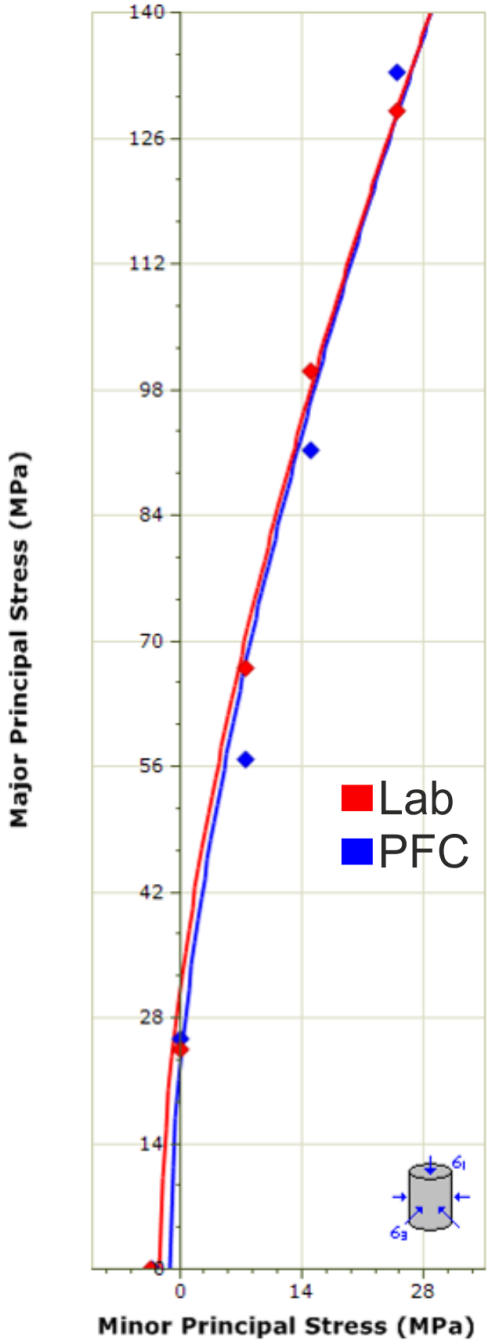

Figure 1.12: A comparison of failure envelopes for both real SHV material in the laboratory and synthetic material in PFC, fitted with a Mohr-Coulomb failure criterion.

1.4 PFC model validation: dome growth at Volcán de Colima

In order to validate the PFC models presented throughout this study, I used a discrete element model created in PFC to simulate lava dome growth at Volcán de Colima, and compared it to observational data (*Walter et al.*, 2019). I used height and radius estimates of the dome during active growth from February to March 2013 due to the high temporal resolution. The method used to create the model is further outlined in Appendix A and Chapter 3, and the results published in *Walter et al.* (2019). The model simulated a magma viscosity of 10^9 Pa s, following estimates of apparent magma viscosity at Volcán de Colima in the range 10^9 to 10^{11} (*Lavallée et al.*, 2007, 2008; *Kendrick et al.*, 2013).

Mechanical properties of the dome rock are hard to determine at a rock-mass scale, despite previous studies on Volcán de Colima andesites at a laboratory scale (*Heap et al.*, 2014, 2016). I therefore created a dome extrusion model in PFC and iteratively changed the modelled mechanical properties until the simulated PFC dome growth matched the observed dome growth. I then used these micro-properties in the calibration procedure outlined in Section 1.3 to determine what the macro-properties of the dome rock must have been. I corrected the dome growth model results to account for the 2D nature of the model. This process enabled definition of the rock properties at Colima at a rock-mass scale, and is fully outlined in Appendix A.4.2.

Limited mechanical data exist for rock from Volcán de Colima and so it is not possible to gain a picture of spatial or temporal heterogeneity. Peak strength of one exemplar rock from Volcán de Colima was found to be 17.5 MPa by *Heap et al.* (2014). I adopted this single value for simplicity. However, in order to match the model morphology to the observed dome morphology, a peak rock strength of ∼3.7 MPa was necessary (Table 1.2, Appendix A.8). This is ∼20% of the lowest laboratory values, and suggested an intense level of fracturing and/or porosity is present in a cooling and dynamically evolving carapace, which significantly affects the rock behaviour at a rock-mass scale (e.g. *Zorn et al.*, 2018). In order to match the observed dome growth, a reduction in Young's modulus was required from 8.1 GPa in the tested dome rock from Volcán de Colima to 3.5 GPa. This not only alludes to the importance of fracturing, but also the importance of scaling both the strength and elastic parameters of material from the laboratory sample scale to a rock mass scale (e.g. *Heap et al.*, 2018).

	Fitted to laboratory data	Fitted to observations
Shear stiffness	1.25 x 10^9 Pa	1.00 x 10^9 Pa
Normal stiffness	1.25 x 10^9 Pa	1.00 x 10^9 Pa
Cohesion	2.70 x 10^7 Pa	5.00 x 10^6 Pa
Friction coefficient	0.84	0.84
Friction angle	38°	38°
Bond modulus	1.10 x 10^{10} Pa	1.60 x 10^9 Pa

Table 1.2: PFC parameters for the talus material in (a) the material that is calibrated to sample-scale laboratory tests of samples from Volcán de Colima (*Heap et al.*, 2014) and (b) the material that is used to fit the observational data and allows us to back-analyse rock-mass strength.

The modelled dome growth showed similar morphology to the observed dome growth at Volcán de Colima during February/March 2013 (Figure 1.13). Early dome growth was dominated by vertical growth and an initial increase in height the explicit width of this growth in the early stage of the model was determined by the initial conditions imposed for the width of the conduit. A height threshold was reached, after which horizontal growth exerted greater control over the lava dome growth. As observed in the camera image analysis, over-steepening occurred on the dome flanks, along with the generation of rubbly spine-type features towards the apex of the dome.

Matching the exact timing of the dome growth phases is challenging, as complete temporal coverage of the extrusion process is not available from observations. The modelled dome started extruding at time zero, and comparisons made to the monitored dome until the point that it started to overflow the crater rim. This gave a fixed frame of reference and allowed comparison against normalised time relative to the dome width.

1.4.1 Implications of the validation model for understanding dome growth

The steep vertical growth seen initially at Volcán de Colima was not reproduced perfectly by this model alone, which required a stronger material during early growth. Possibly, the first magma extrusion could have been more degassed and hence more viscous; the initial vertical growth domain was therefore likely associated with extrusion of a viscous plug and conduit material, before fresh magma reached the surface and spread laterally.

Photographic observations at Volcán de Colima also produced digital image

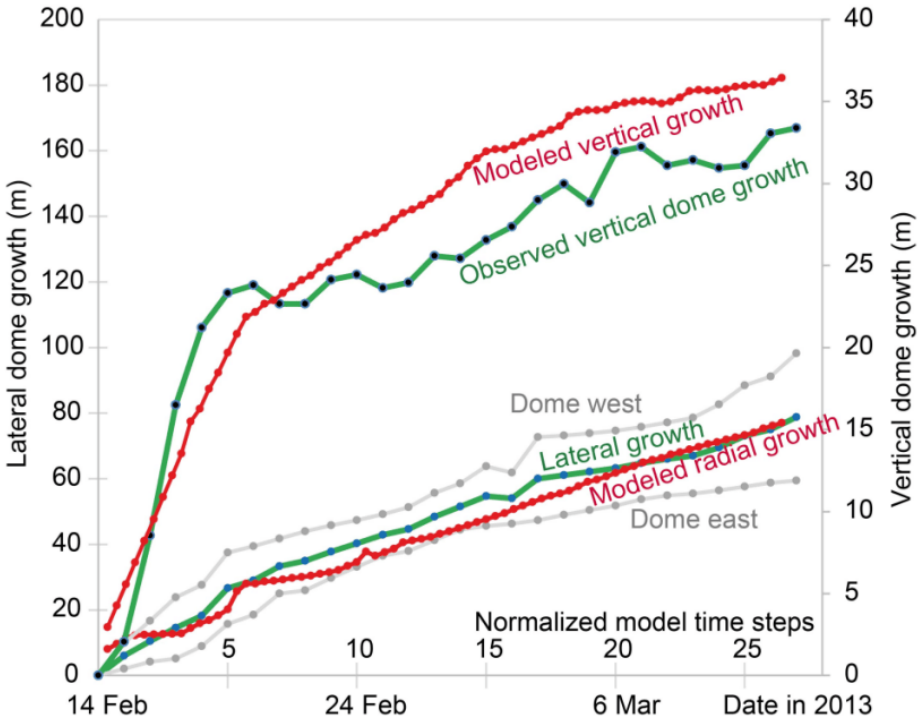

Figure 1.13: Comparison of dome growth camera observations (green curves) and distinct element models (red curves). The lateral (left Y-axis) and vertical dome growth (right Y-axis) are shown separately. The east and west sides of the lateral dome growth are shown in grey, average in green. The initially steep vertical growth and subsequent dominantly lateral growth can be well explained by models. The X-axis shows date for observations, and normalized time for models. Figure adopted from *Walter et al.* (2019).

correlation results (Figure 1.14), enabling identification of different growth regimes. The digital image correlation showed that the dome growth was initially dominated by vertical growth (Figure 1.14a). Once the dome reached a height of 25 m, the dominantly vertical growth regime changed into a primarily lateral growth regime (Figure 1.14b). Occasional short term subsidence of the dome occurred (Figure 1.14c), possibly associated with block rotation or spreading. Continued growth graded into a lateral direction of magma extrusion as the magma reaches the break in slope of the underlying topography (Figure 1.14d), forming a coulée flowing downslope.

I carried out similar analysis on the dome emplaced within the discrete element model by visualising the velocities of the model particles during simulated dome growth, and find very similar dome growth regimes. Initially, the dome is dominated by vertical growth (Figure 1.15a), and then later governed by lateral

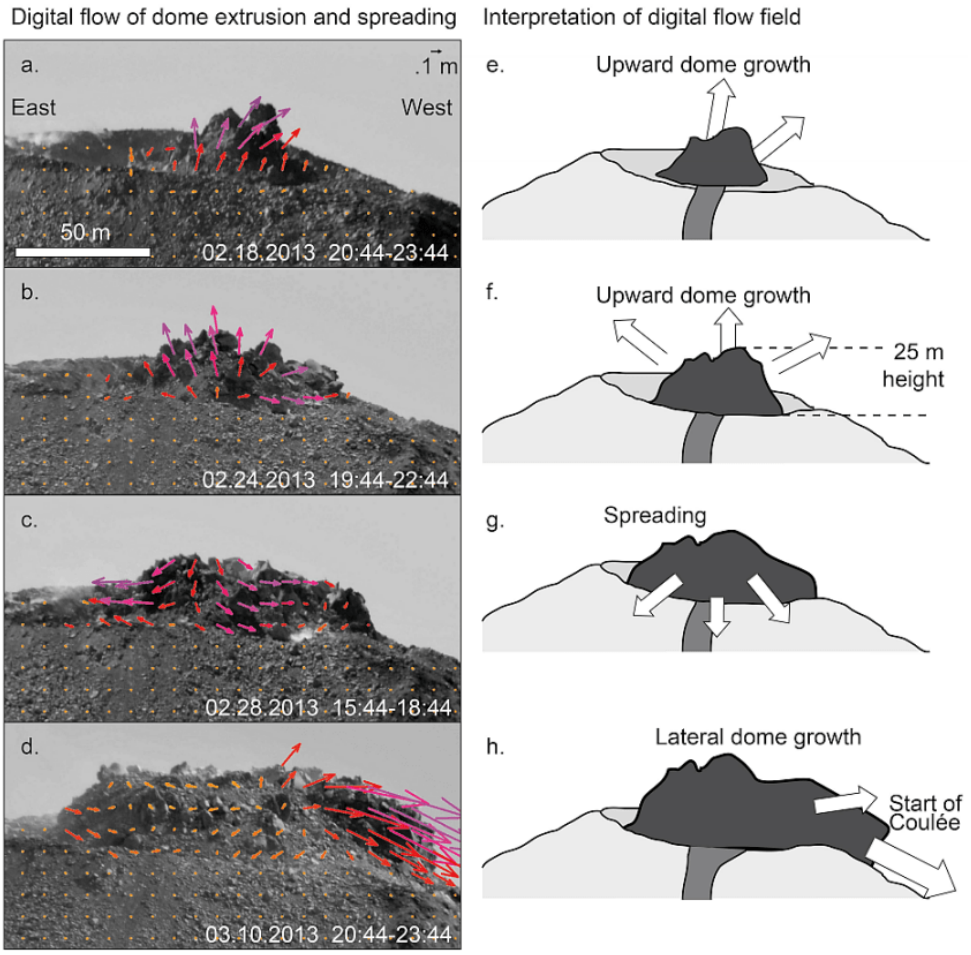

Figure 1.14: Digital image correlation results show the growth of the dome, alongside cartoon interpretations. Figure adopted from *Walter et al.* (2019).

spreading (Figure 1.15b). In Figure 1.15c, the velocity vectors show downhill movement as the material reaches the break in slope, simulating the beginning of coulée growth. The dome growth regime identified in the observed Colima imagery, and the PFC model, is also similar to the observed dome growth at La Soufrière (as in Figure 1.5) and the analogue model results from *Buisson and Merle* (2004, Figure 1.6). Similar growth regimes (initially steep vertical growth, followed by lateral growth) were also seen from observations at Mt. Pelée, St. Vincent, and Mt. Unzen (Figure 1.16).

The good agreement of observed and modelled dome growth shows both qualitatively and quantitatively that this discrete element model is well-placed to simulate dome growth processes. In order to take the model further, I will impose triggering mechanisms onto an emplaced dome in Chapter 3. The other main conclusion from this validation model is that rock properties at rock mass

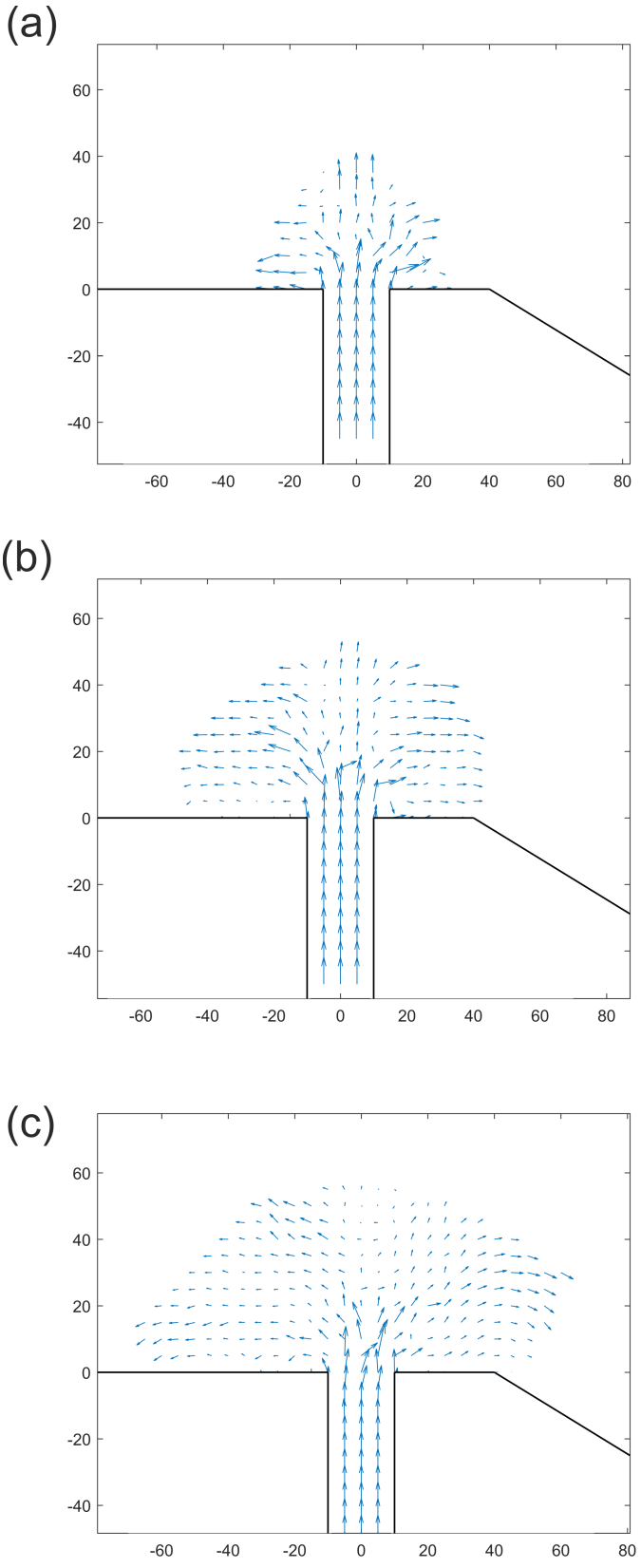

Figure 1.15: Interpolated velocities from the PFC model to classify growth regimes.

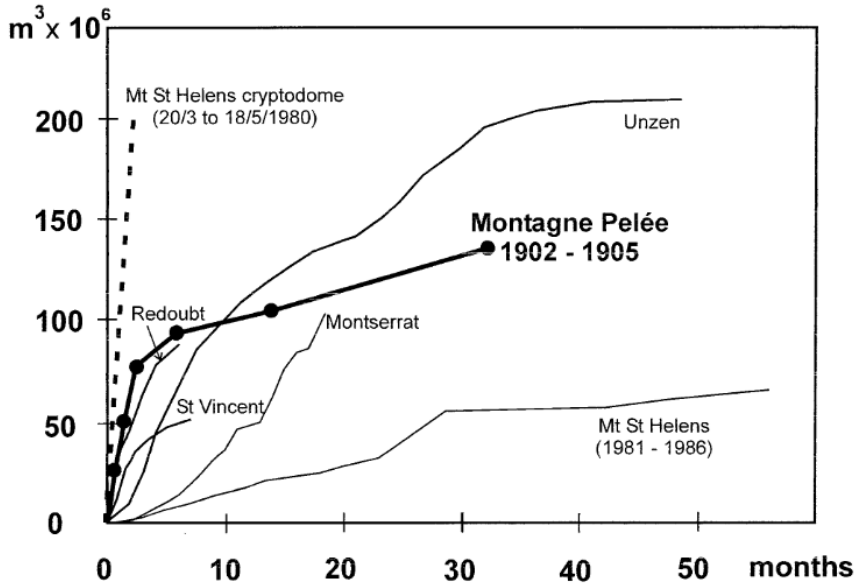

Figure 1.16: Types of lava dome growth, from *Tanguy* (2004).

scale are only a fraction of the equivalent laboratory scale intact rock properties. I found a scaling relationship of approximately 20%, meaning that rock properties determined in the laboratory required an 80% decrease in order to represent behaviour at a rock mass scale. This scaling relationship was in broad alignment with other scaling laws from the literature (see Section 5.2) and will be used in the models presented in Chapter 5.

1.5 Contributions/aims and objectives

The overall aim of this project is to use a combination of techniques (including numerical modelling and laboratory experiments) to better understand the mechanics of lava domes, namely investigating the condition of a lava dome prior to collapse. Consequently I will determine whether the cause of collapse affects the mode of collapse, and how the physical properties of the dome may impact this relationship. To achieve this aim, the specific objectives are:

1. Compile a global and historical database of lava dome collapse events, and the conditions of lava domes prior to collapses.

2. Identify if there are patterns in pre-collapse conditions, particularly identifying the most common collapse mechanisms.

3. Create a new 2D discrete element model, that tracks a lava dome through

its initial emplacement and its later stages of growth, simulating a transition from fluid magma to solid rock. Verify this using observational data.

4. Impose external conditions (the identified common collapse mechanisms) onto the modelled dome; use strain visualisation to examine where failure planes are forming within the dome. Assess how this informs the overall understanding of lava domes.

5. Explore the heterogeneity of erupted products from Soufrière Hills volcano, Montserrat to assess the effect of rock properties on overall dome stability.

6. Incorporate rock heterogeneities into a calibrated dome model, to examine if identified failure modes vary with varied rock properties.

1.6 Thesis roadmap

In **Chapter 2**, I discuss compilation of a global dataset examining the conditions present during individual dome collapse events. Statistical analysis of this dataset enables identification of relationships previously unidentifiable in location-specific studies. I show that there is a statistical relationship between dome growth style and relative dome collapse volume. I also show a statistical dependence of collapse size (both relative and explicit volumes) on causal mechanism. These causal mechanisms are carried forward to inform the work in Chapter 3. The work in this Chapter has been peer reviewed and published in *Bulletin of Volcanology*.

In **Chapter 3**, I develop a new discrete element model in Particle Flow Code to examine the mechanisms of failure after the following conditions are applied to the model: (1) an increase in internal gas overpressures; (2) a switch in extrusion direction; and (3) topographic constraints on lava dome growth. I find two distinct failure mechanisms that relate to different collapse triggers: deep-seated rotational failures, and smaller superficial failures. The work in this Chapter has been peer reviewed and published in *Journal of Volcanology and Geothermal Research*.

In **Chapter 4**, I explore the geomechanical evolution of dome rock properties across the 1995-2010 eruption at Soufrière Hills, Montserrat. This study obtains mechanical data for lava dome products and aims to encourage incorporation of spatial and temporal heterogeneity in dome rock into future numerical models. I show how the mechanical properties of the dome rock correspond to the physical properties of dome rock, and suggest how these may relate to the eruptive

conditions during the emplacement of a temporally-constrained suite of rocks. The work in this Chapter has been peer reviewed and published in *Frontiers in Earth Science*.

In **Chapter 5**, I incorporate the mechanical data presented in Chapter 4 into the Particle Flow Code models presented in Chapter 3. This suite of new models enables me to examine how each of the parts of this multi-faceted investigation tie together to provide us with a clearer understanding of the mechanics of lava dome collapse. I also summarise the key findings from each of the results chapters and discuss the broader implications of these, also giving the future directions for research highlighted by the work within this project.

Bibliography

Blake, S. (1990), *Viscoplastic Models of Lava Domes*, pp. 88–126, Springer Berlin Heidelberg, Berlin, Heidelberg, doi:10.1007/978-3-642-74379-5_5.

Branney, M., and P. Kokelaar (2002), Pyroclastic density currents and the sedimentation of ignimbrites, *Geological Society of London, Memoirs*, *27*.

Buisson, C., and O. Merle (2002), Experiments on internal strain in lava dome cross sections, *Bulletin of Volcanology*, *64*(6), 363–371, doi:10.1007/s00445-002-0213-6.

Buisson, C., and O. Merle (2004), Numerical simulation of strain within lava domes, *Journal of Structural Geology*, *26*(5), 847–853, doi:10.1016/j.jsg.2003.11.017.

Calder, E. S., Y. Lavallée, J. E. Kendrick, and M. Bernstein (2015), Chapter 18 - Lava Dome Eruptions, in *The Encyclopedia of Volcanoes*, pp. 343–362, Academic Press, doi:10.1016/B978-0-12-385938-9.00018-3.

Cho, N. (2008), Discrete element modeling of rock: pre-peak fracturing and dilation, Ph.D. thesis, University of Alberta.

Cho, N., C. Martin, and D. Sego (2007), A clumped particle model for rock, *International Journal of Rock Mechanics and Mining Sciences*, *44*(7), 997–1010, doi:10.1016/j.ijrmms.2007.02.002.

Cundall, P., and O. Strack (1979), A discrete numerical model for granular assemblies, *Geotechnique*, *29*(1), 47–65.

Diederichs, M. (1999), Instability of hard rockmasses: the role of tensile damage and relaxation, Ph.D. thesis, University of Waterloo.

Fink, J. H., and R. W. Griffiths (1998), Morphology, eruption rates, and rheology of lava domes: Insights from laboratory models, *Journal of Geophysical Research*, *103*(10), 527–545, doi:10.1029/97JB02838.

Gonzalez, M., J. Ramirez, and C. Navarro (2002), Summary of the historical eruptive activity of Volcán De Colima, Mexico 1519-2000, *Journal of Volcanology and Geothermal Research*, *117*(1-2), 21–46, doi:10.1016/S0377-0273(02)00233-0.

Griffiths, R. W., and J. H. Fink (1993), Effects of surface cooling on the spreading of lava flows and domes, *Journal of Fluid Mechanics*, *252*, 667–702, doi:10.1017/S0022112093003933.

Hale, A. (2008), Lava dome growth and evolution with an independently deformable talus, *Geophysical Journal International*, *174*(1), 391–417, doi:10.1111/j.1365-246X.2008.03806.x.

Hale, A., and G. Wadge (2005), Computationally Modelling the Lava Dome at Soufrière Hills Volcano, Ph.D. thesis, The University of Reading.

Hale, A., L. Bourgouin, and H. B. Mühlhaus (2007), Using the level set method to model endogenous lava dome growth, *Journal of Geophysical Research*, *112*(B3), B03,213, doi:10.1029/2006JB004445.

Hale, A., E. Calder, S. Loughlin, G. Wadge, and G. Ryan (2009a), Modelling the lava dome extruded at Soufrière Hills Volcano, Montserrat, August 2005-May 2006. Part I: Dome shape and internal structure, *Journal of Volcanology and Geothermal Research*, *187*(1-2), 69–84, doi:10.1016/j.jvolgeores.2009.08.014.

Hale, A., E. Calder, S. Loughlin, G. Wadge, and G. Ryan (2009b), Modelling the lava dome extruded at Soufrière Hills Volcano, Montserrat, August 2005-May 2006. Part II: Rockfall activity and talus deformation, *Journal of Volcanology and Geothermal Research*, *187*(1-2), 69–84, doi:10.1016/j.jvolgeores.2009.08.014.

Hale, A. J., and G. Wadge (2003), Numerical modelling of the growth dynamics of a simple silicic lava dome, *Geophysical Research Letters*, *30*(19), 1–4, doi:10.1029/2003GL018182.

Hale, A. J., and G. Wadge (2008), The transition from endogenous to exogenous growth of lava domes with the development of shear bands, *Journal of Volcanology and Geothermal Research*, *171*(3-4), 237–257, doi:10.1016/j.jvolgeores.2007.12.016.

Harnett, C. E., M. E. Thomas, M. D. Purvance, and J. Neuberg (2018), Using a discrete element approach to model lava dome emplacement and collapse, *Journal of Volcanology and Geothermal Research*, doi:10.1016/j.jvolgeores.2018.06.017.

Heap, M., M. Villeneuve, J. Farquharson, F. Albino, E. Brothelande, and J. L. Got (2018), Towards more realistic values of elastic moduli for volcano modelling, *Tech. Rep. EGU2018-3909*.

Heap, M. J., Y. Lavallée, L. Petrakova, P. Baud, T. Reuschlé, N. R. Varley, and D. B. Dingwell (2014), Microstructural controls on the physical and mechanical properties of edifice-forming andesites at Volcán de Colima, Mexico, *Journal of Geophysical Research: Solid Earth*, *119*(4), 2925–2963, doi:10.1002/2013JB010521.

Heap, M. J., J. Russell, and L. Kennedy (2016), Mechanical behaviour of dacite from Mount St. Helens (USA): A link between porosity and lava dome extrusion mechanism (dome or spine)?, *Journal of Volcanology and Geothermal Research*, *328*, 159–177.

Holohan, E. P., M. P. J. Schöpfer, and J. J. Walsh (2011), Mechanical and geometric controls on the structural evolution of pit crater and caldera subsidence, *Journal of Geophysical Research: Solid Earth*, *116*(7), 1–23, doi:10.1029/2010JB008032.

Holohan, E. P., H. Sudhaus, T. R. Walter, M. P. J. Schöpfer, and J. J. Walsh (2017), Effects of Host-rock Fracturing on Elastic-deformation Source Models of Volcano Deflation, *Scientific Reports*, *7*(1), 10,970, doi:10.1038/s41598-017-10009-6.

Holt, R., J. Kjølaas, I. Larsen, L. Li, A. Gotusso Pillitteri, and E. Sønstebø (2005), Comparison between controlled laboratory experiments and discrete particle simulations of the mechanical behaviour of rock, *International Journal of Rock Mechanics and Mining Sciences*, *42*(7-8 SPEC. ISS.), 985–995, doi:10.1016/j.ijrmms.2005.05.006.

Huppert, H., J. Shepherd, H. Sigurdsson, and R. Sparks (1982), On lava dome growth, with application to the 1979 lava extrusion of the Soufrière of St. Vincent, *Journal of Volcanology and Geothermal Research*, *14*, 199–222, doi:10.1016/0377-0273(82)90062-2.

Husain, T., D. Elsworth, B. Voight, G. Mattioli, and P. Jansma (2014), Influence of extrusion rate and magma rheology on the growth of lava domes: Insights from particle-dynamics modeling, *Journal of Volcanology and Geothermal Research*, *285*, 110–117, doi:10.1016/j.jvolgeores.2014.08.013.

Husain, T., D. Elsworth, B. Voight, G. Mattioli, and P. Jansma (2018), Influence of conduit flow mechanics on magma rheology and the growth style of lava domes, *Geophysical Journal International*, *213*(3), 1768–1784, doi:10.1093/gji/ggy073.

Husain, T., D. Elsworth, B. Voight, G. S. Mattioli, and P. Jansma (2019), Morphologic variation of an evolving dome on the extrusion of finite yield strength magma, *Journal of Volcanology and Geothermal Research*, pp. 51–64, doi:10.1016/j.jvolgeores.2019.01.010.

Iverson, R. M. (1990), Lava domes modeled as brittle shells that enclose pressurized magma, with application to Mount St. Helens, in *Lava Flows and Domes: Emplacement Mechanisms and Hazard Implications*, edited by J. H. Fink, pp. 47–69, Springer Berlin Heidelberg.

James, M. R., and N. Varley (2012), Identification of structural controls in an active lava dome with high resolution DEMs: Volcán de Colima, Mexico, *Geophysical Research Letters*, *39*(22), 1–5, doi:10.1029/2012GL054245.

Kazerani, T., Z. Y. Yang, and J. Zhao (2012), A discrete element model for predicting shear strength and degradation of rock joint by using compressive and tensile test data, *Rock Mechanics and Rock Engineering*, *45*(5), 695–709, doi:10.1007/s00603-011-0153-6.

Kendrick, J. E., Y. Lavallée, K. U. Hess, M. J. Heap, H. E. Gaunt, P. G. Meredith, and D. B. Dingwell (2013), Tracking the permeable porous network during strain-dependent magmatic flow, *Journal of Volcanology and Geothermal Research*, *260*, 117–126, doi:10.1016/j.jvolgeores.2013.05.012.

Kilburn, C. R., and G. Luongo (Eds.) (1993), *Active Lavas: Monitoring and Modelling*, CRC Press.

Lavallée, Y., K. U. Hess, B. Cordonnier, and D. B. Dingwell (2007), Non-Newtonian rheological law for highly crystalline dome lavas, *Geology*, *35*(9), 843–846, doi:10.1130/G23594A.1.

Lavallée, Y., P. G. Meredith, D. B. Dingwell, K. U. Hess, J. Wassermann, B. Cordonnier, A. Gerik, and J. H. Kruhl (2008), Seismogenic lavas and explosive eruption forecasting, *Nature*, *453*(7194), 507–510, doi:10.1038/nature06980.

Maeno, F., and H. Taniguchi (2006), Silicic lava dome growth in the 1934-1935 Showa Iwo-jima eruption, Kikai caldera, south of Kyushu, Japan, *Bulletin of Volcanology*, *68*(7-8), 673–688, doi:10.1007/s00445-005-0042-5.

Nakada, S., Y. Miyake, H. Sato, O. Oshima, and A. Fujinawa (1995), Endogenous growth of dacite dome at Unzen volcano (Japan), 1993-1994, *Geology*, *23*(2), 157–160, doi:10.1130/0091-7613(1995)023⟨0157:EGODDA⟩2.3.CO;2.

Ogburn, S., S. Loughlin, and E. Calder (2015), The association of lava dome growth with major explosive activity (VEI4): DomeHaz, a global dataset, *Bulletin of Volcanology*, *77*(40), doi:10.1007/s00445-015-0919-x.

Potyondy, D. (2015), The bonded-particle model as a tool for rock mechanics research and application: current trends and future directions, *Geosystem Engineering*, *18*(1), 1–28, doi:10.1080/12269328.2014.998346.

Potyondy, D., and P. A. Cundall (2004), A bonded-particle model for rock, *International Journal of Rock Mechanics and Mining Sciences*, *41*(8 SPEC.ISS.), 1329–1364, doi:10.1016/j.ijrmms.2004.09.011.

Potyondy, D. O. (2012), A flat-jointed bonded-particle material for hard rock, *46th US Rock Mechanics/Geomechanics Symposium*, p. 10.

Roche, O., M. A. Gilbertson, J. C. Phillips, and S. S. Sparks (2004), Experimental study of gas-fluidized granular flows with implications for pyroclastic flow emplacement, *Journal of Geophysical Research: Solid Earth*, *109*(10), 1–14, doi:10.1029/2003JB002916.

Saucedo, R., J. Macías, M. Sheridan, M. Bursik, and J. Komorowski (2005), Modeling of pyroclastic flows of Colima Volcano, Mexico: implications for hazard assessment, *Journal of Volcanology and Geothermal Research*, *139*(1-2), 103–115, doi:10.1016/j.jvolgeores.2004.06.019.

Schöpfer, M. P., C. Childs, and J. J. Walsh (2007), Two-dimensional distinct element modeling of the structure and growth of normal faults in multilayer sequences: 1. Model calibration, boundary conditions, and selected results, *Journal of Geophysical Research: Solid Earth*, *112*(10), 1–15, doi:10.1029/2006JB004902.

Smith, G. M., R. Williams, P. J. Rowley, and D. R. Parsons (2018), Investigation of variable aeration of monodisperse mixtures: implications for pyroclastic density currents, *Bulletin of Volcanology*, *80*(8), 1–12, doi:10.1007/s00445-018-1241-1.

Sussman, M., P. Smereka, and S. Osher (1994), A Level Set Approach for Computing Solutions to Incompressible Two-Phase Flow, doi:10.1006/jcph.1994.1155.

Tanguy, J. (2004), Rapid dome growth at Montagne Pelee during the early stages of the 1902-1905 eruption: a reconstruction from Lacroix's data, *Bulletin of Volcanology*, *66*(7), 615–621, doi:10.1007/s00445-004-0344-z.

Voight, B., E. K. Constantine, S. Siswowidjoyo, and R. Torley (2000), Historical eruptions of Merapi Volcano, Central Java, Indonesia, 1768-1998, *Journal of Volcanology and Geothermal Research*, *100*, 69–138.

Wadge, G., P. Jackson, S. M. Bower, A. W. Woods, and E. Calder (1998), Computer simulations of pyroclastic flows from dome collapse, *Geophysical Research Letters*, *25*(19), 3677–3680, doi:10.1029/98GL00710.

Wadge, G., G. Ryan, and E. S. Calder (2009), Clastic and core lava components of a silicic lava dome, *Geology*, *37*(6), 551–554, doi:10.1130/G25747A.1.

Walter, T. R., C. E. Harnett, N. Varley, D. Vargas, J. Salzer, E. U. Zorn, M. Bretón, R. Arámbula, and M. E. Thomas (2019), Imaging the 2013 explosive crater excavation and new dome formation at Volcán de Colima with TerraSAR-X , time-lapse cameras and modelling, *Journal of Volcanology and Geothermal Research*, *369*, 224–237, doi:10.1016/j.jvolgeores.2018.11.016.

Wang, Y., and F. Tonon (2009), Modeling Lac du Bonnet granite using a discrete element model, *International Journal of Rock Mechanics and Mining Sciences*, *46*(7), 1124–1135, doi:10.1016/j.ijrmms.2009.05.008.

Watts, R. B., R. a. Herd, R. S. J. Sparks, and S. R. Young (2002), Growth patterns and emplacement of the andesitic lava dome at Soufrière Hills Volcano, Montserrat, *Geological Society, London, Memoirs*, *21*(1), 115–152, doi:10.1144/GSL.MEM.2002.021.01.06.

Wu, S., and X. Xu (2016), A Study of Three Intrinsic Problems of the Classic Discrete Element Method Using Flat-Joint Model, *Rock Mechanics and Rock Engineering*, *49*(5), 1813–1830, doi:10.1007/s00603-015-0890-z.

Zhang, Q., H. Zhu, L. Zhang, and X. Ding (2011), Study of scale effect on intact rock strength using particle flow modeling, *International Journal of Rock Mechanics and Mining Sciences*, *48*(8), 1320–1328, doi:10.1016/j.ijrmms.2011.09.016.

Zorn, E. U., M. C. Rowe, S. J. Cronin, A. G. Ryan, L. A. Kennedy, and J. K. Russell (2018), Influence of porosity and groundmass crystallinity on dome rock strength: a case study from Mt. Taranaki, New Zealand, *Bulletin of Volcanology*, *80*(4), doi:10.1007/s00445-018-1210-8.

Chapter 2

Presentation and analysis of a worldwide database for lava dome collapse events: the Global Archive of Dome Instabilities (*GLADIS*)

C. E. Harnett[1], M. E. Thomas [1], E. Calder [2], S. Ebmeier [1], A. Telford [3], W. Murphy [1] and J. Neuberg[1]

[1] *School of Earth and Environment, University of Leeds, United Kingdom*
[2] *School of Geosciences, University of Edinburgh, United Kingdom*
[3] *School of Mathematics, University of Leeds, United Kingdom*

Citation: **Harnett, C. E.**, Thomas, M. E., Calder, E. S., Ebmeier, S. K., Telford, A., Murphy, W., and Neuberg, J. (2019). *Presentation and analysis of a worldwide database for lava dome collapse events: the Global Archive of Dome Instabilities (GLADIS).* Bulletin of Volcanology, doi: 10.1007/s00445-019-1276-y.

Abstract

Lava dome collapses generate hazardous pyroclastic flows, rockfalls and debris avalanches. Despite advances in understanding lava dome collapses and their resultant products, the conditions that occur prior to collapse are still poorly understood. Here we introduce the Global Archive of Dome Instabilities (*GLADIS*), a database that compiles worldwide historical dome collapses and their reported properties, including original dome volume (at the time of collapse), dome morphology, emplacement conditions, precursory activity, dome geometry and deposit characteristics. We determine the collapse magnitude for events where possible, using both absolute deposit volumes and relative collapse volume ratios (this being deposit volume as a proportion of original dome volume).

We use statistical analysis to explore whether relationships exist between collapse magnitude and extrusion rate, dome growth style, original dome volume, and causal mechanism of collapse. We find that relative collapse magnitude is independent of both the extrusion rate and the original dome volume. Relative collapse volume ratio is dependent on dome growth style, where endogenous growth is found to precede the largest collapses ($\sim$75% original volume). Collapses that comprise a higher proportion (>50%) of original dome volume are particularly attributed to both gravitational loading and the development of gas overpressure, whilst collapses comprising a small proportion (<10%) of original dome volume are associated with the topography surrounding the dome, and variations in extrusion direction. By providing validation and/or source data, we intend these data on various dome growth and collapse events, and their associated mechanisms, to be the focus of future numerical modelling efforts, whilst the identified relationships with relative collapse volume ratios can inform collapse hazard assessment based on observations of a growing dome.

2.1 Introduction

Lava domes and spines form when viscous magma is extruded but is not able to flow far from the volcanic vent (*Calder et al.*, 2015). Instability of lava domes results in pyroclastic flows, rockfalls, and sometimes debris avalanches, all of which can pose a significant hazard to areas surrounding the edifice (*Voight*, 2000; *Wadge*, 2009). Despite the threat posed by dome collapse, we still know relatively little about the interplay between dome growth conditions and the collapse

mechanisms of lava domes. A broad variety of mechanisms, and triggers, have already been identified for individual collapse events. These include gravitational collapse (*Ui et al.*, 1999), rainfall (*Matthews et al.*, 2002), and gas overpressure (*Voight and Elsworth*, 2000). However, the general conditions that determine which collapse mechanism is dominant are still not clear.

Various modelling strategies have been used to investigate lava dome stability, although many focus on the resultant pyroclastic flows (e.g. *Wadge et al.*, 1998; *Hooper and Mattioli*, 2001; *Saucedo et al.*, 2005) or initial dome emplacement (e.g. *Hale*, 2008; *Hale et al.*, 2009a,b). Perturbation factors likely to cause instability have been considered particularly in numerical models, for example calculation of diffusion of gas pressurisation across a dome (*Voight and Elsworth*, 2000), limit equilibrium (LE) analysis of slope height/stability relationships (*Simmons et al.*, 2005), or a revised LE analysis incorporating rainfall (*Taron et al.*, 2007). Discrete element models have also been designed to test the impact of external triggers on a dome's stability, such as development of gas overpressure or variation in extrusion direction (*Harnett et al.*, 2018).

Understanding previous dome collapse behaviour is an important tool for helping to develop forecasts for future activity (cf. *Ogburn et al.*, 2015; *Sheldrake et al.*, 2016; *Wolpert et al.*, 2016). To improve our ability to respond to volcanic crises involving dome extrusion, it is vital for volcanologists, particularly those advising decision makers, to have access to records from previous dome-forming eruptions that have undergone collapse. If lava dome extrusion begins at a volcano that has not shown dome growth in recorded history, it is important for observatories and the wider volcanological community to have access to a database that details potential trends in behaviour, by examining historical records from similar volcanic systems. This was the case for Soufrière Hills in Montserrat, where dome growth began in 1995 after ∼350 years of no extrusion (*Kokelaar*, 2002).

Many previous studies have highlighted the importance of global databases in volcanology (e.g. *Hédervári*, 1963; *Crisp*, 1984; *Wright et al.*, 2004; *Witham*, 2005; *Geyer and Martí*, 2008; *Donne et al.*, 2010; *Crosweller et al.*, 2012; *Ogburn et al.*, 2015; *Ebmeier et al.*, 2018). However, only a few studies have focussed particularly on dome-building episodes (*DomeHaz*) and pyroclastic flows (*FlowDat*) (*Ogburn*, 2012; *Ogburn and Calder*, 2017). Of these two the *DomeHaz* database of *Ogburn et al.* (2012) contains information about dome-forming eruptions and explosions, which has allowed probabilistic analysis of eruptions and their link to explosive activity (VEI>4) (*Ogburn et al.*, 2015)

as well as analysis of eruption longevity (*Wolpert et al.*, 2016). Instead, *FlowDat* (*Ogburn*, 2012) is a collection of mass flow (e.g. block-and-ash flows, debris avalanches, pumice flows) parameters and mobility metrics, and has been used for probabilistic analysis of metrics such as height/length data and planimetric areas (*Ogburn et al.*, 2016). Despite existing databases, a complete inventory of *individual* dome collapse events for different volcanoes is not currently incorporated into existing databases.

From previous literature (*Voight*, 2000), it is clear that a single volcano can exhibit various collapse styles associated with different dome growth styles and different eruptive phases, ranging from small-scale persistent rockfalls, to large-scale explosive collapse. It is therefore important to assess the nature of each collapse, rather than to attribute a single collapse style to an individual volcano.

In this study we thus collate data about dome collapse events in a Global Archive of Dome Instabilities (*GLADIS*). Dome collapses present a hazard to surrounding regions (e.g. *Mercado et al.*, 1988; *Sato et al.*, 1992; *Genareau et al.*, 2015) and can influence the behaviour of the remaining dome and future dome growth (*Voight and Elsworth*, 2000). We estimate first order statistics of global trends, focusing primarily on dome growth style, extrusion rate and collapse trigger, with the aim of identifying correlations between these and dome collapse magnitude. We also use one way analysis of variance (ANOVA) to undertake statistical analysis on data currently in *GLADIS*. We discuss how these results alongside examples of collapse events from *GLADIS* may influence our understanding of dome collapse processes.

2.2 Database design and structure

To analyse the relationships between dome collapse events and their mechanisms, we have compiled an open-access database that includes 293 individual collapse events from 35 different volcanoes (Table 2.1). The full flat-file database is accessible by joining the *GLADIS* group on VHub (http://vhub.org/groups/domecollapse). Here we summarise the content of *GLADIS* and report relationships between collapse properties and pre-collapse conditions. The database was initially designed using the list of dome-forming volcanoes in *DomeHaz* (*Ogburn et al.*, 2015). Volcanoes that had experienced lava dome collapse were identified and details of those events were compiled. This

was achieved using peer-reviewed literature, the Smithsonian Institution Global Volcanism Program (GVP) (*Venzke et al.*), the Bulletin of the Global Volcanism Network (https://volcano.si.edu), and *FlowDat*. A complete reference list for all entries into the database can be found within *GLADIS*.

Dome collapses are included in the database if they (a) have a known source volcano; (b) have a known year of occurrence; and (c) appear from related literature to be a significant event in the dome growth chronology. The definition of significant event is relative and largely qualitative due to lack of volume data, which is discussed in Section 2.3. Where quantitative data are unavailable, an event is considered significant enough for database inclusion if it is explicitly documented within literature as a collapse, or where there is reference to Merapi-type pyroclastic flows, as these refer specifically to dome collapse products (*Bardintzeff*, 1984).

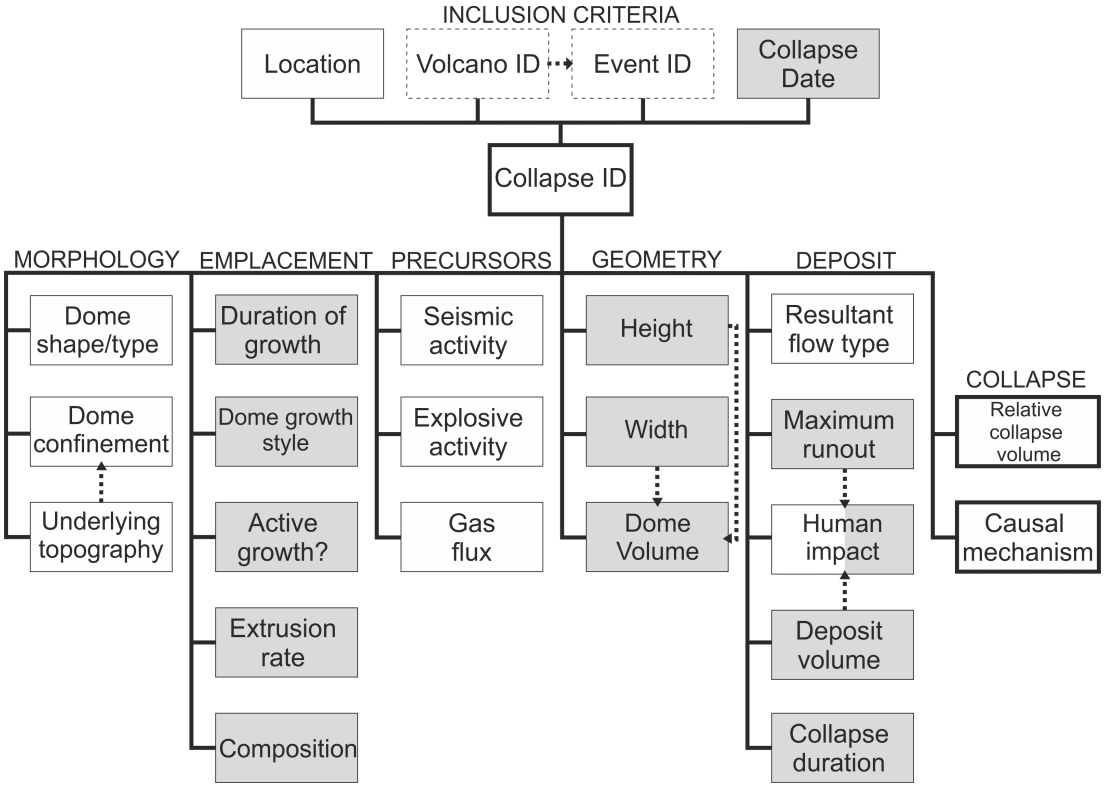

Figure 2.1: Organizational structure of *GLADIS*, dotted boxes show metadata taken directly from GVP (*Venzke et al.*), white boxes show qualitative data, filled boxes show quantitative data or data that have a multiple choice option (i.e. yes or no), and boxes with a thick outline show data that are derived using *GLADIS*. Dotted black lines show conceptual links between processes.

Table 2.1: A list of all volcanoes that have domes in the database, alongside their dominant composition (B = basalt, BA = basaltic andesite, A = andesite, D = dacite, R = rhyolite), the number of collapses and the number of classified collapses in GLADIS.

Volcano name	Dominant composition	Number of collapses in GLADIS	Number of collapses in GLADIS characterised by collapse %
Soufrière Hills volcano, Montserrat	A, BA	69	37
Merapi, Indonesia	A, BA	54	10
Mt. Unzen, Japan	D	33	4
Redoubt, USA	A, BA	15	13
Shiveluch, Russia	A, BA	13	2
Santiaguito, Guatemala	D	13	1
Volcán de Colima, Mexico	A, BA	12	2
Sinabung, Indonesia	A, BA	10	2
Mount St. Helens, USA	D	9	1
Mt. Pelée, Martinique	A, BA	7	0
Bagana, Papua New Guinea	A, BA	7	0
Semeru, Indonesia	A, BA	7	0
Nevado de Toluca, Mexico	A, BA	5	0
Chaitén, Chile	R	4	1
Augustine, USA	A, BA	3	0
Nevado del Huila, Colombia	A, BA	4	0
Karangetang, Indonesia	A, BA	3	1
Paluweh, Indonesia	A, BA	3	0
Bezymianny, Russia	A, BA	3	0
Guagua Pichinicha, Ecuador	D	3	0
Arenal, Costa Rica	A, BA	2	0
Mt. Lamington, Papua New Guinea	A, BA	1	1
Sisters Dome, USA	A, BA	1	1
Ruawahia, Tarawera, New Zealand	R	1	1
Wahanga, Tarawera, New Zealand	R	1	1
La Soufrière, St. Vincent	A, BA	1	0
Galeras, Colombia	A, BA	1	0
Reventador, Ecuador	A, BA	1	0
Cleveland, USA	A, BA	1	0
Cerro Pizarro, Mexico	R	1	0
Dome K-Cerro Chascon, Chile-Bolivia	R	1	0
Catarman, Hibok-Hibok, Philippines	D	1	0
Chao II, Altiplano-Puna, Chile	D	1	0
Etna Buocca, Italy	B	1	0
San Pedro, Chile	A, BA	1	0

Table 2.2: Degree of data completeness and description of data type. Population % is shown for the whole dataset, the post-1950 dataset, and the classified dataset. Population % is calculated by using the number of fields that are filled as a proportion of the number of possible fields (i.e. for each parameter, for each collapse).

Database field	O/C field	Data description and type	Population (%)		
			All	Post-1950	Classified
Location	C	-	100	100	100
Volcano ID	C	adopted from GVP	99	100	100
Eruption ID	C	adopted from GVP	96	100	97
Collapse Date	C	-	100	100	100
Collapse ID	C	unique integer identifier	100	100	100
Dome shape/type	O	based on morphology classification by (*Blake*, 1990) - upheaved plug, Peléean dome, low lava dome, coulée; qualitative information added	11	11	10
Dome confinement	O	qualitative - is the dome growing within a crater?	16	16	28
Underlying topography	O	primarily slope angle, consolidated material or unconsolidated previous collapse remnant?	6	5	6
Duration of growth	O	days	20	22	28
Dome growth style	C	endogenous, exogenous, combination	99	99	99
Active growth?	C	at the time of collapse - yes, no	29	29	13
Extrusion rate	O	in m^3/s, extrusion rate taken as close to collapse as possible, time over which extrusion rate recorded also documented (long-term time averaged rates avoided)	75	81	90

Database field	O/C field	Data description and type	Population (%) All	Post-1950	Classified
Composition	C	B, BA, A, D, R: following Smithsonian magma type codes (*Siebert et al.*, 2010)	100	100	100
Seismic activity	O	qualitative, as reported, e.g. swarm of VTs or increased seismicity	31	33	49
Explosive activity	C	did any associated explosive activity occur prior to/during/after the collapse?	12	12	13
Gas flux	O	SO_2 flux where available, qualitative data added (e.g. increased fumarolic activity)	14	15	5
Width	O	in metres, maximum dimension	5	4	5
Dome volume	O	in $\times 10^6$ m^3	43	45	99
Dome volume measurement type	C	DRE, bulk, bulk+surge	43	45	99
Resultant flow type	O	flow type as documented, no additional interpretation applied, e.g. avalanche, pyroclastic flow, nue ardente	70	71	68
Maximum runout	O	in kilometres, runout from collapse source	44	45	46
Human impact	O	death toll, financial cost due to damage to infrastructure	13	14	18
Deposit volume	O	in $\times 10^6$ m^3	36	38	99
Deposit volume measurement type	C	DRE, bulk, bulk+surge	36	38	99
Collapse duration	O	minutes	20	22	44

Database field	O/C field	Data description and type	Population (%) All	Post-1950	Classified
Causal mechanism for collapse	C	quantitative, where numbers are assigned to each of these mechanisms: gravitational loading, gas overpressure, topography, rain, switch in extrusion direction, other. Qualitative information listed in causalmech source sheet in *GLADIS* (available on VHub)	45	46	72
Relative collapse volume	C	calculated using deposit volume as a proportion of original dome volume	27	28	100
Relative collapse volume determination	C	Calculated from volume, quoted in text	27	28	100

For each collapse event, the major database fields (see Table 2.2) focus primarily on: dome morphology, lava dome emplacement conditions, precursory activity, dome geometry and description of the collapse deposit (usually a block-and-ash deposit). The nature of each database field is indicated in Figure 2.1, and a further explanation of each data field can be found in Table 2.2, where we also define the way in which observations were parametrised. As shown in Table 2.2, certain database fields are open fields for qualitative or quantitative entries (e.g. human impact, deposit volume), whereas other fields are restricted to the entry of multiple choice and therefore termed closed fields (e.g. dome growth style must have one of the following entries: exogenous, endogenous or combination).

These metrics are not exhaustive but do allow us to capture the principal characteristics of the well-documented collapses, as well as the fundamental characteristics of those that are more poorly documented. We note that all data recorded in *GLADIS* are taken directly from the associated source with no re-interpretation by the authors of this study.

2.2.1 Overview of dome collapse regimes in *GLADIS*

The magnitude and frequency of dome collapses, and the longevity of dome growth can vary at a single volcano (*Wolpert et al.*, 2016). Previous work has documented phases of dome growth and associated pauses (*Ogburn et al.*, 2015; *Sheldrake et al.*, 2016). In this study we add the relationship between periods of dome growth and frequency of dome collapse (Figure 2.2). Using the behaviour shown in Figure 2.2, we consider the long term pattern of collapse activity at dome-building volcanoes.

Sheldrake et al. (2016) identify patterns in volcanic behaviour, defining two distinct eruptive regimes: (1) episodic activity, where duration of repose intervals exceeds the eruption duration; and (2) persistent activity, where the duration of the eruptive phases and reposes are comparable. We examine collapse activity in a similar way by showing the collapses at a volcano, binned in number of collapses per year, alongside periods of extrusion (Figure 2.2). We identify three regimes of collapse activity: (1) frequent activity, where collapses are persistently seen during extrusion (for example at Merapi, Indonesia); (2) infrequent activity, where the duration of extrusion without collapse exceeds the duration of extrusion with collapse (for example at Bezymianny, Russia); and (3) time-declining activity, where the number of collapses per year decreases through time (for

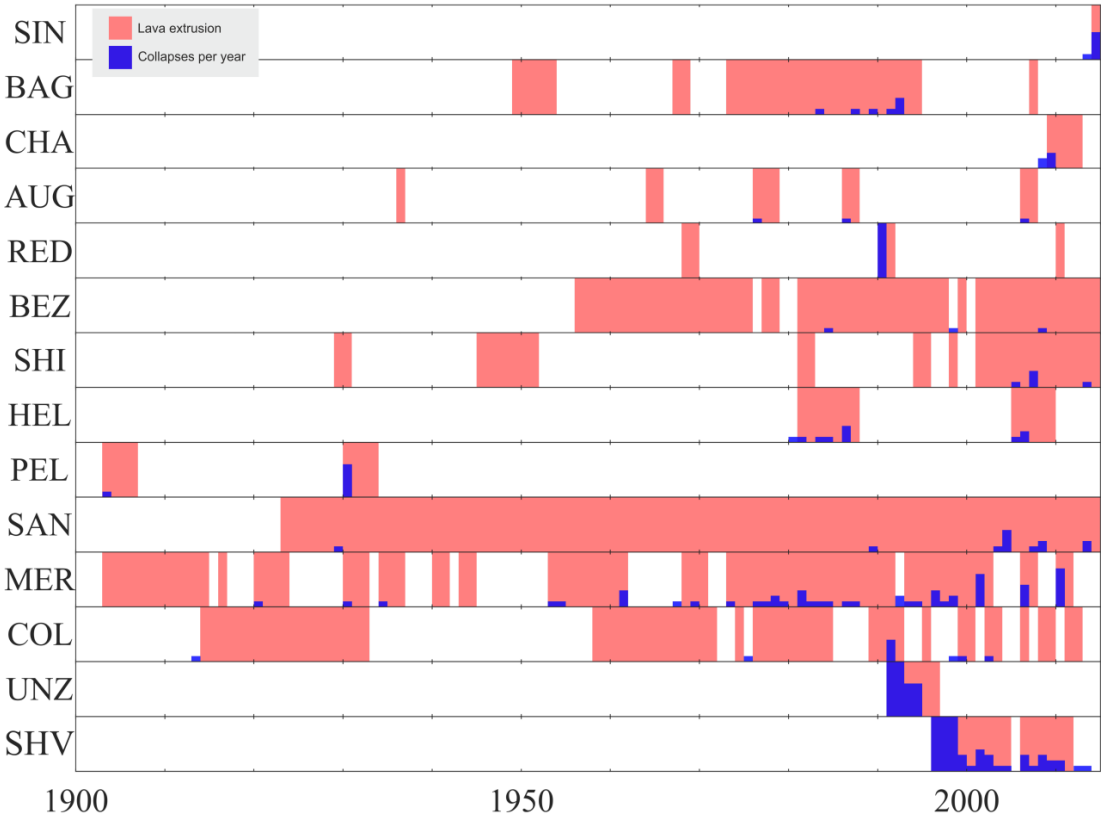

Figure 2.2: Binary plots following *Sheldrake et al.* (2016) indicating whether dome growth was recorded in each year since 1900 using primarily the GVP (*Venzke et al.*) at 15 of the most well documented dome-forming volcanoes in *GLADIS*. Extrusion periods are overlain with collapse frequency, in terms of number of individual collapse events (identified by *GLADIS*) per year, where a full bar indicates 10 collapses per year. There are five instances where more than 10 collapses per year occurred: RED 1990 (15), UNZ 1992 (11), SHV 1996 (13), 1997 (19) and 1998 (11). Labels as follows: SIN Sinabung, Indonesia; BAG Bagana, Papua New Guinea; CHA Chaitén, Mexico; AUG Augustine, USA; RED Redoubt, USA; BEZ Bezymianny, Russia; SHI Shiveluch, Russia; HEL Mt. St. Helens, USA; PEL Pelée, Martinique; SAN Santiaguito, Guatemala; MER Merapi, Indonesia; COL Volcán de Colima, Mexico; UNZ Mt. Unzen, Japan; and SHV Soufrière Hills volcano, Montserrat.

example at Soufrière Hills volcano, Montserrat). From this dataset we are unable to determine if these regimes of collapse activity are mutually exclusive, and hence suggest that time-declining activity could be considered a possible sub-regime of both frequent and infrequent collapse styles. We note that small collapses (e.g. constant rockfalls) may not be accurately represented here, due to under-reporting and observation bias towards larger events. We therefore expect an underestimation of total volume of material shed.

2.2.2 Data completeness and bias

Investigations of global catalogues of explosive eruptions have demonstrated that under-recording of events becomes more significant with increasing time from present, and decreasing eruption magnitude (*Furlan*, 2010; *Brown et al.*, 2014). We assume such a bias also exists within our dataset; this bias is also highly location dependent, and depends on the level of monitoring in place at a volcano. There is no cut-off before which collapse events are excluded from the database, although we expect there may be a problem of under-recording prior to about 1950. In Figure 2.2, we plot collapse events since 1900 from volcanoes where dome collapses are common. For example Merapi exhibits persistent collapse behaviour and if we make the assumption that this is not time dependent, it is likely there are more collapse events before 1950 than those that have been observed and recorded in *GLADIS*. We note that the 28 events (<10% of database events) from before 1950 contribute very little to the global event catalogue (<1% of overall data population).

We define data population here as the number of possible fields that are filled as a proportion of all possible database fields. Overall, for 28 parameters and 293 events, there are a possible 8204 entries; 4514 are populated giving an overall data population of 55%. This is a general degree of population (i.e. this considers all database fields equally) and individual events or parameters (e.g. composition) have a higher degree of population than others (e.g. collapse mechanism). In Table 2.2, population percentage is shown per database field for the whole dataset, the post-1950 dataset, and the dataset for which collapse volume as a percentage of dome volume is known, here called the classified dataset. An empty database field does not necessarily mean lack of activity, e.g. if the field seismic activity is not recorded in the database, it simply shows that no data are documented in *GLADIS*, rather than that no seismic activity occurred.

We expect that observatory reporting culture and capacity will influence data availability. For example, Soufrière Hills volcano is one of 35 volcanoes for which we have dome collapse information, but populates 27% of the database, due to quality of recording during the intensely studied 1995-2010 eruption. Of the 78 events where volume information is available, 37 are from Soufrière Hills volcano. Our analysis is therefore likely to be skewed towards events from Montserrat, but as more data are added to *GLADIS* in years to come, the impact of its current dominance is likely to decrease.

Extrusion rate is another parameter affected by recording in the database.

Extrusion rates are taken from the original literature, and we do not recalculate rates within this study. This data field is however subject to variations in the time period over which the extrusion rate is recorded (ranging from daily estimates from the day of collapse, to rates averaged over the whole eruptive period). Where possible, daily estimates of extrusion rate are used for the statistical analysis within this study, although often only time-averaged rates are available. All available data are used for the statistical analysis, but this likely introduces bias to the results and alludes to the importance of shorter term flux estimates at growing domes.

2.2.3 Metastable domes

GLADIS also includes data on domes that were emplaced and remain stable at the time of reporting. It is difficult to define what constitutes a stable dome over time, and so we define these here as metastable domes, as weathering and alteration over time could still result in instabilities (e.g. *Ball et al.*, 2013). In order to be included in the database, these must be domes that (a) have a citable source of information and (b) have not been completely destroyed by large explosive eruptions or collapses. Unlike the portion of the database recording collapse events, the metastable domes are not required to have a known emplacement date to be included in the database. We record available composition data for 90% of the metastable domes (references for which can be found in *GLADIS*). Of the domes with known composition, 37% (n=31) are basaltic-andesite to andesite, 35% (n=29) dacite and 28% (n=23) rhyolite.

We include these domes in *GLADIS* for completeness because structures that have remained stable over a long time could eventually collapse and therefore potentially provide insight into dome collapse processes. Analysis of these domes is not considered further in this study due to the relative paucity of related data in the associated literature. We note also that if a dome has remained stable for a long period of time (on the order of hundreds of years), the documentation of a later collapse may be reported in the context of landslides or debris avalanches, rather than explicitly named as a dome collapse. If we consider all database fields, only 18% of the metastable dome portion of the database is populated, making any in-depth analysis very difficult.

2.3 Database terminology

2.3.1 Defining collapse

The term *collapse* is used to describe a variety of processes and products resulting from dome instability. In order to build the database, we must more clearly define *collapse*. Collapse processes range from small scale rockfalls to larger scale pyroclastic density currents and even debris avalanches. As one end member, rockfalls are defined as abrupt movements of rocks or boulders that detach from a slope and roll, bounce and slide downslope under the influence of gravity (*Hungr et al.*, 2014). When associated with lava domes, rockfalls are generated by disaggregation of cooled lava from the dome surface (*Calder et al.*, 2002; *Hale et al.*, 2009b) and typically have short runouts of <0.5 km with volumes on the order of magnitude of 10^3 m^3 (*Wadge et al.*, 2014). Hundreds of small scale rockfalls can occur daily during active dome growth periods (*Calder et al.*, 2002). Pyroclastic density currents are considered as the large end member of collapse products and are defined as density-driven mixtures of volcanic particles and gases (*Cole et al.*, 2002). They are generally larger in volume (>10^4 m^3) (*Calder et al.*, 2002) and longer in runout (>0.5 km) than rockfalls. Pyroclastic density currents are the most common deposit type in *GLADIS*, ranging in volume from 10^4 m^3 to 300×10^6 m^3.

Collapses at Soufrière Hills volcano have been quantified and differentiated using the terminology "large" (1-4 $\times$ 10^6 m^3) and "major" (> 4×10^6 m^3) by *Calder et al.* (2002). This is a useful classification at an individual volcano, where successive domes and collapses tend to be of similar magnitudes. A definition based on an absolute volume for one volcano is, however, not necessarily effective, and does not facilitate comparison on a global scale where initial dome volumes range over two orders of magnitude.

Therefore we present a global dome collapse analysis and examine relationships between observed variables and absolute collapse volume (ΔV) and relative collapse volume ratio ($\Delta V/V$, volume of material shed during a collapse event, expressed as a percentage of original dome volume, V). We consider it likely that collapse mechanisms and processes are related to proportion of dome removal rather than absolute dome or collapse volumes, and so using relative collapse volume ratios facilitates comparison of the global dataset.

One challenge in this study is that absolute collapse volumes are not routinely estimated within the literature. Deposit volumes are more commonly reported

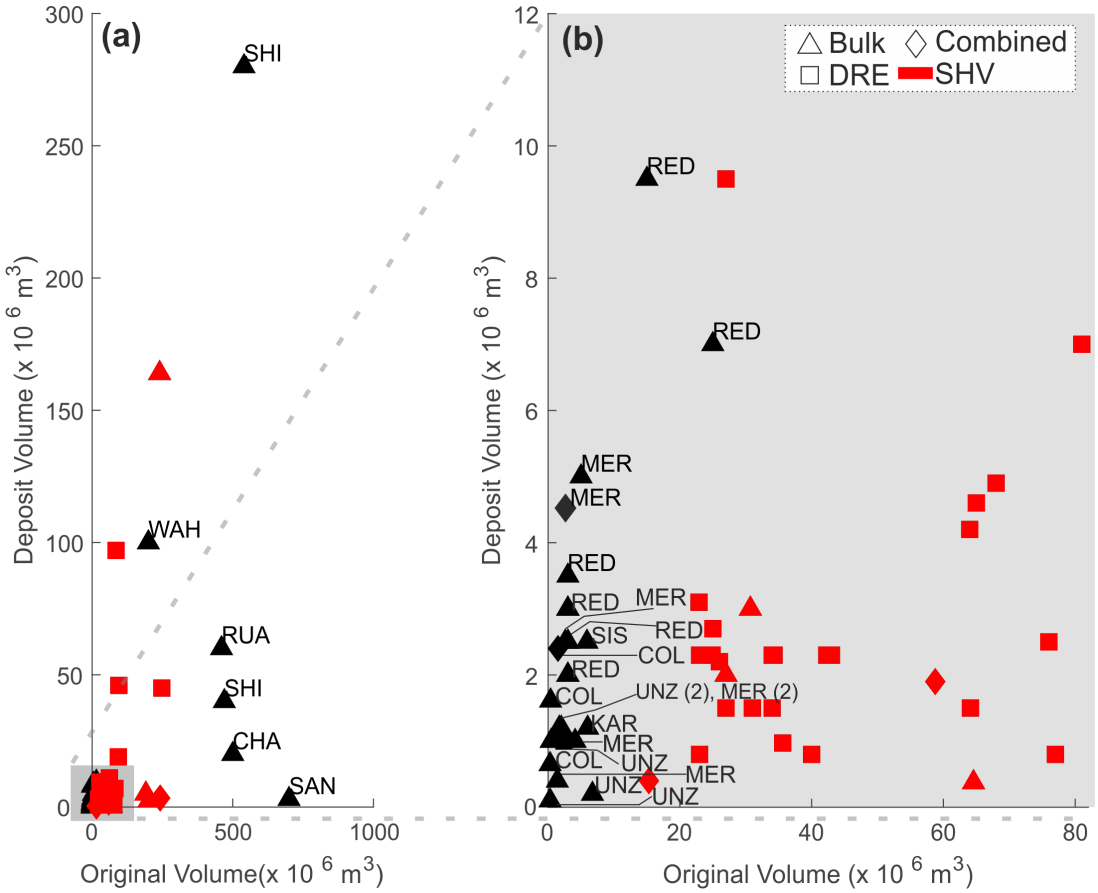

Figure 2.3: **(a)** Original dome volume vs. deposit volume, shown by type of volume measurement (bulk - triangle, DRE - square, combination of both - diamond). All red markers are collapses at Soufrière Hills volcano. See Figure 1 for volcano labelling, with the addition of KAR (Karangetang), Shiveluch (SHI), Sisters Dome (SIS), Wahanga (WAH), and Ruawahia (RUA); and **(b)** as in **(a)** but highlighting smaller absolute original volumes by zooming in on a portion of **(a)** shown by grey shading.

and relate directly to the collapse volume (*Siebert*, 1984). We therefore use deposit volume as a proxy for collapse volume. Reported volumes are often a combination of both dense rock equivalent (DRE) and bulk volumes. Where available, we record both in *GLADIS* and specify the measurement type for each volume entry. When calculating relative collapse volume ratio, we use two of the same measurement types (e.g. both deposit and original dome volume are DRE, or both are bulk); the measurement types in each case are shown in Figure 2.3. To maximise the sample size for statistical analysis, we assume in this study that these different volume measurements are comparable. Where relative collapse volume ratio is explicitly reported within the associated literature, we directly take this value and do not recalculate a percentage.

2.3.2 Defining attributed collapse mechanisms

One database field we focus on in this study is that of causal mechanism (Fig. 2.1). We define causal mechanisms to be processes that occur to change the equilibrium state of the dome and therefore lead to collapse. Causal mechanisms are defined as processes associated with the growth of the dome, e.g. the generation of gas overpressure within the dome (*Voight and Elsworth*, 2000). Instead, we define a triggering mechanism as an external event where the consequence of the event is a change in dome stability, e.g. intense rainfall (*Taron et al.*, 2007). Although the nuance of each term is different, both causes and triggers are treated equally as collapse-driving mechanisms in the remainder of this work.

For the purpose of quantitative data analysis, *GLADIS* currently lists one dominant mechanism for each event based on the conditions and causes for collapse as reported in the associated literature. We recognise that in the majority of cases, multiple processes may be at work and therefore also list full descriptions of mechanisms attributed to each collapse event as qualitative information within *GLADIS*. This information is stored in the mechanism source field of the database, where quotations are given from relevant literature to show determination of the dominant collapse mechanism. We also acknowledge that characterisation of only the dominant mechanism may create bias in analysis of collapse mechanisms, but this limitation comes from the primary literature, rather than re-interpretation in this study.

Interrogating *GLADIS* allows us to identify the most commonly cited mechanisms attributed to collapse. We show the number (n) of occurrences in each case, and we find these mechanisms to be:

1. *Gravitational loading* (n=57) - this focuses on addition of material, through continued extrusion, to the dome system. Where possible, volume and height are recorded as quantitative information in the database. High extrusion rates are not essential for inclusion in this category. We include here over-steepening (i.e. dome flank angle) due to endogenous (*Swanson et al.*, 1987) or exogenous (*Ui et al.*, 1999) growth.

2. *Internal gas overpressures* (n=19) - have been implicated in collapses after observations of explosive eruptions following major dome collapses (*Young et al.*, 1998). Overpressures exist within gas bubbles and lead to dome expansion. Pressurised gas trapped within the dome can weaken the bulk strength of the lava, leading to a decrease in overall dome stability (*Voight*

and Elsworth, 2000). This includes collapses where dome removal is cited in association with explosive activity.

3. *Topography-controlled collapses* (n=15) - defined here as collapses that occur when the size of a dome exceeds the crater size and over-tops the crater walls, likely due to dome and/or crater morphology (*Voight et al.*, 2002). This includes perched domes where the dome is emplaced onto a slope and the collapse is attributed to the effect of the slope itself.

4. *Intense rainfall* (n=14) has been attributed to several collapses as a triggering mechanism, with varying physical models associated. Rainwater can contribute to erosion of the slope toe, leading to undercutting and dome destabilisation (*Carn et al.*, 2004). Percolation of rainwater into a dome through fracture networks and interaction of rainwater with hot gases may create steam that pressurises existing potential failure surfaces (*Matthews et al.*, 2002; *Taron et al.*, 2007). We also consider the influence on local stresses within the dome by rainfall-induced thermal contraction (*Yamasato et al.*, 1998; *Simmons et al.*, 2004).

5. *A switch in extrusion direction* (n=5) - commonly observed immediately before collapse (e.g. *Luckett et al.*, 2008; *Loughlin et al.*, 2010; *Stinton et al.*, 2014). This is most likely attributed to thrust forces associated with emergence of a new lobe on older, cooled dome material, where the new material is able to exert a force onto the adjacent older material (*Calder et al.*, 2015), leading to collapse.

We note that some of these collapse mechanisms depend on the same fundamental physical processes. For example, collapses defined here as topography-controlled collapses are ultimately gravitational in nature. To be categorised as 'topography-controlled' in the database, they must be collapse events that are dependent on the topography, e.g. growing within a crater, and therefore would not have collapsed gravitationally if they had been emplaced onto a horizontal surface.

Less common mechanisms listed in the database include:

1. seismically induced collapses triggered either by regional earthquakes or by large volcano-tectonic earthquakes (*Charbonnier and Gertisser*, 2008; *Platz et al.*, 2012);

2. slumping/deflation leading to undercutting (*Herd et al.*, 2005);

3. weakening caused by weathering, hydrothermal activity or erosion (e.g. *Boudon et al.*, 1998; *Ball et al.*, 2013, 2015).

In the following sections, these mechanisms are grouped into a category called 'other' within the causal mechanism field, as they are cited in only 11% of cases with listed mechanisms.

2.4 Statistical analysis of the database

GLADIS contains information about 293 individual collapses from 35 different volcanoes. We find evidence for statistical dependence of absolute collapse volume on collapse mechanism, and of relative collapse volume ratio on both dome growth style and collapse mechanism. We show that the largest (≥50%) relative collapse volume ratios occur when collapses are attributed to gas overpressures or gravitational loading. Instead, small (<10%) relative collapse volume ratios occur in topography-controlled collapses or those attributed to a switch in extrusion direction. We find no correlation or statistical dependence between the following parameters: absolute collapse volume and extrusion rate (albeit on varied timescales, as defined within *GLADIS* and discussed later); relative collapse volume and extrusion rate, absolute collapse volume and dome growth style, collapse mechanism and original dome volume. The implications of this statistical analysis are discussed in Section 2.5.2.

2.4.1 Overview of data within *GLADIS*

Of these 293 events, 76% (n=222) occurred at andesitic or basaltic-andesite volcanoes, 21% (n=60) at dacitic volcanoes, 3% (n=9) at rhyolitic volcanoes, and <1% (n=1) at a basaltic volcano. We do not attempt to draw relationships between collapse and dome composition due to the dominance of andesitic/basaltic-andesite domes within the database. Deposit volume and original dome volume data are available for 27% of events in the database (n=78), and we focus on these events in the majority of our analysis as the collapse magnitude (absolute and relative) is one of the parameters that would be most useful to forecast for the purpose of hazard assessment. The overall spread of relative collapse volume ratios within *GLADIS* is shown in Figure 2.4.

Of the 78 events in *GLADIS* where relative collapse volume ratio can be calculated, 48.0% (n=35) of events are collapses of <10% of original dome volume.

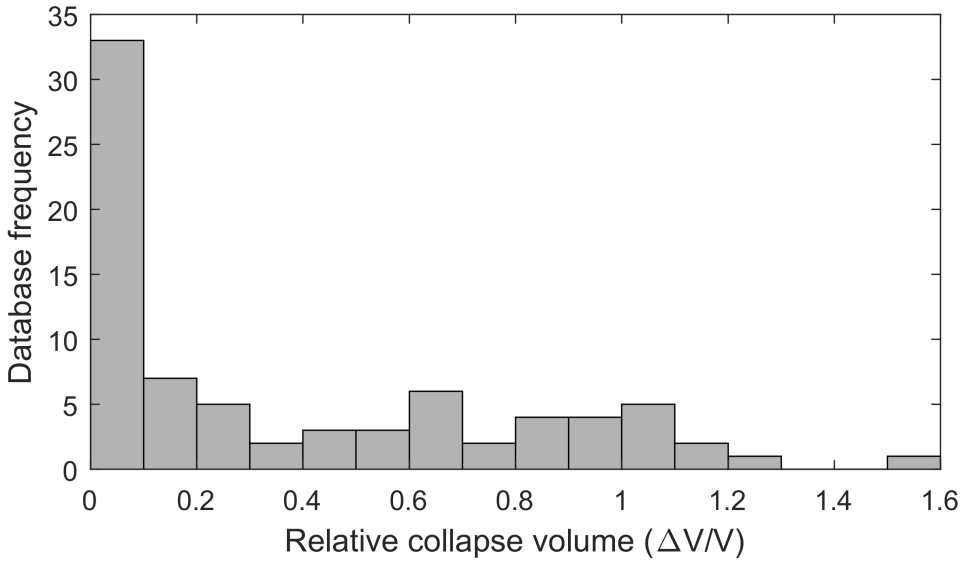

Figure 2.4: Histogram showing the distribution of relative collapse volume ($\Delta V/V$) in *GLADIS*.

There are four collapses in *GLADIS* where the relative collapse volume ratio exceeds 100%: Merapi (Indonesia), 15 June 1984; Redoubt (USA), 14 March 1990; Soufrière Hills volcano (Montserrat), 20 May 2006; and Volcán de Colima (Mexico), 10 July 2015 (Figure 2.4).

For the events at Colima and Merapi, it is likely that the percentage falsely exceeds 100% due to the time resolution of the original dome volume calculations. For example, the collapse at Colima on 10 July 2015 was after the final dome volume measurement, and so original dome volume is extrapolated from the data reported in *Thiele et al.* (2017). We assume that both Merapi and Colima collapses removed significant dome portions, and so these are approximated as 100% collapses in all quantitative analysis. The 14 March 1990 Redoubt event had a deposit volume of 3.5×10^6 m^3, and an original dome volume of 1-5$\times10^6$ m^3. For the purpose of quantitative analysis, we assume a volume of 3×10^6 m^3, which results in a collapse percentage exceeding 100%; we discuss uncertainty associated with Redoubt dome volumes further in Section 2.5.1.

The data for the 2006 Montserrat event has the highest time resolution, and likely the most reliable volume calculations of these 4 events due to close monitoring of this eruption. We suggest therefore that the 114% collapse stems from entrainment of material during the pyroclastic flow process so as to bulk up the volume (*Siebert*, 1984; *Bernard et al.*, 2014) but truly represents a complete dome collapse. Thus, for cases where addition of material to the deposit volume

through entrainment of non-dome material can cause the collapse percentage to exceed 100%, we assume that 100% of the original dome volume has contributed to the collapse.

Despite the uncertainties, we can thus be confident in each case that these are large events that involve complete dome removal. Therefore for all calculations within this study, events for which the collapse percentage exceeds 100% are considered as having a relative collapse volume ratio of 1 (or 100%).

2.4.2 Method of statistical analysis

We use statistical tests to examine the relationship between collapse magnitude and observed parameters: extrusion rate, collapse mechanism, and dome growth style. Collapse magnitude here refers both to absolute collapse volume (ΔV) and relative collapse volume ratio ($\Delta V/V$). Extrusion rate is an example of a continuous variable (i.e. one where any value is possible) and we analyse this using a regression line, where goodness of fit is expressed as an R^2 value. Dome growth style and causal mechanism are both categorical variables (i.e. where only certain values are possible), and for these we use one way analysis of variance (ANOVA) to determine if they are statistically correlated with collapse magnitude.

ANOVA is a technique used to test if there is statistical dependence between groups, by accepting or rejecting a null hypothesis. By using ANOVA, we determine an F-value which can be summarised as the variation between sample means, divided by variation within the samples. A critical F-value (F_{crit}) is identified from the degrees of freedom in the test, and if the calculated F-value exceeds F_{crit}, we conclude a dependent relationship exists between the two variables. A measure of statistical significance (a p-value) is also obtained from an ANOVA test, whereby this value is compared to a given significance level (generally α=0.05). The null hypothesis is accepted (i.e. statistical independence) if the calculated p-value falls below the chosen α value.

2.4.3 Correlation between extrusion rate and collapse magnitude

We first test whether collapse size can be associated with extrusion rate prior to collapse. This analysis is carried out using collapse events where values are contained in *GLADIS* for: original dome volume (V), collapse volume (ΔV), and extrusion rate. All three data fields are populated for 23% (n=68) of the

database.

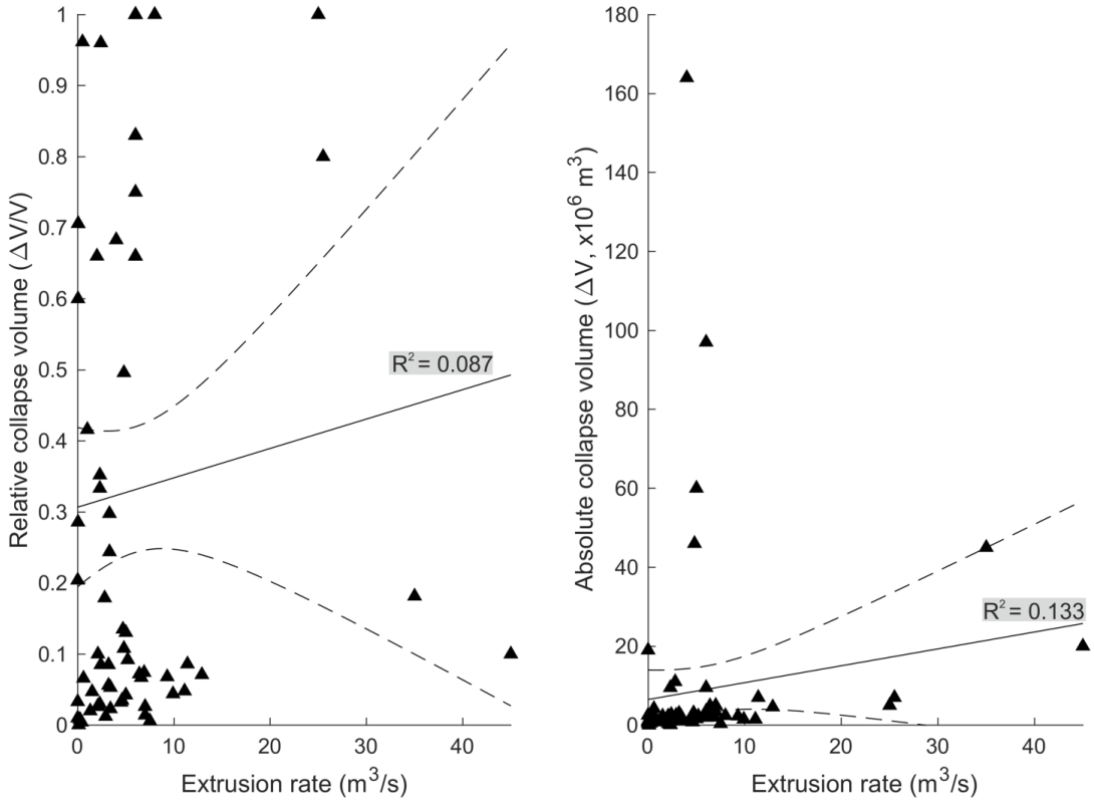

Figure 2.5: Extrusion rate and **(a)** relative collapse volume, and **(b)** absolute collapse volume. Solid line shows line of best fit, and dashed lines show 95% confidence intervals.

We examine the relationship first between relative collapse volume ratio ($\Delta V/V$) and extrusion rate (Figure 2.5a), and then between absolute collapse volume (ΔV) and extrusion rate (Figure 2.5b), showing a regression line and 95% confidence intervals in both cases. We find very low R^2 values for the correlation between extrusion rate and relative collapse volume ratio (R^2<0.10) and absolute collapse volume (R^2<0.13). This shows that there is no apparent correlation between extrusion rate and collapse volume, although we note that this analysis is significantly affected by the variation in time windows over which the extrusion is recorded.

2.4.4 Correlation between dome growth style and collapse magnitude

To test the relationship between collapse size and dome growth style, we use the entries in *GLADIS* where there are data for: original dome volume (V), collapse volume (ΔV) and dome growth style. All three data fields are populated for 25% (n=72) of database entries (Figure 2.6).

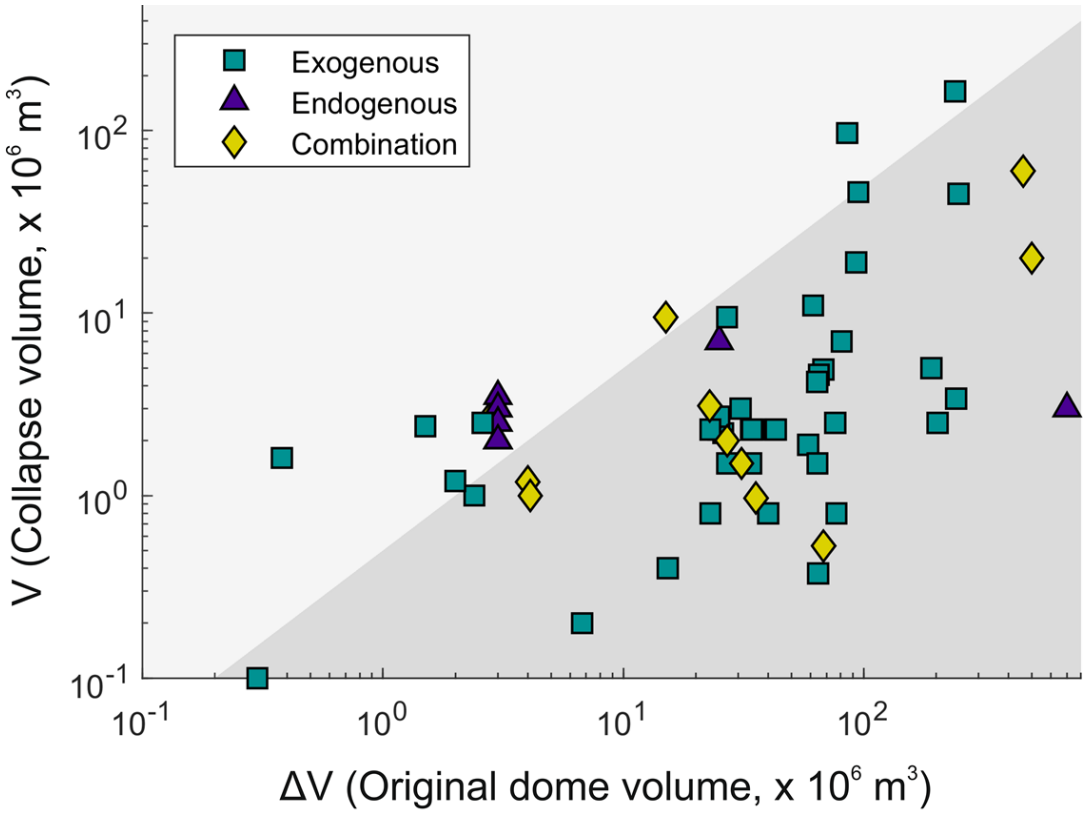

Figure 2.6: Logarithmic plot of original dome volume and collapse volume, shown by dome growth style exogenous (square), endogenous (triangle), and combination (diamond). Grey shading shows <50% collapse percentage.

We first propose a null hypothesis that collapse size is independent of dome growth style. Dome growth is a categorical variable within *GLADIS* and can be: (1) exogenous, where magma can reach the surface and extrude as new lobes or spines; (2) endogenous, where new magma is intruded into the base of the dome causing inflation; or (3) combination, where pulses of both exogenous and endogenous growth are observed. We test whether relative collapse volume ratio ($\Delta V/V$) varies according to dome growth style and find an F-value of 14.1, which means we can reject the null hypothesis (F_{crit}=3.1, p=7.5 × 10^{-6}). This suggests a significant effect of dome growth style on relative collapse volume ratio at a

significance level of α=0.05. The average relative collapse volume ratio for this dataset (where n=72) is 0.34, and the average relative collapse volume ratios for each dome growth group are shown in Table 2.3. The most significant deviation from this mean is for domes that grow endogenously, where the average $\Delta V/V$ is 0.76. We can confirm this significance with a post-hoc analysis using the Bonferroni procedure where we determine that the most statistically significant difference in $\Delta V/V$ between the groups shown in Table 2.3 is between exogenous and endogenous growth (with p=5 $\times$ 10^{-5}). Of the 13 endogenous domes with available volume data, 12 of these are domes from the 1989-90 eruption of Redoubt. It therefore seems likely that our analysis is heavily biased by the data from Redoubt and so the conclusion that relative collapse volume ratio is dependent on dome growth style may not be reliable on a global scale.

We also test the null hypothesis that absolute collapse volume (ΔV) is independent of dome growth style. We find an F-value of 1.9 (F_{crit}=3.1, p=0.16), demonstrating statistical independence. This suggests an insignificant effect of dome growth style on absolute collapse volume, and that growth style has greater effect on proportion of collapse, rather than absolute volume. Average absolute collapse volumes for each dome growth group are given in Table 2.3.

Table 2.3: Average relative collapse ($\Delta V/V$) and absolute collapse volume (ΔV) for groups of exogenous, endogenous and combination dome growth styles. Number in brackets is the number (n) of database entries considered for each mean calculation.

Dome growth style	Average relative collapse volume ratio ($\Delta V/V$)	Average absolute collapse volume (ΔV, 10^6 m^3)
Exogenous	0.24 (n=45)	10.60(n=45)
Endogenous	0.76 (n=13)	2.92 (n=13)
Combination	0.27 (n=14)	30.36 (n=14)

2.4.5 Correlation between collapse mechanism and collapse magnitude

To test the relationship between collapse magnitude and causal mechanism, we use the entries in *GLADIS* where we have values for: original dome volume (V), collapse volume (ΔV), and causal mechanism. All three of these data fields are populated in 18% of events (n=54).

We test the null hypothesis that collapse triggers are independent of original

dome volume. This test gives an F-value of 0.4 (F_{crit}=2.4, p=0.84), so we accept the null hypothesis and conclude that original dome size does not have a major impact on the causal mechanism of collapse.

We next propose the null hypothesis that relative collapse volume ratio ($\Delta V/V$) is independent of the causal mechanism for collapse. We find an F-value of 5.6 (F_{crit}=2.4, p=4×10^{-4}), therefore we reject the null hypothesis and show statistical dependence. This indicates a significant effect of causal mechanism on collapse proportion. The average relative collapse volume ratios for each causal mechanism are shown in Table 2.4.

Table 2.4: Average relative collapse ($\Delta V/V$) and absolute collapse volume (ΔV) for the following causal mechanisms: gravitational, rain, gas overpressures, switch in extrusion direction, topography, other. Number in brackets is the number (n) of entries considered for each mean calculation.

Causal mechanism	Average relative collapse volume ratio ($\Delta V/V$)	Average absolute collapse volume (ΔV, 10^6 m^3)
Gravitational	0.50(n=24)	4.58 (n=24)
Gas	0.68 (n=10)	6.37 (n=10)
Topography	0.08 (n=10)	4.0 (n=10)
Rain	1.0 (n=1)	97.0 (n=1)
Extrusion direction switch	0.05 (n=5)	2.92 (n=5)
Other	0.36 (n=4)	52.95 (n=4)

We again use a Bonferroni post-hoc analysis to find the most significant statistical difference. To do this, we add the one event with a causal mechanism of rain to the 'other' category, as the Bonferroni analysis requires more than one event per group. We find the largest statistical significance lies between causal mechanisms of gravitational loading and topography (p=9×10^{-3}). The average relative collapse volume ratio ($\Delta V/V$) for this dataset (n=54) is 0.4, so we can see that both gravitational loading and topography are outside of this group average. This suggests that collapses caused by topography or a switch in extrusion direction involve, on average, small (≈10%) proportions of original dome volume, whereas collapses caused by gravitational loading on average involve more substantial (≈50%) dome volume fractions. Bonferroni analysis also shows that there is a large statistical significance (p=4×10^{-3}) between the resultant $\Delta V/V$ values for collapses caused by gas pressurisation and those caused by a switch in extrusion direction, with average $\Delta V/V$ values at 0.68 and 0.05 respectively. The collapse mechanisms that lead to the largest

relative volume collapses are gas pressurisation and rainfall interaction, showing that pore fluid pressure plays an important role in dome stability. The collapses in the 'other' category are of significant proportions of dome material (average $\Delta V/V = 0.36$). The events in this category generally occur due to failure of part of the volcanic edifice which causes subsequent dome failure, for example the failure of the south-western wall of English's Crater prior to the 1997 collapse in Montserrat (*Norton et al.*, 2002), or the 2006 event at Merapi that occurred due to loading on an unstable crater wall (*Ratdomopurbo et al.*, 2013).

We follow up this result by testing the null hypothesis that absolute collapse volume (ΔV) is independent of collapse mechanism. We find an F-value of 7.8 (F_{crit}=2.4, p=5 × 10^{-5}), showing statistical dependence. This shows a very significant effect of causal mechanism on absolute collapse volume, and average absolute volumes for each causal mechanism are given in Table 2.4.

The 23 cases of gravitational loading as a causal mechanism are spread across eight volcanoes (Soufrière Hills, Mt. Unzen, Mt. St. Helens, Merapi, Redoubt, Chaitén, Santiaguito, and Volcán de Colima) so we can be confident that these results are not skewed by the prevalence of Soufrière Hills and Redoubt data within the database. However, the data for both switch in extrusion direction and topographic collapse come wholly from Soufrière Hills. This is due to the quality and frequency of observations during this eruption, particularly when considering that the definitive parameters can be hard to detect in real time (especially those that can be more subtle such as switch in extrusion direction). Although not considered here due to availability of volume data, these collapse mechanisms have been observed elsewhere, for example extrusion direction at Mt. St. Helens (*Vallance et al.*, 2008) and topography-controlled collapse at Volcán de Colima (*Hutchison et al.*, 2013). Therefore we suggest this result is still globally applicable.

This analysis does not consider instances when the mechanism has been observed but has not been followed by collapse, and therefore these statistics are relevant only given that a collapse has taken place. This, though, allows us to predict that if gravitational loading and change in extrusion direction were to cause collapses, an event triggered by loading is likely to be larger. From the group average (n=293, $\Delta V/V$=0.37), there is some suggestion that the subset for which causal mechanism is known is slightly biased towards higher values of relative collapse volume ratio. This could be a reporting bias as causal mechanisms are more commonly observed/reported for collapses that remove a more noticeable portion of the dome.

This analysis does not consider collapses with an interpreted causal mechanism but where volume information has not been reported (n=77). Of these 131 (54 with volume data, 77 without) events with listed causal mechanisms, 43% (n=56) are gravitational, 11% (n=14) are rainfall related, 20% (n=26) attributed to gas overpressures or explosive behaviour, 4% (n=5) to a switch in extrusion direction, 12% (n=16) to topography, and 11% (n=14) to various other causes (e.g. weathering, earthquakes or collapse of a crater wall). This suggests that rainfall is particularly under-represented in the dataset with available volume data (n=1 with volume data, n=14 in whole database).

2.5 Discussion and implications

2.5.1 Database uncertainties and reporting bias

We find that relative collapse volume ratio shows a statistically significant dependence on both the reported causal mechanisms, and dome growth styles. These parameters are not always routinely recorded and depend largely on independent observatory culture and also the observation opportunity during an eruption. We suggest therefore that for this type of study looking at forecasting dome collapse, the most important observations to be recorded during dome-forming eruptions that would aid further global statistical analysis are: (a) original dome volume; (b) collapse volume (calculated from the missing dome volume where possible); (c) dome growth style; and (d) cause of collapse.

An ideal analysis would be one where these mechanisms are recorded both when they exist as precursors to collapse and when they exist during base-line activity of volcanic unrest at dome-forming volcanoes. This would allow a more probabilistic analysis of conditions leading to dome collapse, and will be enabled by increases in the frequency of satellite measurements of deformation, topography, and dome surface changes (e.g. *Wang et al.*, 2015; *Arnold et al.*, 2016; *Ebmeier et al.*, 2018; *Walter et al.*, 2019) as well as technical advances in field methods such as Structure from Motion and terrestrial laser scanning (*James and Varley*, 2012; *de Zeeuw-van Dalfsen et al.*, 2017; *Thiele et al.*, 2017).

The largest data uncertainties in *GLADIS* arise from original dome volume estimates at Redoubt. Following the destruction of the February 1990 dome, 11 domes were emplaced and destroyed, all of which have individual volume estimates of 1-5 $\times 10^6$ m^3 (*Miller*, 1994). For all analyses so far in this study, we follow the example of *Miller* (1994) and take an arbitrary average of 3×10^6 m^3,

but this inevitably introduces an uncertainty to collapse volume calculations at Redoubt, and therefore our ANOVA tests throughout.

To test the effect of this uncertainty on our results, we retest independence of collapse volume and causal mechanism/dome growth style (Table 2.5) using the range of original dome volumes, and present this alongside the original analysis using a dome volume of 3×10^6 m^3. The reality is likely that some domes at Redoubt were nearer to 1×10^6 m^3, and some nearer to 5×10^6 m^3 in original volume. We assume each extreme and run ANOVA with all 11 original volumes at 1×10^6 m^3 and then all 11 original dome volumes at 5×10^6 m^3.

Table 2.5: F-value from ANOVA test, and p-value showing significance. Calculated from running ANOVA on causal mechanism and relative collapse volume ratio ($\Delta V/V$), and dome growth style and relative collapse volume ratio ($\Delta V/V$). In each instance, 11 original Redoubt volumes (from 21/2/1990 until 21/4/1990) have been changed to reflect the uncertainty in the original data recording.

	Causal mechanism		*Dome growth style*	
Redoubt original volume	F-value	p-value	F-value	p-value
1×10^6 m^3	6.1	2×10^{-4}	20.9	7.97×10^{-8}
3×10^6 m^3	5.6	4×10^{-4}	14.1	7.53×10^{-6}
5×10^6 m^3	8.2	1×10^{-5}	3.9	2×10^{-3}

We retest the null hypothesis that causal mechanism and relative collapse volume ratio are independent, using a range of original dome volumes at Redoubt (and maintaining the condition that any event with a $\Delta V/V > 1$ is given a $\Delta V/V$ of 1). All F-values exceed F_{crit} of 2.4 (Table 2.5), showing statistical dependence. We also retest the null hypothesis that dome growth style and relative collapse volume ratio are independent, finding again that all F-values exceed the F_{crit} of 3.1 (Table 2.5). It therefore seems that our result that relative collapse volume ratio is dependent on both causal mechanism and dome growth style is valid despite the uncertainty associated with the Redoubt data.

2.5.2 Implications for understanding lava dome collapse

Using ANOVA has allowed us to propose null hypotheses and reject or accept these based on data currently in *GLADIS*. We discuss how these results alongside examples of collapse events from *GLADIS* may influence our understanding of dome collapse processes.

It could be expected that high extrusion rates lead to higher collapse magnitudes (*Husain et al.*, 2014; *Zorn et al.*, 2018). We find that there is no apparent link between extrusion rate and collapse volumes (both absolute and relative). Of the highest recorded extrusion rates in *GLADIS*, we find a range in collapse magnitudes. For example, an extrusion rate of 25 m^3/s preceded a 100% collapse at Merapi on 5 November 2010 (*Pallister et al.*, 2013b), and a rate of 25.5 m^3/s preceded an 80% collapse at Redoubt on 2 January 1990 (*Brantley*, 1990). However, we also find that a 10% collapse at Chaitén on 19 February 2009 was preceded by a 45 m^3/s extrusion rate (*Pallister et al.*, 2013a). Both the Merapi and Redoubt events with relative collapse volume ratios >80% have attributed collapse mechanisms of gas pressurisation, whereas the smaller relative events at Chaitén and Soufrière Hills volcano are attributed to gravitational loading. We infer from this that collapse mechanism has a more significant effect on the resultant collapse than extrusion rate. Therefore qualitative observations designed to indicate the processes behind the collapse mechanisms listed in this study are extremely important, e.g. observed inflation of the dome suggests presence of gas pressure, or qualitative description of added material to the dome surface in one preferred extrusion direction.

We do however note that our analysis of this correlation is affected by the variations in time period over which the extrusion rate is recorded (ranging from daily estimates from the day of collapse, to rates averaged over the whole eruptive period), and so a higher time resolution would aid this. We speculate that extrusion rate may be linked to triggering collapse in a way that is not currently determinable using this dataset. For example, a faster magma ascent rate limits the timescale over which magma outgassing occurs (*Zorn et al.*, 2018), which can contribute to gas pressurisation of the dome (*Sparks*, 1997). Therefore whilst extrusion rate can be linked to explosivity or conceptually to the other collapse mechanisms discussed in this study, we identify no explicit causal link between extrusion rate and collapse magnitude. We suggest instead that the effect of extrusion rate on overall dome stability depends on dome conditions prior to collapse, and the time period over which a high extrusion rate occurs.

In this study we also found that dome growth style (e.g. exogenous, endogenous, combination) influences relative collapse volume ratio but not absolute collapse volume. We suggest this may be due to limited mass wastage at a dome which is emplaced endogenously. For example, the seismological record from the endogenously emplaced 1989-1990 dome at Redoubt shows very few minor rockfalls (*Cornelius and Voight*, 1994), whereas the exogenous domes at

Mt. Unzen and Soufrière Hills experienced a large number of minor rockfalls and pyroclastic flows due to crumbling of the dome carapace and shedding of material during growth (*Sato et al.*, 1992; *Calder et al.*, 2002).

Although this proposed mechanism of limited mass wastage during endogenous growth could explain why endogenous domes are more prone to larger relative collapses, we suggest that this dataset is biased by the endogenous domes at Redoubt. The exogenous domes in *GLADIS* have a huge range in relative collapse volumes, for example 0.6% at Soufrière Hills volcano (5 June 1997) (*Sparks et al.*, 1998; *Calder et al.*, 1999) and 96% at Merapi (11 November 1994) (*Voight et al.*, 2000a,b). The same applies to absolute collapse volumes where we have a range of 10^4 m^3 at Unzen (25 February 1992) (*Ui et al.*, 1999) to 164×10^6 m^3 at Soufrière Hills volcano (12 July 2003) (*Herd et al.*, 2005). Therefore to accept the statistical dependence of relative collapse magnitude on growth style, and the independence of absolute collapse volume from growth style, we suggest more data would be required to remove the Redoubt bias. This analysis particularly benefits from using relative collapse volume ratio. This reinforces the importance of original dome volume measurements in global dome stability analyses, particularly those with high temporal resolution.

We also show that original dome size cannot be used as a predictor of the cause of collapse. For example, two domes emplaced during the 1989-1990 eruption at Redoubt were both clearly linked to explosive collapse (*Miller*, 1994), but the 2 January 1990 collapse was of a 25×10^6 m^3 dome, whereas the 21 April 1990 collapse was of a dome with a volume of 1-5 $\times 10^6$ m^3. *Miller* (1994) suggest that explosive collapse was caused due to circulation of water caused by the ice-filled summit crater at Redoubt. We observe therefore that the explosive fragmentation caused by groundwater vaporisation is scale-insensitive, and suggest that this conclusion of scale independence holds true for the other collapse mechanisms listed.

In this study we demonstrate that collapse mechanism has a significant impact on both absolute and relative collapse volumes. We show that the largest difference in collapse magnitude lies between collapses attributed to gravitational loading and those controlled by topography. For example, collapses at Soufrière Hills volcano on 2 and 3 September 1996 had absolute volumes of 1.5×10^6 m^3 and 3.0×10^6 m^3 (*Calder et al.*, 2002), and relative collapse volume ratios of 5.6% and 8.5% respectively. Both occurred due to overspilling after new lobes had filled up previous collapse scars (*Calder et al.*, 2002). At Redoubt however, a series of gravitational failures (*Miller*, 1994; *Bull and Buurman*, 2013) all exceeded 66%

in relative volume.

The processes of collapse due to gravitational loading and topographical constraint were modelled by *Harnett et al.* (2018), where it was shown that larger relative volumes during gravitational collapse arose from development of a failure plane much deeper within the dome, whereas topography-controlled collapses involved only surface material and development of small-scale rockfalls, agreeing with the statistical analysis presented here. Resultant relative collapse volume ratios were also shown to be significantly different between collapses caused by gas pressurisation and those caused by a switch in extrusion direction. Similar physical processes are found to be the cause of this difference by *Harnett et al.* (2018), where a preferred extrusion direction results in much more superficial failures than gas pressurisation, and therefore this leads to a much smaller relative volume loss.

2.6 Conclusions

By statistically analysing a global and historical database of individual dome collapse events, we are able to examine relationships between collapse magnitude (both absolute and relative) and extrusion rate, dome growth style, and collapse mechanism.

We find that:

1. Short term extrusion rate does not affect relative collapse volume ratio ($\Delta V/V$) or absolute collapse volume (ΔV).

2. Dome growth style impacts relative collapse volume ratio, but does not influence absolute collapse volume. We see that endogenous dome growth is most likely to precede larger relative collapse volume ratios (average $\Delta V/V$=0.76), and exogenous dome growth is most likely to precede smaller relative collapse volumes (average $\Delta V/V$=0.24).

3. Dome volume at the time of collapse does not influence the mechanism of collapse.

4. The mechanism attributed to collapse significantly affects both relative collapse volume ratio ($\Delta V/V$) and absolute collapse volume (ΔV). The most significant statistical difference shows particularly that collapses attributed to gravitational loading (average $\Delta V/V$=0.50) or gas

pressurisation (average $\Delta V/V$=0.68) involve larger dome proportions and topography-controlled collapses (average $\Delta V/V$=0.08) or those caused by a switch in extrusion direction (average $\Delta V/V$=0.05) involve smaller dome proportions.

In this study we identify five key causal mechanisms for collapse: increased gravitational loading associated with dome growth; intense rainfall; increased gas overpressure leading to explosive activity; thrust forces associated with lava lobe extrusion and changing extrusion direction; and the relative size of the dome compared to the crater in which it sits (or the underlying slope). The strongest statistical link found through the analysis in this study exists between collapse size (both relative and absolute) and causal mechanism. We suggest therefore that these mechanisms should be the focus of future lava dome modelling efforts.

Although the *GLADIS* database is not exhaustive in its data collation, it allows us to examine historical and global trends in dome collapse and determine the parameters needed to inform short-term forecasting and hazard assessment at dome-forming volcanoes. Observatories play a key role in monitoring dome-building eruptions and feeding that information into the published literature which has been compiled in *GLADIS*. By adding more detailed recordings of real time volume estimates of the dome and collapse volumes to *GLADIS*, an even more detailed picture of dynamic dome processes will emerge.

Acknowledgements

This type of database would not be possible without daily efforts from observatory staff. We thank also the efforts of Sarah Ogburn in compiling *DomeHaz* and all at the Smithsonian for compiling the GVP both were instrumental in the early creation of *GLADIS*. CEH was funded through a NERC studentship as part of the Leeds York Spheres Doctoral Training Partnership (DTP) (grant number NE/L002574/1). SKE is supported by an Early Career Fellowship from the Leverhulme Trust and by a Living Planet Fellowship from the European Space Agency. We thank Sarah Ogburn and an anonymous reviewer for helpful comments on an earlier version of this manuscript. We also gratefully acknowledge Lucia Capra and Josef Dufek for editorial handling and additional comments that improved the quality of this manuscript.

Bibliography

Arnold, D. W., J. Biggs, G. Wadge, S. K. Ebmeier, H. M. Odbert, and M. P. Poland (2016), Dome growth, collapse, and valley fill at Soufrière Hills Volcano, Montserrat, from 1995 to 2013: Contributions from satellite radar measurements of topographic change, *Geosphere*, *12*(4), 1300–1315, doi:10.1130/GES01291.1.

Ball, J., E. Calder, B. Hubbard, and M. Bernstein (2013), An assessment of hydrothermal alteration in the Santiaguito lava dome complex, Guatemala: implications for dome collapse hazards, *Bulletin of Volcanology*, *75*, 676–694, doi:10.1007/s00445-012-0676-z.

Ball, J., P. Stauffer, E. Calder, and G. Valentine (2015), The hydrothermal alteration of cooling lava domes, *Bulletin of Volcanology*, *77*(12), 102, doi:10.1007/s00445-015-0986-z.

Bardintzeff, J. (1984), Merapi Volcano (Java , Indonesia) and Merapi-Type Nuée Ardente, *Bulletin of Volcanology*, *47*(3), 433–446, doi:10.1007/bf01961217.

Bernard, J., K. Kelfoun, J. L. Le Pennec, and S. Vallejo Vargas (2014), Pyroclastic flow erosion and bulking processes: comparing field-based vs. modeling results at Tungurahua volcano, Ecuador, *Bulletin of Volcanology*, *76*(9), 1–16, doi:10.1007/s00445-014-0858-y.

Blake, S. (1990), *Viscoplastic Models of Lava Domes*, pp. 88–126, Springer Berlin Heidelberg, Berlin, Heidelberg, doi:10.1007/978-3-642-74379-5_5.

Boudon, G., B. Villemant, J. Komorowski, P. Ildefonse, and M. Semet (1998), The hydrothermal system at Soufrière Hills volcano, Montserrat (West Indies): Characterization and role in the on-going eruption, *25*(19), 3693–3696.

Brantley, S. (1990), The Eruption of Redoubt Volcano, Alaska, December 14, 1989 - August 31, 1990, *Tech. rep.*, U.S. Geological Survey.

Brown, S., H. Crosweller, R. S. Sparks, E. Cottrell, N. Deligne, N. Guerrero, L. Hobbs, K. Kiyosugi, S. Loughlin, L. Siebert, and S. Takarada (2014), Characterisation of the Quaternary eruption record: analysis of the Large Magnitude Explosive Volcanic Eruptions (LaMEVE) database, *Journal of Applied Volcanology*, *3*(1), 5, doi:10.1186/2191-5040-3-5.

Bull, K., and H. Buurman (2013), An overview of the 2009 eruption of Redoubt Volcano, Alaska, *Journal of Volcanology and Geothermal Research*, *259*(March 2009), 2–15, doi:10.1016/j.jvolgeores.2012.06.024.

Calder, E., P. Cole, W. Dade, T. Druitt, R. Hoblitt, H. Huppert, L. Ritchie, R. Sparks, and S. Young (1999), Mobility of pyroclastic flows and surges at the Soufrière Hills Volcano, Montserrat, *Geophysical Research Letters*, *26*(5), 537–540.

Calder, E., R. Luckett, R. Sparks, and B. Voight (2002), Mechanisms of lava dome instability and generation of rockfalls and pyroclastic flows at Soufrière Hills Volcano, Montserrat, *Geological Society, London, Memoirs*, *21*, 173–190, doi:10.1144/GSL.MEM.2002.021.01.08.

Calder, E. S., Y. Lavallée, J. E. Kendrick, and M. Bernstein (2015), Chapter 18 - Lava Dome Eruptions, in *The Encyclopedia of Volcanoes*, pp. 343–362, Academic Press, doi:10.1016/B978-0-12-385938-9.00018-3.

Carn, S. A., R. B. Watts, G. Thompson, and G. E. Norton (2004), Anatomy of a lava dome collapse: the 20 March 2000 event at Soufrière Hills Volcano, Montserrat, *Journal of Volcanology and Geothermal Research*, *100*(131), 241–264, doi:10.1016/S0377-0273(03)00364-0.

Charbonnier, S., and R. Gertisser (2008), Field observations and surface characteristics of pristine block-and-ash flow deposits from the 2006 eruption of Merapi Volcano, Java, Indonesia, *Journal of Volcanology and Geothermal Research*, *177*(4), 971–982, doi:10.1016/j.jvolgeores.2008.07.008.

Cole, P. D., E. S. Calder, R. Sparks, A. Clarke, T. H. Druitt, S. Young, R. Herd, C. L. Harford, and G. Norton (2002), Deposits from dome-collapse and fountain-collapse pyroclastic flows at Soufrière Hills Volcano, Montserrat, *Geological Society, London, Memoirs*, *21*, 231–262.

Cornelius, R. R., and B. Voight (1994), Seismological aspects of the 1989-1990 eruption at Redoubt Volcano, Alaska: the Materials Failure Forecast Method (FFM) with RSAM and SSAM seismic data, *Journal of Volcanology and Geothermal Research*, *62*(1-4), 469–498, doi:10.1016/0377-0273(94)90048-5.

Crisp, J. A. (1984), Rates of magma emplacement and volcanic output, *Journal of Volcanology and Geothermal Research*, *20*(3-4), 177–211, doi:10.1016/0377-0273(84)90039-8.

Crosweller, H. S., B. Arora, S. K. Brown, E. Cottrell, N. I. Deligne, N. O. Guerrero, L. Hobbs, K. Kiyosugi, S. C. Loughlin, J. Lowndes, M. Nayembil, L. Siebert, R. S. J. Sparks, S. Takarada, and E. Venzke (2012), Global database on large magnitude explosive volcanic eruptions (LaMEVE), *Journal of Applied Volcanology*, *1*(1), 1–13, doi:10.1186/2191-5040-1-4.

de Zeeuw-van Dalfsen, E., N. Richter, G. González, and T. R. Walter (2017), Geomorphology and structural development of the nested summit crater of Láscar Volcano studied with Terrestrial Laser Scanner data and analogue modelling, *Journal of Volcanology and Geothermal Research*, *329*, 1–12, doi:10.1016/j.jvolgeores.2016.09.018.

Donne, D. D., A. J. Harris, M. Ripepe, and R. Wright (2010), Earthquake-induced thermal anomalies at active volcanoes, *Geology*, *38*(9), 771–774, doi:10.1130/G30984.1.

Ebmeier, S. K., B. J. Andrews, M. C. Araya, D. W. Arnold, J. Biggs, C. Cooper, E. Cottrell, M. Furtney, J. Hickey, J. Jay, R. Lloyd, A. L. Parker, M. E. Pritchard, E. Robertson, E. Venzke, and J. L. Williamson (2018), Synthesis of global satellite observations of magmatic and volcanic deformation: implications for volcano monitoring & the lateral extent of magmatic domains, *Journal of Applied Volcanology*, *7*(1), 1–26, doi:10.1186/s13617-018-0071-3.

Furlan, C. (2010), Extreme value methods for modelling historical series of large volcanic magnitudes, *Statistical Modelling*, *10*(2), 113–132, doi:10.1177/1471082X0801000201.

Genareau, K., S. Cronin, and G. Lube (2015), Effects of volatile behaviour on dome collapse and resultant pyroclastic surge dynamics: Gunung Merapi 2010 eruption, *Geological Society, London, Special Publications*, *410*, 199–218, doi:10.1144/SP410.6.

Geyer, A., and J. Martí (2008), The new worldwide collapse caldera database (CCDB): A tool for studying and understanding caldera processes, *Journal of Volcanology and Geothermal Research*, *175*(3), 334–354, doi:10.1016/j.jvolgeores.2008.03.017.

Hale, A. (2008), Lava dome growth and evolution with an independently deformable talus, *Geophysical Journal International*, *174*(1), 391–417, doi:10.1111/j.1365-246X.2008.03806.x.

Hale, A., E. Calder, S. Loughlin, G. Wadge, and G. Ryan (2009a), Modelling the lava dome extruded at Soufrière Hills Volcano, Montserrat, August 2005-May 2006. Part I: Dome shape and internal structure, *Journal of Volcanology and Geothermal Research*, *187*(1-2), 69–84, doi:10.1016/j.jvolgeores.2009.08.014.

Hale, A., E. Calder, S. Loughlin, G. Wadge, and G. Ryan (2009b), Modelling the lava dome extruded at Soufrière Hills Volcano, Montserrat, August 2005-May 2006. Part II: Rockfall activity and talus deformation, *Journal of Volcanology and Geothermal Research*, *187*(1-2), 69–84, doi:10.1016/j.jvolgeores.2009.08.014.

Harnett, C. E., M. E. Thomas, M. D. Purvance, and J. Neuberg (2018), Using a discrete element approach to model lava dome emplacement and collapse, *Journal of Volcanology and Geothermal Research*, doi:10.1016/j.jvolgeores.2018.06.017.

Hédervári, P. (1963), On the energy and magnitude of volcanic eruptions, *Bulletin Volcanologique*, *25*(1), 373–385, doi:10.1007/BF02596568.

Herd, R., M. Edmonds, and V. Bass (2005), Catastrophic lava dome failure at Soufrière Hills Volcano, Montserrat, 12-13 July 2003, *Journal of Volcanology and Geothermal Research*, *148*(3-4), 234–252, doi:10.1016/j.jvolgeores.2005.05.003.

Hooper, D. M., and G. S. Mattioli (2001), Kinematic modeling of pyroclastic flows produced by gravitational dome collapse at Soufrière Hills volcano, Monstserrat, *Natural Hazards*, *23*(1), 65–86, doi:10.1023/A:1008130605558.

Hungr, O., S. Leroueil, and L. Picarelli (2014), The Varnes classification of landslide types, an update, *Landslides*, *11*(2), 167–194, doi:10.1007/s10346-013-0436-y.

Husain, T., D. Elsworth, B. Voight, G. Mattioli, and P. Jansma (2014), Influence of extrusion rate and magma rheology on the growth of lava domes: Insights from particle-dynamics modeling, *Journal of Volcanology and Geothermal Research*, *285*, 110–117, doi:10.1016/j.jvolgeores.2014.08.013.

Hutchison, W., N. Varley, D. M. Pyle, T. A. Mather, and J. A. Stevenson (2013), Airborne thermal remote sensing of the Volcán de Colima (Mexico) lava dome from 2007 to 2010, *Geological Society, London, Special Publications*, *380*(1), 203–228, doi:10.1144/SP380.8.

James, M. R., and N. Varley (2012), Identification of structural controls in an active lava dome with high resolution DEMs: Volcán de Colima, Mexico, *Geophysical Research Letters*, *39*(22), 1–5, doi:10.1029/2012GL054245.

Kokelaar, P. (2002), Setting, chronology and consequences of the eruption of Soufrière Hills Volcano, Montserrat (1995-1999), *Geological Society, London, Memoirs*, *21*, 1–43.

Loughlin, S., R. Luckett, G. Ryan, T. Christopher, V. Hards, S. De Angelis, L. Jones, and M. Strutt (2010), An overview of lava dome evolution, dome collapse and cyclicity at Soufrière Hills Volcano, Montserrat, 2005-2007, *Geophysical Research Letters*, *37*, doi:10.1029/2010GL042547.

Luckett, R., S. Loughlin, S. De Angelis, and G. Ryan (2008), Volcanic seismicity at Montserrat, a comparison between the 2005 dome growth episode and earlier dome growth, *Journal of Volcanology and Geothermal Research*, *177*(4), 894–902, doi:10.1016/j.jvolgeores.2008.07.006.

Matthews, A., J. Barclay, S. Carn, G. Thompson, J. Alexander, R. Herd, and C. Williams (2002), Rainfall-induced volcanic activity on Montserrat, *Geophysical Research Letters*, *29*, doi:10.1029/2002GL014863.

Mercado, R., W. Rose, O. Matias, and J. Giron (1988), November 1929 Dome Collapse and Piroclastic Flow at Santiaguito Dome, Guatemala, *Eos, Transactions American Geophysical Union*, *69*, 1487.

Miller, T. (1994), Dome growth and destruction during the 1989-1990 eruption of Redoubt Volcano, *Journal of Volcanology and Geothermal Research*, *62*(1-4), 197–212, doi:10.1016/0377-0273(94)90034-5.

Norton, G., R. Watts, B. Voight, G. Mattioli, R. Herd, S. Young, G. Devine, C. Aspinnall, B. Bonadonna, B. Baptie, M. Edmonds, A. Jolly, S. Loughlin, R. Luckett, and R. S. J. Sparks (2002), Pyroclastic flow and explosive activity at Soufrière Hills Volcano, Montserrat. during a period of virtually no magma extrusion (March 1998 to November 1999), *Geological Society, London, Memoirs*, *21*, 467–481.

Ogburn, S. (2012), FlowDat: Mass flow database v2.2.

Ogburn, S., S. Loughlin, and E. Calder (2012), DomeHaz: Dome-forming eruptions database v2.4.

Ogburn, S., S. Loughlin, and E. Calder (2015), The association of lava dome growth with major explosive activity (VEI4): DomeHaz, a global dataset, *Bulletin of Volcanology*, *77*(40), doi:10.1007/s00445-015-0919-x.

Ogburn, S., J. Berger, E. Calder, D. Lopes, A. Patra, E. B. Pitman, R. Rutarindwa, E. Spiller, and R. Wolpert (2016), Pooling strength amongst limited datasets using hierarchical Bayesian analysis, with application to pyroclastic density current mobility metrics, *Statistics in Volcanology*, *2*, 1–26, doi:10.5038/2163-338X.2.1.

Ogburn, S. E., and E. S. Calder (2017), The Relative Effectiveness of Empirical and Physical Models for Simulating the Dense Undercurrent of Pyroclastic Flows under Different Emplacement Conditions, *Frontiers in Earth Science*, *5*(November), doi:10.3389/feart.2017.00083.

Pallister, J., A. Diefenbach, W. Burton, J. Munoz, J. Griswold, L. Lara, J. Lowenstern, and C. Valenzuela (2013a), The Chaitén rhyolite lava dome: Eruption sequence, lava dome volumes, rapid effusion rates and source of the rhyolite magma, *Andean Geology*, *40*(2), 277–294, doi:10.5027/andgeoV40n2-a06.

Pallister, J. S., D. J. Schneider, J. P. Griswold, R. H. Keeler, W. C. Burton, C. Noyles, C. G. Newhall, and A. Ratdomopurbo (2013b), Merapi 2010 eruption-Chronology and extrusion rates monitored with satellite radar and used in eruption forecasting, *Journal of Volcanology and Geothermal Research*, *261*, 144–152, doi:10.1016/j.jvolgeores.2012.07.012.

Platz, T., S. Cronin, J. Procter, V. Neall, and S. Foley (2012), Non-explosive, dome-forming eruptions at Mt. Taranaki, New Zealand, *Geomorphology*, *136*(1), 15–30, doi:10.1016/j.geomorph.2011.06.016.

Ratdomopurbo, A., F. Beauducel, J. Subandriyo, I. Nandaka, C. Newhall, Suharna, D. Sayudi, H. Suparwaka, and Sunarta (2013), Overview of the 2006 eruption of Mt. Merapi, *Journal of Volcanology and Geothermal Research*, *261*, 87–97, doi:10.1016/j.jvolgeores.2013.03.019.

Sato, H., T. Fujii, and S. Nakada (1992), Crumbling of dacite dome lava and generation of pyroclastic flows at Unzen volcano, *Letters to Nature*, *360*, 664–666.

Saucedo, R., J. Macías, M. Sheridan, M. Bursik, and J. Komorowski (2005), Modeling of pyroclastic flows of Colima Volcano, Mexico: implications for hazard assessment, *Journal of Volcanology and Geothermal Research*, *139*(1-2), 103–115, doi:10.1016/j.jvolgeores.2004.06.019.

Sheldrake, T., R. Sparks, K. Cashman, G. Wadge, and W. Aspinall (2016), Similarities and differences in the historical records of lava dome-building volcanoes: Implications for understanding magmatic processes and eruption forecasting, *Earth-Science Reviews*, *160*, 240–263, doi:10.1016/j.earscirev.2016.07.013.

Siebert, L. (1984), Large volcanic debris avalanches: Characteristics of source areas, deposits, and associated eruptions, *Journal of Volcanology and Geothermal Research*, *22*(3-4), 163–197, doi:10.1016/0377-0273(84)90002-7.

Siebert, L., T. Simkin, and P. Kimberly (2010), *Volcanoes of the World*, 3rd ed., 568 pp., University of California Press, Berkeley.

Simmons, J., D. Elsworth, and B. Voight (2004), Instability of exogenous lava lobes during intense rainfall, *Bulletin of Volcanology*, *66*(8), 725–734, doi:10.1007/s00445-004-0353-y.

Simmons, J., D. Elsworth, and B. Voight (2005), Classification and idealized limit-equilibrium analyses of dome collapses at Soufrière Hills volcano, Montserrat, during growth of the first lava dome: November 1995-March 1998, *Journal of Volcanology and Geothermal Research*, *139*(3-4), 241–258, doi:10.1016/j.jvolgeores.2004.08.009.

Sparks, R. S. J. (1997), Causes and consequences of pressurisation in lava dome eruptions, *Earth and Planetary Science Letters*, *150*, 177–189.

Sparks, R. S. J., S. R. Young, J. Barclay, E. S. Calder, P. Cole, B. Darroux, M. A. Davies, T. H. Druitt, C. Harford, R. Herd, M. James, A. M. Lejeune, S. Loughlin, G. Norton, G. Skerrit, M. V. Stasiuk, N. S. Stevens, J. Toothill, G. Wadge, and R. Watts (1998), Magma production and growth of the lava dome of the Soufrière Hills Volcano, Montserrat, West Indies: November 1995 to December 1997, *Geophysical Research Letters*, doi:10.1029/98GL00639.

Stinton, A., P. D. Cole, R. Stewart, H. Odbert, and P. Smith (2014), The 11 February 2010 partial dome collapse at Soufrière Hills Volcano, Montserrat, *Geological Society, London, Memoirs*, *39*, 133–152, doi:10.1144/M39.7.

Swanson, D., D. Dzurisin, R. Holcomb, E. Iwatsubo, W. Chadwick, T. J. Casadevall, J. Ewert, and C. Heliker (1987), Growth of the lava dome at Mount St. Helens, Washington, (USA), 1981-1983, *Geological Society of America, Special Pa.*

Taron, J., D. Elsworth, G. Thompson, and B. Voight (2007), Mechanisms for rainfall-concurrent lava dome collapses at Soufrière Hills Volcano, 20002002, *Journal of Volcanology and Geothermal Research*, *160*, 195–209, doi:10.1016/j.jvolgeores.2006.10.003.

Thiele, S. T., N. Varley, and M. R. James (2017), Thermal photogrammetric imaging: A new technique for monitoring dome eruptions, *Journal of Volcanology and Geothermal Research*, *337*, 140–145, doi:10.1016/j.jvolgeores.2017.03.022.

Ui, T., N. Matsuwo, M. Sumita, and A. Fujinawa (1999), Generation of block and ash flows during the 1990-1995 eruption of Unzen Volcano, Japan, *Journal of Volcanology and Geothermal Research*, *89*, 123–137.

Vallance, J., D. Schneider, and S. Schilling (2008), Growth of the 2004-2006 Lava-Dome Complex at Mount St. Helens, Washington, *A Volcano Rekindled: The Renewed Eruption of Mount St. Helens 2004-2006, U.S. Geological Survey Professional Paper 1750*, pp. 169–208.

Venzke, E., R. Wunderman, and L. McClelland (), Global volcanism, 1968 to present.

Voight, B. (2000), Structural stability of andesite volcanoes and lava domes, *Philosophical Transactions of the Royal Society of London*, *358*, 1663–1703.

Voight, B., and D. Elsworth (2000), Instability and collapse of hazardous gas-pressurized lava domes, *Geophysical Research Letters*, *27*(1), 1–4, doi:10.1029/1999GL008389.

Voight, B., E. K. Constantine, S. Siswowidjoyo, and R. Torley (2000a), Historical eruptions of Merapi Volcano, Central Java, Indonesia, 1768-1998, *Journal of Volcanology and Geothermal Research*, *100*, 69–138.

Voight, B., K. Young, D. Hidayat, Subandrio, M. Purbawinata, A. Ratdomopurbo, Suharna, Panut, D. Sayudi, R. LaHusen, J. Marso, T. L. Murray, M. Dejean, M. Iguchi, and K. Ishihara (2000b), Deformation

and seismic precursors to dome-collapse and fountain-collapse nuées ardentes at Merapi Volcano, Java, Indonesia, 1994-1998, *Journal of Volcanology and Geothermal Research*, *100*(1-4), 261–287, doi:10.1016/s0377-0273(00)00140-2.

Voight, B., J.-C. Komorowski, G. E. Norton, A. B. Belousov, M. Belousova, G. Boudon, P. W. Francis, W. Franz, P. Heinrich, R. S. J. Sparks, and S. R. Young (2002), The 26 December (Boxing Day) 1997 sector collapse and debris avalanche at Soufrière Hills Volcano, Montserrat, *Geological Society, London, Memoirs*, *21*(1), 363–407, doi:10.1144/GSL.MEM.2002.021.01.17.

Wadge, G. (2009), Assessing the pyroclastic flow hazards from dome collapse at Soufrière Hills Volcano, Montserrat, *Studies in Volcanology: The Legacy of George Walker, Specical Publication IAVCEI*, *2*, 211–224.

Wadge, G., P. Jackson, S. M. Bower, A. W. Woods, and E. Calder (1998), Computer simulations of pyroclastic flows from dome collapse, *Geophysical Research Letters*, *25*(19), 3677–3680, doi:10.1029/98GL00710.

Wadge, G., B. Voight, R. Sparks, P. Cole, S. Loughlin, and R. Robertson (2014), An overview of the eruption of Soufrière Hills Volcano, Montserrat from 2000 to 2010, *Geological Society, London, Memoirs*, *39*, 1–40, doi:10.1144/M39.1.

Walter, T. R., C. E. Harnett, N. Varley, D. Vargas, J. Salzer, E. U. Zorn, M. Bretón, R. Arámbula, and M. E. Thomas (2019), Imaging the 2013 explosive crater excavation and new dome formation at Volcán de Colima with TerraSAR-X , time-lapse cameras and modelling, *Journal of Volcanology and Geothermal Research*, *369*, 224–237, doi:10.1016/j.jvolgeores.2018.11.016.

Wang, T., M. P. Poland, and Z. Lu (2015), Dome growth at Mount Cleveland, Aleutian Arc, quantified by time series TerraSAR-X imagery, *Geophysical Research Letters*, pp. 1–8, doi:10.1002/2015GL066784.Received.

Witham, C. S. (2005), Volcanic disasters and incidents: A new database, *Journal of Volcanology and Geothermal Research*, *148*(3-4), 191–233, doi:10.1016/j.jvolgeores.2005.04.017.

Wolpert, R. L., S. E. Ogburn, and E. S. Calder (2016), The longevity of lava dome eruptions, *Journal of Geophysical Research: Solid Earth*, *121*, 676–686, doi:10.1002/2013JB010480.Received.

Wright, R., L. P. Flynn, H. Garbeil, A. J. Harris, and E. Pilger (2004), MODVOLC: Near-real-time thermal monitoring of global volcanism, *Journal of Volcanology and Geothermal Research*, *135*(1-2), 29–49, doi:10.1016/j.jvolgeores.2003.12.008.

Yamasato, H., S. Kitagawa, and M. Komiya (1998), Effect of rainfall on dacitic lava dome collapse at Unzen volcano, Japan, *Papers in Meteorology and Geophysics*, *48*(3), 73–78.

Young, S. R., R. S. J. Sparks, W. P. Aspinall, L. L. Lynch, A. D. Miller, R. E. A. Robertson, and J. B. Shepherd (1998), Overview of the eruption of Soufrière Hills Volcano, Montserrat, 18 July 1995 to December 1997, *Geophysical Research Letters*, *25*(18), 3389–3392, doi:10.1029/98GL01405.

Zorn, E. U., M. C. Rowe, S. J. Cronin, A. G. Ryan, L. A. Kennedy, and J. K. Russell (2018), Influence of porosity and groundmass crystallinity on dome rock strength: a case study from Mt. Taranaki, New Zealand, *Bulletin of Volcanology*, *80*(4), doi:10.1007/s00445-018-1210-8.

Chapter 3

Using a discrete element approach to model lava dome emplacement and collapse

C. E. Harnett[1], M. E. Thomas [1], M. Purvance [2] and J. Neuberg[1]

[1] *School of Earth and Environment, University of Leeds, United Kingdom*
[2] *Itasca Consulting Group, Minneapolis, Minnesota 55401, USA*

Citation: **Harnett, C.E.**, Thomas, M.E., Purvance, M., and Neuberg, J (2018), Using a discrete element approach to model lava dome emplacement and collapse, *Journal of Volcanology and Geothermal Research*, doi:10.1016/j.jvolgeores.2018.06.017

Abstract

Lava dome collapses can lead to explosive activity and pyroclastic flow generation, which makes them one of the most deadly consequences of volcanic activity. The mechanisms linked to a collapse are however still poorly understood and very few numerical models exist that investigate the actual collapse of a lava dome after emplacement. We use a discrete element method implemented in the modelling software Particle Flow Code to investigate lava dome growth, but also go further to test the stability of the dome under the following conditions: increased internal pressure; switch in extrusion direction caused by partial cooling of the dome; and extrusion of lava on to variable underlying topography. We initially show the morphology development of a growing lava dome, and how the rheological boundary between core and talus evolves throughout the lifetime of a dome and with varied solidus pressures. Through visualisation of strain accumulation within the lava dome we show superficial rockfall development due to interaction with topography, whereas large deep-seated failures occur when the dome is exposed to internal overpressures. We show that a switch in extrusion direction promotes a transition from endogenous to exogenous dome growth and leads to lava lobe formation. We demonstrate that lava dome collapse exhibits many features similar to common landslides and by investigating strain patterns within the dome, we can use numerical modelling to understand features that elude field observations.

3.1 Introduction

Lava domes form when magma extrudes from a vent and piles up due to its high viscosity. Once unstable, collapse of a lava dome can generate rockfalls, debris avalanches, and pyroclastic flows. Despite this significant hazard, relationships between active dome extrusion and collapse processes are still not entirely understood (*Voight*, 2000; *Calder et al.*, 2002).

The stability of a lava dome is affected by multiple factors including but not limited to: gravitational collapse due to over-steepening (*Swanson et al.*, 1987); internal gas overpressures (*Sparks*, 1997; *Voight and Elsworth*, 2000; *Elsworth and Voight*, 2001); interaction with intense rainfall (*Matthews et al.*, 2002; *Carn et al.*, 2004; *Elsworth et al.*, 2004; *Taron et al.*, 2007); a switch in extrusion direction (*Loughlin et al.*, 2010); topography underlying the dome (for example, a dome

exceeding the size of the crater in which it sits) (*Voight et al.*, 2002); hydrothermal alteration (*Ball et al.*, 2015); and the fracture state of the dome, both small-scale due to dynamic and explosive dome growth (e.g. *Darmawan et al.*, 2018) and large-scale from local tectonic faulting (e.g. *Walter et al.*, 2015).

Dome morphology also plays an inevitable role in overall dome stability. Different types of domes have been classified by various studies (e.g. *Blake*, 1990; *Watts et al.*, 2002), ranging from pancake domes, coulees, and lava lobes (generally wide and low in height) to Peléean or blocky domes, which have a more extensive talus apron and are taller for a given radius (*Blake*, 1990). Blocky domes can also generate spines, whereby stiff, cooled material extrudes near-vertically (*Watts et al.*, 2002). Blockier/Peléean-style domes are more likely to collapse due to the larger height to radius ratio, and collapses generally involve more material than shallow collapses at pancake-style domes (*Blake*, 1990). The domes modelled in this paper are analogous to blockier domes, rather than pancake domes or coulées.

Despite recent advances in computational modelling of lava domes (*Hale et al.*, 2007; *Hale*, 2008; *Husain et al.*, 2014, 2018), current models focus on understanding initial emplacement dynamics rather than more hazardous aspects of dome collapse. Here we develop the idea, first posed by *Husain et al.* (2014), of using discrete element method (DEM) modelling to reproduce both the emplacement and instability of a lava dome with intermediate silica composition. Previous dome emplacement simulations have mostly employed the finite element method (*Bourgouin et al.*, 2007; *Hale*, 2008; *Hale and Wadge*, 2008; *Hale et al.*, 2009a,b), whereby it is computationally expensive to introduce additional perturbing factors with the intention of initiating collapse. By using a DEM, we are able to start with an initial dome emplacement and apply, in several model scenarios, different mechanisms attributed to dome collapse in the literature. We intend this to be a pilot study to illustrate the potential of the model in simulating dome growth, morphology and collapse, and show this model can be applied in more specific locations with exact scenarios or conditions.

3.2 Methodology

3.2.1 Discrete Element Method

We use Particle Flow Code (PFC), a commercial software developed by *Itasca Consulting Group* (2017), to undertake a two-dimensional analysis of dome

growth and collapse. PFC uses the discrete element method (*Cundall and Strack*, 1979) to simulate an assembly of individual particles that behave as rigid bodies carrying a force and moment that are updated per particle per model time step. The particles interact via contact bonds, defined by individual contact models, which act as point (parallel bonds) or beam (flat-joint bonds) style connections between particles (Fig. 3.1). Bond behaviour is primarily governed by the normal stiffness (k_n, incompressibility) and shear stiffness (k_s) associated with the contact interface, although the bonds also have attributed values for cohesion, tensile strength, and friction. Bond breakage occurs if the tensile or shear strength of the contact is exceeded, which is used to represent damage in the model material. The model calculates an explicit solution to Newtons laws of motion (*Potyondy*, 2016), thus limiting the need to dictate additional particle behaviours. Each particle in this case is not intended to represent an individual crystal or a block of rock, but rather a discrete element for the purpose of computation.

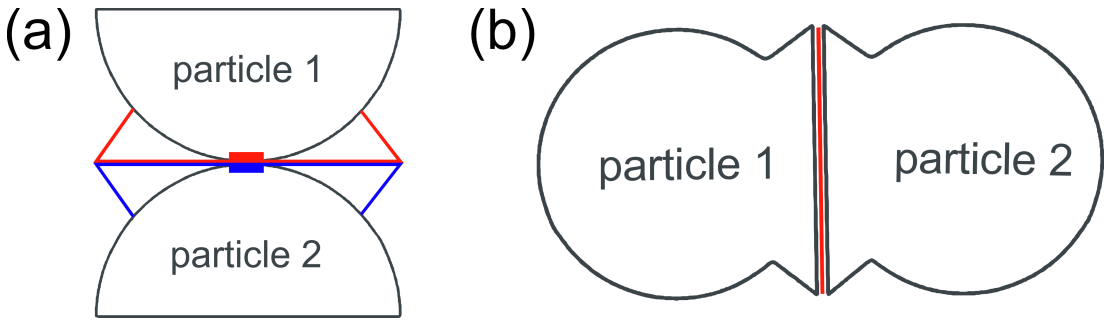

Figure 3.1: **(a)** parallel-bond geometry in PFC; **(b)** flat-joint bond in PFC, showing skirted particle geometry.

DEM is commonly used to study soil and rock mechanics (*Wang and Tonon*, 2009; *Zhang et al.*, 2011) and civil engineering scenarios (*Wang et al.*, 2003; *Jenck et al.*, 2009), and more recently the field of volcanology, to study volcanic processes such as gravitational spreading (*Morgan and McGovern*, 2005a,b), caldera collapse (*Holohan et al.*, 2011, 2015; *Gudmundsson et al.*, 2016) and lava dome growth (*Husain et al.*, 2014). This study differs to previous DEM models of lava dome emplacement (*Husain et al.*, 2014) in that we incorporate new bonding methods in PFC to better represent dome rock properties and explicitly test conditions associated with dome collapse.

3.2.2 Model description

We model a simplified internal dome structure comprising two main units: (1) a frictionless, ductile core and (2) an outer friction-controlled talus region. We use

the term talus to refer to any dome material that is behaving as rock and do not distinguish between talus slopes that have become detached from the dome and the solid, more intact crust of the dome. It is likely there is a transition zone between the core and talus regions, often termed the carapace (e.g. *Wadge et al.*, 2009). However, for simplicity this is not included here as a separate region. This assumption is based on studies suggesting an abrupt rheological change when melt develops a critical crystal content, thus exhibiting material strength that can be characterised as a solid (*Cordonnier et al.*, 2012).

A thermal imaging study by *Hutchison et al.* (2013) showed the outer crust of the dome appears to behave dynamically during dome growth, rather than acting as a stiff, rigid layer. DEM allows the talus to deform independently without imposing a rigid boundary upon the model region, suggesting this method is appropriate for modelling the evolution of both the fluid and solid portions of lava domes.

We do not implement an explicit mechanism for magma reaching the surface, and instead the dome grows through a constant supply of magma into the interior. After initial extrusion conditions are applied the dome is free to grow naturally and this can lead to exogenous spine generation. As with previous dome emplacement simulations (e.g. *Hale*, 2008), we note that our model is best applied to the analysis of large, whole-dome processes; hence, localised flow processes are not fully considered.

The model is initialised by generating a batch of magma in the conduit which is followed by a constant supply of fresh magma. At model initialization, particles are packed within the conduit to ensure that contacts exist at all particle-particle interfaces. Packing is random to avoid hexagonal particle packing (*Potyondy*, 2016), as this can lead to unreliable model behaviour. This packing introduces a randomness to the dome geometry in each model run and leads to dome asymmetry. After magma exits the conduit, its behaviour is governed by: (a) the driving force due to velocity of conduit material; (b) the downward force of gravity; and (c) the force and moment transfer from particle-particle interactions. The magma is driven by an upwards velocity of 2 m/s; this is kept constant in all models as we do not focus on the effect of extrusion rate on dome growth. Mapping this 2D ascent velocity to a 3D extrusion rate would give faster extrusion rates than those used in other discrete element models (*Husain et al.*, 2014, 2018). However, to reduce computation times we simulate a fast end member of extrusion. We note that our simulations run close to real time and therefore a modelled dome would take months to extrude at low ascent velocities, thus

we accelerate the extrusion process and do not explicitly compare modelled timescales to real world observations.

Identifying the transition of ductile core material to talus is crucial in a lava dome emplacement model, as relative core/talus volumes influence dome morphology and therefore stability (*Hale et al.*, 2009a). The solidification of magma is primarily controlled by two mechanisms: the cooling of the lava surface that leads to a solid crust and rheological stiffening, and volatile exsolution caused by decompression which increases the liquidus temperature and therefore promotes crystallisation. Lava domes most commonly form in andesitic-dacitic lavas (*Ogburn et al.*, 2015), where solidification of lava is dominated by degassing-induced crystallisation (*Sparks et al.*, 2000). Cooling can therefore be considered negligible in the solidification process; we follow the example of previous dome emplacement models (*Simmons et al.*, 2005; *Hale*, 2008; *Husain et al.*, 2014) and employ the solidus pressure to mark the transition of magma from a liquid to a crystallised solid state:

$$T_{liq,sol} = a_T + b_T \ln p + c_T \ln p^2 + d_T \ln p^3, \tag{3.1}$$

where T gives the liquidus and solidus temperatures, a_T, b_T, c_T and d_T are constants (*Couch et al.*, 2003; *Melnik and Sparks*, 2005), and p is pressure. *Melnik and Sparks* (2005) use the initial melt composition at SHV (*Couch et al.*, 2003) to experimentally establish the solidus and liquidus temperatures; the best fit to this experimental data derives the constants a_T, b_T, c_T and d_T.

Studies on lava from SHV, a volcano with numerous cycles of dome growth and collapse (*Wadge et al.*, 2010), suggest variable properties (e.g. *Matthews and Barclay*, 2004; *Voight et al.*, 2006) with temperatures ranging from 830°C to 940°C. The method from *Moore et al.* (1998) establishes that the water content is negligible for the given temperature range and composition. In our model we assume that the melt experiences perfect volatile loss at the conduit exit and is dry at the time of emplacement, consistent with low (<0.12%) water contents measured in groundmass from the 1995-1996 Soufrière Hills dome (*Villemant et al.*, 2008). The solidus pressure is therefore between 0.1 MPa and 5 MPa, dependent on temperature (*Hale*, 2008). In a dynamically evolving dome system, it is likely that the solidus pressure evolves too. For model simplicity, we use a fixed value (0.4 MPa) in the starting condition for all collapse models, but we also include a sensitivity analysis of the solidus pressure on core/talus proportions within the dome (Section 3.3.1).

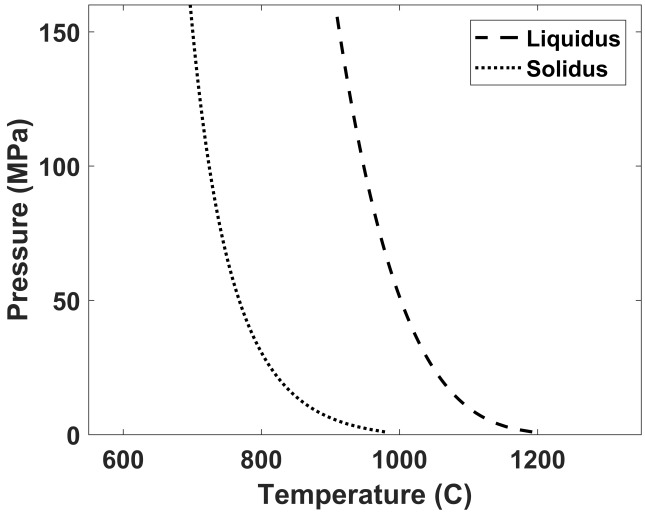

Figure 3.2: Temperature-pressure curve showing the magma solidus using Equation 3.1 derived by *Couch et al.* (2003) for the initial melt composition at Soufrière Hills Volcano, Montserrat.

The so-called "level set method" (*Osher and Sethian*, 1988) is a numerical method previously incorporated into finite element models to track the interface between interior core and outer talus regions (*Hale and Wadge*, 2005; *Hale et al.*, 2007; *Hale and Wadge*, 2008). The evolution of this interface, where important rheological changes occur, is critical to dome stability. *Hale et al.* (2007) presented the benefits of using the level set method in finite element modelling of lava domes, as it allows both the core/talus interface and the flow front to be tracked without re-meshing and therefore reduces computational expense. However when *Husain et al.* (2014) applied this method to DEM models, it resulted in an unlikely morphology of the core/talus boundary. Therefore, instead of using the level set method we simply calculate the maximum principal stress (σ_1; *Jaeger et al.*, 2009) on each individual particle and adapt the particle properties according to when each individual particle reaches the solidus pressure.

$$\sigma_1 = \frac{1}{2}(\sigma_{xx} + \sigma_{yy}) + [\sigma_{xy}^2 + \frac{1}{4}(\sigma_{xx} - \sigma_{yy})^2]^{\frac{1}{4}} \tag{3.2}$$

It is important to note that this transition in properties is unidirectional, so although solidification is considered in the model, re-melting cannot occur. Determining the equivalent particle properties of the ductile core material is challenging as a calibration procedure cannot be performed. We therefore use the micro-properties obtained by *Husain et al.* (2014) through sensitivity analyses. The study focussed particularly on determining the effect of cohesion and bond

stiffness on material behaviour. We correlate the parallel bond stiffness of the core material to magma viscosity by

$$\eta = k_s \Delta t y, \tag{3.3}$$

where η is viscosity, k_s is the shear stiffness of the bond, t is the model time step, and y is the unit length of the material (i.e. particle size). Variation in magma viscosity at SHV can span up to eight orders of magnitude (*Voight et al.*, 1999; *Melnik and Sparks*, 2002; *Couch et al.*, 2003); to simplify our model we assume a constant viscosity. Following the parametric study by *Husain et al.* (2014), we use a shear stiffness of 10^8 Pa in all models; this equates to an effective model viscosity of 10^4 Pa s. We do not vary the micro-properties of the magma material (for a complete list of model parameters, see Appendix B.1).

For the ductile portion of the model we use a parallel-bonded contact model, as the point-style contact does not inhibit rotational resistance and therefore provides the behaviour of a fluid. When an individual particle reaches the solidus pressure, the bond type is updated to a flat-joint bond (*Potyondy*, 2012), where a beam-style contact changes the geometry of the interface so that the particles become skirted in shape (Fig. 3.1). Recent numerical studies have shown that by incorporating this type of particle bond, the material acts more like a solid rock than the more conventional contact models in earlier versions of PFC. This is due to the increased interlocking and maintenance of rotational resistance, even after a contact is broken (*Wu and Xu*, 2016). Using the flat-jointed contact model overcomes many problems seen in earlier PFC studies (*Cho et al.*, 2007; *Holohan et al.*, 2011) and ensures the material is acting like a solid rock in both compression and tension.

We can use analogue models to evaluate the strain field and therefore the likely flow structures within a dome. *Buisson and Merle* (2002) show that flow in the central region of the dome above the conduit is dominated by material ascent due to the driving force of injected magma. Flow in the lateral portions of the dome is primarily horizontal or downward and governed only by gravity. By tracing particle velocities in PFC, we show that our model replicates this well (Fig. 3.3). We also compare this flow structure to dome growth identified by *Walter et al.* (2013) using pixel offsets, where growth directly above the conduit is dominated by upward and vertical movement of magma, and flow in the lateral portions of the dome is primarily away from the conduit and gravity-controlled.

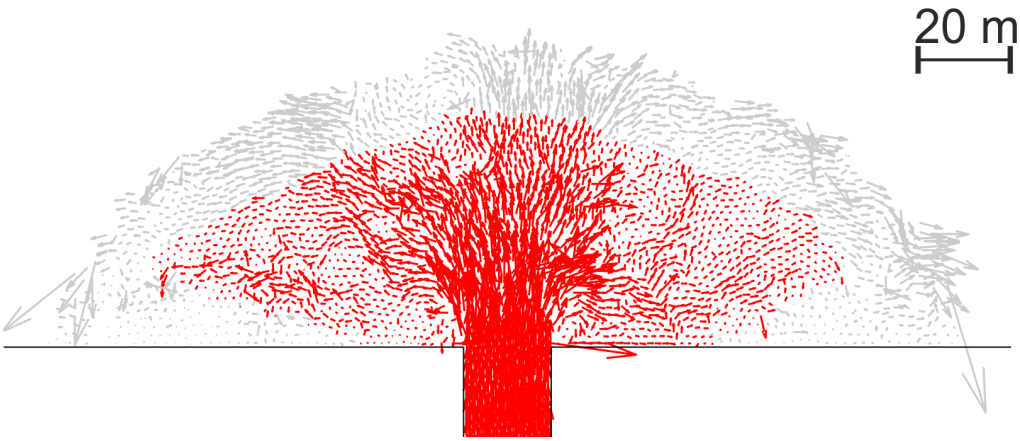

Figure 3.3: Velocity vectors during dome growth, where red is core material and grey is talus material. The relative velocity magnitude is proportional to the size of the arrow, where conduit material has a velocity of 2 m.

3.2.3 Strain modelling

Due to the heterogeneity of displacements in a particle-based model, it can be challenging to establish a link between individual particle displacements and macro-level strain. To bridge this gap, we perform inverse strain modelling (i.e. fitting a strain model to displacement data) in order to visualise localized strain (*Morgan and McGovern*, 2005a; *Holohan et al.*, 2011). This method (*Schöpfer et al.*, 2006) assumes a continuum and the nearest neighbours of each particle are identified and their positions tracked across a given time step. The average displacements are used to calculate a displacement gradient tensor, which can be used to determine the Cauchy-Green deformation tensor. We use the deformation gradient tensor to compute maximum shear strain using

$$\gamma_{max} = \frac{\lambda_{max} - \lambda_{min}}{2(\lambda_{max} \times \lambda_{min})^{\frac{1}{2}}}, \tag{3.4}$$

where γ_{max} is the maximum shear strength, and λ represents the maximum and minimum eigenvalues of the deformation gradient tensor (*Cardozo and Allmendinger*, 2009). We note that we do not consider particle rotation, instead calculating strain based on absolute displacement of each particle centroid. In many cases particles in the models have particularly large strains, for example when a particle rolls down the side of the edifice, simulating a small scale rock fall. These large strains hide smaller strains occurring within the dome, so we plot a strain cut-off criterion in each of our model figures. Shear strains are then normalised to emphasise the relative shear strain in each model. This allows

distinction of where material moves along a boundary (e.g. a fault or a shear plane) from material moving as a block, and is particularly relevant in the case of collapse models as calculating finite strain can allow identification of developing failure planes.

3.3 Model results

In this section, we first focus on the emplacement of a lava dome, followed by sensitivity analyses of dome morphology to both solidus pressure and conduit width. We create a dome emplacement model and use this as a starting condition, enabling application of external factors observed to trigger pyroclastic flow generation or dome collapse. In this initial study, we do not model rainfall-induced collapse due to varied hypotheses for how addition of rainfall to the volcanic system leads to collapse (*Matthews and Barclay*, 2004). We therefore focus on simulating the following three common triggering mechanisms: pressurisation of the dome, a switch in extrusion direction, and topography-controlled collapses.

3.3.1 Dome emplacement

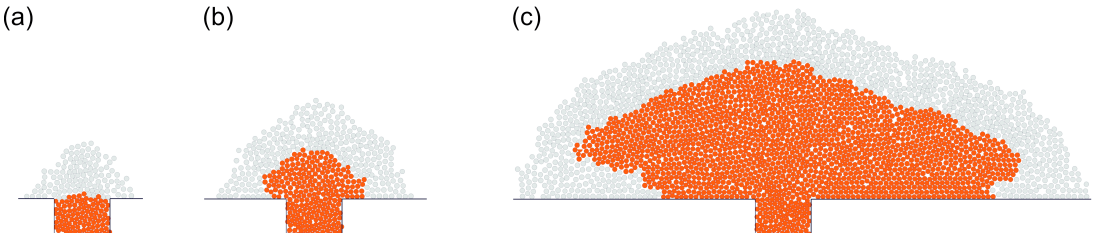

Figure 3.4: Snapshots of growth at **(a)** 5% of final growth, **(b)** 15% of final growth and **(c)** 100% of final growth; red particles show liquid, parallel-bonded core and grey particles shows solid, flat-jointed talus. Solidus pressure = 0.4 MPa. For a comparison of modelled emplacement and theoretical emplacement, see Appendix B.1, and for further information on dynamic growth, see Appendix B.3.

Running a simple dome emplacement model shows a morphology with steep sides and a flatter area towards the apex of the dome (Fig. 3.4). At the beginning of dome growth (Fig. 3.4a), only solid material is extruded as there is no overburden pressure to maintain fluid core material within the dome. Over time, a fluid core is encapsulated by a solid outer talus region (Fig. 3.4b). At the base of the dome there are regions where core material overrides solid talus

material (Fig. 3.4c). Although not investigated further here, presence of a talus substrate beneath the core may have significant impacts on overall dome stability. An area of the dome where core material spreads over underlying talus material can be unstable and cause more explosive activity during retrogressive collapse (*Herd et al.*, 2005; *Hale et al.*, 2009b).

The solidus pressure influences talus thickness, as higher pressures result in a smaller core volume fraction. While our primary models use a solidus pressure of 0.4 MPa, we also show emplaced domes with solidus pressures of 0.2 MPa and 0.8 MPa to demonstrate the effect of solidus pressure on dome morphology (Fig. 3.5), and the potential effects of this are discussed further in Section 3.4.4. We also observe that higher relative talus volume (Table 3.1) results in steeper dome morphology (Fig. 3.5).

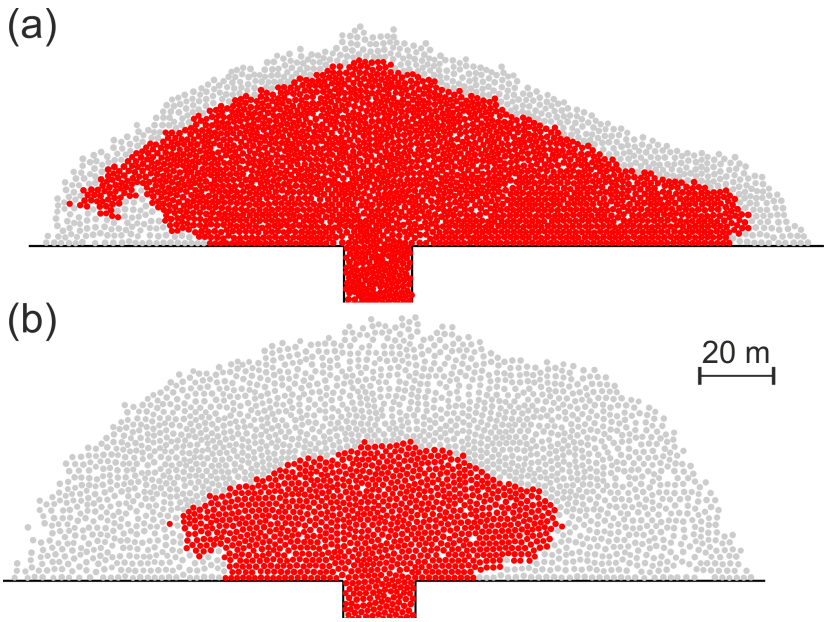

Figure 3.5: PFC dome model emplaced with solidus pressures of **(a)** 0.2 MPa and **(b)** 0.8 MPa. Growth state corresponds to 100% of growth in Fig 3.4c. Red particles show liquid, parallel-bonded core and grey particles show solid, flat-jointed talus.

3.3.2 Sensitivity of dome morphology to conduit diameter

Lava domes vary in morphology due to rheological and mechanical properties (e.g *Blake*, 1990; *Watts et al.*, 2002; *Calder et al.*, 2015). *Blake* (1990) documented variations in observed dome heights from 8 m to 243 m, and radius variations of 20 m to 1093 m. The models in this paper are extruded from a conduit with

	100% of growth	
Solidus	Core (%)	Talus (%)
0.2 MPa	79.0	22.0
0.4 MPa	37.3	62.7
0.8 MPa	34.8	65.2

Table 3.1: Relative core/volume fraction, expressed as a percentage of total extruded material, for solidus pressures of 0.2 MPa, 0.4 MPa and 0.8 MPa. Model parameters for these simulations listed in Appendix B.1.

diameter of 20 m, and domes reached a height of 70 m and width of 210 m, where the dome height limit appears to have been reached, and any magma addition results only in lateral spreading (Appendix B.3). Considering the same rheology, solidus pressure of 0.4 MPa, extrusion rate, and material properties (Fig. 3.6), we use a larger conduit of 50 m to test whether the dome geometry is independent of magma input. The 50 m conduit results in a dome that is 110 m tall, and 340 m wide; this is again approximately a 1:3 height to width ratio. Hence we determine that lava dome morphology is insensitive to conduit diameter, and therefore the models with a conduit diameter of 20 m are indicative of process and morphology at varying scales.

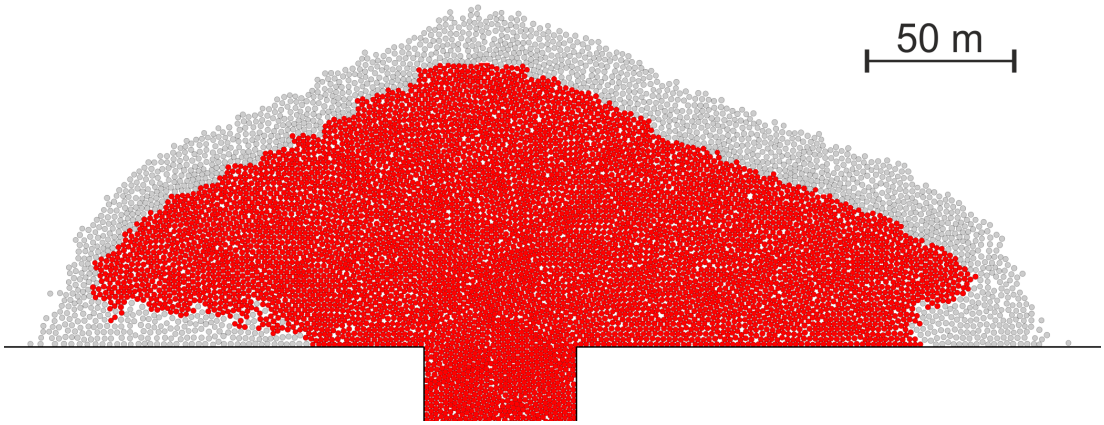

Figure 3.6: PFC dome model with a 50 m conduit, and solidus pressure of 0.4 MPa, where red represents core material and grey represents talus material.

There are similar dome morphologies found between the models with varying conduit diameters. There is also a similar geometry to the core/talus interface, particularly at the base of the dome where both models show core material underlain by talus material. The main difference between the results is the relative proportion of core to talus. In the model with a 20 m conduit, we see 43% talus and 57% core, whereas in the model with a 50 m conduit, we see 23% talus and

77% core material. This can be explained by a low solidus pressure (0.4 MPa) resulting in only a thin shell required to encase the ductile material in the interior of the dome.

Core volume fraction was also estimated by *Hale et al.* (2009a,b) using finite element models, with values of core volume ranging from 26% to 66%. Estimates were made from ground-based radar measurements at SHV (*Wadge et al.*, 2008) and showed that a surprisingly low proportion (∼39%) of the extruded lava remained in the core. We suggest that our relative overestimates of core proportion arise from simulating one continuous extrusion period, rather than a more realistic periodic extrusion. The pauses during periodic extrusion allow further solidification to occur, therefore increasing talus volume. Estimates of talus thickness are difficult to obtain during active dome extrusion. *Dzurisin et al.* (1990) used magnetization to estimate the outer layer thickness of the Mount St. Helens dome as 10-30 m thick. In the 20 m conduit model, we find a talus thickness of 13-23 m (considering only where talus overlies core, and not the distal talus aprons), and for the 50 m conduit model, talus thickness range from 15-20 m. This suggests we have good estimates of talus encasing the core, but could be underestimating talus apron volume.

Despite differences in relative core/talus volumes, the overall shape of the rheological boundary is very similar to that suggested in conceptual models (*Hutchison et al.*, 2013) and existing finite element method models (*Hale et al.*, 2009a,b). This shows that the models are a reasonable approximation, and we use the emplacement models as a starting condition from which to test collapse mechanisms.

3.3.3 Gravity and renewed pressurisation of the dome

Dome collapses are frequently followed by explosive eruptions, suggesting that internal pressurisation is likely to play a role in triggering instabilities in lava domes. This was observed particularly at SHV following collapses in September 1996 and August and September 1997 (*Cole et al.*, 1998; *Voight and Elsworth*, 2000). Pyroclastic flow generation has been observed in conjunction with gas pressurisation at Mt. Unzen (*Sato et al.*, 1992). Tilt deformation prior to dome collapse events also suggests shallow pressurisation and links timing of collapse to maximum pressurisation (*Elsworth and Voight*, 2001).

Voight and Elsworth (2000) modelled a hemispherical dome above a pressurised conduit and calculated gas pressure diffusion across the dome. They

define an isolated block using an inclined arbitrary basal sliding plane, upon which the uplift pressures act. This allows calculation of the factor of safety (a measure of stability defined as the ratio of resisting to disturbing forces) for the isolated and potentially unstable block. The model shows a dome can remain stable in the early stages of pressurisation and not fail until subsequent pulses of pressure are applied to the dome. The authors explain this by suggesting the pressure the critical failure surface must exceed a given threshold, and this may require several oscillations. Previous studies (*Robertson et al.*, 1998; *Voight et al.*, 1998) find gas pressurisation magnitudes of 10 MPa, and *Voight and Elsworth* (2000) find decompression of a dome core by 2-5 MPa can lead to explosive activity.

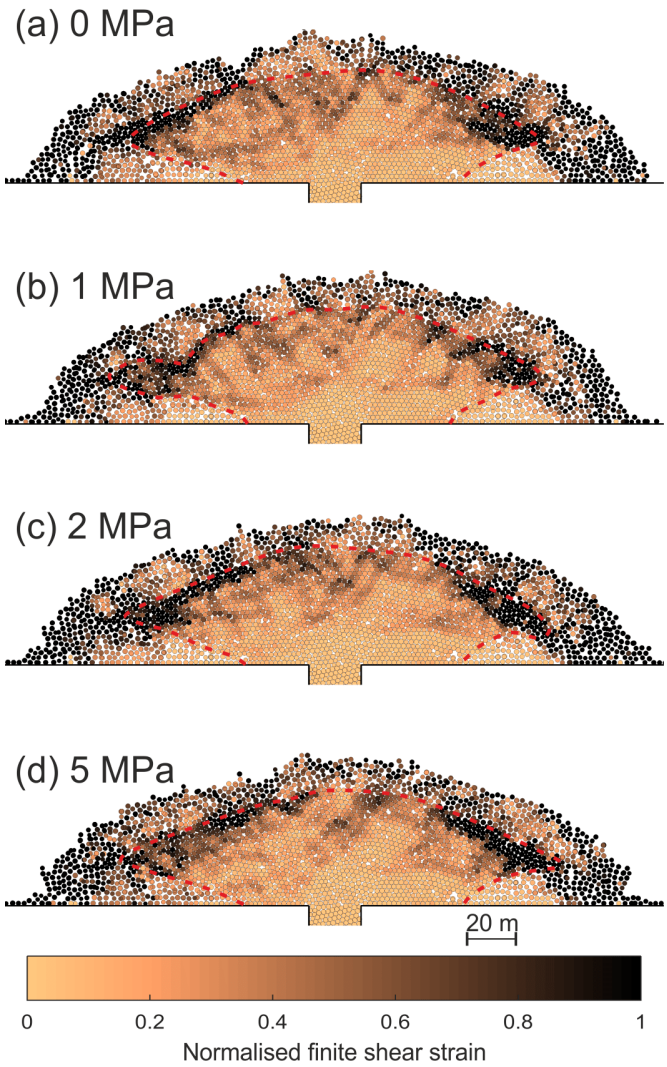

Figure 3.7: PFC dome model following the application of an upward force of **(a)** 0 MPa pressure, **(b)** 1 MPa, **(c)** 2 MPa, **(d)** 5 MPa. Plotted using normalised finite shear strain, where the red dotted line represents the rheological interface between core and talus material. Solidus pressure = 0.4 MPa.

We aim to exploit the advantages of a DEM model by establishing whether it is possible to create a failure surface, rather than examining the effect of pressure on a geometrically simplified pre-existing weakness. After stopping extrusion, we apply an upward force to all material within a hemispherical region above the conduit (where the diameter of this region is equivalent to conduit width), to act as a renewed pressurisation of the system. We add the force in this region due to observations which suggest that processes controlling the dome pressurisation are shallow-level, either deep within the dome interior or in the shallow conduit (*Sparks*, 1997). We also show a model with no applied force (Fig. 3.7a) to isolate the effect of gravity during this process, followed by the application of forces corresponding to pressures of 1 MPa, 2 MPa, and 5 MPa (Figs. 3.7b-d).

Following pressurisation, strain localises around the pre-existing weakness of the rheological boundary. In all cases, small-scale rockfalls occur on the flanks of the dome, caused by over-steepening giving a high slope angle. Strain accumulates much deeper in the dome in all cases, highlighting the development of deep-seated listric shear failure surfaces. The models subjected to both no and low (1 MPa) pressurisation effects show strain accumulation primarily localised at the corners of the core-talus interface, and in isolated regions along the rheological boundary. Domes subjected to higher pressurisation effects (2 MPa, 5 MPa) have more focussed bands of high strain, but these remain located along the boundary.

3.3.4 Sensitivity of pressurisation models to conduit diameter

The dome emplaced with a 50 m conduit diameter is shown in Fig. 3.8, after application of an equivalent 5 MPa pressure. This shows the same scenario as in Fig. 3.7d, and displays very similar strain accumulation to the model with a 20 m conduit. Although the explicit values of strain are lower in the larger dome ($\sim$50% of those in the smaller dome), we still see that strain accumulates along the core/talus boundary, and then within the core of the dome. In the larger dome model, there is also evidence of strain accumulation oblique to the listric shear plane, which has been observed in previous DEM models of rock slope instability (*Wang et al.*, 2003).

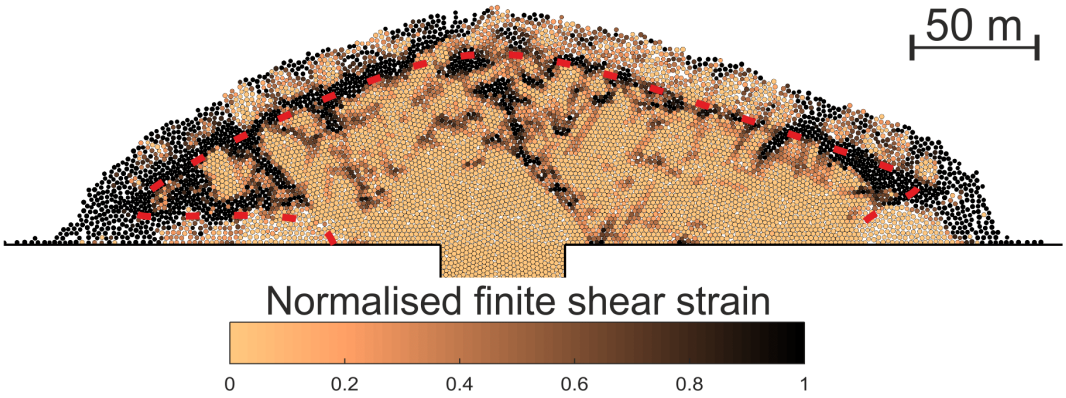

Figure 3.8: PFC dome model with a 50 m conduit after application of 1 MPa radial force, plotted using normalised shear strain, where the red dotted line represents the rheological interface between core and talus material. Solidus pressure = 0.4 MPa.

3.3.5 Switch in extrusion direction

A switch in extrusion direction, or a focussed extrusion direction, has been documented as a precursor to collapse (*Ryan et al.*, 2010; *Stinton et al.*, 2014; *Wadge et al.*, 2014), particularly at SHV due to the high quality of observations. There is no consensus on a proposed mechanism however, and switching extrusion direction has not previously been incorporated into numerical or analogue models. A focussed extrusion direction was observed during the growth of the 2004-2006 lava dome complex at Mount St. Helens (*Vallance et al.*, 2008). Due to cooling of deformed, older 2004-2005 dome rock, later spines experienced thrusting growth and were emplaced on top of the earlier spines. The morphology of the older spines and the decoupling of later spines led to extrusion of the younger spines oblique to horizontal, at angles of up to 54°.

We implement a change in extrusion direction in the model by pausing active emplacement and freezing part of the dome. Displacements in the frozen part of the dome are set to zero to simulate material that has solidified. Once extrusion is resumed, the new material is forced to extrude in a particular direction as it is prevented from spreading naturally by the frozen dome portion.

The results (Fig. 3.9) show firstly that there is a large amount of shear strain localised above the conduit exit. Some of this shear strain accumulates due to fresh material moving alongside the frozen, older dome material. There is however significant strain accumulation in the form of shear bands on both sides of the conduit exit, a feature previously modelled by (*Hale and Wadge*, 2008). Strain is also localised along the lower rheological interface (Fig. 3.9c) between the core

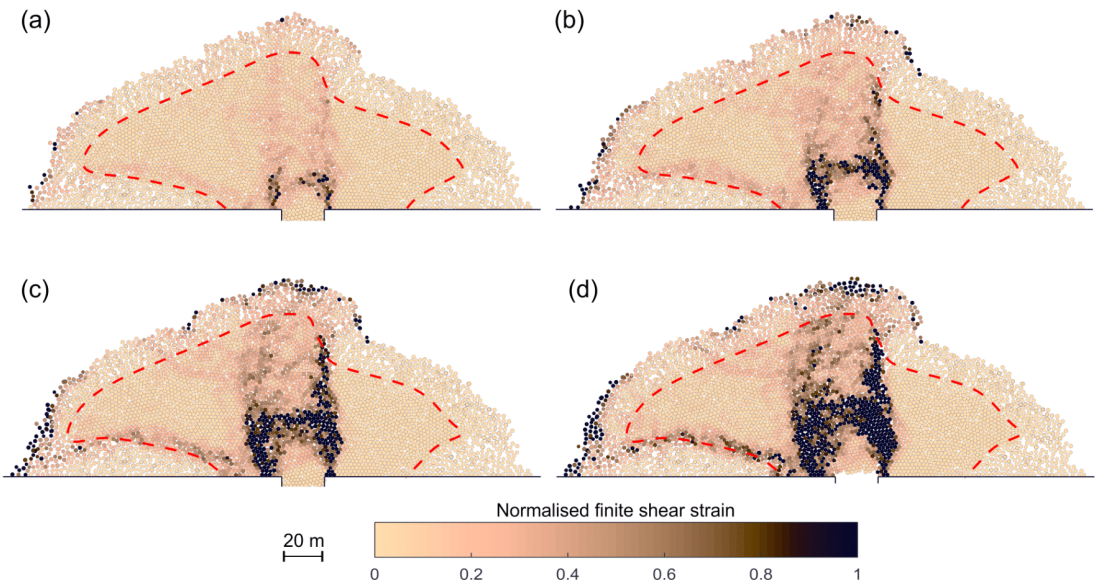

Figure 3.9: PFC dome model where the material to the right of the conduit is frozen and extrusion direction is forced to the left of the conduit, plotted using normalised finite shear strain, where the red dotted line represents the rheological interface between core and talus material. Insets (a) to (d) represent snapshots of increasing model run time. Solidus pressure = 0.4 MPa.

and the talus on the non-frozen side of the dome. Strain accumulates towards the top of the dome sub-parallel to the rheological boundary (Fig. 3.9d), suggesting the formation of a lava lobe that is being pushed out by the incoming material; similar processes were observed in the DEM studies of *Husain et al.* (2018). This is significant in understanding future dome growth and morphology as we observe simulated cooling of one part of the dome to lead to lava lobe formation. The development of a deep, sub-horizontal shear band (Fig. 3.9d) is important for dome stability as it forms a potential failure surface (discussed further in Section 3.4.2). In terms of collapse style, rockfalls are seen to develop progressively throughout time following the focussed extrusion direction, occurring primarily on the over-steepened flanks of the dome.

3.3.6 Topographic effects

Topographic confinement of domes has been observed to control material detachment and pyroclastic flow generation (e.g. *Voight et al.*, 2002). Previous dome growth models inadequately incorporate non-horizontal extrusion planes in controlling dome growth and talus generation, despite field observations of topography's influence (e.g. stiff crater walls buttressing dome emplacement;

Hutchison et al., 2013). Collapses occurring at Montserrat 1995-1997 were often due to dome material over-spilling the previous crater walls (*Cole et al.*, 1998, 2002). We therefore create three end member topographies to test how the dome morphology changes in each case. These are: magma extruding onto a slope (Fig. 3.10a); extruding out of a conduit that is flanked by outward dipping slopes on both sides (Fig. 3.10b); and extruding into a crater (Fig. 3.10c).

The dome extruding onto a slope shows strain accumulation on the downhill flank of the dome (Fig. 3.10a). Interestingly there is little strain accumulation on the uphill portion of the dome, despite the over-steeped flank, suggesting movement as a block and absence of rockfalls. Emplacing the dome at the apex of a flanked topography (Fig. 3.10b) and into a crater (Fig. 3.10c) both show rockfall activity on both slopes. For the crater case, most strain accumulation is seen in the areas where the dome has over-topped the older crater rim (Fig. 3.10c), suggesting that an abrupt change in slope leads to the highest strains. Additionally we see development of several sub-vertical fractures in the dome core (Fig. 3.10c). The development of these large scale shear is not observed in other modelled topographies but could have implications when considering overall material strength.

Due to randomness introduced by initial material packing, our models grow asymmetrically. This is shown particularly in the crater topography model where the rheological boundary differs either side of the dome; core material is underlain by talus on one side, but is in contact with the crater on the other (Fig. 3.10c). The model presented in Fig. 3.10b also shows dome asymmetry, where the degree of over-steepening differs on each side.

3.4 Discussion

3.4.1 Shear band development

The development of shear bands in a material indicates a concentrated region of relatively high displacement. When analysing lava dome morphology, these regions can aid identification of potential failure surfaces, where deformation accumulates to generate zones of weakness. In the model that simulates a focussed extrusion direction (Fig. 3.9), significant strain accumulation occurs around the conduit exit. In models from previous studies (*Hale and Wadge*, 2008), shear bands occur at the junction between the conduit and the base of the dome, as they nucleate where new lava is emplaced adjacent to older lava. Shear band

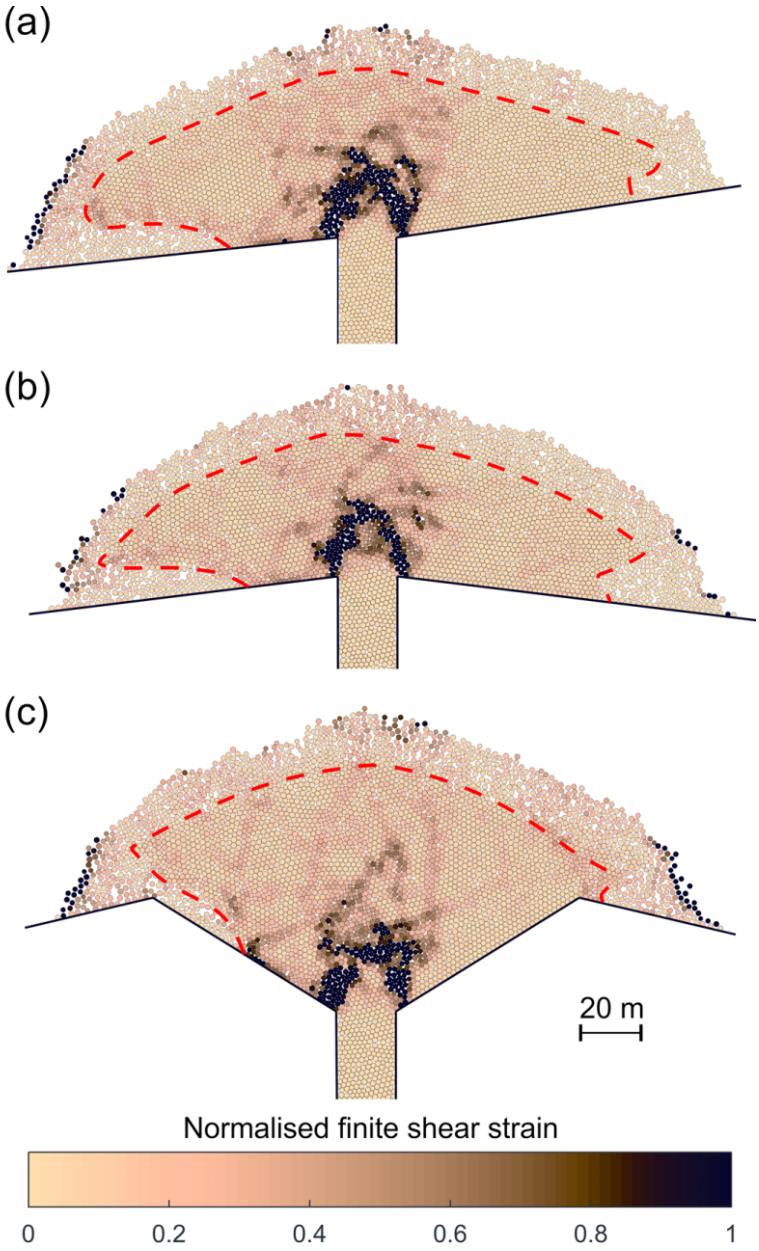

Figure 3.10: PFC dome model extruded using different surface topographies to represent **(a)** dome growth on to a slope; **(b)** growth out of a vent, onto sloped sides; **(c)** growth in a crater, where the dome eventually over-tops crater walls. Rheological boundary between core and talus shown by red dotted line. Solidus pressure = 0.4 MPa.

generation can be a precursor to a transition from exogenous to endogenous growth (i.e. magma forces its way to the surface to create lobes/spines rather than growth caused by magma intrusion and dome expansion; *Fink et al.*, 1990; *Calder et al.*, 2015); this is implied further by propagation of shear bands towards the dome surface over time (Fig. 3.9d). Similar processes were seen by *Buisson*

and Merle (2002), where analogue modelling of dome emplacement revealed that the zone of maximum strain, velocity, and displacement is observed directly above the conduit exit. *Cordonnier et al.* (2009) suggest shearing at the conduit exit can lead to spine formation. The development of shear bands in our PFC model is exaggerated due to the high extrusion rate; these results should therefore be seen as qualitative of process, rather than quantitative. Nevertheless we clearly see that a change in extrusion direction leads to strain accumulation in the centre of the dome that can be interpreted as carving out a pathway for lava to reach the surface and begin exogenous dome growth. This is not observed in the dome that is allowed to spread continuously.

In several models, deep accumulation of shear strain is clearly visible within the dome, whether this is purely along the core/talus boundary (Fig. 3.9) or intersecting the core (e.g. Fig. 3.7). In either case this shear accumulation marks localisation of displacement and the development of a plane of weakness along which material can easily slide or be pushed out of the dome. These zones therefore demonstrate preferential dome cooling can cause lava lobe formation, often leading to over-steepened lava lobe flow fronts which can collapse.

3.4.2 Developing pressurisation models

Due to computational expense we model the pressurisation of the system separately from extrusion. The model with a purely gravitational response (i.e. no simulated pressurisation) shows that strain accumulates at the rheological boundary due to gravitational settling (Fig. 3.7a), but is intensified and focussed by the addition of gas pressure (Figs. 3.7b-d). A natural next step would be to model gas pressure and extrusion as combined processes. We speculate that there would be more outwards movement of talus slopes due to the combined effects of pressurisation and the lateral force of magma influx.

We demonstrate a simple way to add a pressure into a DEM model and complexities could be added to this in future model iterations. For example, the material in our model is allowed to deform, representing an open system that prohibits accumulation of gas pressure within the dome. An alternative scenario which could be incorporated into future models would be a dome with a "sealed cap" which cannot deform and allows a build-up of pressure. Equally it could be possible that a dome experiences reduction in pressure over time, for example due to evolution in the mechanical properties (permeability, fracturing) of the talus (*Sparks*, 1997). In the models presented here, the amount of shear strain

accumulation shows significant material deformation and is therefore irreversible. Our models are acting beyond the elastic regime, and potential failure planes developed would continue to exist as weaknesses in the dome following a reduction in pressure.

3.4.3 Model validation and similarity to conventional landslide studies

It is particularly challenging to validate our failure models, as dome collapse tends to culminate in explosive events. The only method to attempt to understand collapse process is examination of resultant deposits (normally block-and-ash flows). This means that despite hazards associated with lava dome collapse, we do not fully understand strain accumulation in the critical stages prior to collapse. Our models allow us to see a simplified cross-section through the dome interior and begin to reveal methods by which strain accumulates and alters the behaviour and stability state of a lava dome. We find that despite the complex conditions that exist during active lava dome growth (high temperatures, gas overpressure, seismicity), lava domes appear to behave in many ways similarly to traditional landslides events that are commonly easier to observe than lava dome collapses. Particularly we see development of large scale listric shear planes, just as observed in rock or soil slope studies (*Petley et al.*, 2002; *Hungr et al.*, 2014). The actual slope failure process at a lava dome is difficult to discern due to the addition of gas resulting in turbulent pyroclastic density currents; it is therefore impossible to use the deposit to establish the way in which the slope failed (as in landslide studies) because the material completely disintegrates during the pyroclastic flow process. By using this modelling method to understand the generation of strain inside the lava dome, it reveals processes that cannot be otherwise discerned from observational studies.

3.4.4 Model development

We observe that failure plane development within pressurisation models (Fig 3.7) is controlled primarily by the rheological boundary. We develop this hypothesis by pressurising the domes emplaced with solidus pressures of 0.2 MPa and 0.8 MPa (Fig 3.11). In the dome with a solidus pressure of 0.2 MPa (Fig 3.11a), strain accumulates along the rheological boundary but we also see a rotational failure plane generating through the core of the right side of the dome. We suggest

this is due to the low-angle dome morphology, preventing larger scale rockfalls in this area. In the dome with a solidus pressure of 0.8 MPa (Fig 3.11b), strain accumulation reveals listric failure planes that also follow the rheological boundary, albeit deeper in the dome due to the larger talus volume. This sensitivity test shows the importance of the solidus pressure in determining the volume of material involved in potential collapse, as it controls the depth at which the shear plane forms. We suggest therefore that understanding the solidus pressure of a dome is key in assessing collapse hazard.

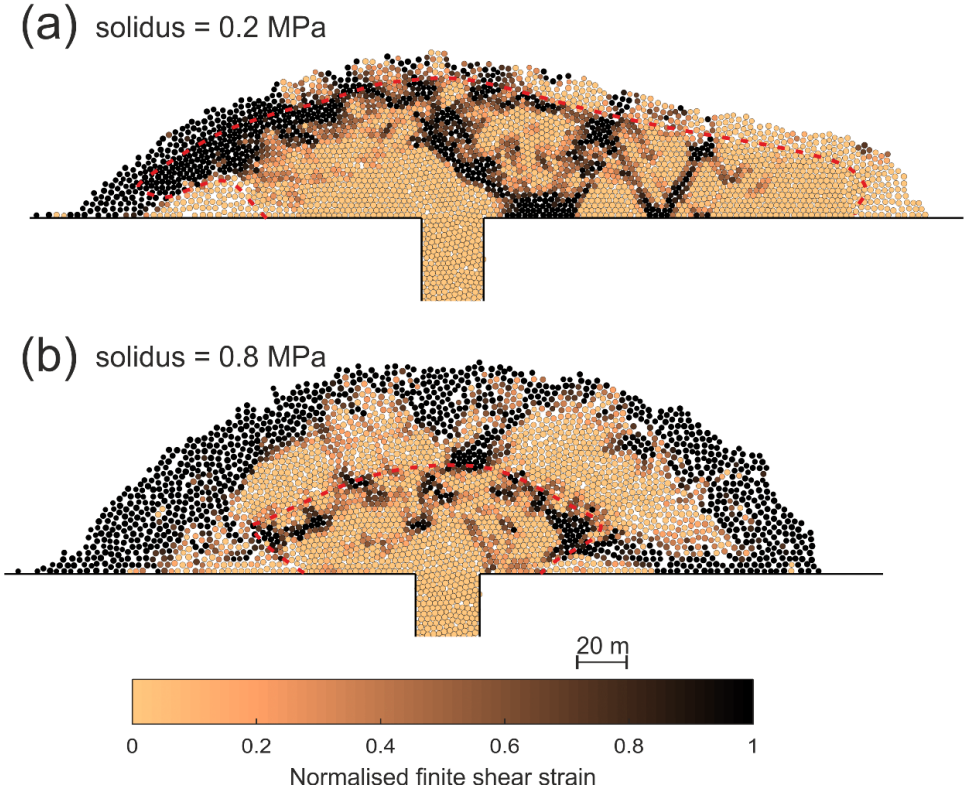

Figure 3.11: PFC dome models, emplaced with solidus pressure of **(a)** 0.2 MPa and **(b)** 0.8 MPa. Both following the application of an upward force that corresponds to a force of 5 MPa, plotted using normalised shear strain, where the red dotted line represents the rheological interface between core and talus material.

Following this, we propose that talus properties are crucial to the way in which shear accumulates around the rheological boundary. In all models presented here, we use assumed rock properties based on initial bond properties of the lava. Laboratory testing can determine mechanical properties of the talus material (e.g. *Smith et al.*, 2011; *Heap et al.*, 2014, 2016). However, these sample-scale properties must be scaled before they can be applied to a volcano-scale model. Despite previous studies investigating this scaling relationship at specific volcanic

sites (*Watters et al.*, 2000; *Okubo*, 2004; *Thomas et al.*, 2004; *Apuani et al.*, 2005), there is no general rule for taking intact laboratory strength and scaling it to rock mass strength in a volcanic environment. The same can be said for understanding elastic moduli at the scale of a volcanic edifice (*Heap et al.*, 2018). A further degree of complexity is introduced in order to generate this calibrated, scaled material within PFC. Fully-scaled talus properties are therefore outside of the scope of this paper, but will be an important step in future model development.

3.5 Conclusions

We employed a discrete element method to develop lava dome models, and were able to simulate two distinct failure mechanisms: (1) shallow, superficial rockfalls and (2) deep-seated listric shear planes. The information that crater-confined domes lead primarily to superficial rockfalls has the potential to feed into hazard assessment, as the models show these collapses to be shallow and relatively low in volume. We showed also that solidus pressure can control the volume of material involved in collapse. However it is important to recognise that trigger mechanisms can act simultaneously to destabilise a dome, a detail future models should consider. Deep-seated listric failure planes are observed following cessation of extrusion and subsequent generation of internal pressure. A collapse of this nature could lead to hot magma in the core being exposed to atmospheric pressure resulting in rapid decompression, explosions and pyroclastic flow generation. Deep shear planes also develop in models simulating switches in extrusion direction, although these are planar in nature and occur along the rheological boundary, showing lava lobe formation which can later lead to collapse.

Through knowledge of lava viscosity and extrusion conditions at a given lava dome, our method can be adapted in other locations to model dome morphology, and therefore the propensity of the dome to collapse. Here we focus on pressurisation of the dome system, a non-horizontal underlying topography, or a change in extrusion direction, but many more scenarios could be analysed in this type of model. By visualising the strain within the dome and showing similar features to those observed in traditional landslide studies, we can begin to use knowledge of landslide processes to better understand the dome collapse process.

The models presented here use an innovative method to examine lava dome collapse, and provide a basic framework to understand the complex

physics of a dynamically evolving system. Many additional factors can now be incorporated into future models to provide a more comprehensive understanding of factors likely to influence the stability of a growing lava dome. These include, for example, talus properties calibrated to real dome rock, a fracture network, successive extrusion events, and spatial/temporal variation in mechanical properties. We demonstrated that using discrete element method modelling is a promising approach for visualising strain generation within a lava dome, and interrogating the relationship between a growing dome and mechanisms that trigger instability.

Acknowledgements

This work was supported by the Leeds York Spheres Doctoral Training Partnership (grant number NE/L002574/1). CEH also acknowledges the value of a place on the Itasca Educational Partnership, and therefore access to the PFC5.0 license. The authors would like to thank Martin Schöpfer and Dan Woodell for contribution of and assistance implementing the strain calculation code. The authors thank Mike Heap and an anonymous reviewer for helpful comments towards this manuscript, as well as Kelly Russell for editorial handling.

Bibliography

Apuani, T., C. Corazzato, A. Cancelli, and A. Tibaldi (2005), Physical and mechanical properties of rock masses at Stromboli: A dataset for volcano instability evaluation, *Bulletin of Engineering Geology and the Environment*, *64*(4), 419–431, doi:10.1007/s10064-005-0007-0.

Ball, J., P. Stauffer, E. Calder, and G. Valentine (2015), The hydrothermal alteration of cooling lava domes, *Bulletin of Volcanology*, *77*(12), 102, doi:10.1007/s00445-015-0986-z.

Blake, S. (1990), *Viscoplastic Models of Lava Domes*, pp. 88–126, Springer Berlin Heidelberg, Berlin, Heidelberg, doi:10.1007/978-3-642-74379-5_5.

Bourgouin, L., A. J. Hale, and A. Arsac (2007), Studying the influence of a solid shell on lava dome growth and evolution using the level set method, *Geophysical Journal International*, *170*, 1431–1438, doi:10.1111/j.1365-246X.2007.03471.x.

Buisson, C., and O. Merle (2002), Experiments on internal strain in lava dome cross sections, *Bulletin of Volcanology*, *64*(6), 363–371, doi:10.1007/s00445-002-0213-6.

Calder, E., R. Luckett, R. Sparks, and B. Voight (2002), Mechanisms of lava dome instability and generation of rockfalls and pyroclastic flows at Soufrière Hills Volcano, Montserrat, *Geological Society, London, Memoirs*, *21*, 173–190, doi:10.1144/GSL.MEM.2002.021.01.08.

Calder, E. S., Y. Lavallée, J. E. Kendrick, and M. Bernstein (2015), Chapter 18 - Lava Dome Eruptions, in *The Encyclopedia of Volcanoes*, pp. 343–362, Academic Press, doi:10.1016/B978-0-12-385938-9.00018-3.

Cardozo, N., and R. W. Allmendinger (2009), SSPX: A program to compute strain from displacement/velocity data, *Computers and Geosciences*, *35*(6), 1343–1357, doi:10.1016/j.cageo.2008.05.008.

Carn, S. A., R. B. Watts, G. Thompson, and G. E. Norton (2004), Anatomy of a lava dome collapse: the 20 March 2000 event at Soufrière Hills Volcano, Montserrat, *Journal of Volcanology and Geothermal Research*, *100*(131), 241–264, doi:10.1016/S0377-0273(03)00364-0.

Cho, N., C. Martin, and D. Sego (2007), A clumped particle model for rock, *International Journal of Rock Mechanics and Mining Sciences*, *44*(7), 997–1010, doi:10.1016/j.ijrmms.2007.02.002.

Cole, P. D., E. S. Calder, T. H. Druitt, R. Hoblitt, R. Robertson, R. S. J. Sparks, and S. R. Young (1998), Pyroclastic flows generated by gravitational instability of the 1996-97 lava dome of Soufrière Hills Volcano, Montserrat, *Geophysical Research Letters*, doi:10.1029/98GL01510.

Cole, P. D., E. S. Calder, R. Sparks, A. Clarke, T. H. Druitt, S. Young, R. Herd, C. L. Harford, and G. Norton (2002), Deposits from dome-collapse and fountain-collapse pyroclastic flows at Soufrière Hills Volcano, Montserrat, *Geological Society, London, Memoirs*, *21*, 231–262.

Cordonnier, B., K. U. Hess, Y. Lavallee, and D. B. Dingwell (2009), Rheological properties of dome lavas: Case study of Unzen volcano, *Earth and Planetary Science Letters*, *279*(3-4), 263–272, doi:10.1016/j.epsl.2009.01.014.

Cordonnier, B., L. Caricchi, M. Pistone, J. Castro, K. Hess, S. Gottschaller, M. Manga, and D. B. Dingwell (2012), The viscous-brittle transition of crystal-bearing silicic melt : Direct observation of magma rupture and healing, *Geology*, *40*(7), 611–614, doi:10.1130/G3914.1.

Couch, S., C. L. Harford, R. S. J. Sparks, and M. R. Carroll (2003), Experimental Constraints on the Conditions of Formation of Highly Calcic Plagioclase Microlites at the Soufrière Hills Volcano , Montserrat, *Journal of Petrology*, *44*(8), 1455–1475.

Cundall, P., and O. Strack (1979), A discrete numerical model for granular assemblies, *Geotechnique*, *29*(1), 47–65.

Darmawan, H., T. R. Walter, K. Sri, I. G. Made, and A. Nandaka (2018), Morphological and structural changes at the Merapi lava dome monitored in 2012 15 using unmanned aerial vehicles (UAVs), *Journal of Volcanology and Geothermal Research*, *349*, 256–267, doi:10.1016/j.jvolgeores.2017.11.006.

Dzurisin, D., R. P. Denlinger, and J. G. Rosenbaum (1990), Cooling rate and thermal structure determined from progressive magnetization of the Dacite Dome at Mount St. Helens, Washington, *Journal of Geophysical Research*, *95*(B3), 2763, doi:10.1029/JB095iB03p02763.

Elsworth, D., and B. Voight (2001), The mechanics of harmonic gas pressurization and failure of lava domes, *Geophysical Journal International*, *145*(1), 187–198, doi:10.1046/j.1365-246x.2001.00370.x.

Elsworth, D., B. Voight, G. Thompson, and S. R. Young (2004), Thermal-hydrologic mechanism for rainfall-triggered collapse of lava domes, *Geology*, *32*(11), 969–972, doi:10.1130/G20730.1.

Fink, J., M. Malin, and S. Anderson (1990), Intrusive and extrusive growth of the Mount St Helens lava dome, *Nature*, *348*(6300), 435–437, doi:10.1038/348435a0.

Gudmundsson, M. T., K. Jónsdóttir, A. Hooper, E. P. Holohan, S. A. Halldórsson, B. G. Ófeigsson, S. Cesca, K. S. Vogfjörd, F. Sigmundsson, T. Högnadóttir, P. Einarsson, O. Sigmarsson, A. H. Jarosch, K. Jónasson, E. Magnússon, S. Hreinsdóttir, M. Bagnardi, M. M. Parks, V. Hjörleifsdóttir, F. Pálsson, T. R. Walter, M. P. J. Schöpfer, S. Heimann, H. I. Reynolds, S. Dumont, E. Bali,

G. H. Gudfinnsson, T. Dahm, M. J. Roberts, M. Hensch, J. M. C. Belart, K. Spaans, S. Jakobsson, G. B. Gudmundsson, H. M. Fridriksdóttir, V. Drouin, T. Dürig, G. Aalgeirsdóttir, M. S. Riishuus, G. B. M. Pedersen, T. van Boeckel, B. Oddsson, M. A. Pfeffer, S. Barsotti, B. Bergsson, A. Donovan, M. R. Burton, and A. Aiuppa (2016), Gradual caldera collapse at Bárdarbunga volcano, Iceland, regulated by lateral magma outflow, *Science*, *353*(6296), aaf8988, doi:10.1126/science.aaf8988.

Hale, A. (2008), Lava dome growth and evolution with an independently deformable talus, *Geophysical Journal International*, *174*(1), 391–417, doi:10.1111/j.1365-246X.2008.03806.x.

Hale, A., and G. Wadge (2005), Computationally Modelling the Lava Dome at Soufrière Hills Volcano, Ph.D. thesis, The University of Reading.

Hale, A., L. Bourgouin, and H. B. Mühlhaus (2007), Using the level set method to model endogenous lava dome growth, *Journal of Geophysical Research*, *112*(B3), B03,213, doi:10.1029/2006JB004445.

Hale, A., E. Calder, S. Loughlin, G. Wadge, and G. Ryan (2009a), Modelling the lava dome extruded at Soufrière Hills Volcano, Montserrat, August 2005-May 2006. Part I: Dome shape and internal structure, *Journal of Volcanology and Geothermal Research*, *187*(1-2), 69–84, doi:10.1016/j.jvolgeores.2009.08.014.

Hale, A., E. Calder, S. Loughlin, G. Wadge, and G. Ryan (2009b), Modelling the lava dome extruded at Soufrière Hills Volcano, Montserrat, August 2005-May 2006. Part II: Rockfall activity and talus deformation, *Journal of Volcanology and Geothermal Research*, *187*(1-2), 69–84, doi:10.1016/j.jvolgeores.2009.08.014.

Hale, A. J., and G. Wadge (2008), The transition from endogenous to exogenous growth of lava domes with the development of shear bands, *Journal of Volcanology and Geothermal Research*, *171*(3-4), 237–257, doi:10.1016/j.jvolgeores.2007.12.016.

Heap, M., M. Villeneuve, J. Farquharson, F. Albino, E. Brothelande, and J. L. Got (2018), Towards more realistic values of elastic moduli for volcano modelling, *Tech. Rep. EGU2018-3909*.

Heap, M. J., Y. Lavallée, L. Petrakova, P. Baud, T. Reuschlé, N. R. Varley, and D. B. Dingwell (2014), Microstructural controls on the physical and

mechanical properties of edifice-forming andesites at Volcán de Colima, Mexico, *Journal of Geophysical Research: Solid Earth*, *119*(4), 2925–2963, doi:10.1002/2013JB010521.

Heap, M. J., J. Russell, and L. Kennedy (2016), Mechanical behaviour of dacite from Mount St. Helens (USA): A link between porosity and lava dome extrusion mechanism (dome or spine)?, *Journal of Volcanology and Geothermal Research*, *328*, 159–177.

Herd, R., M. Edmonds, and V. Bass (2005), Catastrophic lava dome failure at Soufrière Hills Volcano, Montserrat, 12-13 July 2003, *Journal of Volcanology and Geothermal Research*, *148*(3-4), 234–252, doi:10.1016/j.jvolgeores.2005.05.003.

Holohan, E. P., M. P. J. Schöpfer, and J. J. Walsh (2011), Mechanical and geometric controls on the structural evolution of pit crater and caldera subsidence, *Journal of Geophysical Research: Solid Earth*, *116*(7), 1–23, doi:10.1029/2010JB008032.

Holohan, E. P., M. P. Schöpfer, and J. J. Walsh (2015), Stress evolution during caldera collapse, *Earth and Planetary Science Letters*, *421*, 139–151, doi:10.1016/j.epsl.2015.03.003.

Hungr, O., S. Leroueil, and L. Picarelli (2014), The Varnes classification of landslide types, an update, *Landslides*, *11*(2), 167–194, doi:10.1007/s10346-013-0436-y.

Husain, T., D. Elsworth, B. Voight, G. Mattioli, and P. Jansma (2014), Influence of extrusion rate and magma rheology on the growth of lava domes: Insights from particle-dynamics modeling, *Journal of Volcanology and Geothermal Research*, *285*, 110–117, doi:10.1016/j.jvolgeores.2014.08.013.

Husain, T., D. Elsworth, B. Voight, G. Mattioli, and P. Jansma (2018), Influence of conduit flow mechanics on magma rheology and the growth style of lava domes, *Geophysical Journal International*, *213*(3), 1768–1784, doi:10.1093/gji/ggy073.

Hutchison, W., N. Varley, D. M. Pyle, T. A. Mather, and J. A. Stevenson (2013), Airborne thermal remote sensing of the Volcán de Colima (Mexico) lava dome from 2007 to 2010, *Geological Society, London, Special Publications*, *380*(1), 203–228, doi:10.1144/SP380.8.

Itasca Consulting Group, I. (2017), PFC2D (Particle Flow Code in Two Dimensions).

Jaeger, J., N. Cook, and R. Zimmerman (2009), *Fundamentals of Rock Mechanics*, John Wiley & Sons.

Jenck, O., D. Dias, and R. Kastner (2009), Discrete element modelling of a granular platform supported by piles in soft soil - Validation on a small scale model test and comparison to a numerical analysis in a continuum, *Computers and Geotechnics*, *36*(6), 917–927, doi:10.1016/j.compgeo.2009.02.001.

Loughlin, S., R. Luckett, G. Ryan, T. Christopher, V. Hards, S. De Angelis, L. Jones, and M. Strutt (2010), An overview of lava dome evolution, dome collapse and cyclicity at Soufrière Hills Volcano, Montserrat, 2005-2007, *Geophysical Research Letters*, *37*, doi:10.1029/2010GL042547.

Matthews, A., J. Barclay, S. Carn, G. Thompson, J. Alexander, R. Herd, and C. Williams (2002), Rainfall-induced volcanic activity on Montserrat, *Geophysical Research Letters*, *29*, doi:10.1029/2002GL014863.

Matthews, A. J., and J. Barclay (2004), A thermodynamical model for rainfall-triggered volcanic dome collapse, *Geophysical Research Letters*, *31*, doi:10.1029/2003GL019310.

Melnik, O., and R. S. J. Sparks (2002), Dynamics of magma ascent and lava extrusion at Soufrière Hills Volcano, Montserrat, *Geological Society, London, Memoirs*, *21*(1), 153–171, doi:10.1144/GSL.MEM.2002.021.01.07.

Melnik, O., and R. S. J. Sparks (2005), Controls on conduit magma flow dynamics during lava dome building eruptions, *Journal of Geophysical Research B: Solid Earth*, *110*(2), 1–21, doi:10.1029/2004JB003183.

Moore, G., T. Vennemann, and I. S. E. Carmichael (1998), An empirical model for the solubility of H2O in magmas to 3 kilobars, *American Mineralogist*, *83*, 36–42, doi:10.1016/j.jvolgeores.2004.09.019.

Morgan, J. K., and P. J. McGovern (2005a), Discrete element simulations of gravitational volcanic deformation: 1. Deformation structures and geometries, *Journal of Geophysical Research B: Solid Earth*, *110*(5), 1–22, doi:10.1029/2004JB003252.

Morgan, J. K., and P. J. McGovern (2005b), Discrete element simulations of gravitational volcanic deformation: 2. Mechanical analysis, *Journal of Geophysical Research B: Solid Earth*, *110*(5), 1–13, doi:10.1029/2004JB003253.

Ogburn, S., S. Loughlin, and E. Calder (2015), The association of lava dome growth with major explosive activity (VEI4): DomeHaz, a global dataset, *Bulletin of Volcanology*, *77*(40), doi:10.1007/s00445-015-0919-x.

Okubo, C. H. (2004), Rock mass strength and slope stability of the Hilina slump, Kilauea volcano, Hawai'i, *Journal of Volcanology and Geothermal Research*, *138*(1-2), 43–76, doi:10.1016/j.jvolgeores.2004.06.006.

Osher, S., and J. A. Sethian (1988), Fronts propagating with curvature-dependent speed: Algorithms based on Hamilton-Jacobi formulations, *Journal of Computational Physics*, *79*(1), 12–49, doi:10.1016/0021-9991(88)90002-2.

Petley, D. N., M. H. Bulmer, and W. Murphy (2002), Patterns of movement in rotational and translational landslides, *Geology*, *30*(8), 719–722, doi:10.1130/0091-7613(2002)030⟨0719:POMIRA⟩2.0.CO;2.

Potyondy, D. (2016), Material-Modeling Support in PFC [via fistPkg20], *Tech. rep.*, Itasca.

Potyondy, D. O. (2012), A flat-jointed bonded-particle material for hard rock, *46th US Rock Mechanics/Geomechanics Symposium*, p. 10.

Robertson, R., P. D. Cole, R. Sparks, C. Harford, A. Lejeune, A. Miller, M. Murphy, G. Norton, and N. Stevens (1998), The explosive eruption of Soufriere Hills Volcano, Montserrat, West Indies, 17 September, 1996, *Geophysical Research Letters*, *25*(18), 3429–3432.

Ryan, G., S. Loughlin, M. James, L. Jones, E. Calder, T. Christopher, M. Strutt, and G. Wadge (2010), Growth of the lava dome and extrusion rates at Soufrière Hills Volcano, Montserrat, West Indies: 2005-2008, *Geophysical Research Letters*, *37*, doi:10.1029/.

Sato, H., T. Fujii, and S. Nakada (1992), Crumbling of dacite dome lava and generation of pyroclastic flows at Unzen volcano, *Letters to Nature*, *360*, 664–666.

Schöpfer, M. P., C. Childs, and J. J. Walsh (2006), Localisation of normal faults in multilayer sequences, *Journal of Structural Geology*, *28*(5), 816–833, doi:10.1016/j.jsg.2006.02.003.

Simmons, J., D. Elsworth, and B. Voight (2005), Classification and idealized limit-equilibrium analyses of dome collapses at Soufrière Hills volcano, Montserrat, during growth of the first lava dome: November 1995-March 1998, *Journal of Volcanology and Geothermal Research*, *139*(3-4), 241–258, doi:10.1016/j.jvolgeores.2004.08.009.

Smith, R., P. R. Sammonds, H. Tuffen, and P. G. Meredith (2011), Evolution of the mechanics of the 2004-2008 Mt. St. Helens lava dome with time and temperature, *Earth and Planetary Science Letters*, *307*(1-2), 191–200, doi:10.1016/j.epsl.2011.04.044.

Sparks, R. S. J. (1997), Causes and consequences of pressurisation in lava dome eruptions, *Earth and Planetary Science Letters*, *150*, 177–189.

Sparks, R. S. J., M. D. Murphy, A. M. Lejeune, R. B. Watts, J. Barclay, and S. R. Young (2000), Control on the emplacement of the andesitic lava dome of the Soufrière Hills Volcano, Montserrat by degassing-induced crystallization, *Terra Nova*, *12*, 14–20.

Stinton, A., P. D. Cole, R. Stewart, H. Odbert, and P. Smith (2014), The 11 February 2010 partial dome collapse at Soufrière Hills Volcano, Montserrat, *Geological Society, London, Memoirs*, *39*, 133–152, doi:10.1144/M39.7.

Swanson, D., D. Dzurisin, R. Holcomb, E. Iwatsubo, W. Chadwick, T. J. Casadevall, J. Ewert, and C. Heliker (1987), Growth of the lava dome at Mount St. Helens, Washington, (USA), 1981-1983, *Geological Society of America, Special Pa.*

Taron, J., D. Elsworth, G. Thompson, and B. Voight (2007), Mechanisms for rainfall-concurrent lava dome collapses at Soufrière Hills Volcano, 20002002, *Journal of Volcanology and Geothermal Research*, *160*, 195–209, doi:10.1016/j.jvolgeores.2006.10.003.

Thomas, M. E., N. Petford, and E. N. Bromhead (2004), Volcanic rock-mass properties from Snowdonia and Tenerife: implications for volcano edifice strength, *Journal of the Geological Society*, *161*(6), 939–946, doi:10.1144/0016-764903-166.

Vallance, J., D. Schneider, and S. Schilling (2008), Growth of the 2004-2006 Lava-Dome Complex at Mount St. Helens, Washington, *A Volcano Rekindled: The Renewed Eruption of Mount St. Helens 2004-2006, U.S. Geological Survey Professional Paper 1750*, pp. 169–208.

Villemant, B., J. Mouatt, and A. Michel (2008), Andesitic magma degassing investigated through H2O vapour-melt partitioning of halogens at Soufrière Hills Volcano, Montserrat (Lesser Antilles), *Earth and Planetary Science Letters*, *269*(1-2), 212–229, doi:10.1016/j.epsl.2008.02.014.

Voight, B. (2000), Structural stability of andesite volcanoes and lava domes, *Philosophical Transactions of the Royal Society of London*, *358*, 1663–1703.

Voight, B., and D. Elsworth (2000), Instability and collapse of hazardous gas-pressurized lava domes, *Geophysical Research Letters*, *27*(1), 1–4, doi:10.1029/1999GL008389.

Voight, B., R. P. Hoblitt, A. Clarke, A. Lockhart, A. Miller, L. Lynch, and J. McMahon (1998), Remarkable cyclic ground deformation monitored in real-time on Montserrat, and its use in eruption forecasting, *Geophysical Research Letters*, *25*(18), 3405–3408.

Voight, B., R. Sparks, A. Miller, R. C. Stewart, R. P. Hoblitt, A. Clarke, J. Ewart, W. Aspinall, B. Baptie, E. S. Calder, P. D. Cole, T. H. Druitt, C. Hartford, R. Herd, P. Jackson, A. M. Lejeune, A. Lockhart, S. C. Loughlin, R. Luckett, L. Lynch, G. Norton, R. Robertson, I. Watson, R. Watts, and S. Young (1999), Magma Flow Instability and Cyclic Activity at Soufrière Hills Volcano, Montserrat, British West Indies, *Science*, *283*, 1138–1142.

Voight, B., J.-C. Komorowski, G. E. Norton, A. B. Belousov, M. Belousova, G. Boudon, P. W. Francis, W. Franz, P. Heinrich, R. S. J. Sparks, and S. R. Young (2002), The 26 December (Boxing Day) 1997 sector collapse and debris avalanche at Soufrière Hills Volcano, Montserrat, *Geological Society, London, Memoirs*, *21*(1), 363–407, doi:10.1144/GSL.MEM.2002.021.01.17.

Voight, B., A. T. Linde, I. S. Sacks, G. S. Mattioli, R. S. J. Sparks, D. Elsworth, D. Hidayat, P. E. Malin, E. Shalev, C. Widiwijayanti, S. R. Young, V. Bass, A. Clarke, P. Dunkley, W. Johnston, N. McWhorter, J. Neuberg, and P. Williams (2006), Unprecedented pressure increase in deep magma reservoir

triggered by lava-dome collapse, *Geophysical Research Letters*, doi:10.1029/2005GL024870.

Wadge, G., D. G. Macfarlane, H. M. Odbert, M. R. James, J. K. Hole, G. Ryan, V. Bass, S. De Angelis, H. Pinkerton, D. A. Robertson, and S. C. Loughlin (2008), Lava dome growth and mass wasting measured by a time series of ground-based radar and seismicity observations, *Journal of Geophysical Research: Solid Earth*, *113*(8), 1–15, doi:10.1029/2007JB005466.

Wadge, G., G. Ryan, and E. S. Calder (2009), Clastic and core lava components of a silicic lava dome, *Geology*, *37*(6), 551–554, doi:10.1130/G25747A.1.

Wadge, G., R. Herd, G. Ryan, E. Calder, and J. Komorowski (2010), Lava production at Soufrière Hills Volcano, Montserrat: 1995-2009, *Geophysical Research Letters*, *37*, doi:10.1029/2009GL041466.

Wadge, G., B. Voight, R. Sparks, P. Cole, S. Loughlin, and R. Robertson (2014), An overview of the eruption of Soufrière Hills Volcano, Montserrat from 2000 to 2010, *Geological Society, London, Memoirs*, *39*, 1–40, doi:10.1144/M39.1.

Walter, T. R., D. Legrand, H. D. Granados, G. Reyes, and R. Arámbula (2013), Volcanic eruption monitoring by thermal image correlation: Pixel offsets show episodic dome growth of the Colima volcano, *Journal of Geophysical Research: Solid Earth*, *118*(4), 1408–1419, doi:10.1002/jgrb.50066.

Walter, T. R., J. Subandriyo, S. Kirbani, H. Bathke, W. Suryanto, N. Aisyah, H. Darmawan, and P. Jousset (2015), Tectonophysics Volcano-tectonic control of Merapi's lava dome splitting : The November 2013 fracture observed from high resolution TerraSAR-X data, *Tectonophysics*, *639*, 23–33, doi:10.1016/j.tecto.2014.11.007.

Wang, C., D. Tannant, and P. Lilly (2003), Numerical analysis of the stability of heavily jointed rock slopes using PFC2D, *International Journal of Rock Mechanics and Mining Sciences*, *40*, 415–424, doi:10.1016/S1365-1609(03)00004-2.

Wang, Y., and F. Tonon (2009), Modeling Lac du Bonnet granite using a discrete element model, *International Journal of Rock Mechanics and Mining Sciences*, *46*(7), 1124–1135, doi:10.1016/j.ijrmms.2009.05.008.

Watters, R. J., D. R. Zimbelman, S. D. Bowman, and J. K. Crowley (2000), Rock mass strength assessment and significance to edifice stability, Mount Rainier and Mount Hood, Cascade Range volcanoes, *Pure and Applied Geophysics*, *157*(6-8), 957–976, doi:10.1007/s000240050012.

Watts, R. B., R. a. Herd, R. S. J. Sparks, and S. R. Young (2002), Growth patterns and emplacement of the andesitic lava dome at Soufrière Hills Volcano, Montserrat, *Geological Society, London, Memoirs*, *21*(1), 115–152, doi:10.1144/GSL.MEM.2002.021.01.06.

Wu, S., and X. Xu (2016), A Study of Three Intrinsic Problems of the Classic Discrete Element Method Using Flat-Joint Model, *Rock Mechanics and Rock Engineering*, *49*(5), 1813–1830, doi:10.1007/s00603-015-0890-z.

Zhang, Q., H. Zhu, L. Zhang, and X. Ding (2011), Study of scale effect on intact rock strength using particle flow modeling, *International Journal of Rock Mechanics and Mining Sciences*, *48*(8), 1320–1328, doi:10.1016/j.ijrmms.2011.09.016.

Chapter 4

Evolution of mechanical properties of lava dome rocks across the 1995-2010 eruption of Soufrière Hills volcano, Montserrat

C. E. Harnett[1], J. Kendrick [2], A. Lamur [2], M. E. Thomas [1], A. Stinton [3,4], P. A. Wallace [2], J. E. P. Utley [2], W. Murphy [1], J. Neuberg[1], Y. Lavallée[2]

[1] *School of Earth and Environment, University of Leeds, United Kingdom*

[2] *Earth, Ocean and Ecological Sciences, University of Liverpool, United Kingdom*

[3] *Montserrat Volcano Observatory, Flemmings, Montserrat*

[4] *Seismic Research Centre, University of the West Indies, St. Augustine, Trinidad and Tobago*

Citation: **Harnett, C. E.**, Kendrick, J. E., Lamur, A. H., Stinton, A., Wallace, P. A., Utley, J. E. P., Murphy, W., Neuberg, J., and Lavallée, Y. (2019). *Evolution of mechanical properties of lava dome rocks across the 1995-2010 eruption of Soufrière Hills volcano, Montserrat.* Frontiers in Earth Science, 7 (7), doi: 10.3389/feart.2019.00007.

Abstract

Lava dome collapses pose a hazard to surrounding populations, but equally represent important processes for deciphering the eruptive history of a volcano. Models examining lava dome instability rely on accurate physical and mechanical properties of volcanic rocks. Here we focus on determining the physical and mechanical properties of a suite of temporally-constrained rocks from different phases of the 1995-2010 eruption at Soufrière Hills volcano in Montserrat. We determine the uniaxial compressive strength, tensile strength, density, porosity, permeability, and Young's modulus using laboratory measurements, complemented by Schmidt hammer testing in the field.

By viewing a snapshot of each phase, we find the highest tensile and compressive strength in the samples attributed to Phase 4, corresponding to a lower permeability and an increasing proportion of isolated porosity. Samples from Phase 5 show lower compressive and tensile strengths, corresponding to the highest permeability and porosity of the tested materials. Overall, this demonstrates a reliance of mechanical properties primarily on porosity. However, a shift towards increasing prevalence of pore connectivity in weaker samples identified by microtextural analysis demonstrates that here pore connectivity also contributes to the strength and Young's Modulus, as well as controlling permeability. The range in uniaxial compressive strengths is supported using Schmidt hammer field testing. We determine a narrow range in mineralogy across the sample suite, but identify a correlation between increasing crystallinity and increasing strength. We correlate these changes to residency-time in the growing lava dome during the eruption, where stronger rocks have undergone more crystallization. In addition, subsequent recrystallization of silica polymorphs from the glass phase may further strengthen the material.

We suggest the variation in physical and mechanical rock properties shown within the Soufrière Hills eruptive products be included in future structural stability models of the remaining over-steepened dome on Montserrat, and that consideration of rock heterogeneity and its temporal variation if possible, be made in other, similar systems.

4.1 Introduction

Collapse of volcanic flanks and lava domes has been shown to influence subsequent eruptive behaviour (e.g *Voight*, 2000) and represents a major hazard through generation of pyroclastic flows and debris avalanches. Structural stability modelling is therefore vital in understanding the hazard associated with, and the consequences of volcanic collapse events. This has been explored through various modelling efforts, including: analogue modelling (*Vidal and Merle*, 2000; *Andrade and van Wyk de Vries*, 2010; *Cecchi et al.*, 2004; *Tibaldi et al.*, 2006; *Nolesini et al.*, 2013); Limit Equilibrium Methods (LEM; *Apuani et al.*, 2005; *Simmons et al.*, 2005; *Borselli et al.*, 2011; *Schaefer et al.*, 2013; *Dondin et al.*, 2017); Finite Element Modelling (FEM; *Voight and Elsworth*, 2000; *Schaefer et al.*, 2013); Finite Difference Methods (FDM; *Apuani et al.*, 2005; *Le Friant et al.*, 2006) and Discrete Element Modelling (DEM; *Morgan and McGovern*, 2005a,b; *Husain et al.*, 2014; *Harnett et al.*, 2018; *Husain et al.*, 2018). Although modelling studies expand our knowledge of mechanisms of volcanic structural instability, they are often limited by the availability of mechanical data for edifice rock properties.

In particular, a recurrent challenge in modelling volcanic failure is representing the spatial and temporal heterogeneity of material (e.g. *Schaefer et al.*, 2015; *Heap et al.*, 2016a). The logistical difficulties in accessing deposits and outcrops during or after an eruption also prevent direct observation and quantification of erupted material. Numerical models are often forced to adopt 'typical' values for the physical and geomechanical properties of the material from the volcano in question, thus increasing the uncertainties associated with any model. As such, it is important to investigate the spatio-temporal evolution of material forming a volcano.

Volcanic products are typically very heterogeneous, with varied eruptive conditions leading to large ranges in pore architecture (i.e., connected vs. isolated vesicles vs. fractures) and permeability (*Mueller et al.*, 2005; *Heap et al.*, 2014a; *Farquharson et al.*, 2015; *Colombier et al.*, 2017; *Heap et al.*, 2018a). Experimental investigations into volcanic rock properties have increased in recent years, including compressive and tensile strength, elastic properties, and resultant physical changes induced during deformation (e.g. *Lavallée et al.*, 2007, 2008, 2013; *Schaefer et al.*, 2015; *Heap et al.*, 2016a; *Lamur et al.*, 2017; *Marmoni et al.*, 2017; *Coats et al.*, 2018; *Heap et al.*, 2018b), as well as research into the

relationship between activity at dome-building volcanoes and their respective rock properties (e.g. *Smith et al.*, 2009, 2011; *Kendrick et al.*, 2013, 2016; *Heap et al.*, 2015, 2016a; *Kushnir et al.*, 2016; *Lavallée et al.*, 2019). This increase in research has started to show the importance of understanding how mechanical properties of rock influence the eruptive style at a volcano, for example at Mt. St. Helens where porosity, and as such strength, was shown to be a determining factor in whether a lava dome or spine was extruded (*Heap et al.*, 2016a).

Geomechanical properties not only influence eruptive style, but also structural stability. For example, although the interior of a lava dome is subjected to moderate confining pressures, outer talus slopes are often unconfined. This complex stress field influences the development of tensile and shear fractures. Although the mechanical behaviour of materials in compressive stress fields has received most of the attention by the rock physics community in recent decades (e.g. *Paterson and Wong*, 2005), there is more investigation to be done into the tensile rock strength of volcanic materials, whose structural stability is commonly challenged by tensile stresses due to lack of confining and high pore pressure (*Kilburn*, 2018). The tensile strength of rocks is found to be 8% of the compressive strength (*Jaeger et al.*, 2009; *Perras and Diederichs*, 2014), and can be as low as 4% (*Zorn et al.*, 2018). As such, rock failure (even under compressive shear stress) generally follows the nucleation, propagation, and coalescence of tensile fractures (with the exception of supershear rupture; *Das*, 2015). We therefore investigate tensile strength and the ratio to compressive strength, and its relationship to other physical rock properties.

In addition to determining mechanical properties and variation of the physical properties of volcanic rock, it is important to consider how variation in petrology and geochemistry may also influence dome stability. For example at Mt. Unzen a temporal change in chemistry due to phenocryst abundance was shown to correlate with temporal changes in effusion rate (*Nakada and Motomura*, 1999), and such evolution in eruptive style will also alter dome stability. Similarly, the occurrence of secondary mineralization may modify the porous structure and coherence of rocks, affecting the structural stability (*Horwell et al.*, 2013; *Coats et al.*, 2018) especially when water is present in the pore space (*Heap et al.*, 2018c).

Here, we focus on quantifying the physical, mineralogical, and mechanical properties of a temporally-constrained sample set, and the variability of these properties, required as inputs for numerical models assessing dome collapse hazard. To do this, we focus specifically on the Soufrière Hills volcano (SHV),

and we aim to demonstrate the importance of, and encourage incorporation of, rock heterogeneity in future dome stability modelling efforts. In addition to showcasing the range in material properties, we also speculate how these may be temporally-linked to specific phases of the eruption.

4.2 Geological setting

SHV is an andesitic volcanic complex on the Caribbean island of Montserrat, located in the northern Lesser Antilles island arc (Figure 4.1). The current eruption started in July 1995 with a series of phreatic explosions, which led to the emplacement and growth of a lava dome (*Young et al.*, 1998). This was followed by a series of dome growth and collapse cycles, involving large scale pyroclastic density current (PDC) generation and explosive activity. The eruption of SHV included five phases of dome growth (*Wadge et al.*, 2014; *Stinton et al.*, 2017): Phase 1 (15 November 1995 10 March 1998); Phase 2 (27 November 1999 1 August 2003); Phase 3 (1 August 2005 20 April 2007); Phase 4 (separated into Phase 4a: 8 August 2008 8 October 2008, and Phase 4b: 2 December 2008 3 January 2009; *Robertson et al.*, 2009); and Phase 5 (8 October 2009 11 February 2010). These phases were separated by pauses characterized by no magma extrusion, and Phases 3, 4 and 5 were preceded by transitional periods with increases in seismicity and/or ash venting.

Several lava dome collapses occurred throughout the eruptive period, with the largest of these ($>10^7$ m^3) shown in Figure 4.2. The end of the last phase of lava extrusion was marked by a major dome collapse on 11 February 2010 (*Stinton et al.*, 2014b). The scale of collapses throughout the eruption ranged from frequent (up to 140 per day) small scale rockfalls (*Calder et al.*, 2002), to larger whole dome collapses such as the total dome collapse on 12-13 July 2003 (*Herd et al.*, 2005).

Petrological studies of products throughout the eruption have shown that SHV has produced lavas of relatively similar composition hornblende-bearing andesites (*Humphreys et al.*, 2010; *Christopher et al.*, 2014; *Wadge et al.*, 2014), with an increasing proportion of mafic inclusions in later phases (*Barclay et al.*, 2010). Long-term petrology across the eruption was explored by *Christopher et al.* (2014) and although they found systematic changes in Fe-content across time, they concluded that there was no progressive change of bulk composition, with SiO_2-content consistently between 56 and 62% throughout the eruption.

Figure 4.1: Image of Montserrat showing landscape, including topographic lows where pyroclastic deposits have been channelled. Location of sampling sites shown for each phase. Also marked: Soufrière Hills volcano (SHV) summit (red triangle), and Belham River Valley (BRV; where additional Schmidt hammer testing was carried out). Inset shows location of Montserrat in the Caribbean islands.

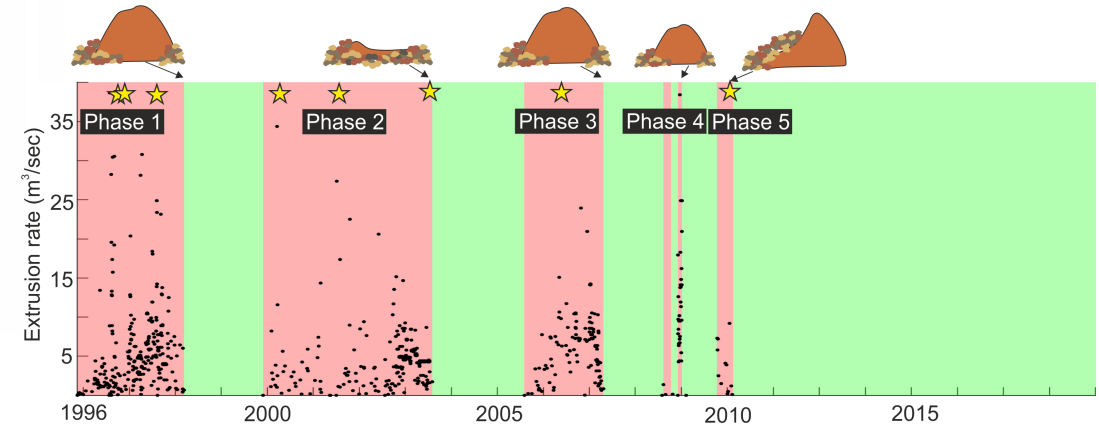

Figure 4.2: Eruption history at Soufrière Hills, Montserrat. Extrusion rate data shown in black, calculated for Phases 1 to 4 using erupted volume data from *Wadge et al.* (2014) and extrusion data for Phase 5 from *Stinton et al.* (2014a). Red shows eruptive phases, whilst green shows pauses in activity. Annotations show state of the dome at the end of each phase (standing dome with relative size indicated, wholesale collapse, partial collapse), and stars mark major ($>10^7$ m^3) dome collapses across the eruption.

However, previous studies have documented that geomechanical rock properties of chemically indistinguishable lavas can vary broadly as a result of distinct pore structures (*Kendrick et al.*, 2013; *Schaefer et al.*, 2015; *Heap et al.*, 2016a), local heterogeneities (*Farquharson et al.*, 2016), anisotropy (*Bubeck et al.*, 2017), and post-emplacement alteration (*Pola et al.*, 2014; *Siratovich et al.*, 2014; *Coats et al.*, 2018). We therefore aim to explore how the petrographic textures of the Soufrière Hills products and the temporal variation in these textures affect both rock strength and volcanic behaviour, even where there is a narrow range in bulk rock compositions.

The quantity and quality of observations recorded throughout the eruption makes SHV an ideal test site for exploring temporal variability in erupted products, as records of collapse events enable linking of specific pyroclastic deposits to specific eruptive phases.

4.3 Materials and experimental methodology

4.3.1 Sampling strategy

For this experimental study, seven block samples were collected from different PDC deposits around SHV. Deposits were selected based on the certainty with which the blocks could be tied to not only a particular collapse, but also to ensure the material was erupted during a given eruptive phase. Hence, deposits that were selected occurred in the middle or towards the end of an eruptive phase to avoid sampling rocks that were extruded in previous phases of activity. Samples can be confidently tied to their respective phase due to the directionality of collapse in each case (Table 4.1). Within each selected deposit, safely accessible blocks were examined and the Schmidt hammer method (detailed below) was employed to gain an overview of variability in material properties in the field. One block was collected from Phase 1, and two blocks collected for each of Phases 3, 4 and 5 (Figure 4.1). No samples were available for Phase 2 due to inaccessibility, and as the majority of the deposits entered the ocean (*Trofimovs et al.*, 2008).

Since the deposition of all samples occurred via PDCs, they are likely to represent the strongest material from each of the phases, as weaker material could have been preferentially broken down by the collapse and transport processes. Whilst we cannot be certain that the material is the most representative of each phase, we present here one of the first temporally-resolved examinations of rock property evolution during an eruption.

Table 4.1: Block labels, their respective phase, and evidence that each sample originates from its attributed phase, alongside summaries of dome activity prior to each of the collapses from which samples in this study are collected.

Phase	**Block**	**Sampled event**	**Evidence that rock originates from this phase**	**Dome activity prior to/during sample-originating collapse**
1	M	21/09/97, collapse	Sample collected from the surface of the still exposed block-and-ash flow deposits in the former village of Farm.	The growing lava dome had over-topped the walls of English's crater in February 1997 (*Loughlin et al.*, 2002) and active extrusion continued prior to the collapse. Collapse likely to be gravitational with possible contribution of a dome-growth direction from N to NE (*Cole et al.*, 2002; *Wadge et al.*, 2014).
3	B, H	20/05/06, whole dome collapse	Samples collected from an isolated boulder on the pyroclastic fan at the mouth of the Tar River valley. Boulder emplaced during dome collapse. Based on photographic evidence from MVO archives.	Collapse preceded by continuous extrusion of SW lobe. Switch in extrusion direction noted on morning of collapse. Large LP earthquake preceded collapse and total dome collapse coincided with peak in rainfall (*Loughlin et al.*, 2010).
4	F, G	29/07/08, explosion	Samples collected from the surface of still exposed flow deposits in Plymouth. Deposit map shown in *Komorowski et al.* (2010).	Explosion on 29 July 2008 marked the start of Phase 4a and was preceded by several days of seismicity and several months of no extrusion.
5	J, K	05/02/10, Vulcanian explosion	Samples collected from surface of block-and-ash flow deposits in Aymer's Ghaut. Based on MVO data and deposit map shown in *Stinton et al.* (2014b).	Explosion on 5 February 2010 occurred during Phase 5 (very shortly before the end of the phase), and was preceded by extrusion of fresh lava.

4.3.2 Sample preparation

From each of the 7 blocks collected, cores were prepared with a diameter of 26 mm and were cut and ground parallel to a nominal length of 52 mm for use in porosity and permeability measurements, and for testing in uniaxial and cyclic loading experiments (sample properties provided in Supplementary Table C.1). Samples were then oven-dried for at least 12 hours at 70°C and thermally equilibrated to ambient conditions before any measurements were performed. All cores were taken at the same orientation within a given block.

One core was prepared from each block with 37 mm diameter and nominal length of 80 mm. The density of these samples (provided in Supplementary Table C.1) was calculated using their mass and sample dimensions, and these samples were used for testing in cyclic loading experiments to determine Young's modulus.

From each of the 7 blocks, 37 mm diameter by 18 mm thick disks were also prepared for use in Brazilian tensile strength tests (Supplementary Table C.2). These samples have an approximate aspect ratio of 1:2 as recommended by ISRM and ASTM.

Sub-samples of each block were taken from offcuts of these cores and set in epoxy, in the same orientation as the cores were prepared. Thick sections were created for mineralogical and textural characterization by polishing and carbon coating the epoxy-mounted samples.

4.3.3 QEMSCAN analysis

Mineralogical and textural analyses were performed on the prepared thick sections. The variation in phase abundances across the sample range was quantified using QEMSCAN (Quantitative Evaluation of Minerals by Scanning electron microscopy) at the University of Liverpool. The QEMSCAN is an automated SEM-EDS (scanning electron microscopy/energy dispersive X-ray spectroscopy) system manufactured by FEI Company.

The QEMSCAN uses a 15 kV electron beam to produce X-ray spectra which provide a semi-quantitative chemical map of the different phases, here at a resolution of 10 μm over an average area of 10.5 mm by 10.5 mm. The identified chemical compositions are compared to known compositions stored in a reference library. Additional mineral and glass chemistry definitions are manually added to the supplied database to ensure all chemical compounds are recognized. Crystallographic features are not discriminated by QEMSCAN,

and so polymorphs of the same composition cannot be differentiated (for example, quartz and cristobalite would both be classified as silica polymorphs by QEMSCAN processing). We then used the iDiscover software to create colour images showing the distribution of mineral phases, and used this data to determine the normalized mineral abundances of the sample as area-percentages.

4.3.4 Schmidt hammer

The Schmidt hammer is a portable, hand-held instrument originally designed for non-destructive index testing of concrete. It records the rebound height of a spring-loaded mass to indicate material strength (*Torabi et al.*, 2011); this 'rebound value' can be correlated to various mechanical properties such as uniaxial (unconfined) compressive strength and Young's modulus (e.g *Deere and Miller*, 1966; *Yasar and Erdogan*, 2004). Schmidt hammer testing has previously been used on volcanic rocks (e.g *Dinçer et al.*, 2004; *Del Potro and Hürlimann*, 2009) and provides a method of collecting in-situ data where outcrop accessibility is problematic. In this study, we used an L-type Schmidt hammer to carry out field testing in accordance with the International Society of Rock Mechanics (ISRM) guidelines (*Ulusay and Hudson*, 1979). The Schmidt hammer rebound values (R_L) were corrected for angle of testing where necessary, following the normalization procedure set out by *Basu and Aydin* (2004); this often results in non-integer rebound values. The Schmidt hammer was calibrated using a steel anvil, which gave a R_L value of 72. Hard rocks such as granites generally have high R_L values of > 50, whereas softer rocks such as chalk are likely to have a R_L value < 30 (*Katz et al.*, 2000; *Ericson*, 2004; *Goudie*, 2013).

We present results of Schmidt hammer tests on 24 blocks, measured during a field campaign in January 2016, from deposits where the eruptive phase is known (4 from Phase 1, 3 from Phase 3, 9 from Phase 4, and 8 from Phase 5). These tests were carried out at the same locations as sample sites (Figure 4.1), but on blocks exceeding 30 cm in all dimensions and therefore these were not collected for laboratory experimentation. We therefore consider the Schmidt hammer data a verification of the collected blocks. We also present results from 28 Schmidt hammer tests on samples located in Belham River Valley (BRV); these cannot be attributed to a specific phase, but from collapse direction information we can determine that these boulders were emplaced during Phases 3-5. This gives additional constraint of the range of expected values.

4.3.5 Physical characterization

Permeability and porosity were determined for all 26 mm diameter cores. The density of each core (ρ_{rock}) was determined by measuring its mass and volume, and calculating the ratio between the two (Supplementary Table C.1, Supplementary Figure C.1). Connected porosity was determined for each core using a helium pycnometer (Micromeritics AccuPyc II 1340), providing sample void volumes with an accuracy of 0.1%. Total porosity was also determined for each of the 7 blocks by creating a powder of the rock sample and measuring its density (ρ_{powder}). Total porosity exceeds connected porosity as it includes calculation of isolated pores that could not be accessed by helium during pycnometry. Total porosity (ρ_{T}) is calculated using

$$\rho_{\mathrm{T}} = \frac{(\rho_{\mathrm{powder}} - \rho_{\mathrm{rock}})}{\rho_{\mathrm{rock}}}. \tag{4.1}$$

Permeability was measured using a benchtop GasPerm permeameter developed by Vinci Technologies. We measured permeabilities of 49 samples using nitrogen as permeating fluid and by imposing a flow rate that created, depending on the permeability of the sample, a minimum pressure differential (ΔP) between the inflow and outflow of 0.5 psi (0.0035 MPa). Measurements were made on each sample at 3 confining pressures. The confining pressure was held constant at each of 100 psi, 200 psi, and 300 psi (0.7, 1.4 and 2.1 MPa) for the duration of the measurement. In cases where Darcian conditions were not achieved (i.e. the flow rate resulted in too high ΔP and turbulent flow/gas slippage in the porous medium), we applied Klinkenberg and Forchheimer's corrections to retrieve the equivalent Darcy permeability.

4.3.6 Uniaxial compressive strength testing

Uniaxial compressive strength (UCS) testing was carried out at ambient (room) temperature on one sample from each block (7 total) using 26 mm diameter samples (for which permeability and porosity had already been determined). The cores were loaded axially at a constant strain rate of 10^{-5} s^{-1} using a 5969 Instron uniaxial benchtop press with a 50 kN load cell at the Experimental Volcanology and Geothermal Research Laboratory at the University of Liverpool. The measured axial displacement was corrected to subtract the compliance of the apparatus (i.e. pistons and frame) during loading. While one sample from each block was loaded to failure to measure the compressive strength, we established

the repeatability of the mechanical data of the materials by determining Young's modulus using 22 stress cycling experiments (see Section 4.3.8), as higher Young's modulus relates to higher peak strength (e.g *Schaefer et al.*, 2015).

4.3.7 Brazilian tensile strength testing

Indirect tensile strength was measured using the Brazil testing method (*Ulusay and Hudson*, 1979), in which a compressive load is applied diametrically to the curved edge of a cylindrical, disc-shaped rock sample. This is a commonly used method to induce tensile failure due to the logistical difficulty of measuring direct tensile strength (*Perras and Diederichs*, 2014). Tensile strength, σ_t, is calculated using the following formula

$$\sigma_{\mathrm{T}} = \frac{2P}{\pi DL}, \tag{4.2}$$

where P is the applied load (N), D is sample diameter (m), and L is sample thickness (m).

In total, 66 samples were prepared at 37 mm diameter (with aspect ratio of 1:2 to meet ISRM standards), and were loaded at a constant deformation rate of 0.0037 mm/s (equivalent diametric strain rate of 10^{-4} s^{-1}), again using the Instron uniaxial press in the Experimental Volcanology and Geothermal Research Laboratory at the University of Liverpool.

4.3.8 Cyclic experiments

The UCS tests were used to inform the cyclic loading tests by defining a threshold of 50% peak stress for each sample type. Cyclic loading experiments were then performed on 22 cores of 26 mm diameter, and 7 cores of 37 mm diameter (both with 2:1 aspect ratio); the samples were axially loaded to this threshold at a constant strain rate of 10^{-5} s^{-1}, and then unloaded at the same rate. This was performed to examine the repeatability of the stress-strain response to loading, and to calculate elastic moduli. By loading only to 50% of peak stress, we considered the rock to behave purely elastically (*Walsh*, 1965; *Nihei et al.*, 2000; *David et al.*, 2012), and therefore assumed that no lasting damage was done to the sample and that it could rebound and recover deformation.

4.3.9 Young's modulus determination

Young's modulus (E) is a key parameter in volcanic modelling (*Hale et al.*, 2009a,b; *Husain et al.*, 2014; *Harnett et al.*, 2018). Young's modulus is traditionally an elastic parameter, defined in GPa, and although these rocks do not behave in a purely linear elastic manner throughout compression, the stress-strain response is linear following crack-closure and prior to damage accumulation (e.g. *Heap and Faulkner*, 2008). Here, to fall confidently within this regime we consider the linear portion of the curve as between 40% and 50% of peak rock strength. Therefore for all 29 cores with 26 mm diameter and 7 cores with 37 mm diameter, we calculate Young's modulus within this range. Following ISRM guidelines (*Ulusay and Hudson*, 1979), we calculate the Young's modulus using

$$E = \frac{\sigma_{50} - \sigma_{40}}{\varepsilon_{50} - \varepsilon_{40}}, \tag{4.3}$$

where σ is stress and ϵ is strain, at a given percentage of peak rock strength (denoted by the subscript).

4.4 Results

4.4.1 Microstructural analysis

QEMSCAN analysis illustrates mineral assemblages and their relative abundance in each of the samples. An exemplar rock from each of Phases 1, 3, 4, and 5 is shown in Figure 4.3, with the remaining rocks from this study shown in Supplementary Figure C.2, and backscattered electron images shown in Supplementary Figure C.3. In addition to colour images showing the mineral distribution and texture in each sample, a grey-scale image shows the pore structure highlighted in black.

We explore mineral abundance within the sample suite, and show the area percentage calculated from QEMSCAN imagery of interstitial glass combined with silica polymorphs, and plagioclase (separated into calcium rich and sodium rich; Figures 4.4a-b). Percentages for all mineral components as a proportion of the solid phase in all samples are shown in Table 4.2.

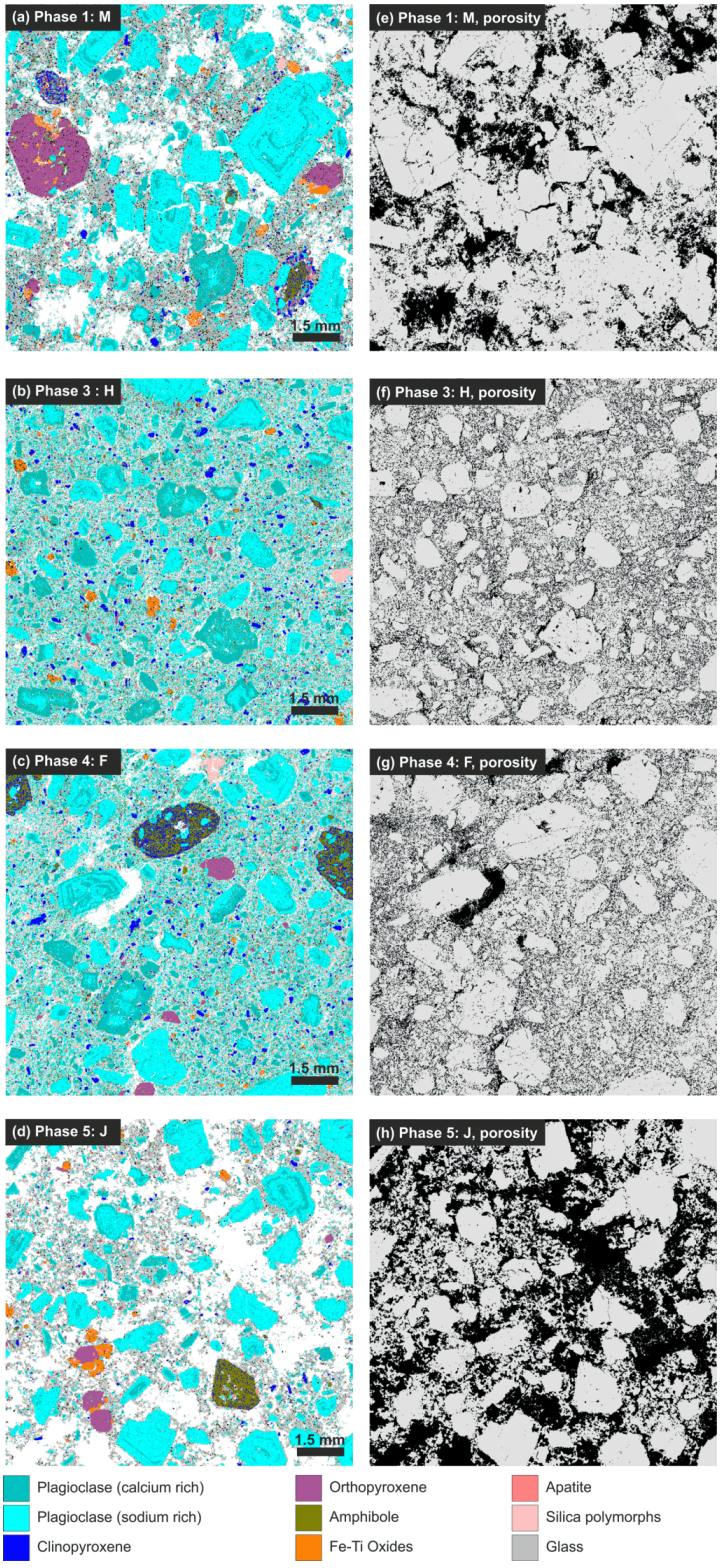

Figure 4.3: **(a-d)** QEMSCAN images showing mineral assemblage in one sample from each phase (other samples provided in Supplementary Figure C.2) the mineralogical key is shown below the images, with white used to portray the pore space. See Table 4.2 for full mineral phase analysis; **(e-h)** pore distribution in one sample from each phase (other samples provided in Supplementary Figure C.2) using processed QEMSCAN images with solid fraction shown in grey, and all porosity in black. Samples from Phases 3 and 4 are denser, with evenly distributed pore-space, whereas samples from Phases 1 and 5 have higher pore content and show pore-localization and a high connectivity. Backscattered electron images for the same samples are shown in Supplementary Figure C.3.

Table 4.2: Quantitative analysis of mineral phases present in each sample, calculated as a percentage area of the solid fraction, and porosity as % of total area, using the 10-μm resolution QEMSCAN analysis of a 10.1 x 10.1 mm^2 area.

Eruption phase		**Phase 1**	**Phase 3**		**Phase 4**		**Phase 5**	
Sample name		SHV-M	SHV-B	SHV-H	SHV-F	SHV-G	SHV-J	SHV-K
Solid Fraction (%)	***Sodium rich plagioclase***	33.42	35.41	39.57	39.48	29.35	36.21	31.26
	Calcium rich plagioclase	17.45	20.58	16.48	14.78	25.95	9.37	11.32
	Clinopyroxene	1.38	3.95	3.24	4.66	5.23	1.56	3.16
	Orthopyroxene	3.89	4.25	4.05	3.24	4.09	3.86	1.6
	Amphibole	1.63	3.62	5.26	6.66	4.99	4.25	10.67
	Fe-Ti Oxides	1.14	1	1.08	0.83	0.49	1.5	1.2
	Glass	23.19	12	11.63	8.75	10.74	29.03	23.66
	Silica polymorphs	10.27	13.13	13.48	16.13	8.68	8.9	10.74
	Smectite	2.38	2.68	2.47	2.18	2.46	2.14	2.33
	Apatite	0.27	0.29	0.22	0.2	0.24	0.37	0.28
	Mg-Fe Phase	0.21	0.37	0.7	1.18	1.12	0.09	0.16
	Biotite	0.04	0.21	0.31	0.32	0.31	0.07	0.04
	Others	0.21	0.22	0.35	0.76	1.67	0.25	0.19
	Unclassified	4.52	2.29	1.18	0.83	4.7	2.39	3.38
	Total excluding porosity	100	100	100	100	100	100	100
	Total crystallinity	66.54	74.87	74.91	75.12	80.6	62.06	65.59
Porosity (%)		20.8	23.69	24.19	20.36	21.55	15.56	28.7

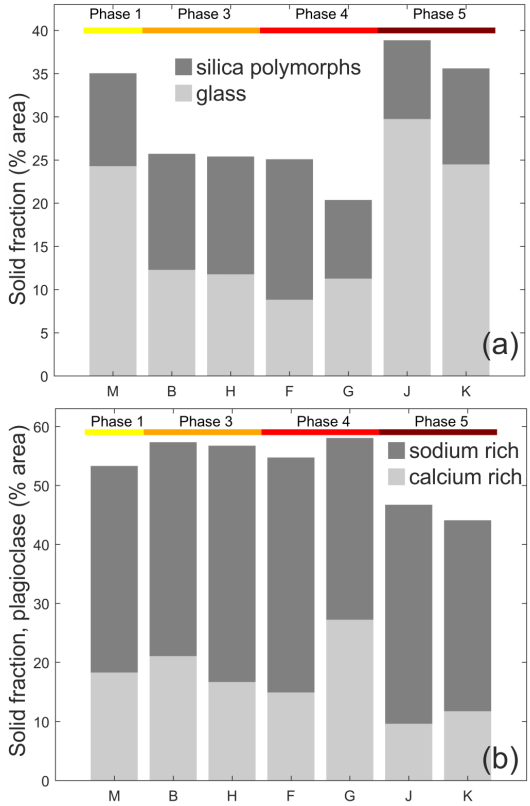

Figure 4.4: Abundances of **(a)** glass and silica polymorphs, the remaining solid fraction is composed of the primary minerals (crystallinity, Table 4.2); **(b)** plagioclase - both sodium rich and calcium rich; shown as percentage area, calculated from 10 μm resolution QEMSCAN images (shown in Figure 3 and Supplementary Figure C.2), and Phase indicated by horizontal bars at the top of each plot.

Plagioclase is dominant across all samples, totalling between 42.5-56.1% with zoned crystals evident in all samples (Figure 4.3). Slight increases in solid fraction total plagioclase content in Samples H and F (Phases 3 and 4) correspond to overall increase in crystallinity of these samples, and as such, slight depletions in total glass and silica polymorph phases (Figure 4.4). There is a higher proportion of interstitial glass compared to silica polymorphs in Samples M and J (Phases 1 and 5) compared to Samples H and F. The glass that is identified by QEMSCAN consists of fine-grained mesostasis which may comprise fine grains of various compositions that are smaller than the X-ray interaction volume of the QEMSCAN instrumentation; it thus may not necessarily represent the mechanical and rheological properties of quenched interstitial melt. Amphiboles are mostly in the form of pseudomorphs of break-down products, and clusters of pyroxene. Clinopyroxene is more dominant than orthopyroxene, particularly in Samples

H and F. Oxides are rare in all samples, and generally occur in the form of micro-phenocrysts.

In addition to having lower crystalline fractions (i.e. more glass and silica polymorphs), Samples M and J also have larger, more heterogeneously distributed pore spaces. Porosity is greatest in Sample J (Table 4.3), and comprises vesicles in between crystals whereas in samples from earlier phases (e.g. Samples H, F), much smaller pore spaces are found within the groundmass. Overall, QEMSCAN analysis shows low variability in the componentry and the mineralogical assemblage throughout the samples tested.

4.4.2 Schmidt hammer

We present the results of 52 Schmidt hammer tests (Figure 4.5), both on blocks from known eruptive phases, and from a random selection of blocks in Belham River Valley (BRV). The data shows that blocks from Phase 5 appear to be the weakest (average R_L = 26.4). Samples from Phases 1, 3 and 4 exhibit similar Schmidt hammer results, with average rebound values of 34.5, 39.7 and 37.4 respectively (Figure 4.5a; raw values given in Supplementary Table C.3).

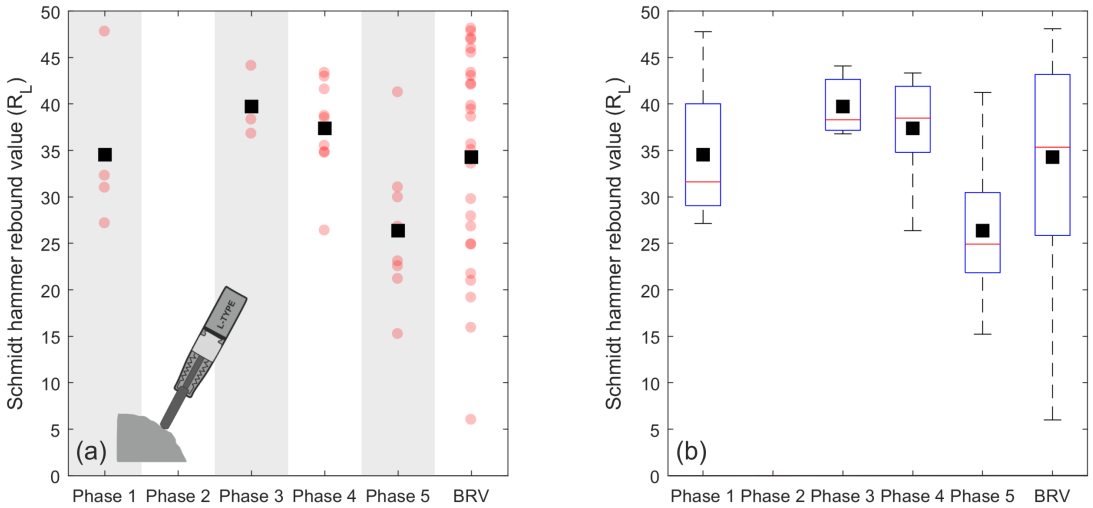

Figure 4.5: **(a)** Schmidt hammer rebound value (R_L) results from field testing at sampling locations for Phases 1, 3, 4 and 5. Belham River Valley (BRV) results show values obtained on a random selection of blocks from Phases 3, 4 and 5. Raw data shown by circles, with the mean R_L for each phase shown by a square;**(b)** box plot diagram to show median (red line), mean (black squares), 25th and 75th percentiles, and range for Schmidt hammer rebound values from each phase. Results from BRV span the overall range in values seen in other phases and highlight that Phase 5 material is the weakest of the erupted products tested, although the maximum R_L across all phases is similar.

The Schmidt hammer rebound values from all of the samples from known eruptive phases have a range of 32.6 from 15.2 to 47.8. The ranges within each phase are 20.6 (Phase 1), 7.3 (Phase 3), 17.0 (Phase 4) and 26.0 (Phase 5); the rebound values from the random boulders in the BRV have a range from 6.0 to 48.1 (a spread of 42.1), showing a similar distribution to that of the temporally-constrained blocks. Assuming there were no systematic variations in rock strength across time, the same variation would be found within the samples from each phase. However, the difference between the spread of randomly sampled blocks (42.1) far exceeds the difference within blocks attributed to a particular phase (max R_L = 26.0 for Phase 5). However, the 25th-75th percentiles of the entire dataset span a relatively narrow range of 21.8 to 42.6, highlighting that the extremes of these values represent rarer outliers (Figure 4.5b).

4.4.3 Physical properties

Connected porosities extend from approximately 20-40% across all samples (Figure 4.6a, Table 4.3), with ranges for Phases 1, 3, 4, and 5 of 8.2%, 3.3%, 4.9%, and 11.0% respectively (all values of both connected and total porosity provided in Supplementary Table C.1). Sample M (Phase 1) has an average connected porosity of 22.8% and an average total porosity of 23.2%. Samples B and H (Phase 3) have very similar porosities to Sample M, with an average connected porosity of 22.6% and a slightly higher average total porosity of 23.8%. Samples F and G (Phase 4) have similar connected porosities with an average of 22.8%, but a higher average total porosity of 25.2%, showing the existence of more isolated pores. Samples J and K (Phase 5) have a noticeably higher porosity than all of the other measured samples, with an average connected porosity of 34.8% and few isolated pores, giving an average total porosity of 35.4%.

Similarly, the density of the 26 mm samples varies from 1.61-2.22 g/cm^3, with average densities for Phases 1, 3, 4, and 5 of 2.13 g/cm^3, 2.14 g/cm^3, 2.14 g/cm^3, and 1.76 g/cm^3, respectively. The density values for Samples M, B, H, F and G are very similar (as observed for porosity), with a clear decrease in density in Samples J and K. The relationship between density and porosity is broadly linear (Supplementary Figure C.1), although deviation from linearity results primarily from the varied abundances of isolated pores.

Permeability across all samples ranges from 10^{-15} to 10^{-11} m^2 (Figure 4.6b, Table 4.3), and relates non-linearly to the connected porosity (Figure 4.6c; all values of permeability are provided in Supplementary Table C.1).

Table 4.3: Physical properties calculated for each sample, using the following methods: (a) average density, measured using a helium pycnometer and the standard deviation for each block; (b) connected porosity: measured using a helium pycnometer and the standard deviation for each block; (c) total porosity, calculated by measuring the density of a powder and using Equation (1) and the standard deviation for each block; and (d) permeability, measured at 100 psi using the GasPerm permeameter.

Phase	**Sample ID**	**Average density and st. dev. (%)**	**Average connected porosity and st. dev. (%)**	**Average total porosity and st. dev. (%)**	**Average permeability (m^2)**
1	M	2.13 ± 0.08	22.3 ± 2.5	23.2 ± 2.8	7×10^{-13}
3	B	2.14 ± 0.02	22.8 ± 0.7	23.3 ± 0.8	1×10^{-13}
	H	2.15 ± 0.03	22.5 ± 1.1	24.3 ± 3.0	1×10^{-13}
4	F	2.14 ± 0.04	22.2 ± 1.2	25.1 ± 3.9	1×10^{-14}
	G	2.13 ± 0.05	23.4 ± 1.7	25.3 ± 1.9	1×10^{-14}
5	J	1.67 ± 0.05	38.5 ± 1.2	38.9 ± 1.8	2×10^{-11}
	K	1.87 ± 0.03	31.1 ± 1.2	31.9 ± 1.1	3×10^{-12}

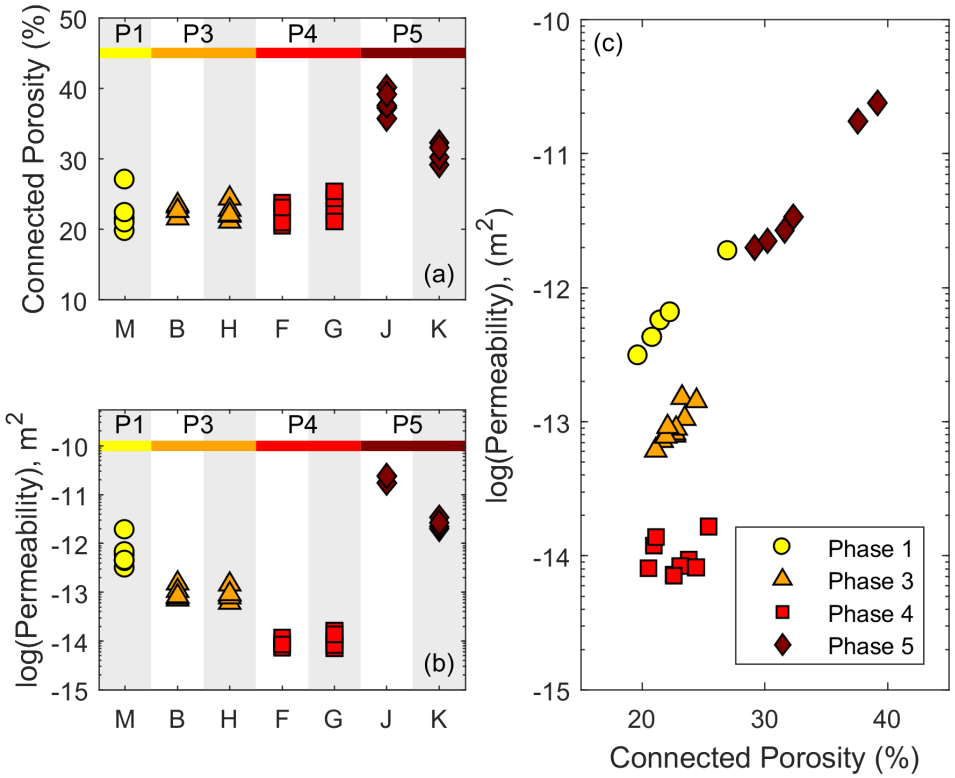

Figure 4.6: Physical properties of 26 mm cores from eruptive Phases 1, 3, 4, and 5: **(a)** connected porosity evolution and **(b)** gas permeability evolution throughout the eruption; **(c)** permeability as a function of porosity for all samples. Results show that porosity is consistent between Phases 1, 3, 4, and increases in Phase 5, whereas permeability systematically decreases from Phase 1 through to Phase 4, and then increases in Phase 5. Phases 1 and 5 follow a near-continuous trend on the porosity-permeability plot, while Phases 3 and 4 plot distinctly, suggesting contrasting pore morphology and connectivity.

Tight clustering is to be expected within one rock sample (e.g. *Schaefer et al.*, 2015), but permeability also remains very consistent between two different blocks attributed to the same eruptive phase (Figures 4.6b, c), even with increased confining pressure (Supplementary Figure C.4). The difference between the permeabilities of samples from each phase is therefore determined to be greater than the variation expected from natural heterogeneity within one block. In the tested samples there is a systematic decrease in permeability from Phases 1 to 4 (Table 4.3), and Phase 5 samples show the maximum permeability across the erupted materials tested, with an average permeability for the samples from Phase 5 of 9.2×10^{-12} m^2 (although some were too permeable to obtain a value). The decrease in permeability across Phases 1 to 4 occurs despite a relatively

constant connected porosity (Figure 4.6c), although the proportion of isolated pores increases across the same range (Supplementary Table C.1).

4.4.4 Uniaxial compressive strength

To maximize data gathering from a limited sample set, we performed UCS testing on one prepared 26 mm sample from each block (Figure 4.7a), resulting in 7 UCS values. Where there are two individual blocks from one phase, we find very similar results between the two blocks (Figure 4.7b), and we confirm the phase repeatability using cyclic loading tests to non-destructively measure Young's modulus for each sample (see Section 4.4.5).

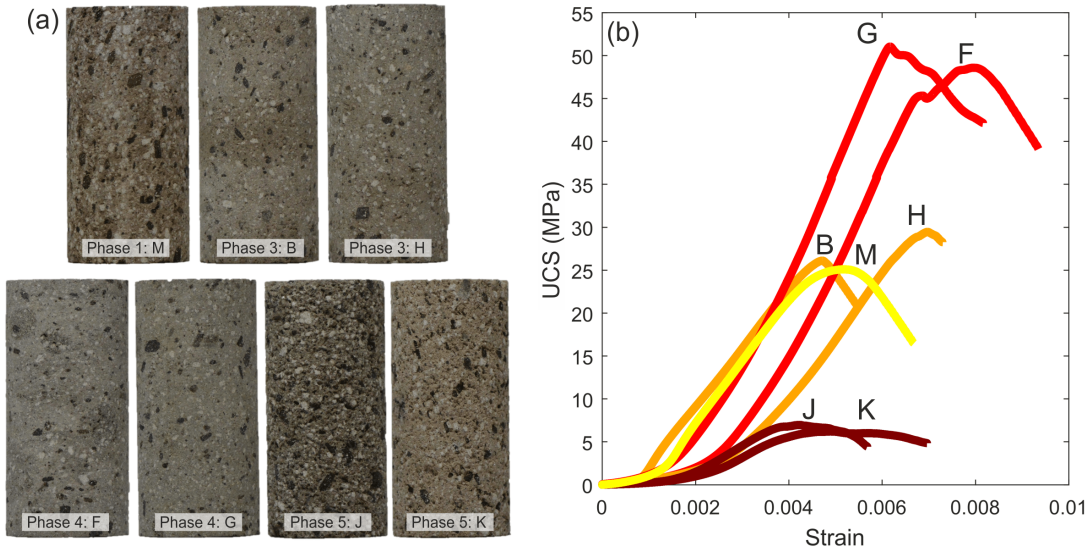

Figure 4.7: **(a)** Photos of one core from each block tested (M, B, H, F, G, J, K), with the corresponding phase marked; **(b)** UCS results from tests carried out at a constant strain rate of 10^{-5} s^{-1} on one core from Phase 1, and two cores from Phases 3, 4 and 5. UCS curves labelled with the block from which each rock was cored. Phase 5 samples show creep-like (i.e., undergoing significant strain prior to failure) behaviour due to high porosity, while the other samples display sharp failure curves.

The results from the UCS tests generally show expected behaviour, where the stress-strain curve can be broken into an initial stage of compaction of pre-existing pores and micro-fractures within the rock, an elastic loading phase, a brief period of strain hardening, and then a fracture marked by a sudden stress drop (Figure 4.7b; as described by *Scholz*, 1968; *Heap and Faulkner*, 2008). The UCS curves for Samples J and K show a more creep-like behaviour due to their high porosity (>30%). These rocks did not exhibit a sharp stress drop, but rather ongoing

compaction of pore spaces within the sample. The maximum load was recorded as the uniaxial compressive strength, and the tests were stopped when the stress showed a marked decrease (more than 10% stress drop) over time, suggesting that the rock had ruptured and was unable to bear any more load.

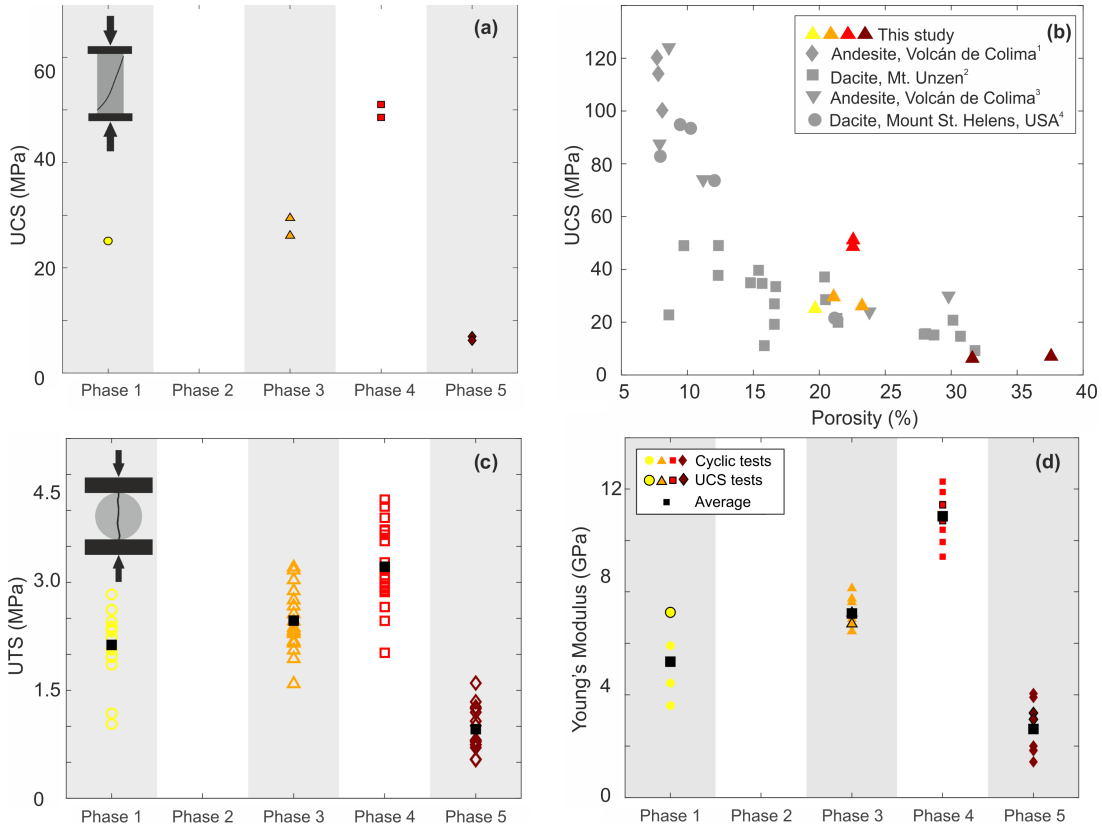

Figure 4.8: **(a)** UCS results. UCS is highest in Phase 4, and lowest in Phase 5, while Phases 1 and 3 are intermediate. **(b)** UCS as a function of porosity, compared with published datasets from other dome-building volcanoes: [1]*Heap et al.* (2018b) (diamonds); [2]*Coats et al.* (2018) (squares); [3]*Heap et al.* (2014a) (downward triangles); [4]*Kendrick et al.* (2013) (circles); **(c)** Tensile strength determined by Brazilian disk testing for samples from eruptive Phases 1, 3, 4 and 5. Each measurement is shown by the hollow markers, with mean tensile strength for each eruptive phase shown by the black squares; **(d)** Young's modulus (E) determined from both UCS and cyclic tests performed on 26 mm diameter cores and shown by phase, with averages shown for each phase (black squares). E is determined using stress/strain between 40% and 50% of the UCS strength value, from the linear portion of stress/strain curve where we assume elastic behaviour.

The results are summarized in Figure 4.8, along with all the mechanical results for each sample. Sample M (Phase 1) has a UCS of 25.1 MPa. For the remaining phases, two tests were carried out (one from each block, Figure 4.8a). The average UCS values for Phases 3, 4, and 5 are 27.8 MPa, 49.8 MPa and 6.6 MPa

respectively (raw sample data are provided in Supplementary Table C.1, with averages and standard deviations provided in Supplementary Table C.4).

The lowest UCS results (<7 MPa) are found in Samples J and K (Phase 5) and correlate to the highest porosity among the samples tested (Figure 4.8b). These samples are more friable and have more evident pore space in hand specimen (Figure 4.7a), and the pore distribution maps from QEMSCAN analysis further highlight the connectivity of the porous network (Figure 4.3). Lower sample porosities correspond to higher uniaxial compressive strengths, however for porosities between 20 and 25%, UCS values vary between 25 MPa and 50 MPa. Although the porosity of these samples is similar, there is a higher proportion of isolated pores and lower permeability in the stronger Samples F and G (Phase 4). The porosity-strength relationship identified in this study fits well with other datasets from dome-building volcanoes (Figure 4.8b).

4.4.5 Cyclic loading and Young's modulus

Similarly to the UCS results, the Young's modulus increases with decreasing porosity across the sample suite. Young's modulus increases from Phase 1 to Phase 3 to Phase 4, with a drop to the lowest values in Phase 5 samples (Figure 4.8c). A higher Young's modulus correlates to lower porosity values, and as such, higher Young's modulus values typically correspond to higher UCS values. Cyclic testing showed good repeatability of mechanical data (i.e. stress-strain curve morphology, Supplementary Figure C.5) within rock types, and to an extent within phases irrespective of sample size (26 or 37 mm diameter). Young's modulus determined from the UCS tests gives average values in Phases 1, 3, 4, and 5 of 7.2 GPa, 7.0 GPa, 11.1 GPa, and 3.2 GPa respectively. We also determined Young's modulus using the cyclic tests, which indicated a range of Young's modulus within each sample suite of less than 3 GPa, and average values for Phases 1, 3, 4, and 5 of 4.6 GPa, 7.2 GPa, 10.9 GPa, and 2.5 GPa respectively. There is good agreement between the Young's modulus values from UCS and cyclic testing, as the same portion (40-50%) of the peak stress of the loading curve was used for the analysis (Figure 4.8c; with raw data in Supplementary Table C.1, and averages and standard deviations given in Supplementary Table C.4). Increasing Young's modulus values correspond to an increasing proportion of isolated porosity and therefore to decreasing permeability (Figure 4.9b).

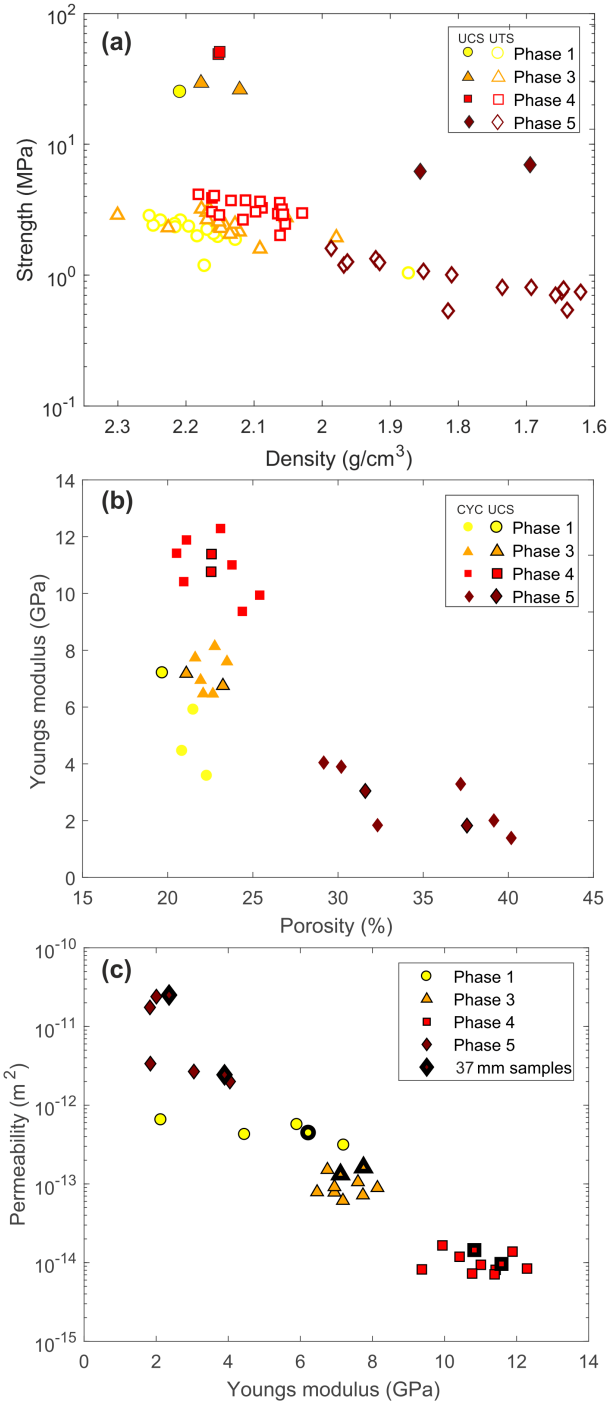

Figure 4.9: **(a)** Uniaxial tensile strength (UTS; hollow symbols) and uniaxial compressive strength (UCS; filled symbols) as a function of rock density (a proxy for porosity, see Supplementary Table C.1, Supplementary Figure C.1); **(b)** Young's modulus as a function of connected porosity, determined from UCS tests (black symbol outlines) and from cyclic tests (no symbol outline); **(c)** Permeability as a function of Young's modulus, for 26 mm samples (thin symbol outline) and 37 mm samples (thick symbol outline).

4.4.6 Tensile strength

We performed 66 Brazilian indirect tensile tests to constrain the tensile strength (UTS; Figure 4.8d) and found UTS averages of 2.13 MPa for Phase 1; 2.47 MPa for Phase 3; 3.22 MPa for Phase 4; and 0.96 MPa for Phase 5 (see averages and standard deviation for each phase in Supplementary Table C.4). The results from the Brazilian disk testing correlate well to the UCS and Young's modulus values, conforming to the trend of lower strength at lower density or higher porosities (Figures 4.8d and 4.9). The variability within each sample set is higher than for UCS (there are more tests), although each phase still has a considerably smaller range than the sample suite as a whole and there is good agreement between the different blocks within the same phase (Supplementary Table C.2).

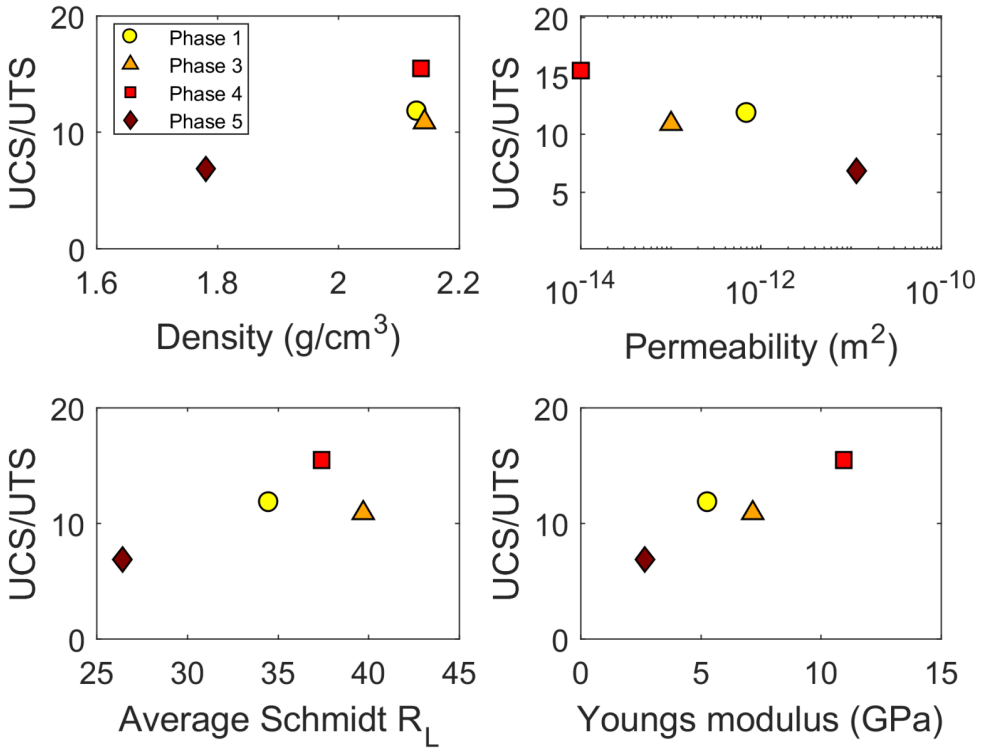

Figure 4.10: **(a)** UCS/UTS ratio as a function of density; **(b)** UCS/UTS ratio as a function of permeability; **(c)** UCS/UTS ratio as a function of average Schmidt hammer rebound value (R_L); and **(d)** UCS/UTS ratio as a function of Young's modulus. Phase averages shown in each case. A higher UCS/UTS ratio correlates to lower permeabilities, higher Schmidt hammer rebound values, and higher Young's modulus values.

4.4.7 UCS/UTS ratio

We show that in our study both compressive and tensile rock strength is inversely proportional to density (Figure 4.9a), and we consider bulk rock density here to be a proxy for total porosity (Supplementary Figure C.1). That said, for a given density the UCS/UTS ratio is highly variable (Figure 4.10a), the ratio for Phases 1, 3, 4 and 5 is 11.8, 10.9, 15.5, and 6.9 respectively. Instead, UCS/UTS ratio systematically decreases with increasing permeability (Figure 4.10b). We also compare the average Schmidt hammer rebound values for each phase to the UCS/UTS ratio, where the Schmidt hammer rebound values increase with increasing UCS/UTS ratio (Figure 4.10c). This is likely due to the sensitivity of the Schmidt hammer to the rock stiffness, as Young's modulus also correlates very well with the UCS/UTS ratio (Figure 4.10d).

4.5 Discussion

4.5.1 Co-variance of physical and mechanical properties

In this study, we have demonstrated a wide range in physical and mechanical properties of dome rock from Soufrière Hills volcano (SHV). We show how these properties vary in relation to one another, and in addition, by gathering these data from temporally-constrained samples, we are able to speculate how this could reflect the changing eruptive behaviour across this well-observed 15-year eruption. We verify the trends observed in our limited laboratory sample suite using Schmidt hammer rebound testing on a wider range of samples in the field, and find R_L values to be in broad agreement with the observed temporal trends of strength and Young's modulus. The identified links in physical and mechanical rock properties are necessary for assessing volcano dynamics, and the temporal relationships could prove important if corroborated using a wider suite of rocks.

The SHV dome rocks examined here range in porosity from 19.7% to 40.2%, with inversely-proportional permeabilities spanning the range from 10^{-15} to 10^{-11} m^2. Our corresponding densities of 1.61-2.34 g/cm^3 also agree well with the range of densities measured on 85 blocks from block-and-ash flows in 1997 and to the porosity range of 15.1-45.5% observed for a smaller subset of these 1997 lava samples (*Formenti and Druitt*, 2003). Moreover this spectrum of our samples exceeds the porosity and permeability range spanned by banded pumice samples collected from block-and-ash flow deposits at SHV (*Farquharson and*

Wadsworth, 2018). The strength of the dome rocks measured at SHV varies by almost an order of magnitude from 6.2 MPa to 51.1 MPa in compression, and 0.5 MPa to 4.1 MPa in tension, which show a non-linear decrease with increasing porosity and permeability. We demonstrate a higher UCS/UTS ratio for stronger, stiffer material, highlighting the different effect of pore connectivity on compressive and tensile strength. This is an important consideration when modelling structural dome instability, as using a constant UCS/UTS ratio in numerical models could result in overestimation of a dome's tensile strength, and therefore underestimation of the failure likelihood of the unconfined portion of lava domes. The current SHV dome at Montserrat may have cooled to an extent where viscous flow no longer dominates eruptive behavior (*Ball et al.*, 2015); as such, tests of rock properties at ambient temperatures are relevant to the modelling of ongoing stability of the volcano, but moreover, a number of studies have demonstrated that the strength of volcanic rock at elevated temperature is either comparable (*Heap et al.*, 2014a, 2018b) or higher (*Schaefer et al.*, 2015; *Coats et al.*, 2018) than at room temperature, suggesting that domes are at their weakest following cooling.

For the same sample suite, Young's modulus values range from 1.4 GPa to 12.3 GPa and correspond to higher values in less porous, denser samples (Figure 4.9b). A strong correlation is shown between Young's modulus and sample permeability (Figure 4.9c), where lower permeabilities correlate to higher stiffness values. This suggests a dependence of Young's modulus on not only porosity, but also pore connectivity, which also controls the permeability.

Mechanical data from experiments show a general trend of increasing strength (compressive and tensile) and stiffness in samples from Phase 1 to Phase 4, with a corresponding decrease in permeability (and increasing proportion of isolated pores). The samples from Phase 5 show significantly lower strength and stiffness and have both the highest porosity and permeability. Therefore porosity can be considered as a controlling factor in both strength and stiffness of volcanic rocks (as described previously for other volcanic rocks; *Heap et al.*, 2014b, 2016b; *Schaefer et al.*, 2015; *Colombier et al.*, 2017; *Marmoni et al.*, 2017; *Coats et al.*, 2018). We compare the correlation between porosity and uniaxial compressive strength in this dataset to published data from other dome-building volcanoes (Volcán de Colima, Mexico, Mount St. Helens, USA, and Mt. Unzen, Japan) and find that our samples fit well with existing data (Figure 4.8b). Although we speculate that the properties identified in this study could suggest a temporal evolution in mechanical behaviour at Soufrière Hills, we show here that examining

the mechanical properties as a function of the physical rock properties may be more appropriate.

Although cracks are present in these samples (particularly in Sample M), we note that the samples in this study do not show the pervasive micro-fractured textures that have been observed in similar andesites from Volcán de Colima (*Heap et al.*, 2014a). The QEMSCAN images highlighting porosity (Figure 4.3e-h) show that the samples with higher porosities (e.g. Sample J from Phase 5) have larger, more heterogeneously distributed pore space with a higher degree of connectivity. *Lamur et al.* (2017) showed that the addition of a macro fracture in samples with relatively high porosity (above 18%) has little impact on the resultant permeability, and as such we surmise that permeability in our sample suite is controlled by pre-existing pore connectivity, rather than pervasive fractures.

Further, we also demonstrate that pore morphology and connectivity has an important control on mechanical properties (UCS, UTS, and Young's modulus); where total porosity is similar (Phases 1, 3 & 4), lower connectivity (and thus permeability) in Phase 1, then Phase 3, and finally lowest in Phase 4, corresponds to a significant increase in compressive (7% from Phase 1 to 3 and 85% from Phase 3 to 4) and tensile (16% from Phase 1 to 3 and 30% from Phase 3 to 4) strength, and stiffness (Young's modulus, 35% from Phase 1 to 3 and 53% from Phase 3 to 4). By showing that the rocks are not heavily micro-fractured and pore connectivity is a controlling factor in mechanical behaviour, we also demonstrate that differences found between the rocks in this study are unlikely to be due to damage during transport in pyroclastic density currents, and rather represent the textural heterogeneity of the eruptive products.

In order to establish whether porosity is exerting the only control on the mechanical properties of the rocks tested here, we also examine the mineralogy of the samples. Variation in glass, silica polymorph and plagioclase content is non-systematic through time, although we do see co-variance of a number of physical and mechanical properties. For example, total crystallinity (Table 4.2) as a proportion of the solid fraction of each sample (i.e. excluding the glass and silica polymorph phase) correlates positively to the mechanical behaviour (Figure 4.11), with the lowest crystallinity (Phase 5, 62-66% crystallinity) corresponding to the lowest rock strength and Young's modulus (UTS = 1.0 MPa, UCS = 6.6 MPa, YM = 2.9 GPa), and the highest crystallinity (Phase 4, 75-81% crystallinity) corresponding to the highest rock strength and Young's modulus (UTS = 2.8 MPa, UCS = 49.9 MPa, YM = 10.7 GPa). Such relationships of strengthening

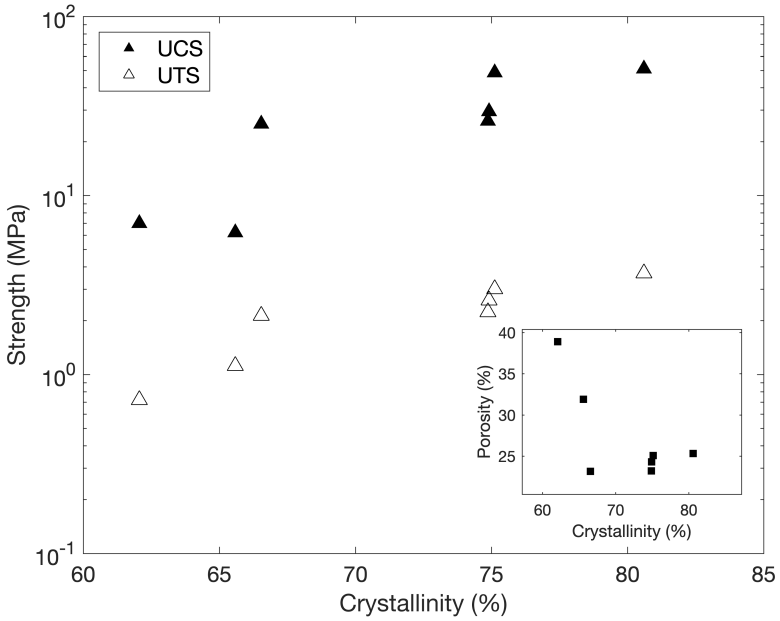

Figure 4.11: Rock strength as a function of crystallinity, where solid markers show uniaxial compressive strength (UCS) and hollow markers show tensile strength (UTS). Inset shows correlation between crystallinity and porosity.

with increasing crystallinity have been noted in partially crystalline polymers (e.g. *Brady*, 1976). The crystallinity-strength relationship at a dome-building volcano was discussed by *Bain et al.* (2018), where low crystallinity samples were associated with low repose times between volcanic explosions, and therefore low residency times within the upper conduit and dome. We speculate that a longer residence time at elevated temperature within the volcano leads to increased densification of material as well as increased crystallization. This could have particular importance when considering the likely mechanical behaviour of dome rock.

The relationship between crystal fraction and strength was modelled up to 40% crystallinity by *Heap et al.* (2016b), who found that UCS decreased with increasing crystal content up to 15%; our system differs in that it exceeds the maximum loose packing as the groundmass has crystallized and interlocked in-situ, and thus is contrasting to the simplified two-phase system modelled in *Heap et al.* (2016b). As observed by previous work (e.g *Zorn et al.*, 2018), porosity and crystallinity are inversely proportional (Figure 4.11); the more porous samples have lower crystallinity and are more glassy than the denser samples. Thus despite the correlation between crystallinity and strength, it is difficult to determine if there is an independent effect of crystallinity with the

sample suite tested, as porosity is generally believed to impart the greatest control on strength (e.g *Kendrick et al.*, 2013; *Heap et al.*, 2014a, 2016b; *Farquharson et al.*, 2015; *Schaefer et al.*, 2015; *Coats et al.*, 2018).

We also use Schmidt hammer testing to support the laboratory results. The Schmidt hammer is a well-known tool for field testing to infer both UCS and Young's modulus (*Katz et al.*, 2000; *Ylmaz and Sendr*, 2002; *Dinçer et al.*, 2004; *Yagiz*, 2009). We do not directly correlate our Schmidt hammer results to UCS values here due to the variability in published correlations, however we see that the raw data from the Schmidt hammer index testing shows a similar trend to UCS results (Figures 4.10b, c). This supports our UCS data by providing analysis of a larger sample set, although the Schmidt hammer results differ from the UCS results by indicating a more similar strength between the samples from Phase 3 and Phase 4. The slight discrepancy between the Schmidt hammer data and the experimental results likely arises from the sensitivity of the Schmidt hammer to sample porosity (*Yasar and Erdogan*, 2004; *Aydin and Basu*, 2005; *Yagiz*, 2009). As the rock porosities appear to have very similar ranges in Phases 1, 3, and 4, we suggest the Schmidt hammer is insensitive to the small differences in pore connectivity, as evidenced by the permeability differences which seem to correlate to tensile and compressive strength as well as stiffness observed in the mechanical tests. The Schmidt hammer does however show clearly that the samples from Phase 5 are the weakest material tested.

4.5.2 Links to eruptive activity

We find a slight increase in strength from Phase 1 to Phase 3 (Figures 4.8a, c, d), as well as slightly lower permeabilities than those from Phase 1 and a significant increase in glass recrystallization to silica polymorphs which can serve to block pores by vapor phase deposition (*Horwell et al.*, 2013) and decrease permeability. The lack of explosions during Phase 3 (*Wadge et al.*, 2014) and enhanced residence time in the lava dome as a result could explain these textural differences to the earlier phases of the eruption. Phase 3 had one major collapse on the 20 May 2006 (from which the Phase 3 samples in this study are collected) compared to several collapses in the earlier phases. The average extrusion rates are however very similar in Phase 1 and Phase 3, at 4.5 m^3s^{-1} and 5.3 m^3s^{-1} respectively. This could explain the similar porosities between the samples from each phase (e.g. *Collombet*, 2009), and therefore the similarities in strength (e.g. *Coats et al.*, 2018). It is important to note that the extrusion rates within each phase were

highly variable, as shown in Figure 4.2, and therefore the rock properties defined in the study are likely to be determined by short-term emplacement conditions, rather than representative of the whole eruptive phase.

Unlike the other eruptive phases at Soufrière Hills, Phase 4 occurred in 2 short episodes from 8 August 2008 until 8 October 2008, and then from 2 December 2008 until 3 January 2009 (*Stinton et al.*, 2017). The samples from Phase 4 are collected from the explosion on 29 July 2008 and are the strongest of the erupted products tested here. The other rocks in this study are samples from events that occurred during periods of active extrusion and so are likely to have been stored in the dome for shorter time periods, whereas the Phase 4 products follow a period of quiescence and are likely to have had longer residence times within the lava dome, or have been excavated material from the conduit. Previous work (*Horwell et al.*, 2013) has shown that recrystallization that occurs after emplacement of material within the dome is likely to increase the fraction of silica polymorphs (likely to be cristobalite) at the expense of glass. *Horwell et al.* (2013) suggested that by additionally filling pore space with recrystallized silica polymorphs, rock strength may be increased; although it is difficult to distinguish between all the contributing variables, recrystallization of interstitial glass to silica polymorphs (Table 4.2) is highest in the strongest samples, present in Phases 3 and 4.

It is clear here that understanding the events preceding each collapse (Table 4.1) is an important factor in determining a rock's history, and therefore its likely mechanical properties. For example, although the samples from Phases 4 and 5 in this study are both collected from deposits that are associated with explosions, they exhibit very different mechanical properties. The 29 July 2008 event marked the beginning of Phase 4a and was preceded by no extrusion (Table 4.1); therefore, the material from this event is likely to be mechanically distinct from material that collapses during extrusion. This is important to feed into future numerical models, as it suggests increased mechanical strength from alteration following increased repose time.

Phase 5 at SHV was also short-lived compared to Phases 1 and 3, but was punctuated by several vulcanian explosions and did not contain the frequent small scale collapses seen in Phase 1 (*Stinton et al.*, 2014a). The time-averaged extrusion rate during Phase 5 is estimated at 7 m^3s^{-1}. The samples from Phase 5 have larger phenocrysts than samples from the previous two phases (Figure 4.3), suggesting a longer crystallisation time of magma prior to the final ascent and eruption. This could be due to the absence of wholesale dome collapse after May 2006 (Figure 4.2), that plugged the upper conduit, preventing magma extrusion.

We also suggest that the high permeability of the Phase 5 samples contributes to efficient outgassing of the dome, leading to relatively degassed magma; as previously observed by *Cole et al.* (2014).

All dome material emplaced from the beginning of the eruption in 1995 until May 2006 was removed by repeated collapse events (*Wadge et al.*, 2014). Extrusion resumed almost immediately after the May 2006 collapse, and dome growth in Phases 4 and 5 occurred primarily on top of the remaining Phase 3 dome. The February 2010 collapse likely removed most of the material emplaced in Phase 4, suggesting the dome that still remains on Montserrat mostly comprises material emplaced in Phases 3 and 5. We suggest therefore that future modelling efforts of the current dome include rock heterogeneity (both temporal, and spatial if available), as this could significantly influence overall structural stability (e.g. *Schaefer et al.*, 2013).

4.6 Conclusions

We present here a study of the physical and mechanical properties of a suite of temporally-constrained rocks from Soufrière Hills volcano (SHV). We clearly demonstrate the variability and co-variance of physical and mechanical rock properties (porosity, permeability, UCS, UTS, Young's modulus, and Schmidt hardness) across a broad spectrum volcanic rocks, representative of the extruded products of SHV (e.g. *Formenti and Druitt*, 2003). These parameters vary extensively for the materials tested. Across all phases, we observe a range in connected porosity of 19.7-40.2%, permeability of 10^{-15} to 10^{-11} m^2, tensile strength of 0.53-4.15 MPa, compressive strength of 6.2-51.1 MPa, Young's modulus of 1.39-12.29 GPa, and Schmidt hammer rebound values of 12.5-47.9. We find that while porosity has a dominant control on strength and Young's modulus, higher pore connectivity (at a given porosity) also weakens material, decreases the UCS/UTS ratio and enhances permeability by up to two orders of magnitude. In addition, we show how more crystalline samples have lower porosity, and have the lowest proportion of pristine glass. Both higher total crystallinity, and higher recrystallization of glass into silica polymorphs correlate with higher strength and Young's modulus in our sample suite, though these also correlate positively to the control porosity has on strength and thus crystallinity is judged to have a lesser influence.

The temporal evolution, from the samples tested in the laboratory and field

in this study, indicates an increase in rock strength from Phase 1 to Phase 3 to Phase 4, and then shows a large decrease in strength in samples from Phase 5 of the eruption, with all samples following the same physical and mechanical relationships as defined above. We acknowledge that the samples tested in this study only provide us with a snapshot during the phases of a complicated eruptive history at SHV, and that more samples would be required from varied locations to test if this trend is truly observed for the eruption as a whole. However, our dataset demonstrates a large range in mechanical properties (strength, stiffness) that can be linked to the rock's texture (porosity, crystallinity) and permeability, and we use field Schmidt hammer testing to support the laboratory investigation, finding good correlation.

We conclude that even at a volcano with a narrow range of eruptive material and chemical composition, taking single values for mechanical parameters is insufficient for the purpose of numerical modelling. Consequently, the inclusion of temporal and spatial heterogeneity should be strongly considered in future structural stability models.

Acknowledgements

CEH was funded through a NERC studentship as part of the Leeds York Spheres Doctoral Training Partnership (DTP) (grant number NE/L002574/1). JN acknowledges the Centre for the Observation and Modelling of Earthquakes, Volcanoes and Tectonics (COMET). YL acknowledges financial support from the European Research Council Starting Grant on Strain Localisation in Magma (SLiM, no. 306488). We are in debt to the Montserrat Volcano Observatory and its staff for assistance during the field campaign, namely Paddy Smith, Karen Pascal and Rod Stewart. CEH thanks Ben Todd, Eduardo Morgado, and Ruth Amey for software assistance. We would like to thank FEI Company of Hilsboro Oregon, and Prof. Richard H. Worden of the University of Liverpool, for the very significant support with Qemscan® WellSite SEM hardware and iDiscover® software, allowing us to acquire extensive high quality Qemscan® datasets.

Bibliography

Andrade, S. D., and B. van Wyk de Vries (2010), Structural analysis of the early stages of catastrophic stratovolcano flank-collapse using analogue models,

Bulletin of Volcanology, *72*(7), 771–789, doi:10.1007/s00445-010-0363-x.

Apuani, T., C. Corazzato, A. Cancelli, and A. Tibaldi (2005), Stability of a collapsing volcano (Stromboli, Italy): Limit equilibrium analysis and numerical modelling, *Journal of Volcanology and Geothermal Research*, *144*(1-4 SPEC. ISS.), 191–210, doi:10.1016/j.jvolgeores.2004.11.028.

Aydin, A., and A. Basu (2005), The Schmidt hammer in rock material characterization, *Engineering Geology*, *81*(1), 1–14, doi:10.1016/j.enggeo.2005.06.006.

Bain, A. A., E. S. Calder, J. A. Cortés, G. P. Cortés, and S. Loughlin (2018), Textural and geochemical constraints on andesitic plug emplacement prior to the 2004-2010 vulcanian explosions at Galeras volcano, Colombia, *Bulletin of Volcanology*, *81*(1), doi:10.1007/s00445-018-1260-y.

Ball, J., P. Stauffer, E. Calder, and G. Valentine (2015), The hydrothermal alteration of cooling lava domes, *Bulletin of Volcanology*, *77*(12), 102, doi:10.1007/s00445-015-0986-z.

Barclay, J., R. A. Herd, B. R. Edwards, T. Christopher, E. J. Kiddle, M. Plail, and A. Donovan (2010), Caught in the act: Implications for the increasing abundance of mafic enclaves during the recent eruptive episodes of the Soufrière Hills Volcano, Montserrat, *Geophysical Research Letters*, *37*(19), n/a–n/a, doi:10.1029/2010GL042509.

Basu, A., and A. Aydin (2004), A method for normalization of Schmidt hammer rebound values, *International Journal of Rock Mechanics and Mining Sciences*, *41*(7), 1211–1214, doi:10.1016/j.ijrmms.2004.05.001.

Borselli, L., L. Capra, D. Sarocchi, and S. De la Cruz-Reyna (2011), Flank collapse scenarios at Volcán de Colima, Mexico: A relative instability analysis, *Journal of Volcanology and Geothermal Research*, *208*(1-2), 51–65, doi:10.1016/j.jvolgeores.2011.08.004.

Brady, D. G. (1976), The crystallinity of poly(phenylene sulfide) and its effect on polymer properties, *Journal of Applied Polymer Science*, *20*(9), 2541–2551, doi:10.1002/app.1976.070200921.

Bubeck, A., R. J. Walker, D. Healy, M. Dobbs, and D. A. Holwell (2017), Pore geometry as a control on rock strength, *Earth and Planetary Science Letters*, *457*, 38–48, doi:10.1016/j.epsl.2016.09.050.

Calder, E., R. Luckett, R. Sparks, and B. Voight (2002), Mechanisms of lava dome instability and generation of rockfalls and pyroclastic flows at Soufrière Hills Volcano, Montserrat, *Geological Society, London, Memoirs*, *21*, 173–190, doi:10.1144/GSL.MEM.2002.021.01.08.

Cecchi, E., B. van Wyk de Vries, and J. M. Lavest (2004), Flank spreading and collapse of weak-cored volcanoes, *Bulletin of Volcanology*, *67*(1), 72–91, doi:10.1007/s00445-004-0369-3.

Christopher, T. E., M. C. Humphreys, J. Barclay, K. Genareau, S. M. De Angelis, M. Plail, and A. Donovan (2014), Petrological and geochemical variation during the Soufrière Hills eruption, 1995 to 2010, *Geological Society, London, Memoirs*, *39*(1), 317–342, doi:10.1144/M39.17.

Coats, R., J. E. Kendrick, P. A. Wallace, T. Miwa, A. J. Hornby, J. D. Ashworth, T. Matsushima, and Y. Lavallée (2018), Failure criteria for porous dome rocks and lavas: A study of Mt. Unzen, Japan, *Solid Earth*, *9*(6), 1299–1328, doi:10.5194/se-9-1299-2018.

Cole, P. D., E. S. Calder, R. Sparks, A. Clarke, T. H. Druitt, S. Young, R. Herd, C. L. Harford, and G. Norton (2002), Deposits from dome-collapse and fountain-collapse pyroclastic flows at Soufrière Hills Volcano, Montserrat, *Geological Society, London, Memoirs*, *21*, 231–262.

Cole, P. D., P. Smith, J.-C. Komorowski, F. Alfano, C. Bonadonna, A. Stinton, T. Christopher, H. M. Odbert, and S. Loughlin (2014), Chapter 4 Ash venting occurring both prior to and during lava extrusion at Soufrière Hills Volcano, Montserrat, from 2005 to 2010, *Geological Society, London, Memoirs*, *39*(1), 71–92, doi:10.1144/M39.4.

Collombet, M. (2009), Two-dimensional gas loss for silicic magma flows: Toward more realistic numerical models, *Geophysical Journal International*, *177*(1), 309–318, doi:10.1111/j.1365-246X.2008.04086.x.

Colombier, M., F. B. Wadsworth, L. Gurioli, B. Scheu, U. Kueppers, A. Di Muro, and D. B. Dingwell (2017), The evolution of pore connectivity in volcanic rocks, *Earth and Planetary Science Letters*, *462*, 99–109, doi:10.1016/j.epsl.2017.01.011.

Das, S. (2015), Supershear earthquake ruptures - theory, methods, laboratory experiments and fault superhighways: an update, in *Perspectives on*

European Earthquake Engineering and Seismology. Geotechnical, Geological and Earthquake Engineering., vol. 39, edited by A. Ansal, pp. 1–20, Springer, Cham, doi:10.1007/978-3-319-07118-3.

David, E. C., N. Brantut, A. Schubnel, and R. W. Zimmerman (2012), Sliding crack model for nonlinearity and hysteresis in the uniaxial stress-strain curve of rock, *International Journal of Rock Mechanics and Mining Sciences*, *52*, 9–17, doi:10.1016/j.ijrmms.2012.02.001.

Deere, D. U., and R. P. Miller (1966), Engineering classification and index properties for intact rock, *Tech. rep.*, Air Force Weapons Laboratory, Kirtland Air Force Base, New Mexico.

Del Potro, R., and M. Hürlimann (2009), A comparison of different indirect techniques to evaluate volcanic intact rock strength, *Rock Mechanics and Rock Engineering*, *42*(6), 931–938, doi:10.1007/s00603-008-0001-5.

Dinçer, I., A. Acar, I. Çobanolu, and Y. Uras (2004), Correlation between Schmidt hardness, uniaxial compressive strength and Young's modulus for andesites, basalts and tuffs, *Bulletin of Engineering Geology and the Environment*, *63*(2), 141–148, doi:10.1007/s10064-004-0230-0.

Dondin, F. J., M. J. Heap, R. E. Robertson, J. F. Dorville, and S. Carey (2017), Flank instability assessment at Kick-'em-Jenny submarine volcano (Grenada, Lesser Antilles): a multidisciplinary approach using experiments and modeling, *Bulletin of Volcanology*, *79*(1), doi:10.1007/s00445-016-1090-8.

Ericson, K. (2004), Geomorphological surfaces of different age and origin in granite landscapes: An evaluation of the Schmidt hammer test, *Earth Surface Processes and Landforms*, *29*(4), 495–509, doi:10.1002/esp.1048.

Farquharson, J., M. J. Heap, N. R. Varley, P. Baud, and T. Reuschlé (2015), Permeability and porosity relationships of edifice-forming andesites: A combined field and laboratory study, *Journal of Volcanology and Geothermal Research*, *297*, 52–68, doi:10.1016/j.jvolgeores.2015.03.016.

Farquharson, J. I., and F. B. Wadsworth (2018), Upscaling permeability in anisotropic volcanic systems, *Journal of Volcanology and Geothermal Research*, *364*, 35–47, doi:10.1016/j.jvolgeores.2018.09.002.

Farquharson, J. I., M. J. Heap, Y. Lavallée, N. R. Varley, and P. Baud (2016), Evidence for the development of permeability anisotropy in lava domes and volcanic conduits, *Journal of Volcanology and Geothermal Research*, *323*, 163–185, doi:10.1016/j.jvolgeores.2016.05.007.

Formenti, Y., and T. H. Druitt (2003), Vesicle connectivity in pyroclasts and implications for the fluidisation of fountain-collapse pyroclastic flows, Montserrat (West Indies), *Earth and Planetary Science Letters*, *214*(3-4), 561–574, doi:10.1016/S0012-821X(03)00386-8.

Goudie, A. S. (2013), The Schmidt Hammer and Related Devices in Geomorphological Research, *Treatise on Geomorphology*, *14*, 338–345, doi:10.1016/B978-0-12-374739-6.00398-5.

Hale, A., E. Calder, S. Loughlin, G. Wadge, and G. Ryan (2009a), Modelling the lava dome extruded at Soufrière Hills Volcano, Montserrat, August 2005-May 2006. Part I: Dome shape and internal structure, *Journal of Volcanology and Geothermal Research*, *187*(1-2), 69–84, doi:10.1016/j.jvolgeores.2009.08.014.

Hale, A., E. Calder, S. Loughlin, G. Wadge, and G. Ryan (2009b), Modelling the lava dome extruded at Soufrière Hills Volcano, Montserrat, August 2005-May 2006. Part II: Rockfall activity and talus deformation, *Journal of Volcanology and Geothermal Research*, *187*(1-2), 69–84, doi:10.1016/j.jvolgeores.2009.08.014.

Harnett, C. E., M. E. Thomas, M. D. Purvance, and J. Neuberg (2018), Using a discrete element approach to model lava dome emplacement and collapse, *Journal of Volcanology and Geothermal Research*, doi:10.1016/j.jvolgeores.2018.06.017.

Heap, M. J., and D. R. Faulkner (2008), Quantifying the evolution of static elastic properties as crystalline rock approaches failure, *International Journal of Rock Mechanics and Mining Sciences*, *45*(4), 564–573, doi:10.1016/j.ijrmms.2007.07.018.

Heap, M. J., Y. Lavallée, L. Petrakova, P. Baud, T. Reuschlé, N. R. Varley, and D. B. Dingwell (2014a), Microstructural controls on the physical and mechanical properties of edifice-forming andesites at Volcán de Colima, Mexico, *Journal of Geophysical Research: Solid Earth*, *119*(4), 2925–2963, doi:10.1002/2013JB010521.

Heap, M. J., T. Xu, and C. feng Chen (2014b), The influence of porosity and vesicle size on the brittle strength of volcanic rocks and magma, *Bulletin of Volcanology*, *76*(9), 1–15, doi:10.1007/s00445-014-0856-0.

Heap, M. J., J. I. Farquharson, P. Baud, Y. Lavallée, and T. Reuschlé (2015), Fracture and compaction of andesite in a volcanic edifice, *Bulletin of Volcanology*, *77*(6), doi:10.1007/s00445-015-0938-7.

Heap, M. J., J. Russell, and L. Kennedy (2016a), Mechanical behaviour of dacite from Mount St. Helens (USA): A link between porosity and lava dome extrusion mechanism (dome or spine)?, *Journal of Volcanology and Geothermal Research*, *328*, 159–177.

Heap, M. J., F. B. Wadsworth, T. Xu, C. feng Chen, and C. Tang (2016b), The strength of heterogeneous volcanic rocks: A 2D approximation, *Journal of Volcanology and Geothermal Research*, *319*, 1–11, doi:10.1016/j.jvolgeores.2016.03.013.

Heap, M. J., T. Reuschlé, J. I. Farquharson, and P. Baud (2018a), Permeability of volcanic rocks to gas and water, *Journal of Volcanology and Geothermal Research*, *354*, 29–38, doi:10.1016/j.jvolgeores.2018.02.002.

Heap, M. J., R. Coats, C. feng Chen, N. Varley, Y. Lavallée, J. Kendrick, T. Xu, and T. Reuschlé (2018b), Thermal resilience of microcracked andesitic dome rocks, *Journal of Volcanology and Geothermal Research*, *367*, 20–30, doi:10.1016/j.jvolgeores.2018.10.021.

Heap, M. J., J. I. Farquharson, A. R. Kushnir, Y. Lavallée, P. Baud, H. A. Gilg, and T. Reuschlé (2018c), The influence of water on the strength of Neapolitan Yellow Tuff, the most widely used building stone in Naples (Italy), *Bulletin of Volcanology*, *80*(6), doi:10.1007/s00445-018-1225-1.

Herd, R., M. Edmonds, and V. Bass (2005), Catastrophic lava dome failure at Soufrière Hills Volcano, Montserrat, 12-13 July 2003, *Journal of Volcanology and Geothermal Research*, *148*(3-4), 234–252, doi:10.1016/j.jvolgeores.2005.05.003.

Horwell, C. J., B. J. Williamson, E. W. Llewellin, D. E. Damby, and J. S. Le Blond (2013), The nature and formation of cristobalite at the Soufrière Hills volcano, Montserrat: Implications for the petrology and stability of silicic lava domes, *Bulletin of Volcanology*, *75*(3), 1–19, doi:10.1007/s00445-013-0696-3.

Humphreys, M. C., M. Edmonds, T. Christopher, and V. Hards (2010), Magma hybridisation and diffusive exchange recorded in heterogeneous glasses from Soufrière Hills Volcano, Montserrat, *Geophysical Research Letters*, *37*(4), doi:10.1029/2009GL041926.

Husain, T., D. Elsworth, B. Voight, G. Mattioli, and P. Jansma (2014), Influence of extrusion rate and magma rheology on the growth of lava domes: Insights from particle-dynamics modeling, *Journal of Volcanology and Geothermal Research*, *285*, 110–117, doi:10.1016/j.jvolgeores.2014.08.013.

Husain, T., D. Elsworth, B. Voight, G. Mattioli, and P. Jansma (2018), Influence of conduit flow mechanics on magma rheology and the growth style of lava domes, *Geophysical Journal International*, *213*(3), 1768–1784, doi:10.1093/gji/ggy073.

Jaeger, J., N. Cook, and R. Zimmerman (2009), *Fundamentals of Rock Mechanics*, John Wiley & Sons.

Katz, O., Z. Reches, and J.-C. Roegiers (2000), Evaluation of mechanical rock properties using a Schmidt Hammer, *International Journal of Rock Mechanics and Mining Sciences*, *37*, 723–728.

Kendrick, J. E., R. Smith, P. Sammonds, P. G. Meredith, M. Dainty, and J. S. Pallister (2013), The influence of thermal and cyclic stressing on the strength of rocks from Mount St. Helens, Washington, *Bulletin of Volcanology*, *75*(7), 1–12, doi:10.1007/s00445-013-0728-z.

Kendrick, J. E., Y. Lavallée, N. R. Varley, F. B. Wadsworth, O. D. Lamb, and J. Vasseur (2016), Blowing Off Steam: Tuffisite Formation As a Regulator for Lava Dome Eruptions, *Frontiers in Earth Science*, *4*(April), 1–15, doi:10.3389/feart.2016.00041.

Kilburn, C. R. J. (2018), Forecasting Volcanic Eruptions: Beyond the Failure Forecast Method, *Frontiers in Earth Science*, *6*(September), 1–15, doi:10.3389/feart.2018.00133.

Komorowski, J., Y. Legendre, T. Christopher, M. Bernstein, R. Stewart, E. Joseph, N. Fournier, L. Chardot, A. Finizola, G. Wadge, R. Syers, C. Williams, and V. Bass (2010), Insights into processes and deposits of hazardous vulcanian explosions at Soufrière Hills Volcano during 2008 and

2009 (Montserrat, West Indies), *Geophysical Research Letters*, *37*(11), 1–6, doi:10.1029/2010GL042558.

Kushnir, A. R., C. Martel, J. L. Bourdier, M. J. Heap, T. Reuschlé, S. Erdmann, J. C. Komorowski, and N. Cholik (2016), Probing permeability and microstructure: Unravelling the role of a low-permeability dome on the explosivity of Merapi (Indonesia), *Journal of Volcanology and Geothermal Research*, *316*, 56–71, doi:10.1016/j.jvolgeores.2016.02.012.

Lamur, A., J. E. Kendrick, G. H. Eggertsson, R. J. Wall, J. D. Ashworth, and Y. Lavallée (2017), The permeability of fractured rocks in pressurised volcanic and geothermal systems, *Scientific Reports*, *7*(1), 1–9, doi:10.1038/s41598-017-05460-4.

Lavallée, Y., K. U. Hess, B. Cordonnier, and D. B. Dingwell (2007), Non-Newtonian rheological law for highly crystalline dome lavas, *Geology*, *35*(9), 843–846, doi:10.1130/G23594A.1.

Lavallée, Y., P. G. Meredith, D. B. Dingwell, K. U. Hess, J. Wassermann, B. Cordonnier, A. Gerik, and J. H. Kruhl (2008), Seismogenic lavas and explosive eruption forecasting, *Nature*, *453*(7194), 507–510, doi:10.1038/nature06980.

Lavallée, Y., P. M. Benson, M. J. Heap, K. U. Hess, A. Flaws, B. Schillinger, P. G. Meredith, and D. B. Dingwell (2013), Reconstructing magma failure and the degassing network of domebuilding eruptions, *Geology*, *41*(4), 515–518, doi:10.1130/G33948.1.

Lavallée, Y., M. Heap, U. Kueppers, J. E. Kendrick, and D. B. Dingwell (2019), The fragility of Volcan de Colima - a material constraint, in *Volcan de Colima - Managing the Threat*, edited by N. R. Varley and J. Komorowski, springer v ed., Berlin.

Le Friant, A., G. Boudon, J. Komorowski, P. Heinrich, and M. Semet (2006), Potential Flank-Collapse of Soufrière Volcano, Guadeloupe, Lesser Antilles? Numerical Simulation and Hazards, *Natural Hazards*, *39*, 381–393, doi:10.1007/s11069-005-6128-8.

Loughlin, S., E. Calder, A. Clarke, P. Cole, R. Luckett, M. Mangan, D. Pyle, R. Sparks, B. Voight, and R. Watts (2002), Pyroclastic flows and surges

generated by the 25 June 1997 dome collapse, Soufrière Hills Volcano, Montserrat, *Geological Society, London, Memoirs*, *21*(1), 191–209, doi:10.1144/GSL.MEM.2002.021.01.09.

Loughlin, S., R. Luckett, G. Ryan, T. Christopher, V. Hards, S. De Angelis, L. Jones, and M. Strutt (2010), An overview of lava dome evolution, dome collapse and cyclicity at Soufrière Hills Volcano, Montserrat, 2005-2007, *Geophysical Research Letters*, *37*, doi:10.1029/2010GL042547.

Marmoni, G. M., S. Martino, M. J. Heap, and T. Reuschlé (2017), Multiphysics Laboratory Tests for Modelling Gravity-driven Instabilities at Slope Scale, *Procedia Engineering*, *191*, 142–149, doi:10.1016/j.proeng.2017.05.165.

Morgan, J. K., and P. J. McGovern (2005a), Discrete element simulations of gravitational volcanic deformation: 1. Deformation structures and geometries, *Journal of Geophysical Research B: Solid Earth*, *110*(5), 1–22, doi:10.1029/2004JB003252.

Morgan, J. K., and P. J. McGovern (2005b), Discrete element simulations of gravitational volcanic deformation: 2. Mechanical analysis, *Journal of Geophysical Research B: Solid Earth*, *110*(5), 1–13, doi:10.1029/2004JB003253.

Mueller, S., O. Melnik, O. Spieler, B. Scheu, and D. B. Dingwell (2005), Permeability and degassing of dome lavas undergoing rapid decompression: An experimental determination, *Bulletin of Volcanology*, *67*(6), 526–538, doi:10.1007/s00445-004-0392-4.

Nakada, S., and Y. Motomura (1999), Petrology of the 1991-1995 eruption at Unzen: effusion pulsation and groundmass crystallization, *Journal of Volcanology and Geothermal Research*, *89*, 173–196.

Nihei, K. T., L. B. Hilbert, N. G. Cook, S. Nakagawa, and L. R. Myer (2000), Frictional effects on the volumetric strain of sandstone, *International Journal of Rock Mechanics and Mining Sciences*, *37*(1-2), 121–132, doi:10.1016/S1365-1609(99)00098-2.

Nolesini, T., F. Di Traglia, C. Del Ventisette, S. Moretti, and N. Casagli (2013), Deformations and slope instability on Stromboli volcano: Integration of GBInSAR data and analog modeling, *Geomorphology*, *180-181*, 242–254, doi:10.1016/j.geomorph.2012.10.014.

Paterson, M. S., and T.-f. Wong (2005), *Experimental rock deformation - the brittle field*, second edi ed., Springer, New York.

Perras, M. A., and M. S. Diederichs (2014), A Review of the Tensile Strength of Rock: Concepts and Testing, *Geotechnical and Geological Engineering*, *32*(2), 525–546, doi:10.1007/s10706-014-9732-0.

Pola, A., G. B. Crosta, N. Fusi, and R. Castellanza (2014), General characterization of the mechanical behaviour of different volcanic rocks with respect to alteration, *Engineering Geology*, *169*, 1–13, doi:10.1016/j.enggeo.2013.11.011.

Robertson, R., K. Babal, V. Bass, T. Christopher, L. Chardot, M. Fergus, N. Fournier, M. Higgins, E. Joseph, J. Komorowski, H. Odbert, R. Simpson, P. Smith, R. Stewart, J. Stone, R. Syers, B. Taisne, and P. Williams (2009), Report for the Scientific Advisory Committee on Montserrat Volcanic Activity, Prepared for SAC13: 7-9 September, 2009, *Tech. rep.*, Montserat Volcano Observatory.

Schaefer, L. N., T. Oommen, C. Corazzato, A. Tibaldi, R. Escobar-Wolf, and W. I. Rose (2013), An integrated field-numerical approach to assess slope stability hazards at volcanoes: The example of Pacaya, Guatemala, *Bulletin of Volcanology*, *75*(6), 1–18, doi:10.1007/s00445-013-0720-7.

Schaefer, L. N., J. E. Kendrick, T. Oommen, Y. Lavallée, and G. Chigna (2015), Geomechanical rock properties of a basaltic volcano, *Frontiers in Earth Science*, *3*(June), 1–15, doi:10.3389/feart.2015.00029.

Scholz, C. H. (1968), Microfracturing and the inelastic deformation of rock in compression, *Journal of Geophysical Research*, *73*(4), 1417–1432, doi:10.1029/JB073i004p01417.

Simmons, J., D. Elsworth, and B. Voight (2005), Classification and idealized limit-equilibrium analyses of dome collapses at Soufrière Hills volcano, Montserrat, during growth of the first lava dome: November 1995-March 1998, *Journal of Volcanology and Geothermal Research*, *139*(3-4), 241–258, doi:10.1016/j.jvolgeores.2004.08.009.

Siratovich, P. A., M. J. Heap, M. C. Villenueve, J. W. Cole, and T. Reuschlé (2014), Physical property relationships of the Rotokawa Andesite, a significant

geothermal reservoir rock in the Taupo Volcanic Zone, New Zealand, *Geothermal Energy*, *2*(10), doi:10.1186/s40517-014-0010-4.

Smith, R., P. R. Sammonds, and C. R. J. Kilburn (2009), Fracturing of volcanic systems: Experimental insights into pre-eruptive conditions, *Earth and Planetary Science Letters*, *280*(1-4), 211–219, doi:10.1016/j.epsl.2009.01.032.

Smith, R., P. R. Sammonds, H. Tuffen, and P. G. Meredith (2011), Evolution of the mechanics of the 2004-2008 Mt. St. Helens lava dome with time and temperature, *Earth and Planetary Science Letters*, *307*(1-2), 191–200, doi:10.1016/j.epsl.2011.04.044.

Stinton, A., P. Cole, H. Odbert, T. Christopher, G. Avard, and M. Bernstein (2014a), Dome growth and valley fill during Phase 5 (8 October 2009-11 February 2010) at the Soufrière Hills Volcano, Montserrat, *Geological Society, London, Memoirs*, *39*, 113–131, doi:10.1144/M39.6.

Stinton, A., P. D. Cole, R. Stewart, H. Odbert, and P. Smith (2014b), The 11 February 2010 partial dome collapse at Soufrière Hills Volcano, Montserrat, *Geological Society, London, Memoirs*, *39*, 133–152, doi:10.1144/M39.7.

Stinton, A., V. Bass, T. Christopher, N. Edgecome, M. Fergus, K. Pascal, M. Smith, R. Stewart, and R. Syers (2017), MVO Scientific Report for Volcanic Activity between 1 April and 30 September 2017, *Tech. rep.*, Montserrat Volcano Observatory.

Tibaldi, A., A. Bistacchi, F. A. Pasquarè, and L. Vezzoli (2006), Extensional tectonics and volcano lateral collapses: Insights from Ollagüe volcano (Chile-Bolivia) and analogue modelling, *Terra Nova*, *18*(4), 282–289, doi:10.1111/j.1365-3121.2006.00691.x.

Torabi, S. R., M. Ataei, and M. Javanshir (2011), Application of Schmidt rebound number for estimating rock strength under specific geological conditions, *Journal of Mining and Environment*, *1*(2), 1–8.

Trofimovs, J., R. Sparks, and P. Talling (2008), Anatomy of a submarine pyroclastic flow and associated turbidity current: July 2003 dome collapse, Soufrière Hills volcano, Montserrat, West Indies, *Sedimentology*, *55*, 617–634, doi:10.1111/j.1365-3091.2007.00914.x.

Ulusay, R., and J. Hudson (Eds.) (1979), *The Complete ISRM Suggested Methods for Rock Characterization: Testing and Monitoring 1974-2006*, Compilation arranged by the ISRM Turkish National Group Ankara, Turkey.

Vidal, N., and O. Merle (2000), Reactivation of basement faults beneath volcanoes: A new model of flank collapse, *Journal of Volcanology and Geothermal Research*, *99*(1-4), 9–26, doi:10.1016/S0377-0273(99)00194-8.

Voight, B. (2000), Structural stability of andesite volcanoes and lava domes, *Philosophical Transactions of the Royal Society of London*, *358*, 1663–1703.

Voight, B., and D. Elsworth (2000), Instability and collapse of hazardous gas-pressurized lava domes, *Geophysical Research Letters*, *27*(1), 1–4, doi:10.1029/1999GL008389.

Wadge, G., B. Voight, R. Sparks, P. Cole, S. Loughlin, and R. Robertson (2014), An overview of the eruption of Soufrière Hills Volcano, Montserrat from 2000 to 2010, *Geological Society, London, Memoirs*, *39*, 1–40, doi:10.1144/M39.1.

Walsh, J. B. (1965), The effect of cracks on the uniaxial elastic compression of rocks, *Journal of Geophysical Research*, *70*(2), 399–411, doi:10.1029/JZ070i002p00399.

Yagiz, S. (2009), Predicting uniaxial compressive strength, modulus of elasticity and index properties of rocks using the Schmidt hammer, *Bulletin of Engineering Geology and the Environment*, *68*(1), 55–63, doi:10.1007/s10064-008-0172-z.

Yasar, E., and Y. Erdogan (2004), Estimation of rock physicomechanical properties using hardness methods, *Engineering Geology*, *71*(3-4), 281–288, doi:10.1016/S0013-7952(03)00141-8.

Ylmaz, I., and H. Sendr (2002), Correlation of Schmidt hardness with unconfined compressive strength and Young's modulus in gypsum from Sivas (Turkey), *Engineering Geology*, *66*(3-4), 211–219, doi:10.1016/S0013-7952(02)00041-8.

Young, S. R., R. S. J. Sparks, W. P. Aspinall, L. L. Lynch, A. D. Miller, R. E. A. Robertson, and J. B. Shepherd (1998), Overview of the eruption of Soufrière Hills Volcano, Montserrat, 18 July 1995 to December 1997, *Geophysical Research Letters*, *25*(18), 3389–3392, doi:10.1029/98GL01405.

Zorn, E. U., M. C. Rowe, S. J. Cronin, A. G. Ryan, L. A. Kennedy, and J. K. Russell (2018), Influence of porosity and groundmass crystallinity on dome rock strength: a case study from Mt. Taranaki, New Zealand, *Bulletin of Volcanology*, *80*(4), doi:10.1007/s00445-018-1210-8.

Chapter 5

Discussion and conclusions

This final chapter presents a summary of the key techniques and findings so far and I also show how the findings from each chapter can be brought together by presenting a suite of models that explore the effect of rock properties on dome stability. Finally I discuss how this influences the overall state of knowledge regarding lava dome collapse. For specific discussions and conclusions related to the publications presented in this thesis, I refer the reader to the relevant sections within Chapters 2, 3, and 4.

5.1 Effect of rock strength on dome stability

In Chapter 3, I highlighted that talus properties were crucial to the accumulation of shear strain within the dome. It is clear from the results in Chapter 4 that rock strength can be highly variable in volcanic environments, and more realistic rock properties must be estimated by scaling the properties determined in the laboratory. Therefore in this final Chapter, I present a new suite of models that incorporate the rock properties identified for SHV products (Chapter 4) into the DEM models presented in Chapter 3 to investigate the effect of rock strength on overall dome stability.

Incorporating strengthening of rock properties during active dome growth is not yet implemented in the models presented in Chapter 3, hence I use the emplaced domes shown in Figures 3.4 and 3.5 as initial conditions for models investigating the effect of rock strength on dome stability. By using the models presented in Chapter 3 as initial conditions, I am testing the relative effect of rock strength on a given dome morphology and acknowledge that the reality of development of dome-scale rock strength during active growth is more complex.

The models presented in Chapter 3 were uncalibrated, as the talus material simply adopted the properties of the fluid core material, but with additional bonding to ensure behaviour as a solid. The modelled scenarios presented here are created using the methodologies outlined in Appendix A.1 and in order to explore the effect of rock strength, I define three different rock property scenarios, shown quantitatively in Table 5.1:

1. **Intact strong:** the model is calibrated to the strongest intact rock properties found at Soufrière Hills. This corresponds to the average properties of Phase 4 material (Table C.4).

2. **Intact weak:** the model is calibrated to the weakest intact rock properties found at Soufrière Hills. This corresponds to the average properties of Phase 5 material (Table C.4).

3. **Rock-mass:** The model is calibrated to rock-mass properties, referring here to a scaled version of the weakest Phase 5 properties. For this scaling, the original rock properties are reduced by 80% (i.e. a fifth of the original properties), following the Volcán de Colima model validation shown in Section 1.4. This is in alignment with other scaling relationships proposed in the literature, as discussed in Section 5.2.

Table 5.1: Mechanical properties (Uniaxial Compressive Strength, Uniaxial Tensile Strength, and Young's modulus) for each of the modelled rock strength scenarios. Intact strong rock properties correspond to the strongest identified SHV products (Phase 4) and intact weak rock properties correspond to the weakest identified SHV products (Phase 5); SHV phase averages shown in Table C.4.

	UCS (MPa)	UTS (MPa)	E (GPa)
Intact strong	49.82	3.22	10.94
Intact weak	6.59	0.96	2.67
Rock-mass	1.32	0.19	0.53

The uncalibrated models presented in Chapter 3 are significantly weaker than the rock-mass models presented here, as shown by the PFC micro-properties attributed to each model scenario (Table 5.2). The magma properties are kept constant between all scenarios, as I do not explore the effect of viscosity on dome morphology or stability; a discussion of sensitivity to fluid properties in DEM can be found in *Husain et al.* (2014).

Table 5.2: PFC micro-properties used to achieve the macro-behaviour for the following scenarios: uncalibrated (Chapter 3), rock-mass (20% of Phase 5), intact weak (Phase 5), intact strong (Phase 4). Bond properties shown as named in PFC: fj_{ten} = tensile strength, fj_{coh} = cohesion, *emod* = Young's modulus, fj_{kn} = normal stiffness, and fj_{ks} = shear stiffness.

	fj_{ten} (Pa)	fj_{coh} (Pa)	*emod* (Pa)	fj_{kn} (Pa)	fj_{ks} (Pa)
Uncalibrated	1.0×10^5	1.0×10^6	2.0×10^8	1.0×10^8	1.0×10^8
Rock-mass	8.0×10^5	1.3×10^6	1.2×10^9	6.4×10^8	6.4×10^8
Intact Weak	4.0×10^6	7×10^6	5.6×10^9	3.0×10^9	3.0×10^9
Intact Strong	1.4×10^7	5.4×10^7	2.4×10^{10}	1.3×10^{10}	1.3×10^{10}

5.1.1 Gravitational failure

I show domes with incorporated rock properties (each scenario shown in Table 5.1) for each of the solidus pressures explored in Section 3.3.1 (0.2 MPa, 0.4 MPa, and 0.8 MPa). In each case, the initial conditions are taken as the respective fully emplaced domes shown in Figures 3.4 and 3.5. This initial condition is restored, and extrusion ceased in order to isolate the effect of gravity on the dome. In addition to these scenarios, I show a cooled dome, whereby the dome has all been turned to talus in the model and there is no longer any fluid material in the centre. All models are shown at the same model age to ensure fair comparison.

All modelled scenarios are visualised using both normalised shear strain (Figures 5.1, 5.3, and 5.5), as explained in Section 3.2.3, and lateral displacement (Figures 5.2, 5.4, 5.6). Lateral displacement (i.e. x-direction only) is used as a quantitative measure for instability. Total displacement (in both x and y directions) is shown by the magnitude and direction of arrows. Visualising total displacement highlights where there is a rotational nature to the slope movement. By isolating the lateral displacement, I focus on the material that has the most potential to lead to landsliding, as the accepted definition of a landslide by *Varnes* (1958) was "downward and outward" movement.

I use area percentage of material displaced more than 1 m as analogous to relative collapse volume ($\Delta V/V$, Chapter 2), and refer to it as the 'unstable material volume' herein, in order to quantitatively explore the sensitivity of dome stability to rock strength. This is an arbitrary cut-off designed to show where the potential for large-scale failure is, and in all figures, displacement is shown on a gradual colour scale from 0-5 m displacement. To limit computational time, I do not model the whole collapse process, but rather highlight areas of developing instability.

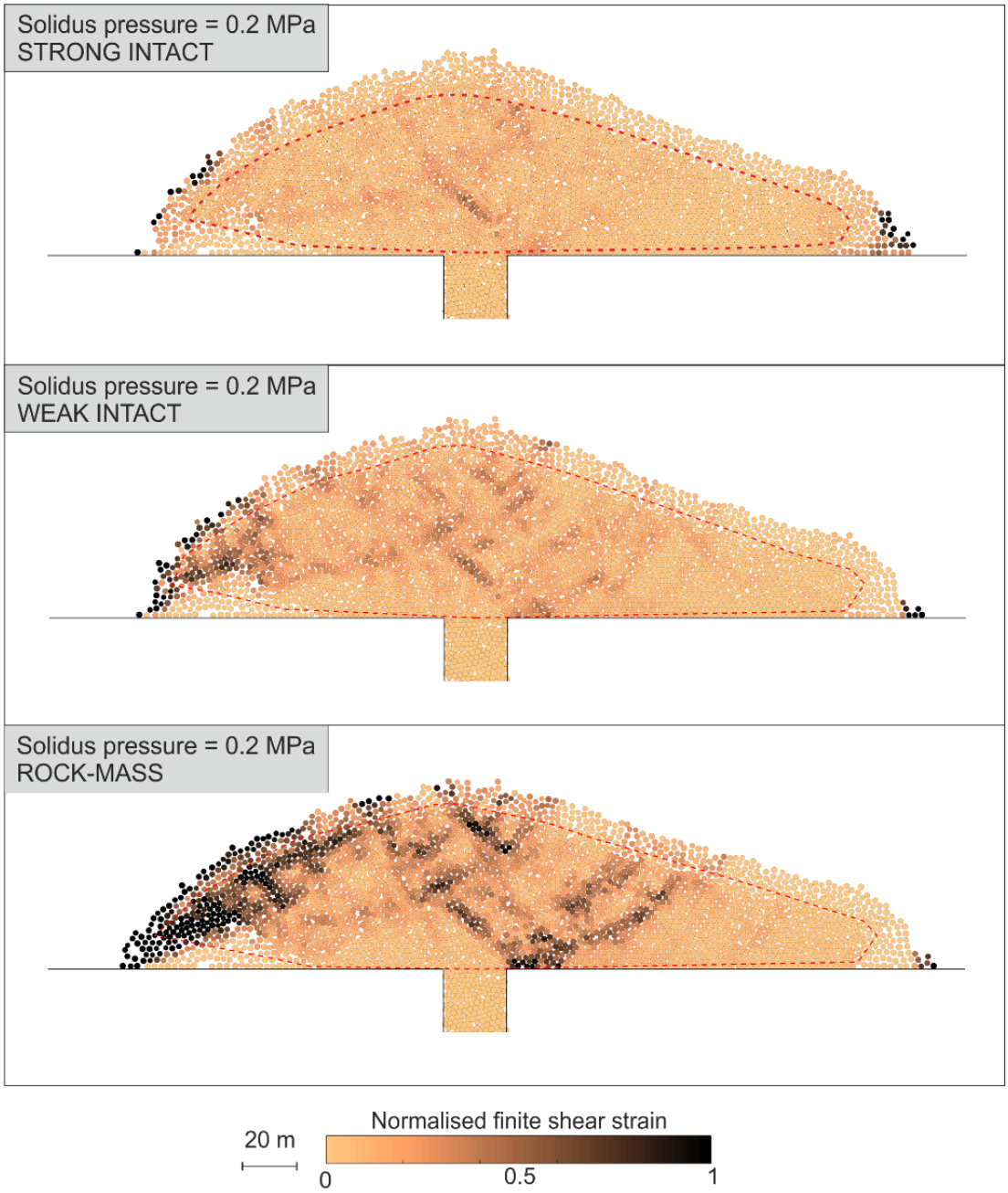

Figure 5.1: PFC model results using a solidus pressure of 0.2 MPa (see Figure 3.5a for initial condition), and testing the stability of the dome for talus with intact strong properties talus with intact weak properties, and talus with rock-mass properties. All panels visualised using normalised shear strain.

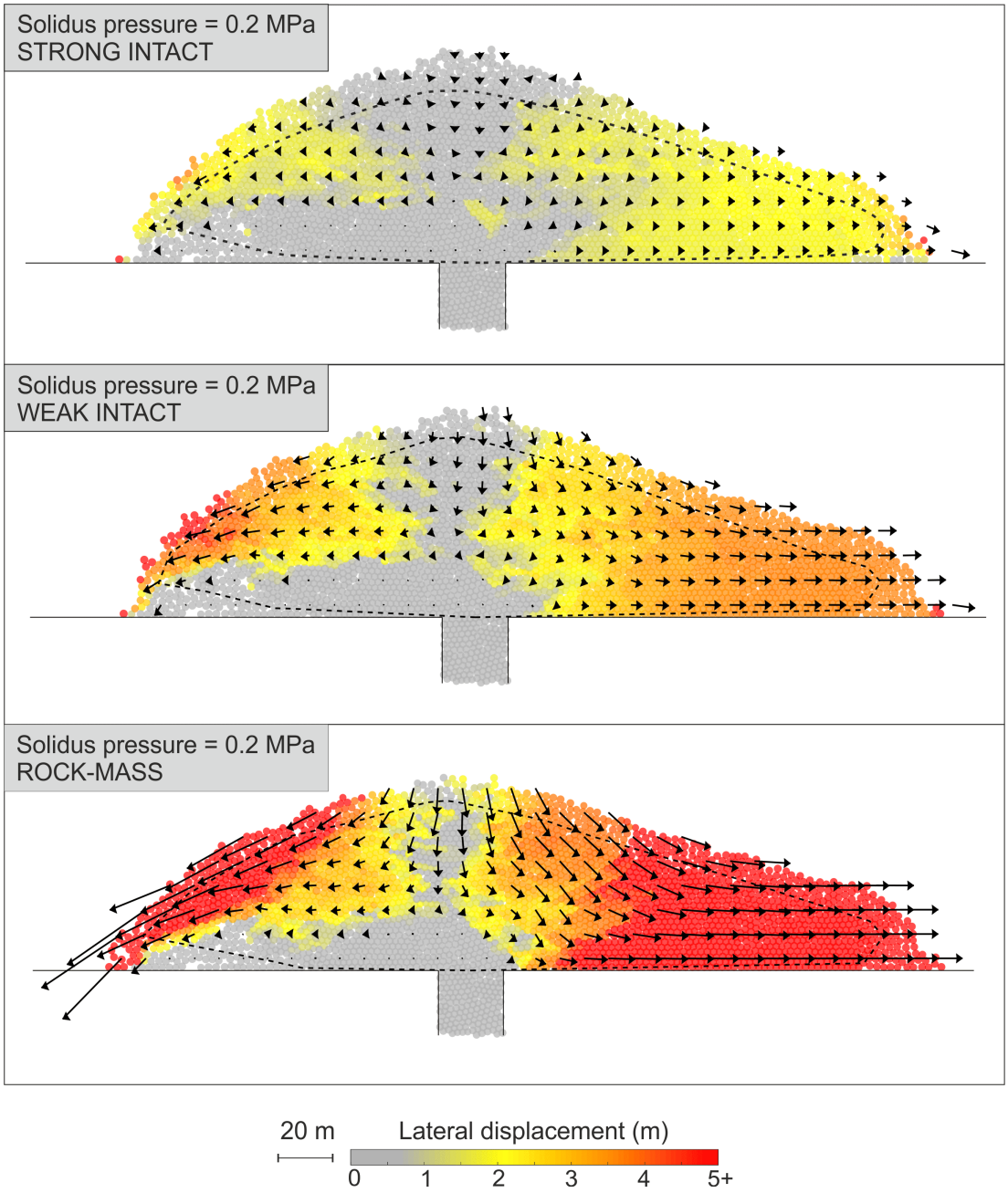

Figure 5.2: PFC model results using a solidus pressure of 0.2 MPa (see Figure 3.5a for initial condition), and testing the stability of the dome for talus with intact strong properties, talus with intact weak properties, and talus with rock-mass properties. All panels visualised by displacement, where colour shows lateral displacement, and arrows show total displacement (>0.5 m). Arrow length is proportional to displacement, and maximum displacement = 19.8 m.

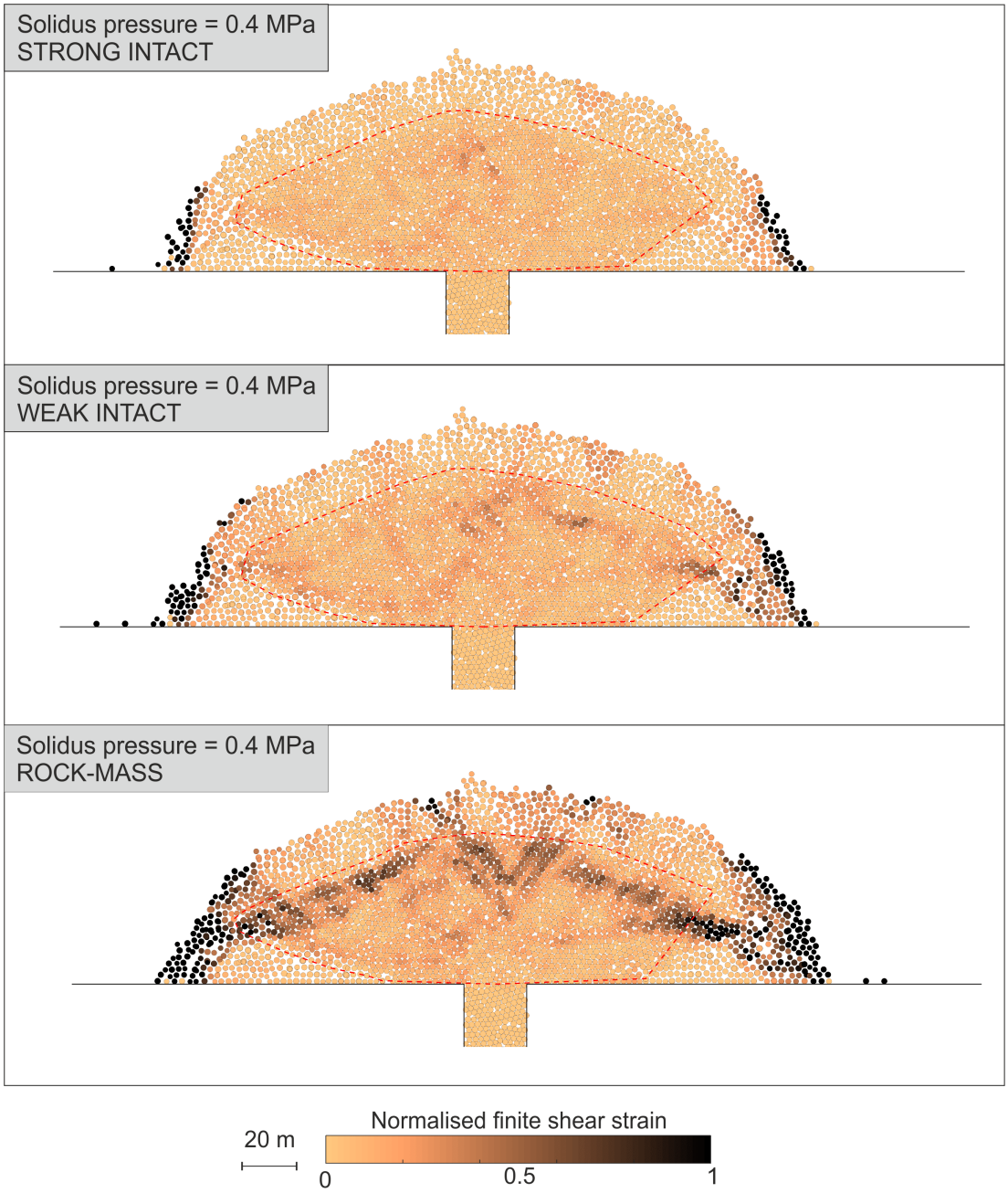

Figure 5.3: PFC model results using a solidus pressure of 0.4 MPa (see Figure 3.4c for initial condition), and testing the stability of the dome for talus with intact strong properties talus with intact weak properties, and talus with rock-mass properties. All panels visualised using normalised shear strain.

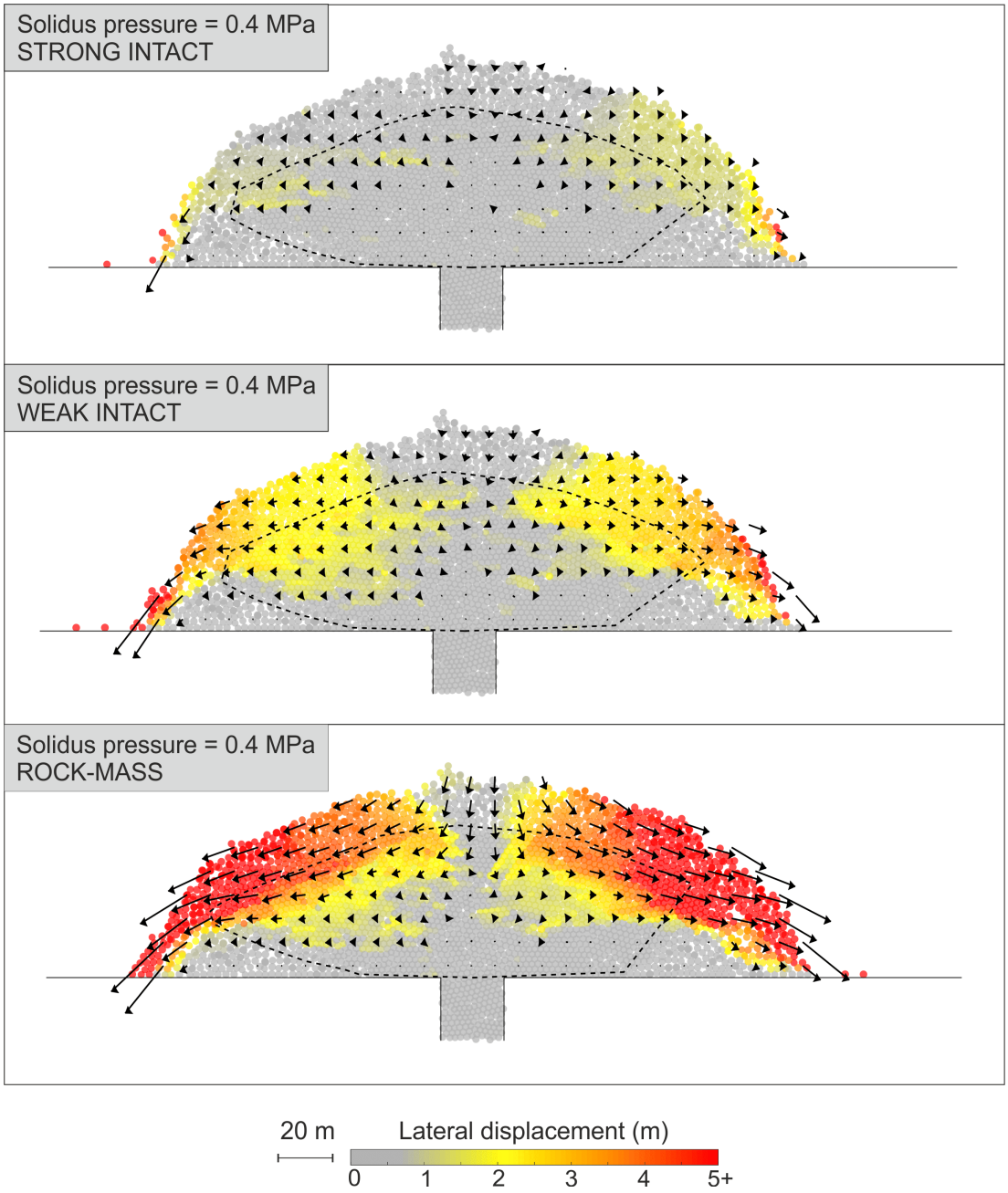

Figure 5.4: PFC model results using a solidus pressure of 0.4 MPa (see Figure 3.4c for initial condition), and testing the stability of the dome for talus with intact strong properties, talus with intact weak properties, and talus with rock-mass properties. All panels visualised by displacement, where colour shows lateral displacement, and arrows show total displacement (>0.5 m). Arrow length is proportional to displacement, and maximum displacement = 15.7 m.

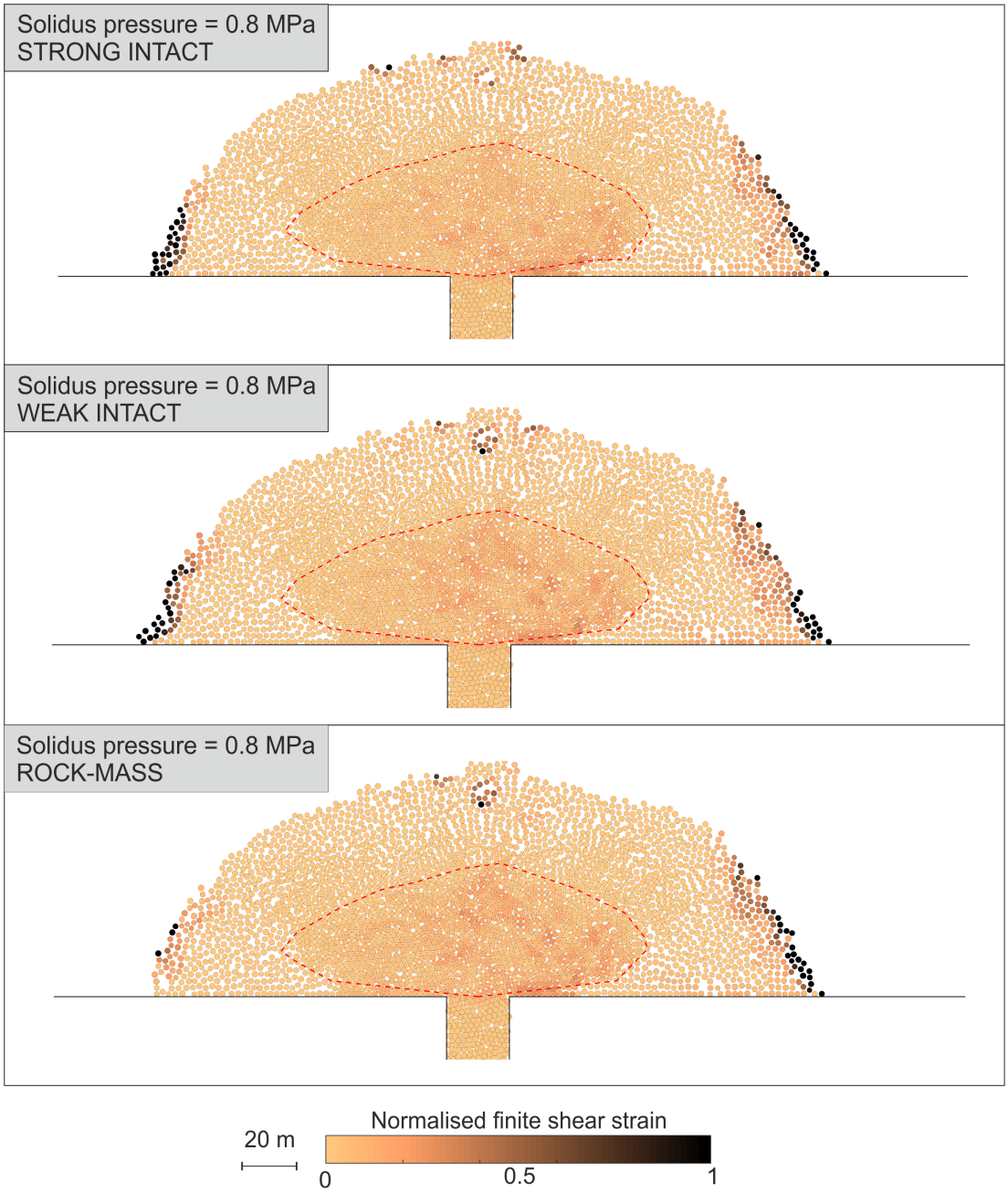

Figure 5.5: PFC model results using a solidus pressure of 0.8 MPa (see Figure 3.5b for initial condition), and testing the stability of the dome for talus with intact strong properties talus with intact weak properties, and talus with rock-mass properties. All panels visualised using normalised shear strain.

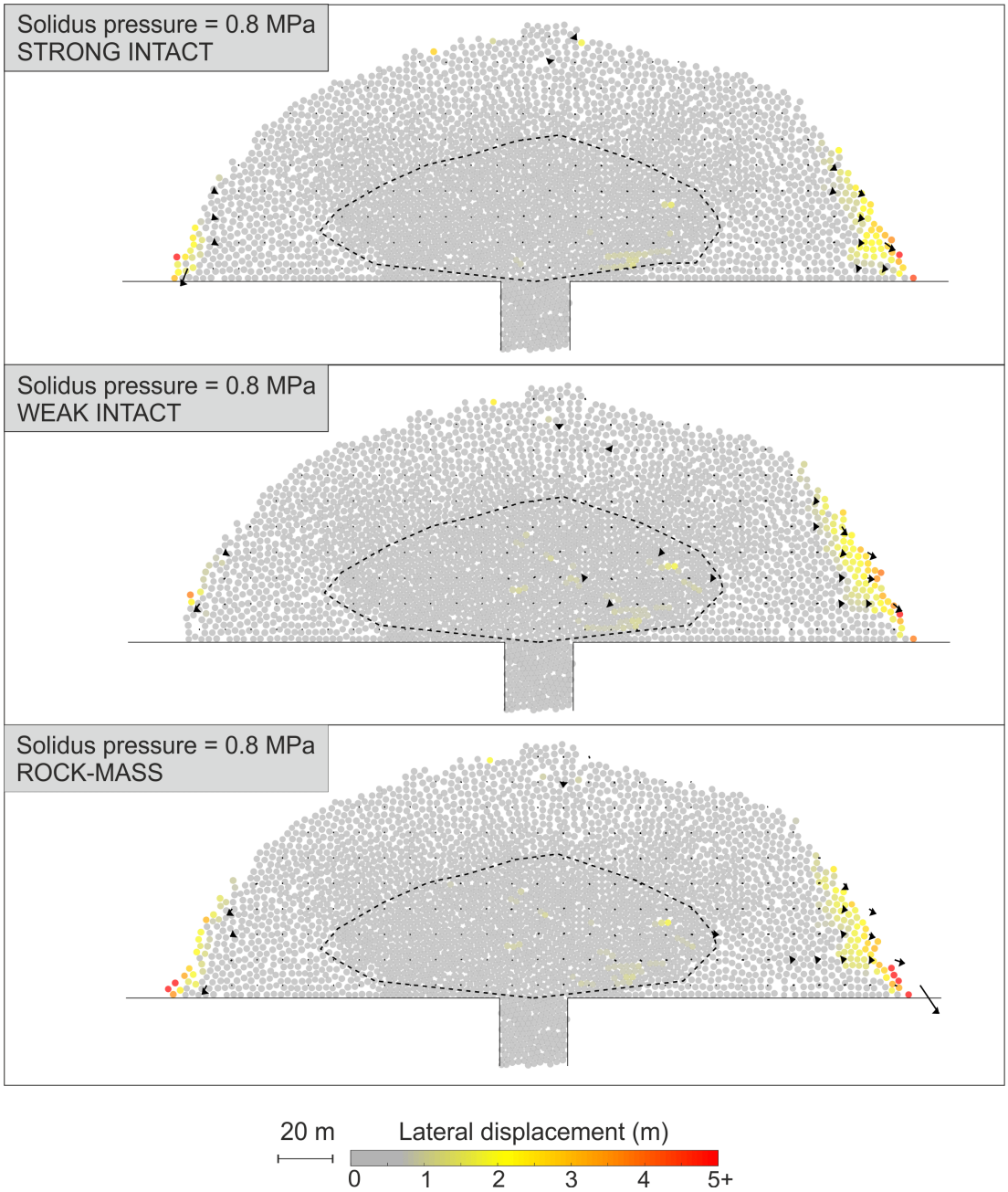

Figure 5.6: PFC model results using a solidus pressure of 0.8 MPa (see Figure 3.5b for initial condition), and testing the stability of the dome for talus with intact strong properties, talus with intact weak properties, and talus with rock-mass properties. All panels visualised by displacement, where colour shows lateral displacement, and arrows show total displacement (>0.5 m). Arrow length is proportional to displacement, and maximum displacement = 6.7 m.

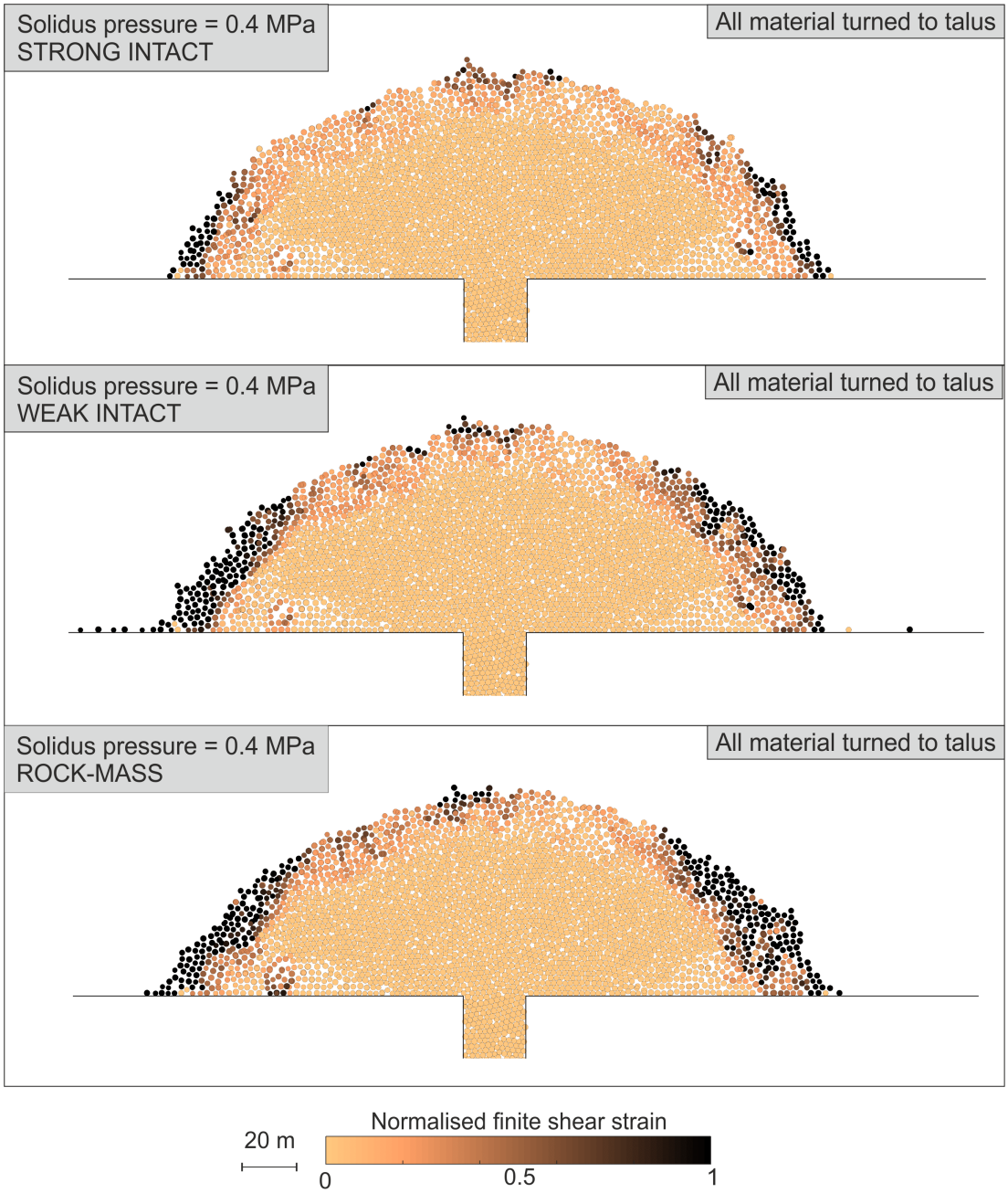

Figure 5.7: PFC model results for a dome emplaced with a solidus pressure of 0.4 MPa (see Figure 3.4c for initial condition), but all turned to rock to simulate a cooled lava dome. Stability of the dome tested for talus with intact strong properties talus with intact weak properties, and talus with rock-mass properties. All panels visualised using normalised shear strain.

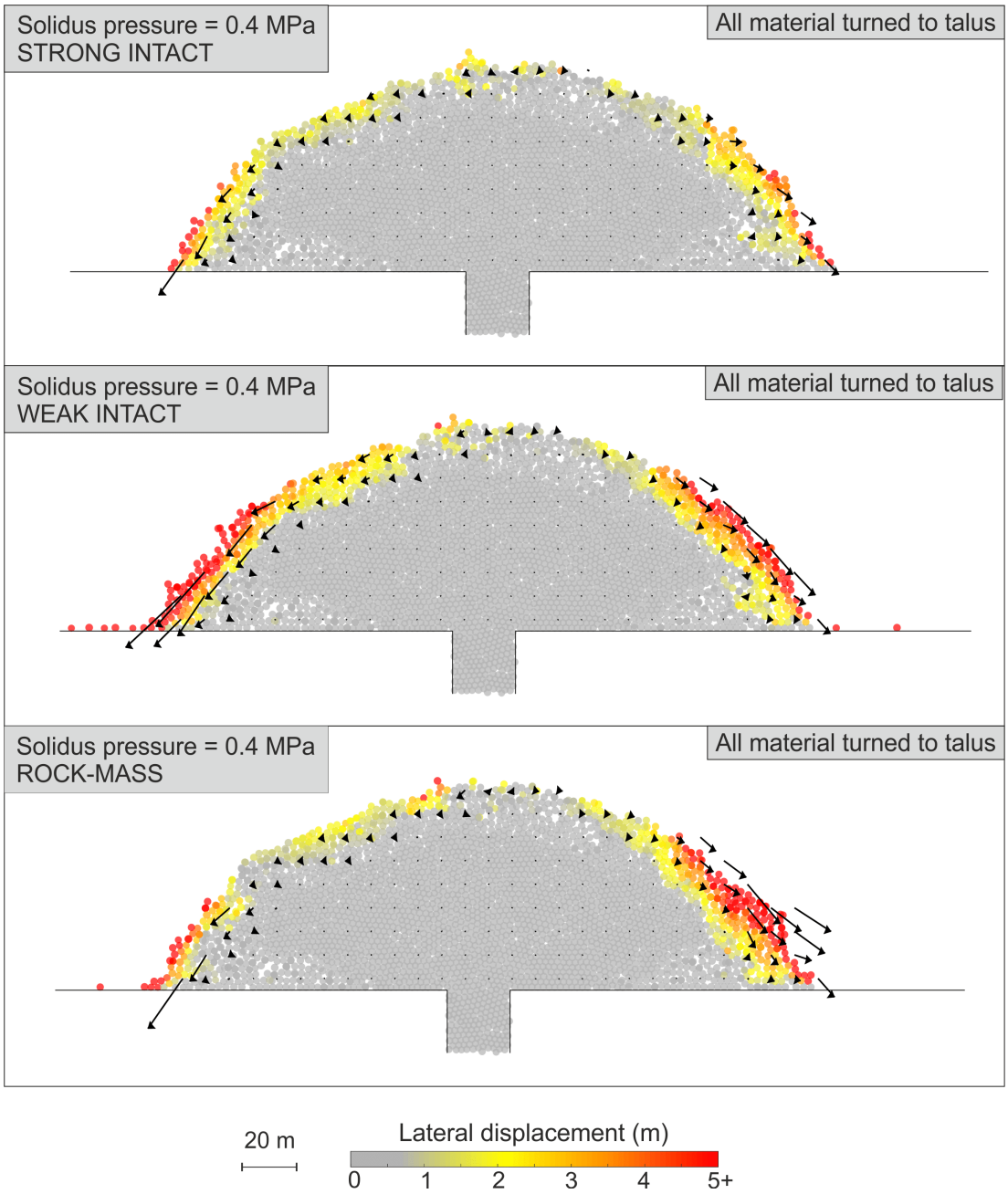

Figure 5.8: PFC model results for a dome emplaced with a solidus pressure of 0.4 MPa (see Figure 3.4c), but all turned to rock to simulate a cooled lava dome. Stability of the dome for talus with intact strong properties, talus with intact weak properties, and talus with rock-mass properties. All panels visualised by displacement, where colour shows lateral displacement, and arrows show total displacement (>0.5 m). Arrow length is proportional to displacement, and maximum displacement = 7.2 m.

Table 5.3: Summary table showing the percentage of material that has displaced by >3 m, >2 m, and >1 m, for all modelled scenarios. This includes solidus pressures of 0.2 MPa, 0.4 MPa, 0.8 MPa, and the scenario where the whole dome is solid rock. This is done for calibrated rock strength scenarios of strong, weak, and rock-mass.

		Strong			Weak			Rock-mass		
		>3 m	>2 m	>1 m	>3 m	>2 m	>1 m	>3 m	>2 m	>1 m
Solidus	0.2 MPa	0.36	1.12	46.15	27.42	47.6	67.73	54.47	64.74	79.36
	0.4 MPa	0.41	0.83	4.11	4.21	14.4	42.91	34.97	42.81	58.82
	0.8 MPa	0.14	0.51	1.55	0.28	0.67	2.03	0.31	1.86	2.43
	All rock	1.73	3.91	10.96	7.14	11.12	17.68	8.28	12.05	19.23

In all cases, the unstable material volume increases as rock strength decreases, with the maximum unstable volumes in domes with rock-mass properties. In the dome with solidus pressure of 0.4 MPa, presented first in Chapter 3 and used here as the initial condition, the dome with intact weak properties has an unstable material volume (displacement >1 m) of 42.9%, whereas the dome with rock-mass properties has an unstable material volume of 58.8% (Table 5.3). This shows the impact that rock property scaling can have on numerical model outputs, discussed further in Section 5.2. The sensitivity analysis of solidus pressure also shows that lower solidus pressures result in higher unstable material volumes; this is likely due to the large proportion of liquid material decreasing the strength of the dome as a whole. This supports the conclusion in Chapter 3 that solidus pressure can control the volume of material involved in collapse, and shows that the same result is given by the model following incorporation of realistic rock properties.

5.1.2 Internal pressurisation

I also investigate the effect of rock strength on domes subjected to increased internal pressurisation. Similarly to the models isolating the effect of gravity on dome stability, the models in this section begin by initialising a fully emplaced dome as an initial condition, where extrusion has ceased. Following the methodology outlined in Section 3.3.3, an upward force equivalent to a 5 MPa pressure was applied to a hemispherical region above the conduit exit. This was carried out for the three rock property scenarios (intact strong, intact weak, and rock-mass) and visualised using normalised shear strain (Figures 5.11) and displacement (Figure 5.12). These models again show that displacement increases as rock strength decreases. In both the intact weak and rock-mass property scenarios, displacement is seen to accumulate within the core material, showing the development of a potential deep-seated failure plane. The rotational nature of the failure is highlighted by the vertical motion of material towards the apex of the dome, and complete lateral motion of the material on the flanks of the dome (e.g. Figure 5.12c).

The analysis of relative collapse volumes in *GLADIS* suggested that dome failure due to internal pressurisation involved a greater proportion of the dome than gravitational failures (average of 68% compared to an average of 50%). Calculating the unstable material volume in the models allows comparison of failures due to gravity and internal pressurisation within the models, as well as relative to the database analysis. For all modelled scenarios using intact

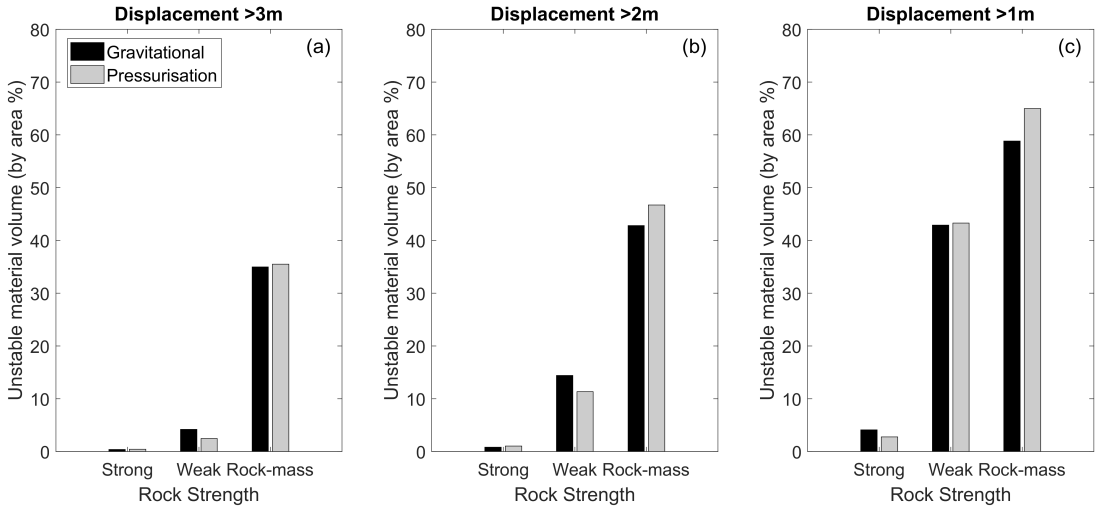

Figure 5.9: Unstable material volumes (by area %) from PFC models for purely gravitational scenarios (black) and internal pressurisation scenarios (grey) for each of the different rock strength scenarios. This is shown as a function of displacement: **(a)** displacement > 3 m; **(b)** displacement between 2 and 3 m; and **(c)** displacement between 1 and 2 m.

properties, the proportions of unstable material are found to be lower than those from *GLADIS*. The models using rock-mass properties however show that 59% of material has been displaced by more than 1 m in the model subjected purely to gravitational forces, and 65% of material has been displaced by more than 1 m in the model with internal pressurisation (Figure 5.9). These compare well to the averages from *GLADIS*. In the models with higher rock strengths, little difference is seen between the gravitational and pressurised models. This is likely due to the upward force acting against the downward gravitational force, thus balancing out the resisting and disturbing forces in the system. The rock-mass scenario shows the largest difference in unstable material volumes between pressurisation and gravitational models. This could be explained using the theory set out by *Voight and Elsworth* (2000), whereby the weak rock allows development of a failure plane due to the effect of gravity, and the upward force acts on this failure plane to further mobilise the overlying rock unit.

For a fuller exploration of the ways in which pressurisation (shown here by an upward force) affects a lava dome, the model would need to explicitly consider rock permeability. This has been shown to control overall rock strength both in this study (Chapter 4) and studies by other authors (e.g *Mueller et al.*, 2005, 2008). It would also be necessary to incorporate fractures into the rock-mass to provide pathways of outgassing; this is currently beyond the capabilities of this software.

5.1.3 Effect of dome size

A conclusion from Chapter 2 was that the dome volume at the time of collapse does not influence the mechanism of collapse. In Chapter 3, deep-seated rotational failures were identified in both the large (conduit width = 50 m) and small (conduit width = 20 m) domes, supporting the conclusion from *GLADIS* that collapse mechanism is insensitive to original dome volume. To verify this conclusion is still supported by models with realistic rock properties, I show a large dome, emplaced with a solidus pressure of 0.4 MPa for each of the rock property scenarios (Figures 5.13, 5.14). Limited shear strain accumulation is seen in the intact strong and weak scenarios (Figures 5.13a, b), likely because material is moving as a coherent block. When visualising the model scenarios by displacement, development of deep-seated rotational failure planes are evident in all scenarios, with displacement increasing as rock strength decreases.

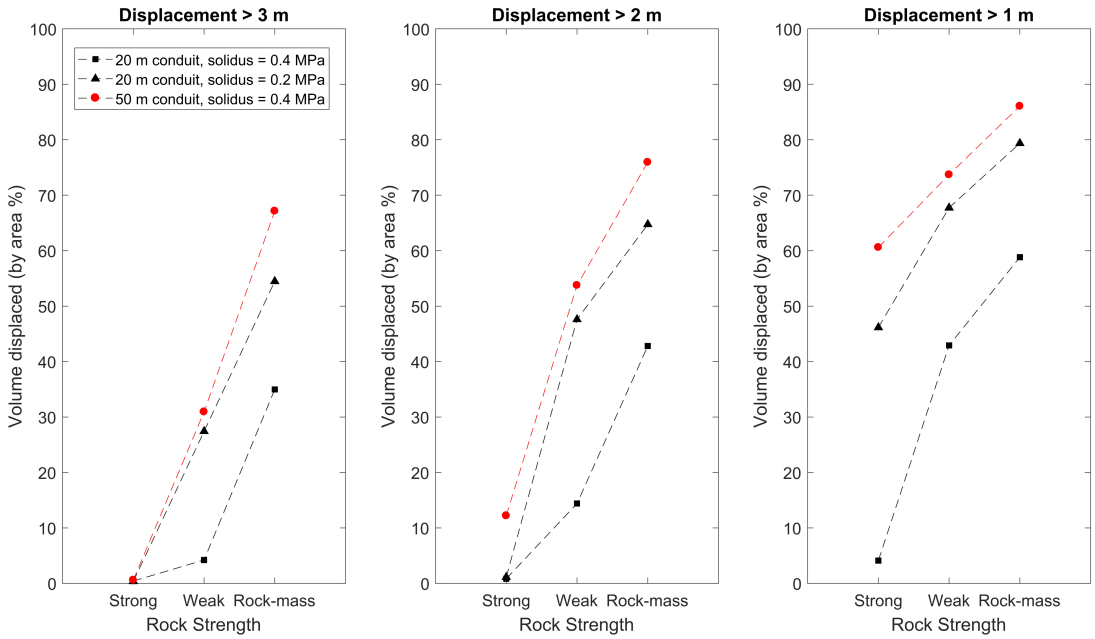

Figure 5.10: Comparison of unstable material volume (by area %) for dome emplaced using a 20 m conduit and solidus pressure of 0.4 MPa (squares), dome emplaced using a 20 m conduit and solidus pressure of 0.2 MPa (triangles) and dome emplaced using a 50 m conduit and solidus pressure of 0.4 MPa, for **(a)** displacement > 3 m, **(b)** displacement between 2 m and 3 m, and **(c)** displacement between 1 m and 2 m.

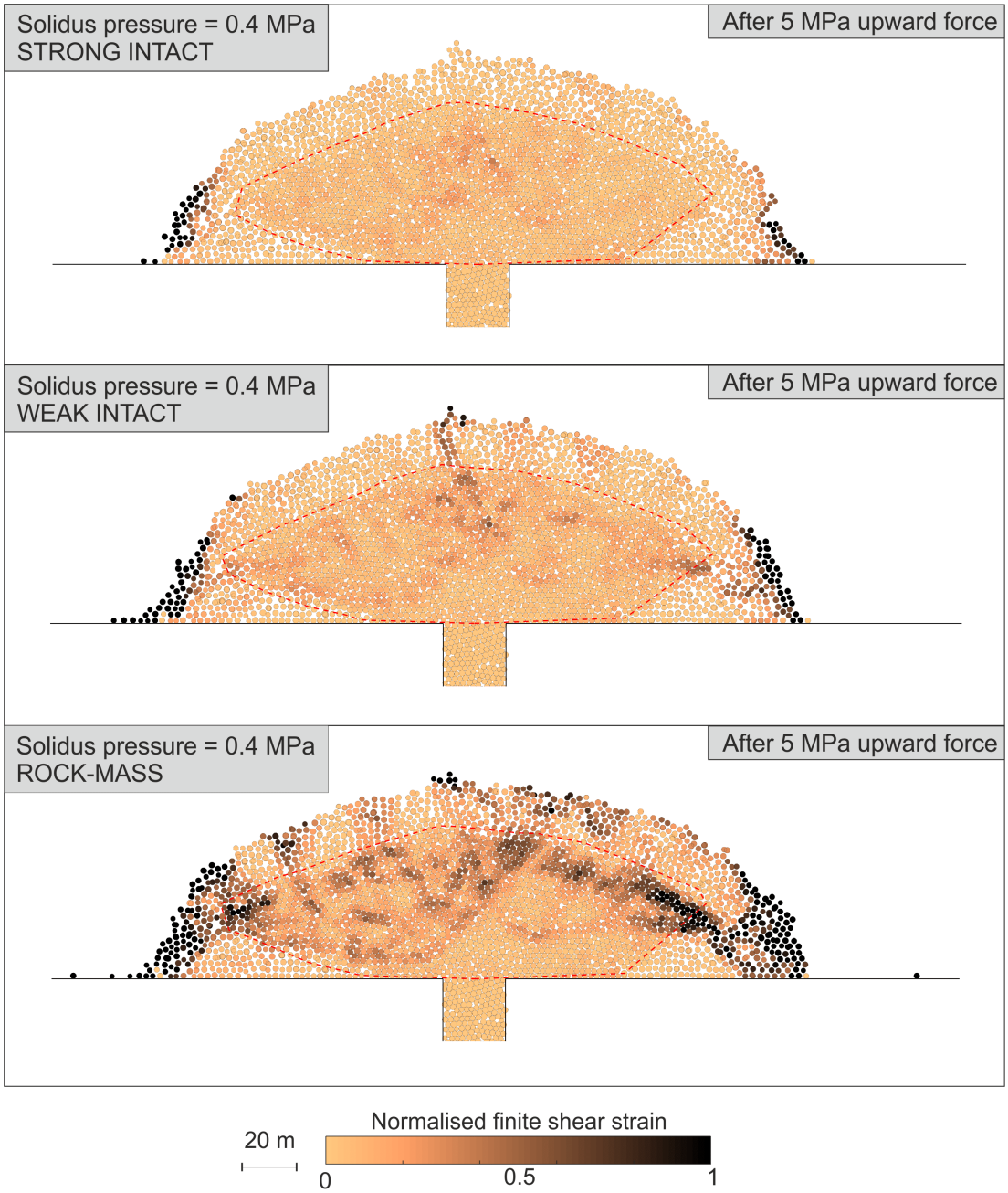

Figure 5.11: PFC model results using a solidus pressure of 0.4 MPa (see Figure 3.4c for initial condition) after application of 5 MPa internal pressure, and testing the stability of the dome for talus with intact strong properties talus with intact weak properties, and talus with rock-mass properties. All panels visualised using normalised shear strain.

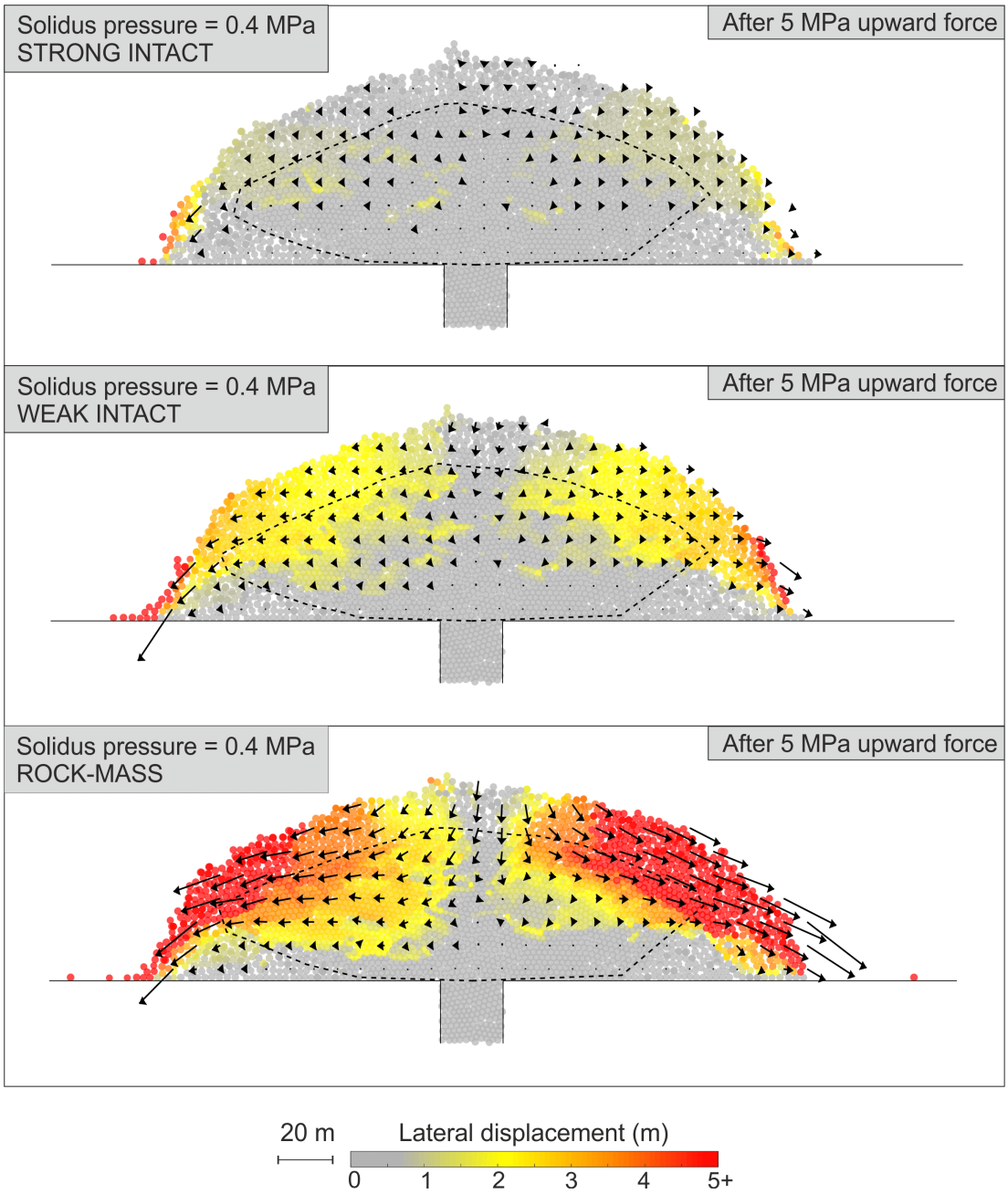

Figure 5.12: PFC model results using a solidus pressure of 0.4 MPa (see Figure 3.4c for initial condition) after application of 5 MPa internal pressure, and testing the stability of the dome for talus with intact strong properties, talus with intact weak properties, and talus with rock-mass properties. All panels visualised by displacement, where colour shows lateral displacement, and arrows show total displacement (>0.5 m). Arrow length is proportional to displacement, and maximum displacement = 16.0 m.

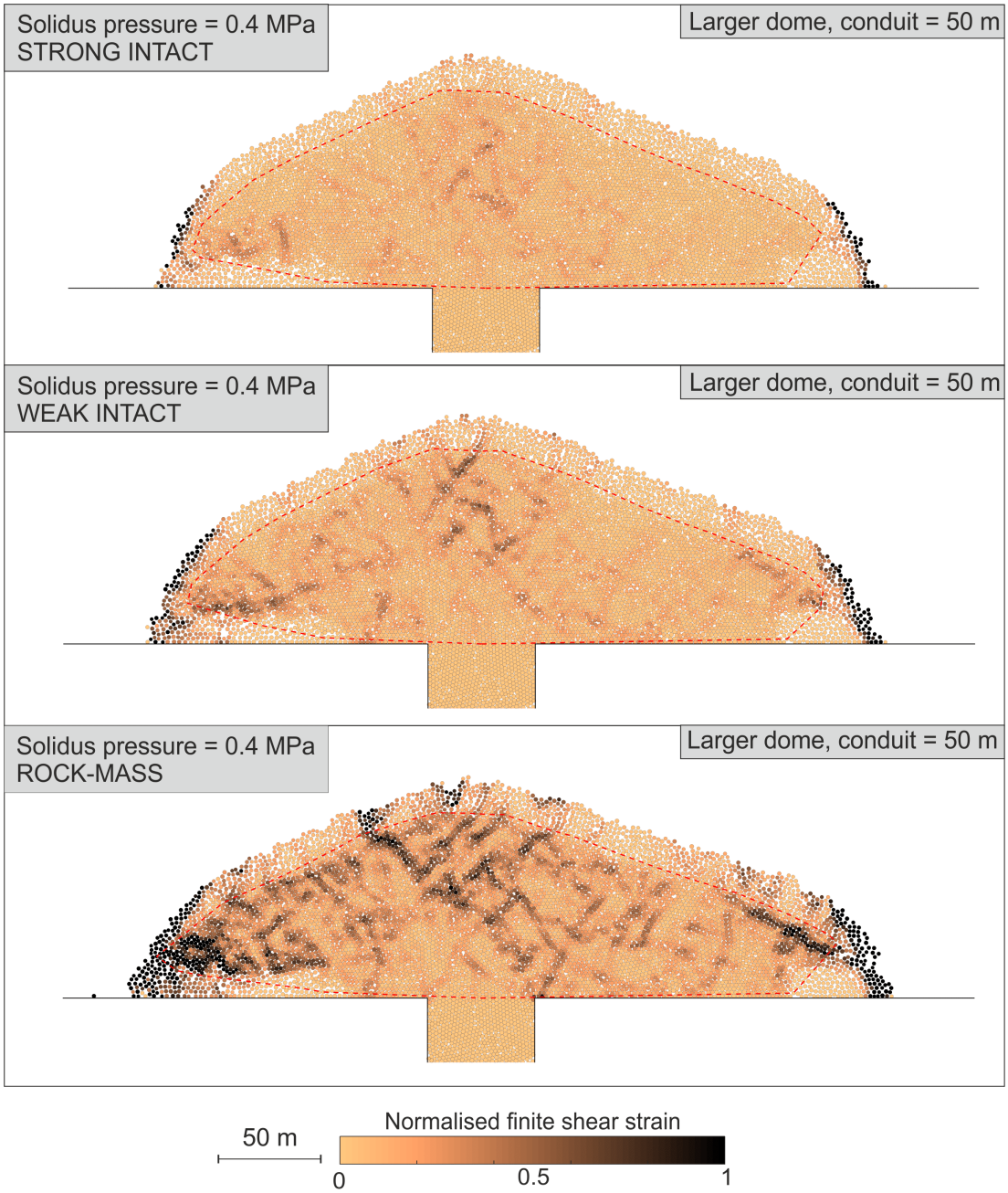

Figure 5.13: PFC model results using a conduit width of 50 m and solidus pressure of 0.4 MPa (see Figure 3.6 for initial condition), and testing the stability of the dome for talus with intact strong properties talus with intact weak properties, and talus with rock-mass properties. All panels visualised using normalised shear strain.

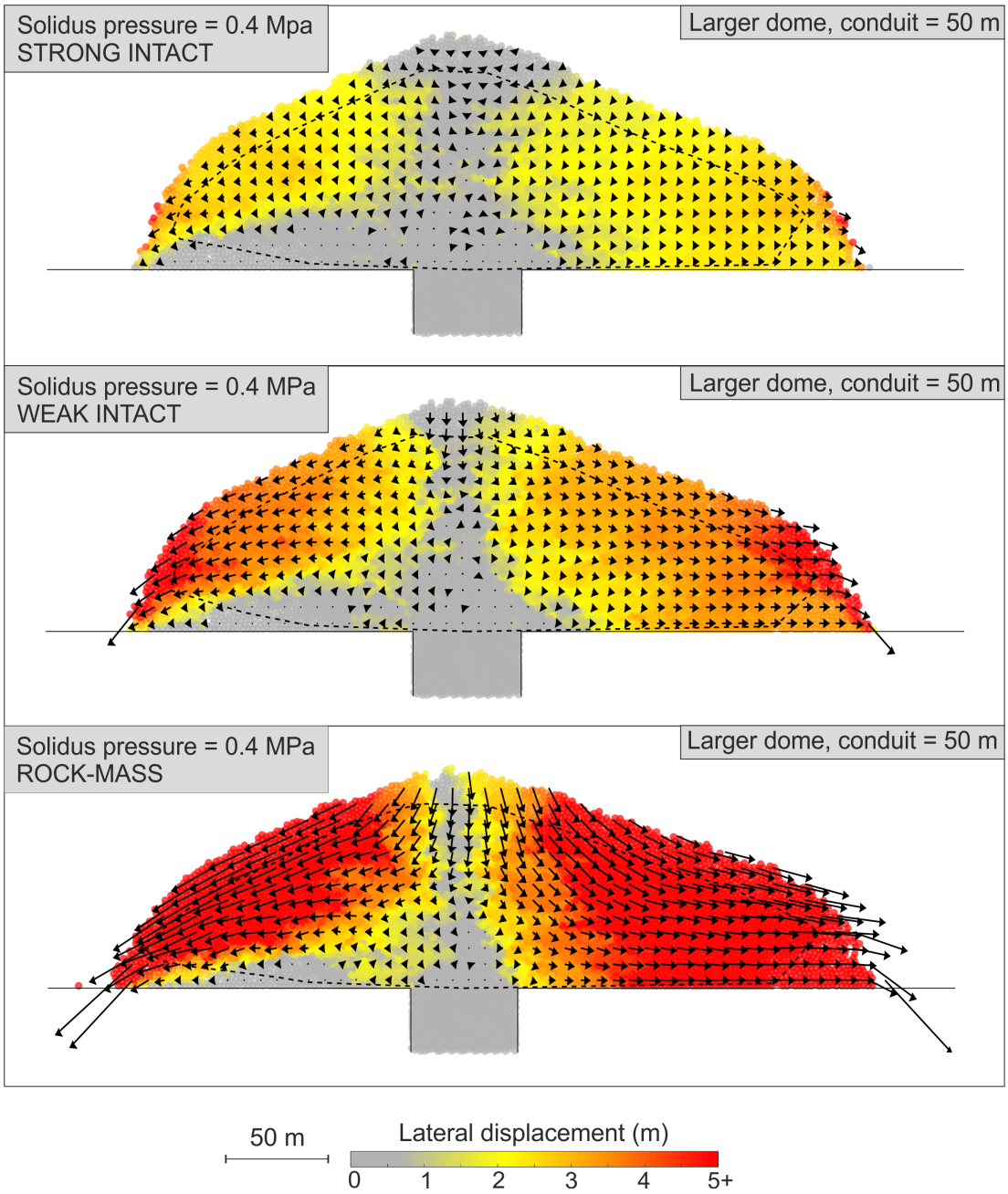

Figure 5.14: PFC model results using a conduit width of 50 m and solidus pressure of 0.4 MPa (see Figure 3.6 for initial condition), and testing the stability of the dome for talus with intact strong properties, talus with intact weak properties, and talus with rock-mass properties. All panels visualised by displacement, where colour shows lateral displacement, and arrows show total displacement (>0.5 m). Arrow length is proportional to displacement, and maximum displacement = 32.7 m.

I conclude therefore that the collapse mechanism is scale independent, but the unstable material volume is influenced by original dome size. As shown in Section 3.3.2, the height/width ratio is approximately 1:3 in both the large and small dome, suggesting that the emplacement process is scale independent in these models. The collapse process, however, is linked to scale: for example, 74% of the large dome with intact weak properties has been displaced more than 1 m, whereas this is only 68% (Figure 5.10) for the small dome. It is logical for the larger dome to have higher relative volumes of unstable material as there is a larger mass and the absolute height is larger, therefore the material has higher gravitational potential energy. The similar collapse mechanisms could also be influenced by the similar morphologies of both domes. The effect of dome geometry is not explored further in this project, but could be explored by incorporating rock strength development throughout emplacement (further discussed in Section 5.4).

The core/talus proportions are affected by dome size; relative core volume fraction also affects the unstable material volume, as concluded in Chapter 3. The small dome with a solidus pressure of 0.4 MPa had a core proportion of 37.3% and talus proportion of 62.7% (Table 3.1) whereas the large dome with a solidus pressure of 0.4 MPa had 23.0% core and 77.0% talus. Despite the difference in core/talus proportions between the various modelled scenarios, all domes in this study fit the theory of *Griffiths and Fink* (1993) who found that a dome of 1 km width only requires an outer crust of 10 m in order to control dome spreading. The thinnest outer talus layer is observed in the model with a solidus pressure of 0.2 MPa, where the minimum talus thickness is ∼3 m for a dome of overall thickness of 220 m (Figure 3.5).

5.2 Rock property scaling

The effect of scale on rock properties has been widely discussed in geotechnical literature, with a general consensus that there is a considerable reduction in strength with increasing sample size. Creating a robust relationship between sample size and strength becomes challenging at larger sample sizes due to the practical difficulties in conducting large scale compression testing. The relationship between sample size and strength is shown to be non-linear by *Hoek and Brown* (1980) (Figure 5.15). The scale effect is attributed within the literature to increased heterogeneity at increased sample size and greater probability that micro-cracks will coalesce, leading to unstable crack propagation

and large scale damage to the rock-mass (*Hoek and Brown*, 1997; *Stavrou and Murphy*, 2018). At the intact laboratory scale, it is also unlikely that large discontinuities are not accounted for, e.g. when the discontinuity spacing at rock-mass scale exceeds the laboratory scale sample size. According to the *Hoek and Brown* (1980) scaling law, a 50 mm sample should be scaled to approximately 80% of its intact strength in order to represent a 200 mm sample (Figure 5.15).

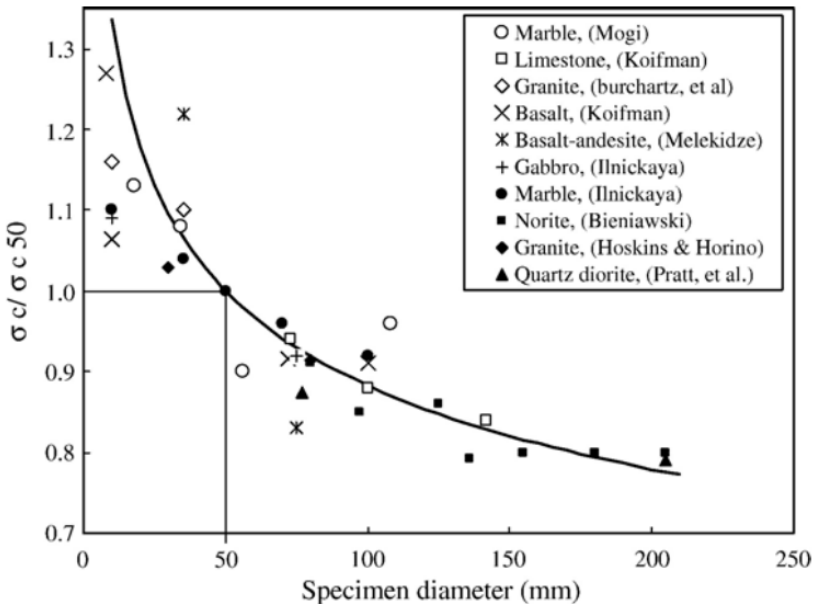

Figure 5.15: Effect of sample size on uniaxial compressive strength of intact rock, from *Hoek and Brown* (1980), where the y-axis is the strength, normalised by the strength of a 50 mm diameter sample.

There have been even fewer studies exploring the relationship between sample size and Young's modulus (e.g. *Pratt et al.*, 1972; *Yoshinaka et al.*, 2008). Studies so far have suggested little to no impact of sample size on Young's modulus, however these studies do not compare the same testing methods. In recent years, there has been increasing evidence that Young's modulus values should be scaled for application to volcanic rock-masses due to the unique fracture state found particularly in a dome carapace (e.g *Heap et al.*, 2018a).

Scale effects have been explored for geotechnical applications through the use of the Rock Mass Rating (RMR; *Bieniawski*, 1978) and Geological Strength Index (GSI; *Hoek et al.*, 1992; *Hoek and Brown*, 1994), where rock-mass strength is reduced based on different geological conditions. RMR considers the spacing, condition and orientation of discontinuities alongside the uniaxial compressive strength of the material and qualitatively classifies the rock from "very poor rock" to "very good rock". GSI characterises blocky rock-masses by determining

the interlock of blocks, and the condition of discontinuities (*del Potro and Hürlimann*, 2008), and this ranges from intact/massive, to laminated/sheared as end members. GSI relates qualitative RMR values to quantitative adaptations of the Hoek-Brown criterion, thus giving predicted compressive strength values for a rock-mass. *Bieniawski* (1989) suggested that rock-mass strength is as little as 15% of its intact equivalent. Both the RMR and GSI schemes have been applied in volcanic environments by previous authors (*Watters et al.*, 2000; *Okubo*, 2004; *Thomas et al.*, 2004; *Heap et al.*, 2018b). The study by *Thomas et al.* (2004) found a 96% reduction in compressive strength between intact samples and the rock-mass scale.

It is clear that there is not a standard rule for applying intact properties to the rock-mass scale. Therefore I use the scaling determined by the model of Volcán de Colima (rock-mass strength = 20% of intact rock strength, as determined in Section 1.4) as it is specific to lava domes.

A recent study by *Heap et al.* (2018b) determined a talus rock strength of 110 MPa in the laboratory, and using the generalised Hoek-Brown failure criterion and a GSI of 50 (very blocky, fair-good rock-mass), determine a scaled dome strength of 6.6 MPa. This estimate does not consider the effect of the viscous dome core on the overall dome strength and is therefore likely an overestimate. In this study, I have estimated a rock-mass dome strength of 3.7 MPa at Volcàn de Colima (Section 1.4.1), and of 1.32 MPa at SHV (Table 5.1). These are on the same order of magnitude as the estimates from *Heap et al.* (2018b); as these estimates are derived from models that include both solid talus and a viscous dome core, they are expectedly lower as the dome core decreases the overall strength of the edifice. Assessing these findings in conjunction with those from *Heap et al.* (2018b) shows how much weaker the overall dome strength is compared to laboratory estimates of single blocks.

The models conducted as part of this study have therefore shown that the inclusion of scaled mechanical properties is crucial to any study of volcanic instability, and I have shown that incorporating rock strength at a rock-mass scale can increase possible unstable material volumes by up to a factor of four (Figure 5.9). This agrees with other recent work highlighting the importance of rock property scaling within volcanological models, particularly with regards to lava dome instability (*Heap et al.*, 2018a,b).

5.3 Wider implications

5.3.1 Timescales

As discussed in Section 3.2.2, the simulations in this model run close to real time and for this reason, I am unable to explicitly compare modelled timescales to real world timescales. In the model of dome growth at Volcán de Colima (Section 1.4), I was able to compare the height and radius evolution of the dome by defining known points in the model time. I was able to define (in both the imagery and the model) the point in time at which the dome grew sufficiently to reach the break in slope. Using this and a known start of extrusion, I could normalise model time to reflect the observational data, thus allowing comparison of the dimensions on the same timescale, but shown in terms of normalised model time steps (Figure 1.13).

The emplacement and collapse models presented throughout Chapter 3 and in Section 5.1.1 of this Chapter are however difficult to relate to a real timescale. They remain indicative of process, and by showing the domes at the same model age, the amount of strain in a given time period can be fairly compared. Given the successful demonstration of modelling lava dome emplacement and evolution using the methods presented here, I suggest that in order to work towards truly *predictive* models, the simulations would need to be adapted for one specific eruptive scenario and left to run so that real timescales could be discerned. This could make it possible to suggest timings of collapse relative to milestones in dome growth being reached, but would require high performance computing and significant optimisation of code to ensure that models could be run on a timescale useful to decision makers.

5.3.2 Growth style

The numerical models presented throughout this project explicitly represent endogenous domes, as dome growth occurs through addition of magma to the base of the dome, rather than by reaching the dome surface and extruding as lava lobes or spines. The presence of shear bands in the model (Section 3.4.1) suggested that exogenous dome growth could occur, but it is not directly simulated in the models. *Hale et al.* (2009a) discusses this in relation to the suite of FEM models summarised in Section 1.2.2, where their suite of finite element models is only grown endogenously as exogenous growth requires the implementation of

additional physics which is still not fully understood or able to be refined using finite elements. *Husain et al.* (2018) suggest that it is possible to model exogenous dome growth in PFC by varying both the flow rate and magma viscosity; low flow rates and high viscosity lead to exogenous growth of spines, whilst high flow rates and lower viscosities result in endogenous growth. Viscosity and flow rate are kept constant in all models presented here, and so this could explain why the same exogenous growth is not clearly observed.

Purely showing endogenous dome growth could also be a result of simulating one continuous period of extrusion. It is more likely that a dome grows via pulses of magma flux that are separated by pauses characterised by no extrusion (as at SHV, shown by the eruptive history in Figure 4.2). Pauses in extrusion would allow a greater degree of cooling to occur, likely creating a thicker intact shell of the dome. I speculate that incorporating pauses of extrusion into PFC could lead to exogenous growth being observed - the force associated with new magma input into the dome could exceed the tensile strength of the talus, causing large-scale fracturing, hence creating a new pathway for magma to reach the surface. Accurate simulation of this would require a more time-dependent method of tracking the core/talus transition, as the pressure-dependent method currently used would not result in additional solidification during a pause in extrusion.

In Chapter 2, I showed that collapse events preceded by endogenous dome growth were likely to be of a larger relative volume than those preceded by exogenous dome growth, with an average relative collapse volume of 76% compared to 24%. This suggests that by modelling endogenous growth in this study, I have investigated the scenario where the largest relative fraction of the dome is susceptible to instability. I speculate that domes grown exogenously would be more susceptible to planar slide type failures (*Hungr et al.*, 2014), as successive layers of similar strength material could act as planes of pre-existing weakness. This relates to the idea of toughness of a volcanic edifice proposed by *Gudmundsson* (2009), whereby fractures are able to propagate more easily through layers with similar mechanical properties.

5.4 Future work

In this project, I have demonstrated the benefit of statistically analysing a global database, an endeavour shown to benefit the field of volcanology by other previous studies (*Acocella*, 2007; *Brown et al.*, 2014; *Ogburn et al.*, 2015). I suggest that

this database be updated with details of future lava dome collapses as more data will only strengthen statistical analysis.

I have also demonstrated how the physical properties of lava dome rock can influence overall dome stability. I have highlighted potential temporal variability in these properties, and suggest that this theory could be tested with a more extensive study of temporally-constrained rocks from the Soufrière Hills eruption.

The primary area that provides the most exciting avenues for development following the findings from this project are found within the numerical model. In this section, I outline avenues of potential exploration for increasing the applicability of the modelling methodology presented throughout this project.

5.4.1 Simulating simultaneous processes

Trigger mechanisms

The most compelling avenue for further research that has emerged from this study is the incorporation of simultaneous processes within the dome, an endeavour that was too computationally expensive to be achieved in the time of this project. Most simply, this includes simulating the triggering processes identified in Chapter 2 as combined forces acting upon the dome. For example, how does internal pressurisation affect a dome that has undergone a switch in extrusion direction? I speculate that more complex modes of failure would result from modelling external triggers acting together to destabilise the dome.

Combined extrusion with trigger mechanisms

It would also be a crucial next step to continue extrusion during the application of external triggering mechanisms. In Chapter 3, I speculated that combining extrusion with internal pressurisation would result in more outwards movement of talus slopes. I suggest therefore that magma influx would act similarly to internal pressurisation, in that new material exerts an outwards force on the existing material above the surface. This development would eradicate the need to use an initial condition in the pressurisation models shown in Section 3.3.3 and Section 5.1.2.

Solidification and cooling

The effect of dome cooling is simulated using solidification as a function of solidus pressure. To implement this in PFC, the model calculates the pressure on any

particle by calculating the weight of the column of material above the particle. This is not only a uni-directional change (solidification is allowed but remelting is not), but the process only occurs whilst active dome growth is being modelled. This means that once an initial condition has been initiated (e.g. the rock strength models presented at the beginning of this chapter), the solidification process is no longer occurring. This is beneficial as it limits computational expense, but it limits the ability for the core to react to changes in pressure caused by deformation of the dome. I believe incorporating solidification after cessation of extrusion is unlikely to change the identified collapse styles in the models presented here, as there is not sufficient movement of the talus material to dramatically alter the proportion of dome core. If the models were run for a sufficient time to allow strain development large enough to show total collapse of a dome flank, the time dependent solidification of dome core would be crucial to dome morphology evolution.

By implementing solidus pressure as a proxy for the cooling process, temperature is not explicitly incorporated within the models in this project. Due to the uncertainties related to core/talus proportions within a lava dome, its temperature profile is poorly understood. *Ball et al.* (2015) calculate temperature profiles for crater-confined and perched dome geometries one year after being extruded, and propose a maximum temperature of 180°C at the conduit, and 140°C for the majority of the dome system.

Shorter term temperature profiles are harder to discern, and very little research has been conducted into the temperature of the talus during active growth. If cooling only occurs by conduction of heat, an approximate cooling timescale can be calculated using:

$$l = \sqrt{\kappa t}, \tag{5.1}$$

where l is the talus thickness, κ is the thermal diffusivity of the rock, and t is the cooling time (*Turcotte and Schubert*, 2002). By considering a thermal diffusivity of $\sim 10^{-6}$ (*Huppert et al.*, 1982), a 15 m thick talus will take approximately 7 years to cool by conduction. The cooling timescale of the talus will be complicated by the heat loss that occurs through the presence of fractures and rainfall (*Dzurisin et al.*, 1990), and the heat circulation that occurs when hydrothermal systems are present in the edifice. In addition, crystallisation induced by cooling releases latent heat, which further increases the time it takes to cool (*Turcotte and Schubert*, 2002). Cooling therefore is likely to have a negligible effect on a dome's

temperature profile in the interior of the dome, and talus temperatures likely remain elevated for a long period of time following dome emplacement.

Therefore an important question for consideration is the effect of this heat on the strength of talus rock. A study conducted by *Heuze* (1983) investigated the mechanical properties of granitic rocks at high temperature, and showed very little difference in mechanical behaviour for Westerly Granite at temperatures up to 500°C, with marked decreases in strength only occurring at 900°C. This agrees with a study by *Stesky et al.* (1974) that shows no effect of temperature on the frictional stresses of Westerly granite up to 600°C. This suggests subjecting igneous rocks to temperatures lower than their solidification temperature does not have a significant impact on their mechanical properties.

There are limited studies into the mechanical behaviour of volcanic rocks at elevated but sub-magmatic temperatures. *Heap et al.* (2014a) conducted extensive laboratory testing into the physical and mechanical properties of edifice-forming andesite from Volcán de Colima. The authors compared rock behaviour at ambient temperatures (∼25°C) to behaviour at 450°C and found no impact of temperature on strength, and differences in elastic moduli (Young's modulus, Poisson's ratio) that fall within the range of sample variability. *Heap et al.* (2018b) investigated the effect of thermal stresses (e.g. transient exposure to high temperatures) on the mechanical behaviour of lava dome rock. Their study concluded that the strength of andesite is in fact higher at increased temperatures, but when scaled strength estimates are examined (through application of the generalised Hoek-Brown failure criterion), dome strength is largely unchanged by high temperatures unless clay materials are present due to hydrothermal alteration (*Rosas-Carbajal et al.*, 2016).

As discussed in Chapter 4, the general consensus from the literature is that exposure to volcanic rocks at temperatures below their solidification temperature either results in comparable strengths (*Heap et al.*, 2014a, 2018b) or higher strengths (*Schaefer et al.*, 2015; *Coats et al.*, 2018) than at room temperature, suggesting that domes are at their weakest following cooling. For this reason, using rock properties determined from room temperature experiments is adequate.

Gaining strength during growth

At the beginning of this Chapter, I presented the relative importance of rock strength on dome stability scenarios using an initial condition of a fully-emplaced

dome. This is a simplistic approach, as the rock properties of the talus are likely to play a key role in determining the morphology of the growing dome. For example, a lower strength is likely to result in a more pancake-style dome, whereas a higher rock strength gives a blockier dome. In order to explore this, high performance computing would be required in order to allow the strength of the talus to change over time. A better physical understanding of this process would also be imperative as many studies suggest that the strength of the dome reduces upon cooling due to contraction and micro-fracturing (*Schaefer et al.*, 2015; *Coats et al.*, 2018; *Lamur et al.*, 2018).

The strength obtained by the modelled material upon its transition from fluid magma to solid rock does not change following continued dome growth. Although this is based on studies suggesting an abrupt rheological change when critical crystal fraction is reached (Section 3.2.2 *Cordonnier et al.*, 2012), the time-dependence of volcanic rock strength during initial cooling has not been thoroughly researched. For this reason, there could be merit in investigating a strengthening of the talus over time, and incorporate a graded strength where minimum strength is observed closest to the core and maximum strength at the outermost edges of the intact talus layer.

5.4.2 Dome type

There have been several classifications of dome type in previous literature (Section 1.1.3, Figure 1.3). All of the modelled domes presented in this project are most similar to the Peléean domes defined by *Blake* (1990) as they fulfil the height/radius relationship of 0.774±0.160 (Table D.1). Peléean domes are of particular relevance to the modelled domes in this Chapter, as *Blake* (1990) suggested that Peléean domes are more sensitive to the mechanical properties of the talus than the other, shallower dome types. In order to fully investigate a wider suite of dome types, sensitivity of the models to magma rheology would need to be explored. As discussed by *Husain et al.* (2014, Section 1.2.2), this would occur through variation of stiffness in PFC, and the main avenue of research would be to determine whether the relationship between collapse mode and unstable material volume is the same for pancake domes as for Peléean domes.

5.4.3 Spatial heterogeneity

Spatial and temporal heterogeneity at volcanoes is commonly discussed as one of the major hurdles in volcanic modelling (*Voight*, 2000; *Thomas et al.*, 2004; *Schaefer et al.*, 2013), with decreases in strength attributed to collapse events (e.g. *Reid et al.*, 2010; *Ball et al.*, 2015). Identifying the nature of spatial heterogeneity is of particular importance as alternating layers of strong and weak volcanic material have been shown to increase the overall edifice strength; this is because alternating layers of strength encourages arrest or deflection of dykes by increasing the edifice toughness, thus increasing the energy required to promote large-scale fracturing (*Gudmundsson*, 2009, 2012; *Heap et al.*, 2014b). If spatially distinct volcanic units with different strengths can be identified (e.g. a strong lobe to the north, and a weak lobe to the south), one could perhaps more simply forecast where material is susceptible to failure.

After identifying temporal heterogeneity during the Soufrière Hills eruption, the logical next step would be to identify spatial heterogeneity as a function of the temporal evolution of the dome. This is not possible at Soufrière Hills due to the nature of the collapses; although the current dome is known to be primarily composed of material from Phases 3 and 5, the spatial distribution of these units is unknown.

To demonstrate the potential effect of spatial rock heterogeneity on overall dome stability, I model an extreme end member scenario where one side of the dome is prevented from moving (i.e. representing the strongest possible rock), and decrease the rock strength on the other side of the dome to be equivalent to rock-mass properties. During early timesteps and prior to large-scale displacement, visualising strain accumulation shows a potential rotational failure plane (Figure 5.16), as seen in the gravitational failure models in Section 3.3.3. These models firstly show that the potential failure plan visualised by strain accumulation is a good indicator of the plane along which collapse occurs. Secondly, by emphasising an extreme spatial heterogeneity, it is possible to create a steep collapse scar, similar to that seen in the present day dome on Montserrat. These models suggest spatial heterogeneity and scaling of rock properties should be strongly considered in lava dome stability models.

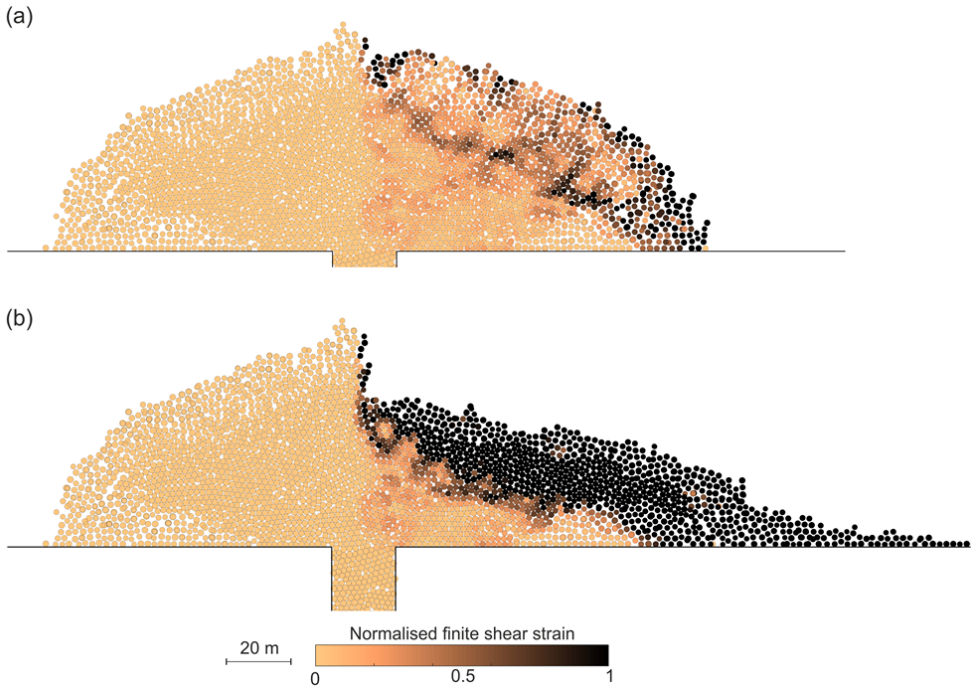

Figure 5.16: Modelled dome with displacement on the left side forced to be zero, and the right side of the dome simulated with rock-mass properties. Domes are visualised by finite shear strain, and show **(a)** the dome during early timesteps prior to large-scale displacement, and **(b)** large-scale displacement.

5.4.4 Fracture networks

As discussed in Section 5.2, discontinuities have a significant impact on the strength of rock at a rock-mass scale. There has not yet been a thorough investigation into discontinuity spacing and scale common to lava domes.

This has been incorporated into the numerical models presented in this chapter by scaling the intact rock strength. Although this considers the impact of fractures on overall strength, it does not consider the geometrical effect of individual large-scale discontinuities. For example, the gas pressurisation models presented by *Voight and Elsworth* (2000) define an arbitrary basal sliding plane through a hemispherical dome, thus isolating a potentially unstable block (Figure 5.17). This models how internal pressure acts as an uplift force onto this failure plane, thus destabilising the slope. The inclination of this basal plane, and the block detachment from a steep rear surface, depend on the existing fracture state of the dome.

Even an extensive field campaign would be limited in its ability to determine the fracture network that exists at a lava dome. Fieldwork undertaken in May 2016 as part of this project at Mt. Unzen in Japan suggested that at least

two different fracture systems are likely to exist at a lava dome: (1) orthogonal fractures (Figure 5.18) that occur due to cooling-induced contraction, similar to the process that forms columnar jointing (*Lamur et al.*, 2018); and (2) onion-skin fractures (Figure 5.19), previously observed by various other authors (*Cole*, 1970; *Nairn et al.*, 2001; *Yokoyama*, 2005; *Maeno and Taniguchi*, 2006). There is suggestion from the literature (e.g. *Fink and Griffiths*, 1998; *Voight and Elsworth*, 2000; *Bull et al.*, 2013) that radial fractures are also common; these provide a third fracture geometry for incorporation into numerical models.

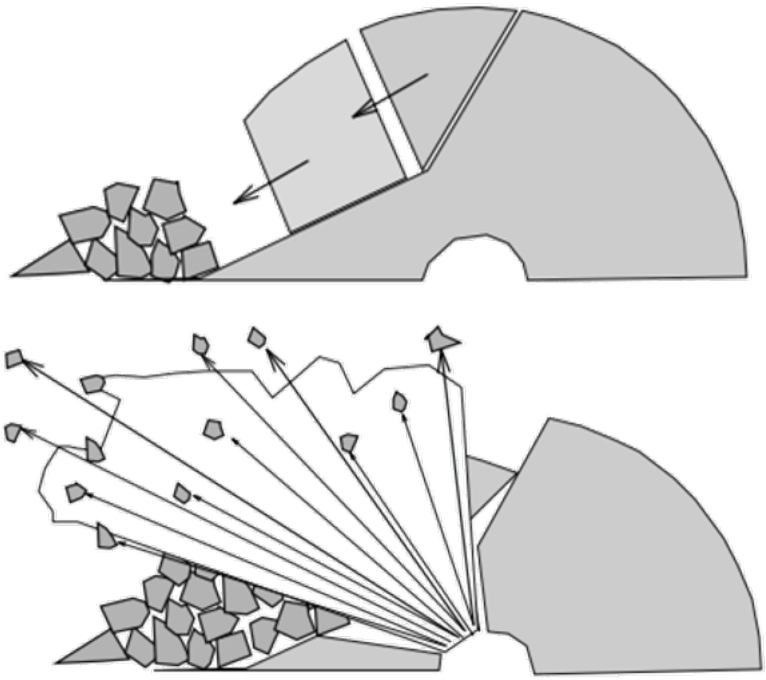

Figure 5.17: Schematic view of dome collapse, whereby diffusive pressure acts on a pre-existing failure plane. Uplift and downslope forces act as disturbing forces driving block movement along the failure plane, thus rapidly exposing the hot dome core to atmospheric pressure, resulting in potential for a directed explosion. Modified from *Voight and Elsworth* (2000).

5.4.5 Talus behaviour

In Chapter 3, I defined talus as any dome material in the system that behaves as rock and throughout the modelling work, I did not distinguish between talus slopes that have become detached from the dome, and the solid, more intact crust of the dome. This is similar to the previous modelling approach by *Hale et al.* (2009a,b). In the model, talus behaves as a coherent rock unit. Behaviour of

Figure 5.18: Photo of near-orthogonal fractures at the upper spine at Mt. Unzen. Outcrop approximately 8 m high.

Figure 5.19: Photo of onion-skin fractures shown on spine at the top of Mt. Unzen, spine is approximately 40 m high.

particles that detach from this rock unit is controlled only by friction, where the balls are assumed to no longer possess cohesion and are unable to form bonds with any balls that they later come into contact with (i.e. simulating a rockfall, where rocks would bounce off of other rocks, rather than create bonds). In this aspect, talus slopes are simulated on the outer flanks of the dome, as in the schematic from *Hutchison et al.* (2013) (Figure 5.20). Within the model this requires a sufficient installation gap (the minimal distance between contacting balls) to be defined in order for the detached ball to no longer be bonded to its neighbouring balls. The definition of this gap has not been fully explored within this project, and I suggest therefore that the volume of detached talus slopes is likely underestimated, whilst the volume of intact talus crust is overestimated. This is particularly evident in photos from the top of the current lava dome at Mt. Unzen (e.g. Figures 5.21, 5.22), where the surface is blocky and superficial activity is likely controlled by the nature of the blocky talus, rather than the underlying solid dome crust.

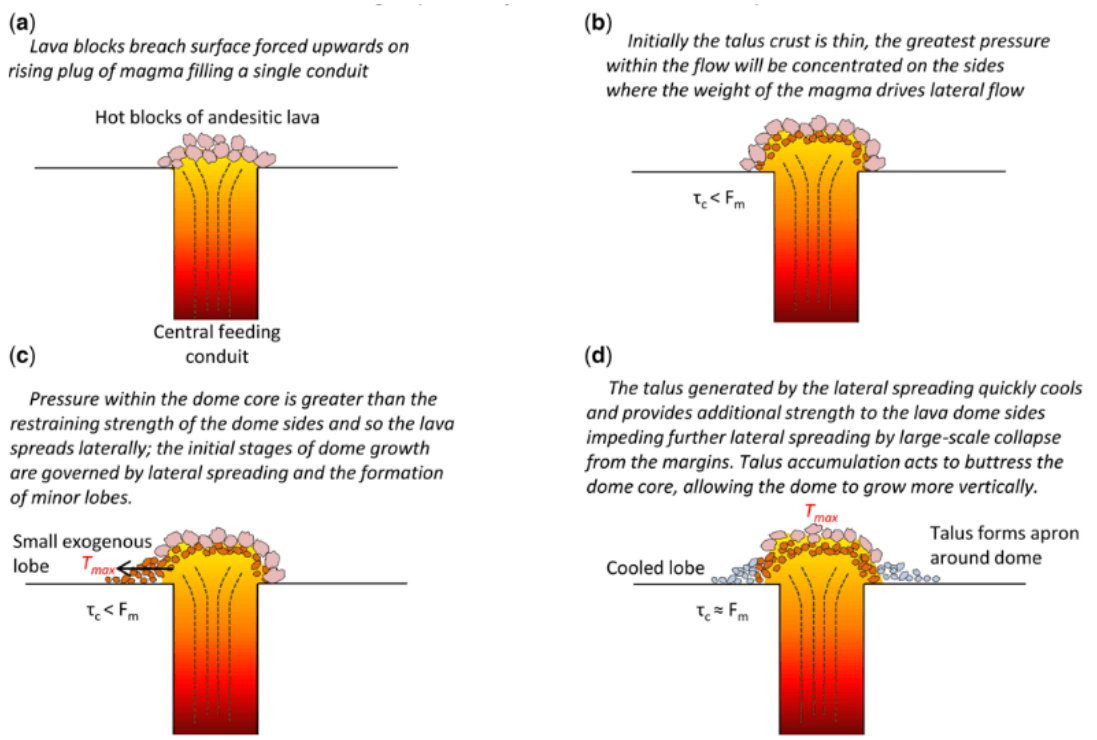

Figure 5.20: Thermal-mechanical framework for dome emplacement and subsequent dome growth at Volcán de Colima, based on observations between February 2007 and December 2010. The symbols τ_c and F_m show magnitude of the restraining strength of talus material (both detached and intact) compared to spreading force of the viscous core material. From *Hutchison et al.* (2013).

An interesting avenue of further model development would therefore be to

explore the generation and behaviour of the talus slopes as a distinct material from the intact talus. This exploration could also benefit from explicitly incorporating a carapace layer into the model (as in Figure 1.1). The behaviour of this could be analogised to brittle magma failure (e.g. *Coats et al.*, 2018).

It could also be beneficial to address the two types of talus behaviour (intact and detached) using additional modelling methodologies; this could be particularly useful for modelling long term dome stability following emplacement. For example, in the latest version of PFC, it is possible to build a coupled discrete element/finite volume model by integrating PFC and FLAC, another software package from Itasca Consulting Group Inc. Recent unpublished work (e.g. Appendix D.1) has shown that coupling the two software allows both a boundary-type model to be coupled with a particle-type model. This could be applied to a lava dome by using the boundary-type model to simulate the lava dome core and intact talus and using the particle-type model to only simulate the detached talus. This would be particularly applicable to explore small-scale talus readjustments, for example ongoing rockfalls at Soufrière Hills which still occur weekly despite almost a 10-year pause in extrusion.

5.4.6 Extrusion rate

I use an ascent rate of 2 m/s in all models presented in this study. This is kept constant throughout this study in order to simplify the number of variables introduced into the model and to allow manageable model run times. The conclusions from *GLADIS* also suggested that extrusion rate was not a determining factor in relative or absolute collapse volume (Figure 2.5). Although this conclusion could be affected by the extrusion rate data availability incorporated into the database, I chose to focus on the parameters more clearly linked to collapse volume, such as collapse mechanism.

The chosen ascent rate is accelerated in order to decrease model runtime and is therefore unrealistically high, but it is possible to use the current codes to run simulations using a slower, more frequently observed ascent velocity. PFC codes cannot strictly be parallelised but PFC is multi-threaded, so would most efficiently work on a single processing unit with multiple cores. This was not possible within the project, but would allow exploration of more realistic extrusion rates, thus allowing timescales to be predicted (Section 5.3.1). Variation in extrusion rate could also allow explicit investigation of exogenous dome growth, as discussed by *Husain et al.* (2018). The importance of extrusion rate in

Figure 5.21: The top of the dome at Mt. Unzen, showing large collapsed spine features, and blocky surface. Author for scale.

Figure 5.22: The top of the dome at Mt. Unzen, with a view over Shimabara in the background.

determining maximum volume loss during collapse has also been discussed within volcano monitoring and observation literature, for example by *Cole et al.* (1998) at SHV, and so it is clear that the effect of extrusion rate requires further investigation before the models presented in this project could be applied in real-time monitoring.

5.5 Summary and key findings

The overall aim of this project was to combine different techniques in order to advance understanding of lava dome mechanics, particularly by investigating conditions that exist at a lava dome prior to collapse. In this thesis, I have explored the topic of lava dome collapse in five main ways:

1. **Statistical analysis of a global dataset:**
   By compiling a database of individual collapse events, I was able to explore if relationships exist between collapse parameters. I showed that relative and absolute collapse volumes are not statistically linked to extrusion rates, and the mechanism of collapse is not linked to the original dome volume. I also demonstrated that endogenous dome growth precedes larger relative collapses (∼75% of the dome).
   Key findings: the mechanism attributed to collapse significantly affects the resultant collapse volume, with failures due to gravitational loading or internal pressurisation the largest of all explored collapse mechanisms (Chapter 2).

2. **Development of a numerical model to simulate emplacement and collapse of a lava dome:**
   I created a discrete element model (DEM) in Particle Flow Code (PFC) to simulate the emplacement of a lava dome, starting from an initial condition of a magma-filled conduit, simulating extrusion using the solidus pressure to control the transition from magma to rock. I validated this model by comparing modelled extrusion (height and width evolution) with observational extrusion data from Volcán de Colima in Mexico. This model showed that dome emplacement was initially dominated by vertical growth, and once the dome reached a critical height, growth occurred primarily through lateral spreading. I also calculated the necessary rock-mass strength that was required in order for the modelled data to match the observational data.

Key findings: a discrete element model was able to match observational dome growth data, and the dome rock properties at rock-mass scale were 80% lower than the laboratory intact rock properties (Section 1.4).

3. **Use of the numerical model to explore collapse mechanisms:**
   I showed how the DEM replicates emplacement and the sensitivity of emplacement to solidus pressure, with lower solidus pressures resulting in a higher core volume fraction. The rheological boundary between core and talus was also shown as highly influential in controlling the location of potential failure plane development, acting as a plane of pre-existing weakness in the dome. I used the emplaced model as an initial condition for the application of triggers identified in Chapter 2 as mechanisms likely to cause collapse. I simulated the following conditions: increased internal pressurisation; a switch in extrusion direction; and extrusion of lava on to non-horizontal topography.
   Key findings: I identified two distinct failure mechanisms: (1) shallow, superficial rockfalls, and (2) deep-seated listric shear planes; the latter of these was linked to gravitational failure or internal pressurisation, whilst smaller rockfall dominated collapse was linked to topographic constraint (Chapter 3). I also concluded that in order to make models more accurate, realistic lava dome rock properties should be incorporated.

4. **Determination of rock properties at Soufrière Hills volcano:**
   I conducted a laboratory investigation into a suite of temporally-constrained rocks from the eruption at Soufrière Hills. By characterising physical and mechanical rock properties (porosity, permeability, uniaxial compressive strength, uniaxial tensile strength, Young's modulus), I found a maximum rock strength in Phase 4 products, and a minimum rock strength in Phase 5 products, suggesting also a temporal evolution in rock strength. I used Schmidt hammer field testing and QEMSCAN mineralogical analysis to support the experimental investigation.
   Key findings: I demonstrated the wide range in physical and mechanical rock properties for the first time for Soufrière Hills, providing the building blocks for exploring dome rock heterogeneity and its effect on overall dome stability using numerical models.

5. **Testing the effect of variable rock properties on modelled dome stability:**

I calibrated the model to three rock property scenarios: intact strong (corresponding to Phase 4, SHV), intact weak (corresponding to Phase 5, SHV), and rock-mass (corresponding to 20% of weak properties). Using an emplaced dome as a starting condition and simulating collapse due to gravitational loading and due to increased pressurisation, I showed that models with rock-mass properties show much more displacement than those with intact rock properties.

Key findings: I showed that the most significant difference in modelled displacement occurs between the models with intact rock properties (strong or weak) and those with rock-mass properties. This suggests that determining the scaling relationship between measured and realistic rock properties could have greater influence on model behaviour than the identification of heterogeneity in the field.

5.6 Concluding remarks

In this project I have explored lava dome collapse using three different methods: (1) statistical analysis of a global, historical database (*GLADIS*); (2) development of a new discrete element method model that simulates lava dome emplacement and collapse; and (3) exploration of rock properties and how they are linked to dynamics of a dome-building eruption and their influence on stability. I used the database to define the factors most commonly attributed as preceding dome collapse. I then used a subset of these factors (switch in extrusion direction, gravitational failure, internal pressurisation, topographical constraint) as input scenarios for the numerical modelling, to test the impact of external triggers on an emplaced dome. I showed that deep-seated, high proportion dome collapses occur due to gravitational instability and internal pressurisation, whilst smaller collapses occur due to topographical constraints. Lastly, I characterised the mechanical properties of dome rock from the Soufrière Hills eruption, identifying possible temporal evolution and large-scale variation. I incorporated end-member mechanical rock properties into the numerical model to show that scaled properties of the rock-mass created a significantly less stable dome than incorporating intact laboratory properties into the model.

The major obstacles faced in order to have greater understanding of lava dome collapse are the internal structure (relative core/talus volume fractions and fracture networks) and a grasp on the timing of collapse given the physical

state of the dome. The numerical modelling presented here shows a promising avenue of research, where additional complexities could continue to be added in order to address different research questions related to lava dome collapse. This work has contributed to the field of knowledge by showing how different drivers of collapse produce different scales of collapse, and this will be key in moving towards forecasting collapse events. Numerical modelling and rock mechanics are often researched as separate fields, but this project has shown that it is through combination of these techniques that the field can truly advance.

Bibliography

Acocella, V. (2007), Understanding caldera structure and development: An overview of analogue models compared to natural calderas, *Earth-Science Reviews*, *85*(3-4), 125–160, doi:10.1016/j.earscirev.2007.08.004.

Ball, J., P. Stauffer, E. Calder, and G. Valentine (2015), The hydrothermal alteration of cooling lava domes, *Bulletin of Volcanology*, *77*(12), 102, doi:10.1007/s00445-015-0986-z.

Bieniawski, Z. T. (1978), Determining rock mass deformability: experience from case histories, *International Journal of Rock Mechanics and Mining Sciences and*, *15*(5), 237–247, doi:10.1016/0148-9062(78)90956-7.

Bieniawski, Z. T. (1989), *Engineering rock mass clasifications: a complete manual for engineers and geologists in mining, civil, and petroleum engineering.*, John Wiley & Sons.

Blake, S. (1990), *Viscoplastic Models of Lava Domes*, pp. 88–126, Springer Berlin Heidelberg, Berlin, Heidelberg, doi:10.1007/978-3-642-74379-5_5.

Brown, S., H. Crosweller, R. S. Sparks, E. Cottrell, N. Deligne, N. Guerrero, L. Hobbs, K. Kiyosugi, S. Loughlin, L. Siebert, and S. Takarada (2014), Characterisation of the Quaternary eruption record: analysis of the Large Magnitude Explosive Volcanic Eruptions (LaMEVE) database, *Journal of Applied Volcanology*, *3*(1), 5, doi:10.1186/2191-5040-3-5.

Bull, K., S. Anderson, A. Diefenbach, R. Wessels, and S. Henton (2013), Emplacement of the final lava dome of the 2009 eruption of Redoubt Volcano, Alaska, *Journal of Volcanology and Geothermal Research*, *259*, 334–348, doi:10.1016/j.jvolgeores.2012.06.014.

Coats, R., J. E. Kendrick, P. A. Wallace, T. Miwa, A. J. Hornby, J. D. Ashworth, T. Matsushima, and Y. Lavallée (2018), Failure criteria for porous dome rocks and lavas: A study of Mt. Unzen, Japan, *Solid Earth*, *9*(6), 1299–1328, doi:10.5194/se-9-1299-2018.

Cole, J. W. (1970), Structure and eruptive history of the Tarawera Volcanic Complex, *New Zealand Journal of Geology and Geophysics*, *13*(4), 879–902, doi:10.1080/00288306.1970.10418208.

Cole, P. D., E. S. Calder, T. H. Druitt, R. Hoblitt, R. Robertson, R. S. J. Sparks, and S. R. Young (1998), Pyroclastic flows generated by gravitational instability of the 1996-97 lava dome of Soufrière Hills Volcano, Montserrat, *Geophysical Research Letters*, doi:10.1029/98GL01510.

Cordonnier, B., L. Caricchi, M. Pistone, J. Castro, K. Hess, S. Gottschaller, M. Manga, and D. B. Dingwell (2012), The viscous-brittle transition of crystal-bearing silicic melt : Direct observation of magma rupture and healing, *Geology*, *40*(7), 611–614, doi:10.1130/G3914.1.

del Potro, R., and M. Hürlimann (2008), Geotechnical classification and characterisation of materials for stability analyses of large volcanic slopes, *Engineering Geology*, *98*(1-2), 1–17, doi:10.1016/j.enggeo.2007.11.007.

Dzurisin, D., R. P. Denlinger, and J. G. Rosenbaum (1990), Cooling rate and thermal structure determined from progressive magnetization of the Dacite Dome at Mount St. Helens, Washington, *Journal of Geophysical Research*, *95*(B3), 2763, doi:10.1029/JB095iB03p02763.

Fink, J. H., and R. W. Griffiths (1998), Morphology, eruption rates, and rheology of lava domes: Insights from laboratory models, *Journal of Geophysical Research*, *103*(10), 527–545, doi:10.1029/97JB02838.

Griffiths, R. W., and J. H. Fink (1993), Effects of surface cooling on the spreading of lava flows and domes, *Journal of Fluid Mechanics*, *252*, 667–702, doi:10.1017/S0022112093003933.

Gudmundsson, A. (2009), Toughness and failure of volcanic edifices, *Tectonophysics*, *471*(1-2), 27–35, doi:10.1016/j.tecto.2009.03.001.

Gudmundsson, A. (2012), Strengths and strain energies of volcanic edifices: Implications for eruptions, collapse calderas, and landslides, *Natural Hazards and Earth System Science*, *12*(7), 2241–2258, doi:10.5194/nhess-12-2241-2012.

Hale, A., E. Calder, S. Loughlin, G. Wadge, and G. Ryan (2009a), Modelling the lava dome extruded at Soufrière Hills Volcano, Montserrat, August 2005-May 2006. Part I: Dome shape and internal structure, *Journal of Volcanology and Geothermal Research*, *187*(1-2), 69–84, doi:10.1016/j.jvolgeores.2009.08.014.

Hale, A., E. Calder, S. Loughlin, G. Wadge, and G. Ryan (2009b), Modelling the lava dome extruded at Soufrière Hills Volcano, Montserrat, August 2005-May

2006. Part II: Rockfall activity and talus deformation, *Journal of Volcanology and Geothermal Research*, *187*(1-2), 69–84, doi:10.1016/j.jvolgeores.2009.08.014.

Heap, M., M. Villeneuve, J. Farquharson, F. Albino, E. Brothelande, and J. L. Got (2018a), Towards more realistic values of elastic moduli for volcano modelling, *Tech. Rep. EGU2018-3909*.

Heap, M. J., Y. Lavallée, L. Petrakova, P. Baud, T. Reuschlé, N. R. Varley, and D. B. Dingwell (2014a), Microstructural controls on the physical and mechanical properties of edifice-forming andesites at Volcán de Colima, Mexico, *Journal of Geophysical Research: Solid Earth*, *119*(4), 2925–2963, doi:10.1002/2013JB010521.

Heap, M. J., T. Xu, and C. feng Chen (2014b), The influence of porosity and vesicle size on the brittle strength of volcanic rocks and magma, *Bulletin of Volcanology*, *76*(9), 1–15, doi:10.1007/s00445-014-0856-0.

Heap, M. J., R. Coats, C. feng Chen, N. Varley, Y. Lavallée, J. Kendrick, T. Xu, and T. Reuschlé (2018b), Thermal resilience of microcracked andesitic dome rocks, *Journal of Volcanology and Geothermal Research*, *367*, 20–30, doi:10.1016/j.jvolgeores.2018.10.021.

Heuze, F. E. (1983), High-temperature mechanical, physical and Thermal properties of granitic rocks- A review, *International Journal of Rock Mechanics and Mining Sciences and*, *20*(1), 3–10, doi:10.1016/0148-9062(83)91609-1.

Hoek, E., and E. Brown (1980), *Underground Excavation in Rock*, The Institution of Mining and Metallurgy, London.

Hoek, E., and E. Brown (1994), *Underground Excavations in Rock*, 3 ed., CRC Press, London.

Hoek, E., and E. Brown (1997), Practical estimates of rock mass strength, *International Journal of Rock Mechanics and Mining Sciences*, *34*(8), 1165–1186, doi:10.1016/S1365-1609(97)80069-X.

Hoek, E., D. Wood, and S. Shah (1992), A modified Hoek-Brown criterion for jointed rock masses, *Proceedings of the rock mechanic symposium. International Society of Rock Mechanics Eurock" 92*, pp. 209–214.

Hungr, O., S. Leroueil, and L. Picarelli (2014), The Varnes classification of landslide types, an update, *Landslides*, *11*(2), 167–194, doi:10.1007/s10346-013-0436-y.

Huppert, H., J. Shepherd, H. Sigurdsson, and R. Sparks (1982), On lava dome growth, with application to the 1979 lava extrusion of the Soufrière of St. Vincent, *Journal of Volcanology and Geothermal Research*, *14*, 199–222, doi:10.1016/0377-0273(82)90062-2.

Husain, T., D. Elsworth, B. Voight, G. Mattioli, and P. Jansma (2014), Influence of extrusion rate and magma rheology on the growth of lava domes: Insights from particle-dynamics modeling, *Journal of Volcanology and Geothermal Research*, *285*, 110–117, doi:10.1016/j.jvolgeores.2014.08.013.

Husain, T., D. Elsworth, B. Voight, G. Mattioli, and P. Jansma (2018), Influence of conduit flow mechanics on magma rheology and the growth style of lava domes, *Geophysical Journal International*, *213*(3), 1768–1784, doi:10.1093/gji/ggy073.

Hutchison, W., N. Varley, D. M. Pyle, T. A. Mather, and J. A. Stevenson (2013), Airborne thermal remote sensing of the Volcán de Colima (Mexico) lava dome from 2007 to 2010, *Geological Society, London, Special Publications*, *380*(1), 203–228, doi:10.1144/SP380.8.

Lamur, A., Y. Lavallée, F. E. Iddon, A. J. Hornby, J. E. Kendrick, F. W. Von Aulock, and F. B. Wadsworth (2018), Disclosing the temperature of columnar jointing in lavas, *Nature Communications*, *9*(1), doi:10.1038/s41467-018-03842-4.

Maeno, F., and H. Taniguchi (2006), Silicic lava dome growth in the 1934-1935 Showa Iwo-jima eruption, Kikai caldera, south of Kyushu, Japan, *Bulletin of Volcanology*, *68*(7-8), 673–688, doi:10.1007/s00445-005-0042-5.

Mueller, S., O. Melnik, O. Spieler, B. Scheu, and D. B. Dingwell (2005), Permeability and degassing of dome lavas undergoing rapid decompression: An experimental determination, *Bulletin of Volcanology*, *67*(6), 526–538, doi:10.1007/s00445-004-0392-4.

Mueller, S., B. Scheu, O. Spieler, and D. B. Dingwell (2008), Permeability control on magma fragmentation, *Geology*, *36*(5), 399–402, doi:10.1130/G24605A.1.

Nairn, I. a., S. Self, J. W. Cole, G. S. Leonard, and C. Scutter (2001), Distribution, stratigraphy, and history of proximal deposits from the c. AD 1305 Kaharoa eruptive episode at Tarawera Volcano, New Zealand, *New Zealand Journal of Geology and Geophysics*, *44*(3), 467–484, doi:10.1080/00288306.2001.9514950.

Ogburn, S., S. Loughlin, and E. Calder (2015), The association of lava dome growth with major explosive activity (VEI4): DomeHaz, a global dataset, *Bulletin of Volcanology*, *77*(40), doi:10.1007/s00445-015-0919-x.

Okubo, C. H. (2004), Rock mass strength and slope stability of the Hilina slump, Kilauea volcano, Hawai'i, *Journal of Volcanology and Geothermal Research*, *138*(1-2), 43–76, doi:10.1016/j.jvolgeores.2004.06.006.

Pratt, H. R., A. D. Black, W. S. Brown, and W. F. Brace (1972), The effect of speciment size on the mechanical properties of unjointed diorite, *International Journal of Rock Mechanics and Mining Sciences and*, *9*(4), 513–516, doi:10.1016/0148-9062(72)90042-3.

Reid, M. E., T. E. Keith, R. E. Kayen, N. R. Iverson, R. M. Iverson, and D. L. Brien (2010), Volcano collapse promoted by progressive strength reduction: New data from Mount St. Helens, *Bulletin of Volcanology*, *72*(6), 761–766, doi:10.1007/s00445-010-0377-4.

Rosas-Carbajal, M., J. C. Komorowski, F. Nicollin, and D. Gibert (2016), Volcano electrical tomography unveils edifice collapse hazard linked to hydrothermal system structure and dynamics, *Scientific Reports*, *6*(July), 1–11, doi:10.1038/srep29899.

Schaefer, L. N., T. Oommen, C. Corazzato, A. Tibaldi, R. Escobar-Wolf, and W. I. Rose (2013), An integrated field-numerical approach to assess slope stability hazards at volcanoes: The example of Pacaya, Guatemala, *Bulletin of Volcanology*, *75*(6), 1–18, doi:10.1007/s00445-013-0720-7.

Schaefer, L. N., J. E. Kendrick, T. Oommen, Y. Lavallée, and G. Chigna (2015), Geomechanical rock properties of a basaltic volcano, *Frontiers in Earth Science*, *3*(June), 1–15, doi:10.3389/feart.2015.00029.

Stavrou, A., and W. Murphy (2018), Quantifying the effects of scale and heterogeneity on the confined strength of micro-defected rocks, *International Journal of Rock Mechanics and Mining Sciences*, *102*(November 2017), 131–143, doi:10.1016/j.ijrmms.2018.01.019.

Stesky, R. M., W. F. Brace, D. K. Riley, and P. Y. F. Robin (1974), Friction in faulted rock at high temperature and pressure, *Tectonophysics*, *23*(1-2), 177–203, doi:10.1016/0040-1951(74)90119-X.

Thomas, M. E., N. Petford, and E. N. Bromhead (2004), Volcanic rock-mass properties from Snowdonia and Tenerife: implications for volcano edifice strength, *Journal of the Geological Society*, *161*(6), 939–946, doi:10.1144/0016-764903-166.

Turcotte, D. L., and G. Schubert (2002), *Geodynamics*, second ed., The Press Syndicate of the University of Cambridge, Cambridge, UK.

Varnes, D. J. (1958), Landslide types and processes, in *Landslides and engineering practice*, pp. 20–47, Highway Research Board.

Voight, B. (2000), Structural stability of andesite volcanoes and lava domes, *Philosophical Transactions of the Royal Society of London*, *358*, 1663–1703.

Voight, B., and D. Elsworth (2000), Instability and collapse of hazardous gas-pressurized lava domes, *Geophysical Research Letters*, *27*(1), 1–4, doi:10.1029/1999GL008389.

Watters, R. J., D. R. Zimbelman, S. D. Bowman, and J. K. Crowley (2000), Rock mass strength assessment and significance to edifice stability, Mount Rainier and Mount Hood, Cascade Range volcanoes, *Pure and Applied Geophysics*, *157*(6-8), 957–976, doi:10.1007/s000240050012.

Yokoyama, I. (2005), Growth rates of lava domes with respect to viscosity of magmas, *Annals of Geophysics*, *48*(6), 957–971, doi:10.4401/ag-3246.

Yoshinaka, R., M. Osada, H. Park, T. Sasaki, and K. Sasaki (2008), Practical determination of mechanical design parameters of intact rock considering scale effect, *Engineering Geology*, *96*(3-4), 173–186, doi:10.1016/j.enggeo.2007.10.008.

Appendix A

Supplementary Material for Chapter 1

The material presented in Appendix A.4 was included as online Supplementary Material in the following publication:
Walter, T. W., **Harnett, C. E.**, Varley, N., Bracamontes, D.V., Salzer, J., Zorn, E. U., Bretón, Arámbula, R., and Thomas, M. E. (2019). *Imaging the 2013 explosive crater excavation and new dome formation at Volcán de Colima with TerraSAR-X, time-lapse cameras and modelling.* Journal of Volcanology and Geothermal Research, 369, pp. 224-237, doi:10.1016/j.jvolgeores.2018.11.016.

A.1 Methodology: DEM modelling

The DEM works through a calculation cycle on every timestep of the model (Figure A.1): the contact mechanics are used to update the forces and moments in the model. These are used to determine the individual particle accelerations, which are used to determine the velocities and new positions of each particle.

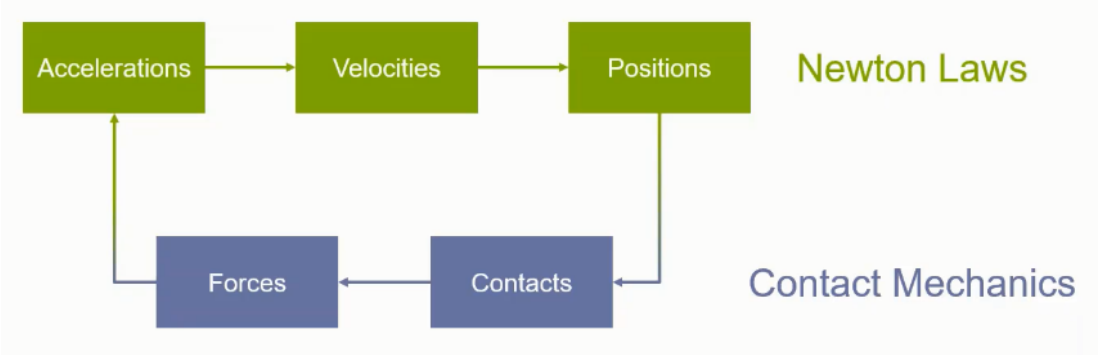

Figure A.1: Calculation cycle in DEM. Credit: Mariana Sousani.

Newton's laws of motions are used to calculate the rotational and translational motion of each particle. Particle rotation is calculated using:

$$M = I\frac{\delta w}{\delta t}, \tag{A.1}$$

where M is the contact torque, I is the moment of inertia, w is the angular acceleration, and t is the timestep. Translational movement is calculating by

$$m\frac{\delta v}{\delta t} = F_g + F_C + F_{nc}, \tag{A.2}$$

where m is particle mass, $\frac{dv}{dt}$ is translational acceleration (change in velocity per change in time), F_g is the gravitational force, F_c is the contact force, and F_{nc} is the non-contact force.

Once the positions have been updated, the timestep calculations are complete and the algorithm searches again for the contacts. An advantage of DEM is that contacts can be updated and created throughout cycling.

DEM can use a hard-sphere or a soft-sphere approach; this determines whether particle overlaps are allowed within the model. Particle Flow Code (PFC), the model used throughout this project, uses a soft-sphere approach, meaning that the particles are rigid but small overlaps are allowed. This is thought to allow a more accurate evaluation of model forces.

A.2 Theory of Particle Flow Code

PFC enables the user to divide a rock mass into discretized smaller elements called particles, the size and geometry of which are determined by the user. These particles do not necessarily represent crystals or rock fragments, but rather allow the user to model the forces acting within the system by defining the forces controlling particle-particle interactions. The model system (particles, contacts, forces) is updated at every time step using the discrete element method (*Cundall and Strack*, 1979).

Particle interactions are controlled by both the deformability and strength criteria of the contacts between the particles. Each flat-joint bond has a finite strength, both in shear and tension. These are represented by the tensile strength (fj_{ten}) and the shear strength respectively, where the shear strength (τ_C) is derived from the Mohr-Coulomb failure criterion:

$$\tau_C = C_b - \sigma \tan\phi_b, \tag{A.3}$$

where C_b is the bond cohesion, σ is the normal stress at the contact, and ϕ_b is the angle of friction.

When the stress imposed upon a ball (i.e. the shear or tensile stress at the contact location) exceeds the tensile or cohesive strength, the bond breaks. After bond breakage, particle behaviour is controlled by the friction coefficient, and tensile and cohesive strengths no longer play any part in the material response.

The deformability parameters feeding into particle behaviour are shear stiffness (fj_{ks}), normal stiffness (fj_{kn}), and effective modulus (fj_{emod}). The stiffness values are used to compute the normal and shear forces, as required for the force-displacement law used in PFC. Shear force (F_s) is defined using

$$F_s = -k_s \Delta U_s, \tag{A.4}$$

where U_s is the shear displacement. Normal force F_n is defined using

$$F_n = k_n (D_{eq} - d^{A,B}) n, \tag{A.5}$$

where D_{eq} is the equilibrium distance between two particles (set when the contact was initially created), $d^{A,B}$ is the current distance between the two particles, and n is the unit vector pointing from the centre of sphere A to sphere B.

The effective modulus contributes to the macro Young's modulus of the

material and is a read-only property within PFC (fj_{emod}). It relates to the stiffness parameters (input by the user) by

$$k_n = \frac{fj_{emod}}{L}, \tag{A.6}$$

where L is the sum of the radii of the two balls in contact.

Once the user creates particles and defines the forces between them, this synthetic material can be calibrated with the mechanical behaviour of a rock by simulating laboratory experiments. These methods will be further discussed in Section 1.3. To illustrate a simple example of a PFC model environment, I use a volcanic pile of particles to demonstrate how collapse can be initiated by lowering the angle of friction on one side of the dome (Figure A.2).

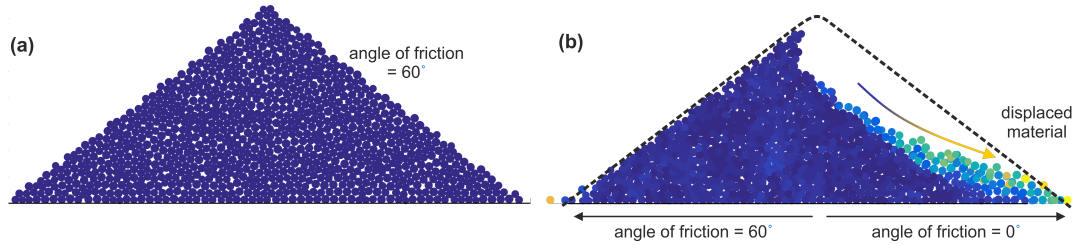

Figure A.2: **(a)** A mechanically stable test dome that has reached equilibrium under gravity, after completion of the procedure for generating a PFC material with low locked-in stresses (as outlined in Appendix A.2.2); and **(b)** the same test dome after the angle of friction for half the dome has been reduced.

Particles in a PFC model are described as bodies to illustrate that they have a finite mass and a well-defined surface (*Potyondy*, 2016); bodies are further classified as balls, clumps, or walls. Balls are rigid disks with unit thickness in PFC2D (compared to spherical bodies in PFC3D) (*Itasca*, 2016), whereas clumps are irregularly-shaped. Only balls will be implemented in the models in this study. Surfaces are provided by walls, whereby the forces between the balls/clumps and the wall can also be defined.

It is important to note that the condition of the 2D models is neither explicitly plane stress or plane strain, but rather the out-of-plane forces and displacements are neglected in the calculations of force, moment and displacement (*Potyondy*, 2017).

A.2.1 Contact mechanics

The forces between the particles are defined by the nature of the contacts that exist between neighbouring particles. These contacts are created and deleted

based on the proximity of the particles to their neighbouring particles (or particles and their proximity to walls). Each contact stores a force and a moment, the behaviour of which is defined by contact models; these are fundamental to creating a realistic material in PFC as they determine mechanical behaviour. In the models presented throughout this work, the parallel-bonded contact model (PBM) and flat-jointed contact model (FJM) will be implemented (please refer forward to Figure 3.1 for schematics).

Parallel-bonded contact model

The linear PBM provides behaviour of two interfaces; the first is the most basic linear contact that can be implemented in PFC, and the second acts in parallel to the first interface. These interfaces are "infinitesimal, linear elastic (no-tension) and frictional" (*Potyondy*, 2016), and carry both a force and moment. The second interface is required in order to resist relative rotation, and rather than imposing a Coulomb limit on the shear force, the behaviour of this second interface is linear until the maximum stress (defined by the user) is exceeded causing bond breakage. If a parallel bond is broken in this way, the material reverts to being linearly-bonded: in this instance, it will be primarily controlled by the linear friction coefficient. This can be compared to a pile of sand; the linearly-bonded material will act as dry sand and will settle at its natural angle of repose, whereas parallel-bonded material will act similarly to wet sand, where the moisture represents the additional strength that is determined by the bond strength.

The most important properties required to use the PBM are: effective modulus; stiffness ratio (normal to shear); friction coefficient; friction angle; and installation gap. It is also necessary to define the linear properties that will be used in the case of bond breakage; these are: effective modulus; stiffness ratio; and friction coefficient. Full description of how these contacts control particle behaviour are provided by *Potyondy and Cundall* (2004).

In the models presented in this study, the PBM is used to define magma before crystallisation to rock. This is done in order to adopt the PBM micro-property values defined by *Husain et al.* (2014) in all modelled fluid material. *Husain et al.* (2014) carried out a comprehensive sensitivity analysis to establish how material behaviour was affected by each of the PB properties; we use this analysis to define micro-properties that give the most reasonable lava dome morphology. Parallel bonds are used to model fluid in this work, in order to restrict particles from

rotating relative to each other (*Husain et al.*, 2014) and giving a material that behaves as a highly-viscous fluid.

Parallel bonds were used to create a Bonded Particle Model (BPM) in PFC, which is said to replicate the behaviour of solid rock (*Potyondy and Cundall*, 2004; *Potyondy*, 2015; *Cundall et al.*, 2008), whereby they assume that rock can be represented as a heterogeneous material comprised of cemented grains. The cement is not a true cement such as in sandstone, but rather a notional cement that represents the granular interlock present in crystalline rocks. After following a specific material genesis procedure (see Section A.2.2), the final bonded material represents an intact rock that is homogeneously isotropic at a scale larger than the grain size (*Itasca*, 2016). However, the BPM encountered three main problems:

1. Unrealistically low UCS/TS ratio
2. Unrealistically low angle of internal friction
3. Repeated tests only provide a linear failure envelope

Wu and Xu (2016) explain that the primary flaw in the BPM is that spherical particles do not provide adequate grain interlocking, and so the number of contact points per particle is too small. They also suggest that spherical particles cannot properly reproduce rotational resistance, as they lead to excessive rolling. For these reasons, parallel bonds are used in any fluid modelling in this project to replicate the work of *Husain et al.* (2014, 2018), but when modelling solid rock, the flat-jointed contact model, a later improvement to the BPM, is used.

Flat-jointed contact model

The problems identified with the BPM were addressed with several following contact models, such as the clustered particle model (*Potyondy and Cundall*, 2004), the clumped particle model (*Cho et al.*, 2007) and the grain-based particle model (*Potyondy*, 2010). These all focussed on changing the shape of the particles in order to address the problems related to the particle shape giving unrealistic material behaviour. The newest update to Itasca presented the flat-jointed contact model (FJM; Figure A.3, Figure 3.1).

The FJM changes the shape of the contact that exists in the conventional BPM, to create a skirted particle (*Wu and Xu*, 2016; *Potyondy*, 2012). This provides increased grain interlocking and rotational resistance. Unlike the previous models, the flat-joint particle bond is not deleted following bond

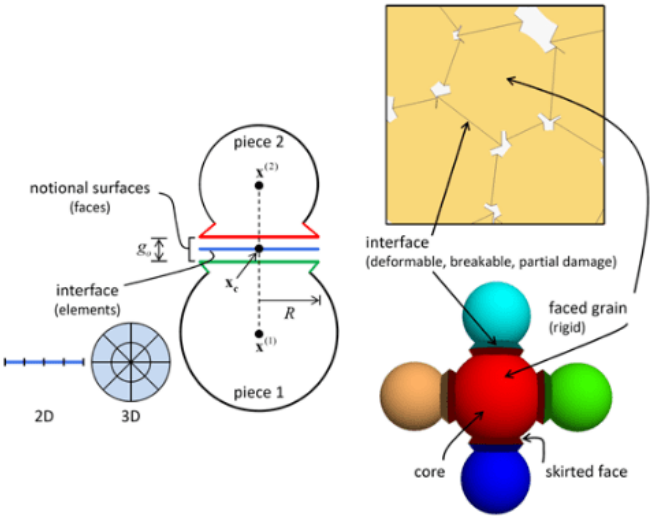

Figure A.3: A flat-jointed contact (left) and a flat-jointed material (right), from *Itasca* (2016).

breaking; this means that rotational resistance is maintained after the contact is broken so the excessive rolling seen in the BPM does not occur using the FJM. The contact itself is a flat line and is made of several individual elements; this means that the surface can experience partial damage.

The increased grain interlock ensures that a flat-jointed material is able to better match the ratio of uniaxial compressive strength to tensile strength when the material is calibrated with laboratory experiments on real rock. *Potyondy* (2012) suggests therefore that the FJM supersedes the BPM and although this is still a simplistic interpretation of rock behaviour, any calibrated model can be used to study, and make quantitative analysis of rock damage. Therefore, the FJM is used throughout this work where solid rock behaviour is intended.

A.2.2 Material generation

The material genesis procedure is crucial in order to achieve correct calibration of a material, and must be completed before simulating any larger scenarios in PFC. As outlined by *Potyondy and Cundall* (2004), the material genesis procedure follows five steps:

1. *Compact initial assembly:* Arbitrarily placed particles are generated to fill a rectangular vessel with frictionless walls. A small particle-wall overlap is assigned, and the number of particles is assigned to give an initial porosity of 16%. This ensures a tight initial packing. The particles are installed at

50% of their original size to ensure no overlaps, and then increased to their final size and allowed to rearrange under zero friction.

2. *Install specified isotropic stress:* Particle radii are reduced to give a specified isotropic stress (this is 1% of the UCS). This step of the process reduces the locked-in forces.

3. *Reduce the number of floating particles:* A floating particle is defined as a particle that has fewer than three contacts. In order to obtain a well connected material, the radii of the floating particles are increased until the number of unbonded particles is considerably reduced.

4. *Install parallel bonds:* Parallel bonds are installed between all particles within a given proximity, and parallel bond properties and friction coefficient are assigned.

5. *Remove from material vessel:* To complete the material genesis procedure, the vessel walls are deleted and the material is allowed to relax. This generates locked-in forces that are likely to exist in a rock sample.

A.2.3 Limitations of the DEM method

1. *2-dimensional models*
   The 2D nature of the models in this work limits the real-world application of these models, as they cannot be used to infer directions of instability. A simple dome emplacement model was run in PFC3D to explore whether 3D modelling was a possible avenue of further research. 3D modelling was not further explored due to the computational expense of modelling in 3D: runtime for the simplest 2D model = 1.5 hours, whereas runtime for the simplest 3D model = 21 days. I therefore use only 2D modelling, and use this to test relative rather than absolute impact of causal mechanisms on stability in Chapter 3.

2. *Particle rigidity*
   Material deformation occurs in PFC via contact breaking, rather than by particle shape change. However, Potyondy and Cundall (*Potyondy and Cundall*, 2004) argue that this is reasonable when material deformation is mostly controlled by movement along interfaces, e.g. through sliding and rotation of the particles.

3. *Model resolution* It is important to choose a particle size that provides a compromise between high model resolution and reasonable computation time. Itasca have shown that the macroscopic elastic constants, and uniaxial compressive strength of rocks using the BPM and FJM are independent of particle size in 2D (*Potyondy and Cundall*, 2004; *Potyondy*, 2012). However the tensile strength is shown to be dependent on particle size (*Potyondy*, 2012), and so once material is calibrated with a small particle size, I repeat the uniaxial compressive strength and tensile strength experiments within PFC to ensure that the macroscopic behaviour is the same at a much larger particle size (equivalent to the ball radius used in the final model) to ensure that macro-behaviour is as expected. Figure A.4 shows how similar dome geometries are visualised using different particle sizes.

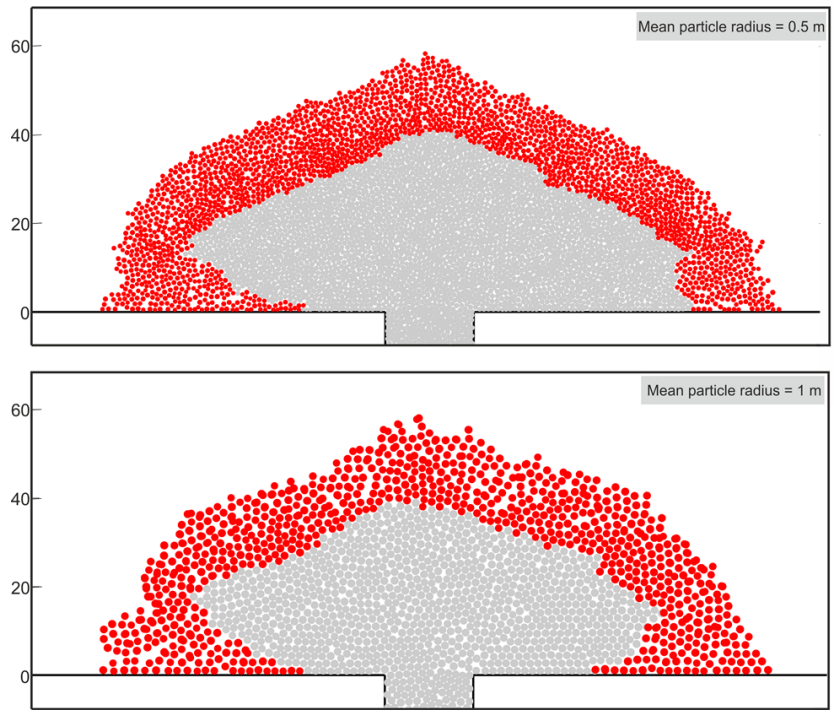

Figure A.4: Visualising dome geometry using a mean particle size of 1 m and 0.5 m, where red material is fluid core, and grey material is solid talus.

A.3 Supplementary Figures

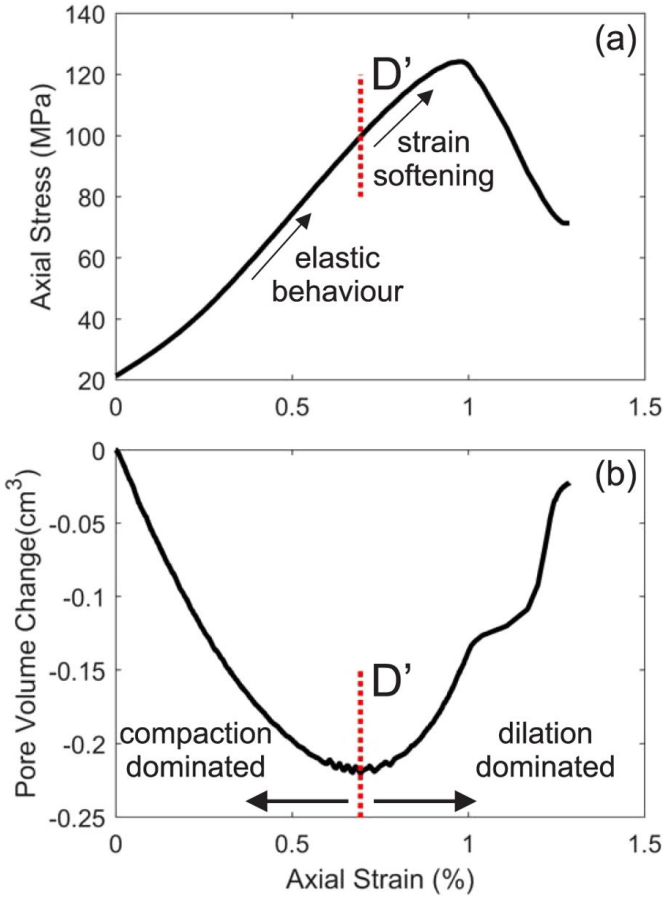

Figure A.5: Description of D' depicted by the dotted line, as defined by *Heap et al.* (2009), where **(a)** shows stress-strain data, and how D' shows the onset of strain softening, and **(b)** shows how D' can be defined using the associated pore volume change during a compressive laboratory test. Figure taken from *Harnett et al.* (2018).

A.4 Volcán de Colima model: supplementary information

The model is initialised with lava material in the conduit and topography that matches the observed topography from the high resolution time lapse camera. For simplicity, the topography within the crater is assumed to be horizontal. A vertical velocity is given to all material in the conduit to simulate extrusion.

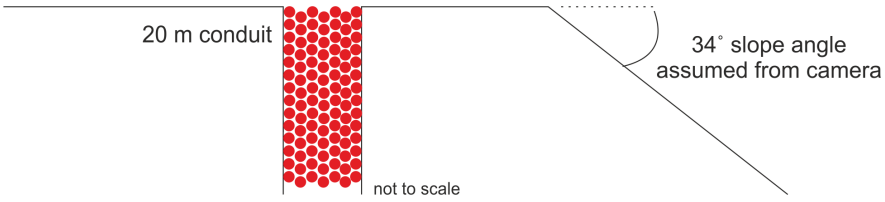

Figure A.6: Conceptual diagram of model setup.

The surface boundaries in this instance are given purely frictional properties. This ensures, for example, that particles do not endlessly roll downhill. There are otherwise no cohesive bond properties between balls and boundaries.

In order to equate the timescales between the observations and the model scenario, we use the start of extrusion as Time 0 in each case, and the point at which the dome reaches the break in slope as Time 1. We then adopt normalised time between these two end points.

A.4.1 Material calibration

Material behaviour is controlled in PFC by the micro-properties that exist at the contacts between particles. These micro-properties are not equivalent to the macro-properties of the material as a whole. Therefore, a calibration procedure is required to determine the micro-properties that result in the same macro-behaviour of the model material to the real material in the laboratory (Figure A.7).

We then iteratively adapt these parameters to fit the modelled dome extrusion to the observational data. Once the two datasets match, we can use the parameters to back-analyse the required intact rock strength (Figure A.8).

A.4.2 3D correction

Complex models in PFC in 3D are very computationally expensive, and so the models in this paper are presented in 2D. However, there are limitations to

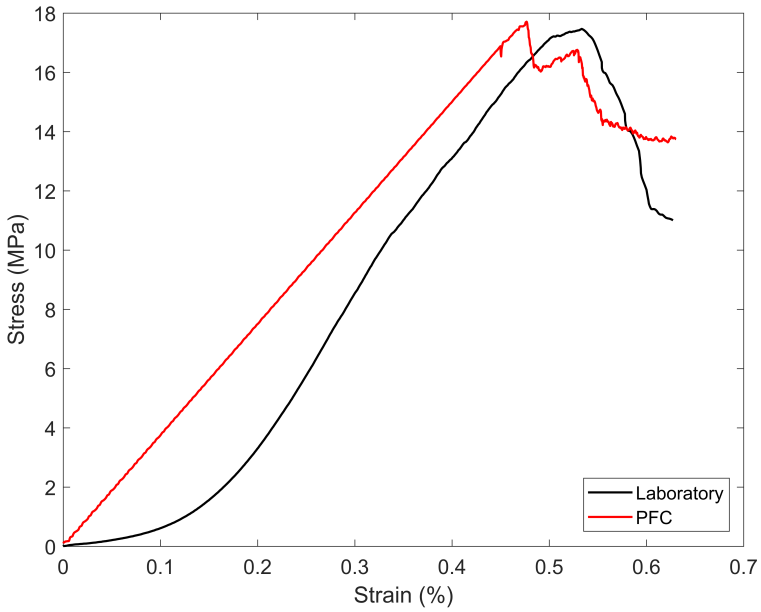

Figure A.7: Stress-strain curves showing the macro-scale behaviour from the laboratory material (*Heap et al.*, 2014) and the PFC material. Peak stress of laboratory tested material = 17.5 MPa, Young's modulus = 8.1 GPa.

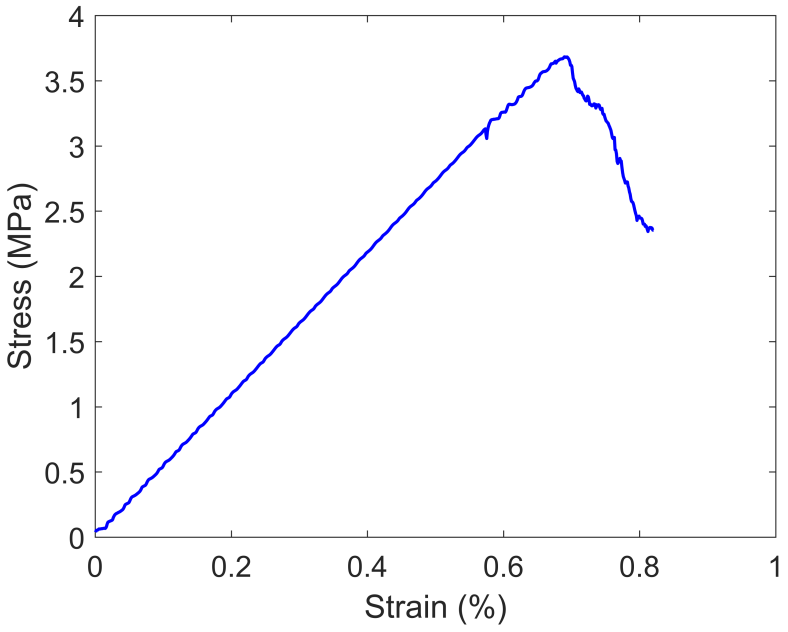

Figure A.8: Stress-strain response from the PFC material that is required to fit the observational data from the time-lapse camera at Colima. Peak stress = 3.7 MPa, Young's modulus = 5.5 GPa.

comparing the 2D method with the 3D observational data. To overcome this, we perform a calibration of the PFC data. By extruding material using the same model parameters in both 2D and 3D, we see that in 2D, the model gains more height as it cannot spread laterally in several directions (Figure A.9). This results in an overestimate of height (by approximately 33%) and an underestimate in width (by approximately 33%). We apply these correction factors to the data presented.

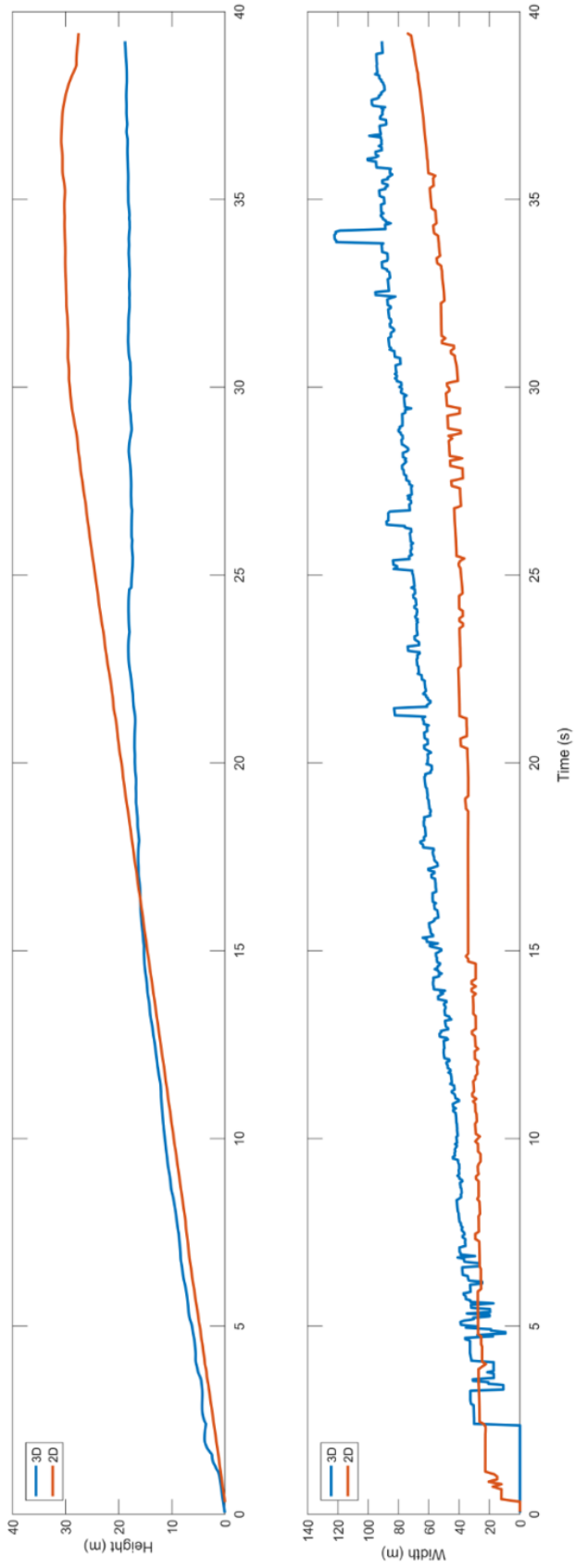

Figure A.9: Height and width evolution of a PFC dome in 2D and 3D

Bibliography

Cho, N., C. Martin, and D. Sego (2007), A clumped particle model for rock, *International Journal of Rock Mechanics and Mining Sciences*, *44*(7), 997–1010, doi:10.1016/j.ijrmms.2007.02.002.

Cundall, P., and O. Strack (1979), A discrete numerical model for granular assemblies, *Geotechnique*, *29*(1), 47–65.

Cundall, P. A., M. E. Pierce, and D. Mas Ivars (2008), Quantifying the Size Effect of Rock Mass Strength, *1st Southern Hemisphere International Rock Mechanics Symposium*, (July).

Harnett, C. E., P. M. Benson, P. Rowley, and M. Fazio (2018), Fracture and damage localization in volcanic edifice rocks from El Hierro, Stromboli and Tenerife, *Scientific Reports*, *8*(1), 1942, doi:10.1038/s41598-018-20442-w.

Heap, M. J., P. Baud, P. G. Meredith, a. F. Bell, and I. G. Main (2009), Time-dependent brittle creep in darley dale sandstone, *Journal of Geophysical Research: Solid Earth*, *114*(7), B07,203, doi:10.1029/2008JB006212.

Heap, M. J., Y. Lavallée, L. Petrakova, P. Baud, T. Reuschlé, N. R. Varley, and D. B. Dingwell (2014), Microstructural controls on the physical and mechanical properties of edifice-forming andesites at Volcán de Colima, Mexico, *Journal of Geophysical Research: Solid Earth*, *119*(4), 2925–2963, doi:10.1002/2013JB010521.

Husain, T., D. Elsworth, B. Voight, G. Mattioli, and P. Jansma (2014), Influence of extrusion rate and magma rheology on the growth of lava domes: Insights from particle-dynamics modeling, *Journal of Volcanology and Geothermal Research*, *285*, 110–117, doi:10.1016/j.jvolgeores.2014.08.013.

Husain, T., D. Elsworth, B. Voight, G. Mattioli, and P. Jansma (2018), Influence of conduit flow mechanics on magma rheology and the growth style of lava domes, *Geophysical Journal International*, *213*(3), 1768–1784, doi:10.1093/gji/ggy073.

Itasca (2016), PFC 5.0 Documentation, *Tech. rep.*, Itasca Consulting Group.

Potyondy, D. (2015), The bonded-particle model as a tool for rock mechanics research and application: current trends and future directions, *Geosystem Engineering*, *18*(1), 1–28, doi:10.1080/12269328.2014.998346.

Potyondy, D. (2016), Material-Modeling Support in PFC [via fistPkg20], *Tech. rep.*, Itasca.

Potyondy, D., and P. A. Cundall (2004), A bonded-particle model for rock, *International Journal of Rock Mechanics and Mining Sciences*, *41*(8 SPEC.ISS.), 1329–1364, doi:10.1016/j.ijrmms.2004.09.011.

Potyondy, D. O. (2010), A grain-based Model for Rock: Approaching the True Microstructure, in *Rock Mechanics in the Nordic Countries*, vol. 2010.

Potyondy, D. O. (2012), A flat-jointed bonded-particle material for hard rock, *46th US Rock Mechanics/Geomechanics Symposium*, p. 10.

Potyondy, D. O. (2017), Mateiral-Modeling Support in PFC [fistPkg25], *Tech. rep.*, Itasca, Minneapolis, Minnesota.

Wu, S., and X. Xu (2016), A Study of Three Intrinsic Problems of the Classic Discrete Element Method Using Flat-Joint Model, *Rock Mechanics and Rock Engineering*, *49*(5), 1813–1830, doi:10.1007/s00603-015-0890-z.

Appendix B

Supplementary Material for Chapter 3

The materials presented in Appendix B.1 and Appendix B.3 were included as online Supplementary Material in the following publication:

Harnett, C.E., Thomas, M.E., Purvance, M., and Neuberg, J. (2018), *Using a discrete element approach to model lava dome emplacement and collapse*, Journal of Volcanology and Geothermal Research, 359, pp.68-77, doi:10.1016/j.jvolgeores.2018.06.017.

B.1 Comparison of emplacement to theoretical model

We can compare the modelled 2D dome growth to an analytical solution of the height development through time. To do this, we calculate that the height is proportional to the square root of the time using the method outlined here:

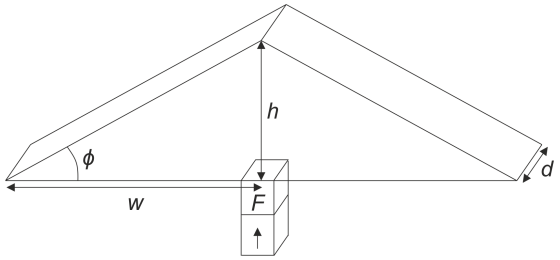

Figure B.1: A conceptual sketch to support the analytical solution of height and its evolution through time.

The 2D volume of the dome, V, can be calculated using

$$V = hwd \ ,$$

where h is dome height, w is dome radius, and d is unit depth (i.e. 1 m). Assuming $\frac{h}{w}$ is constant,

$$\frac{h}{w} = \tan\phi,$$

$$w = \frac{h}{\tan\phi}$$

$$V = \frac{h^2}{\tan\phi}$$

where ϕ is the angle of friction of the dome material. The dome volume at a given time (t) can also be expressed in terms of material flux, F:

$$V = Ft$$

Equating both expressions for volume gives

$$Ft = \frac{h^2}{\tan\phi}$$

Rearranging for h gives

$$h = \sqrt{Ft\ \tan\phi}$$

$$\therefore h \propto t^{\frac{1}{2}}.$$

Figure B.2 shows the height evolution in a modelled PFC dome, and compares it to the analytical solution where height is calculated as being proportional to $\sqrt{t}$. The dome growth fits well to this analytical solution apart from in the initial 5-10 timesteps. This is because the geometry of the initial material that exits the conduit in PFC is controlled by the conduit initialisation. Overall, this comparison supports the use of PFC as an efficient geometry model for dome growth.

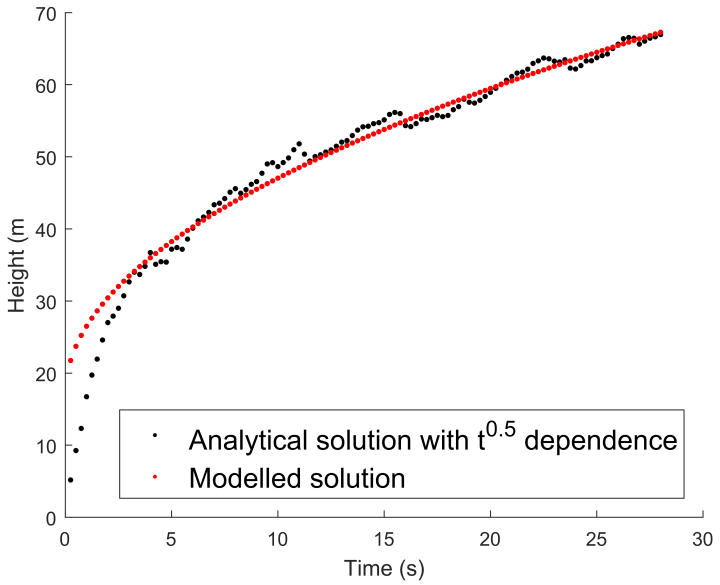

Figure B.2: Dome height evolution for a simple dome growth model (presented in Chapter 3 and used as the initial condition for Chapter 5 models) compared to an analytical solution where height is proportional to $t^{\frac{1}{2}}$.

B.2 Supplementary Tables

Table B.1: Model parameters used in initial emplacement model. This model is used as the starting condition for all models that test collapse triggers parameters kept constant in each of these secondary models. Parallel bond parameters relate to the core material, and flat-joint parameters relate to the talus material. Note the expressions in parentheses relate to conventional parameter naming in PFC.

Parameter	Value
Parallel bond shear stiffness (pb_kn)	1×10^8 Pa
Parallel bond normal stiffness (pb_ks)	1×10^8 Pa
Parallel bond cohesion (pb_coh)	1×10^6 Pa
Parallel bond friction angle (pb_fa)	0
Flatjoint shear stiffness (fj_kn)	1×10^8 Pa
Flatjoint normal stiffness (fj_ks)	1×10^8 Pa
Flatjoint cohesion(fj_coh)	1×10^6 Pa
Flatjoint friction coefficient (fj_fric)	0.84
Flatjoint friction angle (fj_fa)	38°
Average particle radius	1 ± 0.2 m
Conduit ascent velocity	2 m/s

B.3 Additional material

The second item of Supplementary Material for this article refers to an animation of lava dome emplacement from PFC. This is available online as part of the journal material and can be found at the following URLs: https://tinyurl.com/harnett2018 or https://www.sciencedirect.com/science/article/pii/S0377027318301148

Appendix C

Supplementary Material for Chapter 4

The material presented in Appendix C was included as online Supplementary Material in the following publication:

Harnett, C. E., Kendrick, J. E., Lamur, A. H., Stinton, A., Wallace, P. A., Utley, J. E. P., Murphy, W., Neuberg, J., and Lavallée, Y. (2018). *Evolution of mechanical properties of lava dome rocks across the 1995-2010 eruption of Soufrière Hills volcano, Montserrat.* Frontiers in Earth Science, 7 (7), doi: 10.3389/feart.2019.00007

C.1 Supplementary Tables

Table C.1: Raw data for connected porosity, total porosity, permeability, Young's modulus and UCS for all samples in this study. The top row for each block shows properties of one 37 mm diameter core for each block, with the remaining samples all at 26 mm diameter core. The IDs shown in bold represent a 37 mm core that is sub-cored to produce the 26 mm core of the same ID number.
* clear pervasive fracture through sample, failed during cyclic testing (i.e. below 50% of pre-established UCS)
** did not behave elastically during the cyclic testing, not considered in data plots or averaging calculations
*** too permeable to be measured on the GasPerm

Phase	Block	ID	Density (g/cm^3)	Conn. por. (%)	Total por. (%)	Perm at 100 psi (m^2)	Perm at 200 psi (m^2)	Perm at 300 psi (m^2)	E (GPa)	UCS (MPa)
1	M	**4**	2.26	-	-	4.42×10^{-13}	4.12×10^{-13}	3.99×10^{-13}	6.23	-
		2	2.21	19.69	20.34	3.11×10^{-13}	2.92×10^{-13}	2.80×10^{-13}	7.2	25.1
		3	2.15	21.51	22.51	5.67×10^{-13}	5.17×10^{-13}	4.96×10^{-13}	5.91	-
		4	2.18	20.85	21.54	4.24×10^{-13}	3.98×10^{-13}	3.86×10^{-13}	4.45	-
		7	2.14	22.3	22.87	6.51×10^{-13}	5.93×10^{-13}	5.63×10^{-13}	3.58	-
		8	1.98	26.99	28.58	1.88×10^{-13}	1.69×10^{-12}	1.59×10^{-12}	-*	-
3	B	**4**	2.34	-	-	1.62×10^{-13}	1.22×10^{-13}	1.13×10^{-13}	7.75	-
		2	2.12	23.24	23.75	1.51×10^{-13}	1.49×10^{-13}	1.47×10^{-13}	6.75	26.1
		3	2.17	21.61	22.05	7.19×10^{-14}	7.07×10^{-14}	6.96×10^{-14}	7.74	-
		4	2.12	23.48	24.28	1.06×10^{-13}	9.96×10^{-14}	9.71×10^{-14}	7.6	-

Phase	Block	ID	Density (g/cm^3)	Conn. por. (%)	Total por. (%)	Perm at 100 psi (m^2)	Perm at 200 psi (m^2)	Perm at 300 psi (m^2)	E (GPa)	UCS (MPa)
3	B	51	2.15	22.65	22.8	7.88×10^{-14}	7.55×10^{-14}	7.39×10^{-14}	6.46	-
	H	**9**	2.33	-	-	1.32×10^{-13}	1.13×10^{-13}	1.05×10^{-13}	7.11	-
		2	2.18	21.09	23.2	6.13×10^{-14}	5.98×10^{-14}	5.91×10^{-14}	7.18	29.5
		6	2.09	24.4	26.25	1.43×10^{-13}	1.33×10^{-13}	1.25×10^{-13}	-**	-
		7	2.14	22.76	24.42	8.91×10^{-14}	8.60×10^{-14}	8.42×10^{-14}	8.14	-
		8	2.16	21.93	23.76	7.80×10^{-14}	7.57×10^{-14}	7.44×10^{-14}	6.95	-
		9	2.16	22.08	23.9	9.15×10^{-14}	8.37×10^{-14}	8.11×10^{-14}	6.47	-
4	F	**6**	2.27	-	-	1.44×10^{-14}	1.13×10^{-14}	1.04×10^{-14}	10.83	-
		1	2.2	20.52	22.74	8.10×10^{-15}	7.48×10^{-15}	7.20×10^{-15}	11.42	-
		2	2.11	23.77	26	9.38×10^{-15}	8.81×10^{-15}	8.54×10^{-15}	11.01	-
		3	2.15	22.55	24.57	7.26×10^{-15}	6.72×10^{-15}	6.41×10^{-15}	10.77	48.6
		5	2.09	20.94	26.76	1.19×10^{-14}	1.09×10^{-14}	1.04×10^{-14}	10.42	-
		6	2.13	23.1	25.32	8.41×10^{-15}	7.82×10^{-15}	7.59×10^{-15}	12.29	-
	G	**32**	2.28	-	-	9.63×10^{-15}	8.10×10^{-15}	7.67×10^{-15}	11.58	-

Phase	Block	ID	Density (g/cm^3)	Conn. por. (%)	Total por. (%)	Perm at 100 psi (m^2)	Perm at 200 psi (m^2)	Perm at 300 psi (m^2)	E (GPa)	UCS (MPa)
4	G	31	2.15	22.57	24.78	7.09×10^{-15}	6.78×10^{-15}	6.55×10^{-15}	11.39	51.1
		32	2.1	24.38	26.47	8.20×10^{-15}	7.81×10^{-15}	7.54×10^{-15}	9.37	-
		41	2.07	25.4	27.56	1.65×10^{-14}	1.50×10^{-14}	1.39×10^{-14}	9.94	-
		61	2.22	21.1	22.5	1.38×10^{-14}	1.32×10^{-14}	1.26×10^{-14}	11.89	-
5	J	**1**	1.83	-	-	2.51×10^{-11}	2.08×10^{-11}	1.89×10^{-11}	2.36	-
		1	1.61	40.17	41.17	-***	-***	-***	1.39	-
		2	1.69	37.2	38.13	-***	-***	-***	3.29	-
		4	1.68	37.57	36.47	1.75×10^{-11}	1.65×10^{-11}	1.58×10^{-11}	1.83	7.0
		5	1.65	39.15	39.81	2.40×10^{-11}	2.26×10^{-11}	2.14×10^{-11}	2.01	-
	K	**2**	2.03	-	-	2.44×10^{-12}	2.16×10^{-12}	2.07×10^{-12}	3.89	-
		1	1.91	29.16	30.17	2.00×10^{-12}	1.89×10^{-12}	1.83×10^{-12}	4.05	-
		2	1.89	30.19	31.05	2.24×10^{-12}	2.06×10^{-12}	1.99×10^{-12}	3.9	-
		3	1.83	32.32	33.22	$3.37E \times 10^{-12}$	3.02×10^{-12}	2.83×10^{-12}	1.84	-
		36	1.84	32.08	32.85	2.98×10^{-12}	2.74×10^{-12}	2.56×10^{-12}	-**	-

Phase	Block	ID	Density (g/cm^3)	Conn. por. (%)	Total por. (%)	Perm at 100 psi (m^2)	Perm at 200 psi (m^2)	Perm at 300 psi (m^2)	E (GPa)	UCS (MPa)
5	K	9	1.86	31.6	32.28	2.68×10^{-12}	2.47×10^{-12}	2.35×10^{-12}	3.05	6.2

Table C.2: Raw data for tensile strength results obtained by Brazilian disk testing.

Phase	Block	Core ID	Length (mm)	Diameter (mm)	Calculated density (g/cm^3)	Tensile strength (MPa)
1	M	1	23.7	37	2.14	2.08
		03	17.9	36.9	2.22	2.45
		31	20.1	36.8	2.13	1.86
		04	20.3	37	2.24	2.62
		41	21	36.9	2.22	2.32
		05	23.5	37	2.16	2.06
		06	21.9	37	2.17	2.23
		07	22.2	36.9	2.2	2.35
		08	23.6	36.8	2.25	2.38
		09	19.5	37	2.21	2.62
		10	20.1	36.9	2.25	2.83
		11	16.3	36.9	2.15	1.96
		12	20.2	36.9	2.18	1.98
		13	18.9	36.9	2.17	1.18
		14	18.8	36.9	1.87	1.03
3	B	2	16.4	36.9	2.09	1.59
		03	17.2	36.7	2.3	2.88
		04	19.9	36.9	2.14	2.37
		041	20.8	36.9	2.14	2.06
		05	17	36.8	2.12	2.15
		072	16.2	36.9	2.15	2.34
	H	1	24.8	37	2.13	2.18
		011	24.9	36.9	2.15	2.56

Phase	Block	Core ID	Length (mm)	Diameter (mm)	Calculated density (g/cm^3)	Tensile strength (MPa)
3	H	012	28.1	36.9	2.15	2.29
		02	20.3	36.9	2.18	3.21
		031	23.7	37	2.17	3.03
		032	18.8	37	2.17	3.17
		05	26.4	36.9	2.13	2.46
		051	23.3	38.4	1.98	1.94
		08	16.6	36.9	2.23	2.31
		081	16.6	36.9	2.05	2.75
		09	22.7	36.9	2.17	2.67
4	F	01	18.4	37.7	2.16	3.06
		012	24.6	37.6	2.12	2.66
		02	17	37.6	2.07	2.95
		03	18.7	37.8	2.15	2.89
		031	24.5	37.8	2.1	3.05
		032	23.5	37.8	2.11	3.73
		04	21.7	37.8	2.03	2.98
		05	18.9	37.7	2.06	3.57
		051	22.5	37.8	2.16	3.9
		06	23.3	37.8	2.05	2.46
		061	21.8	37.7	2.06	2.92
		071	19.4	37.7	2.06	2.02
		072	22.3	37.6	2.06	2.86
	G	03	17.1	37.9	2.09	3.27
		031	22.6	37.8	2.16	4.05

Phase	Block	Core ID	Length (mm)	Diameter (mm)	Calculated density (g/cm^3)	Tensile strength (MPa)
4	G	032	19.6	37.7	2.13	3.72
		04	17.8	37	2.18	4.15
		042	16.5	37.1	2.06	3.19
		061	16.6	37.9	2.09	3.66
5	J	01	23.6	36.9	1.65	0.78
		02	18.2	36.9	1.65	0.74
		03	19.5	37	1.66	0.71
		04	18.2	36.9	1.62	0.74
		05	19.5	36.9	1.64	0.54
		06	16.9	37	1.69	0.81
	K	01	19.9	36.9	1.97	1.19
		012	21.8	36.9	1.92	1.34
		036	21.8	36.9	1.96	1.27
		04	21.7	36.9	1.92	1.25
		05	18.8	36.9	1.74	0.81
		05	23.8	36.9	1.85	1.07
		051	22.3	36.9	1.81	1.01
		09	18.3	36.9	1.99	1.6
		091	19.8	36	1.82	0.53

Table C.3: Mean Schmidt hammer values, and width, depth and height of each block given in cm; * where dimension not exposed.

Phase	Width	Depth	Height	Mean R_L
1	143	*	*	29.05
	109	72	56	24.8
	135	228	*	30.5
	85	62	81	47.9
3	1000	500	600	37.25
	800	400	300	35.55
	500	450	200	43.75
4	600	400	150	34.1
	300	300	200	37.45
	125	42	68	33.35
	550	200	300	23.95
	280	200	150	40.9
	300	150	300	37.7
	250	150	150	33.25
	182	157	138	42.9
	280	350	450	42.45
5	800	300	600	20.3
	500	400	300	40.55
	700	500	400	29.1
	450	800	400	12.5
	450	800	400	24.4
	400	250	300	27.9
	175	124	163	19.7
	350	600	300	18.2

Phase	Width	Depth	Height	Mean R_L
BRV Samples	94	49	67	45.95
	107	107	57	26.8
	97	115	53	38.6
	82	52	63	24.85
	136	70	72	35.05
	113	62	57	19.15
	86	58	42	24.9
	112	94	66	42.05
	92	34	42	15.9
	104	48	86	21.7
	87	73	75	34
	94	82	69	45.5
	82	51	32	39.4
	204	197	114	47.05
	84	95	53	6
	51	47	14	43.35
	258	139	132	27.9
	77	86	32	48.1
	104	93	95	47.8
	84	95	53	20.95
	62	49	25	35.65
	180	122	113	43
	116	72	47	33.55
	62	53	33	42.15
	84	40	67	34.15
	67	59	35	46.9

Phase	Width	Depth	Height	Mean R_L
BRV Samples	120	96	62	39.8
	66	48	35	29.75

Table C.4: For each of Uniaxial Compressive Strength (UCS), Uniaxial Tensile Strength (UTS), and Youngs modulus (E): number of tests, average, and standard deviation for each phase.

	UCS			**UTS**			E		
Phase	# of tests	Av. (MPa)	Std. Dev. (MPa)	# of tests	Av. (MPa)	Std. Dev. (MPa)	# of tests	Av. (GPa)	Std. Dev. (GPa)
1	1	25.11	n/a	15	2.13	0.5	4	5.29	1.39
3	2	26.9	1.68	17	2.47	0.44	8	7.16	0.58
4	2	49.82	1.23	19	3.22	0.56	9	10.94	0.88
5	2	6.59	0.38	15	0.96	0.32	8	2.67	0.96

C.2 Supplementary Figures

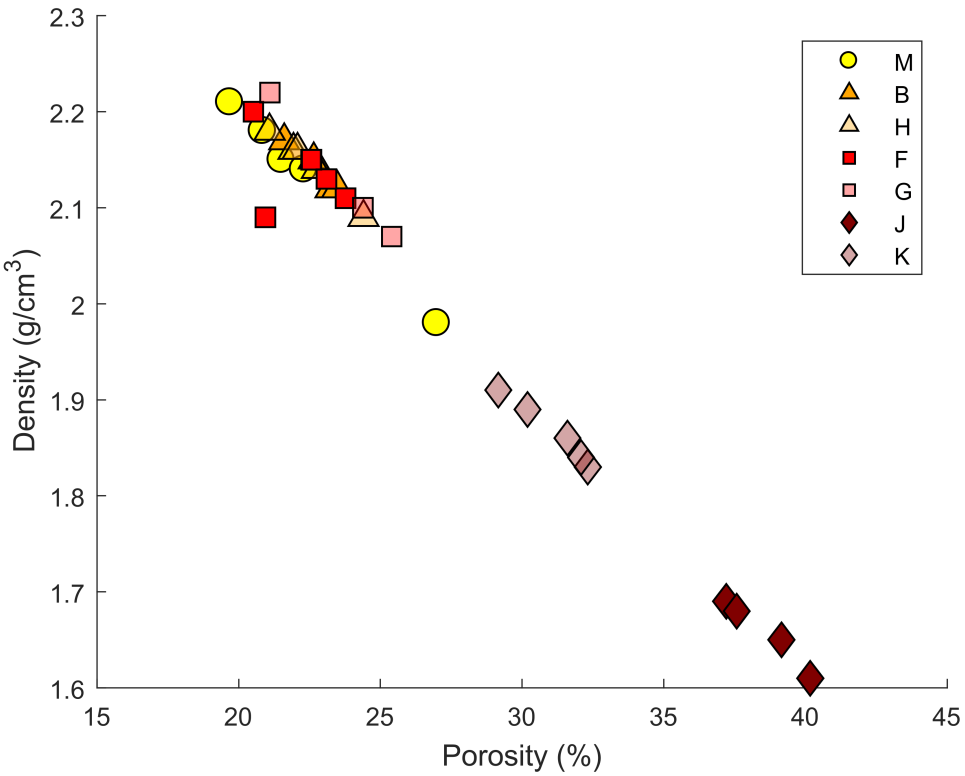

Figure C.1: Rock density as function of total porosity, shown by block label. The data show a near-linear relationship (raw values in Supplementary Table 1).

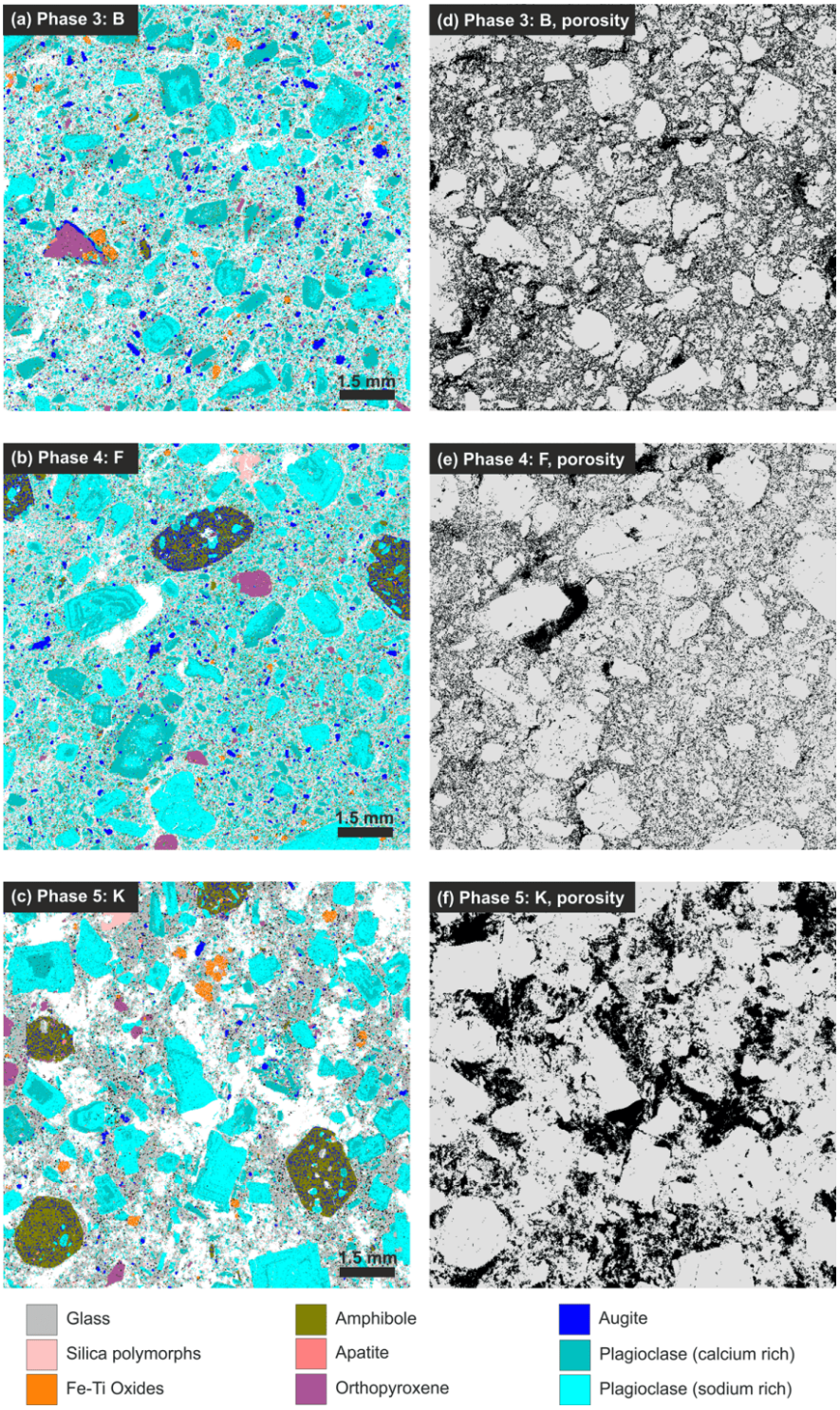

Figure C.2: **(a-c)** QEMSCAN images showing mineral assemblage in remaining samples from each phase key shown below images and white shows porosity in all cases; **(d-f)** processed QEMSCAN images where all minerals are shown in gray, and all porosity is highlighted in black.

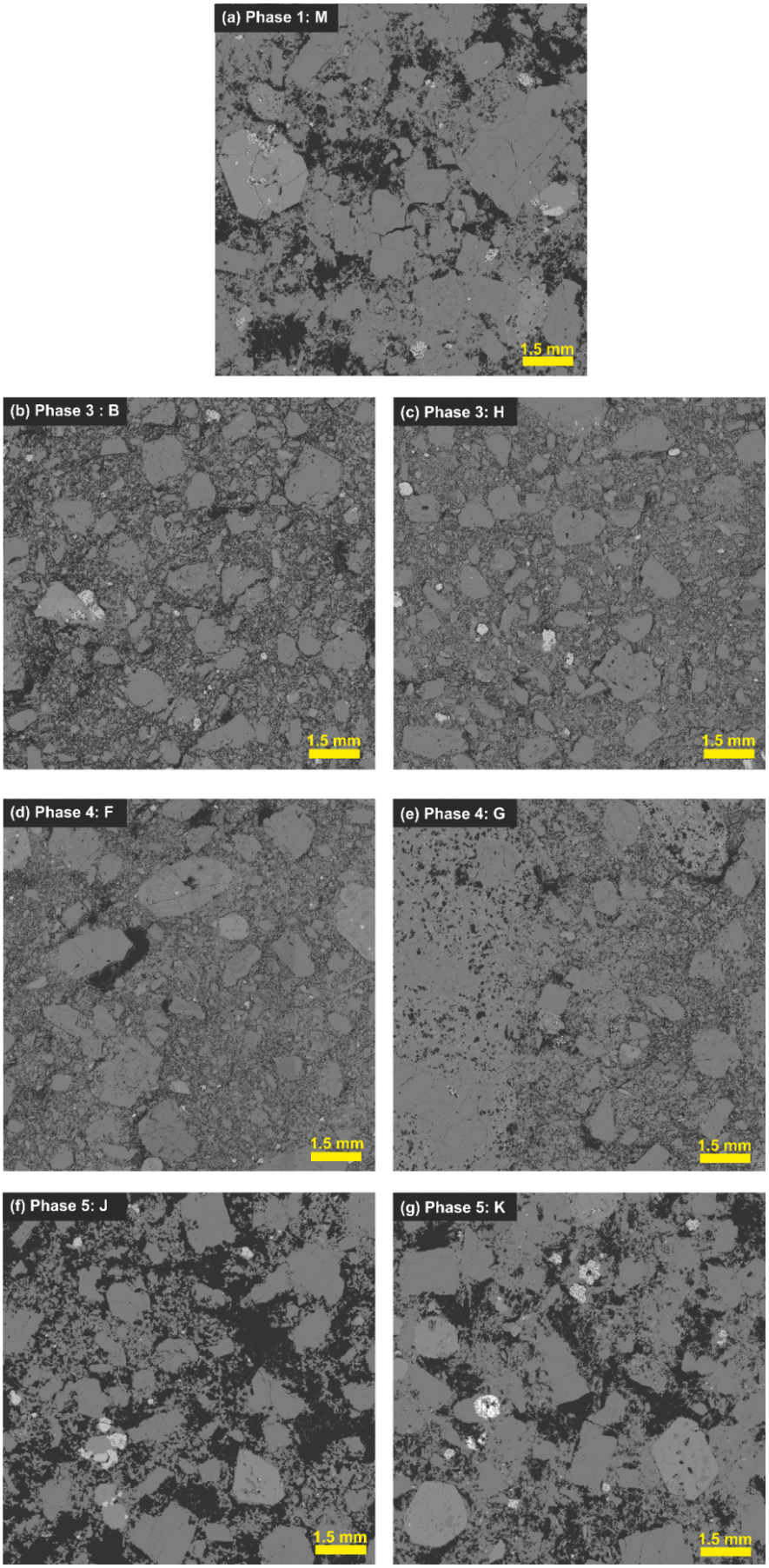

Figure C.3: Back scattered electron images for each of the rocks analyzed using the QEMSCAN. Each panel corresponds to the equivalent rock section shown in Figure 3 and Supplementary Figure 2.

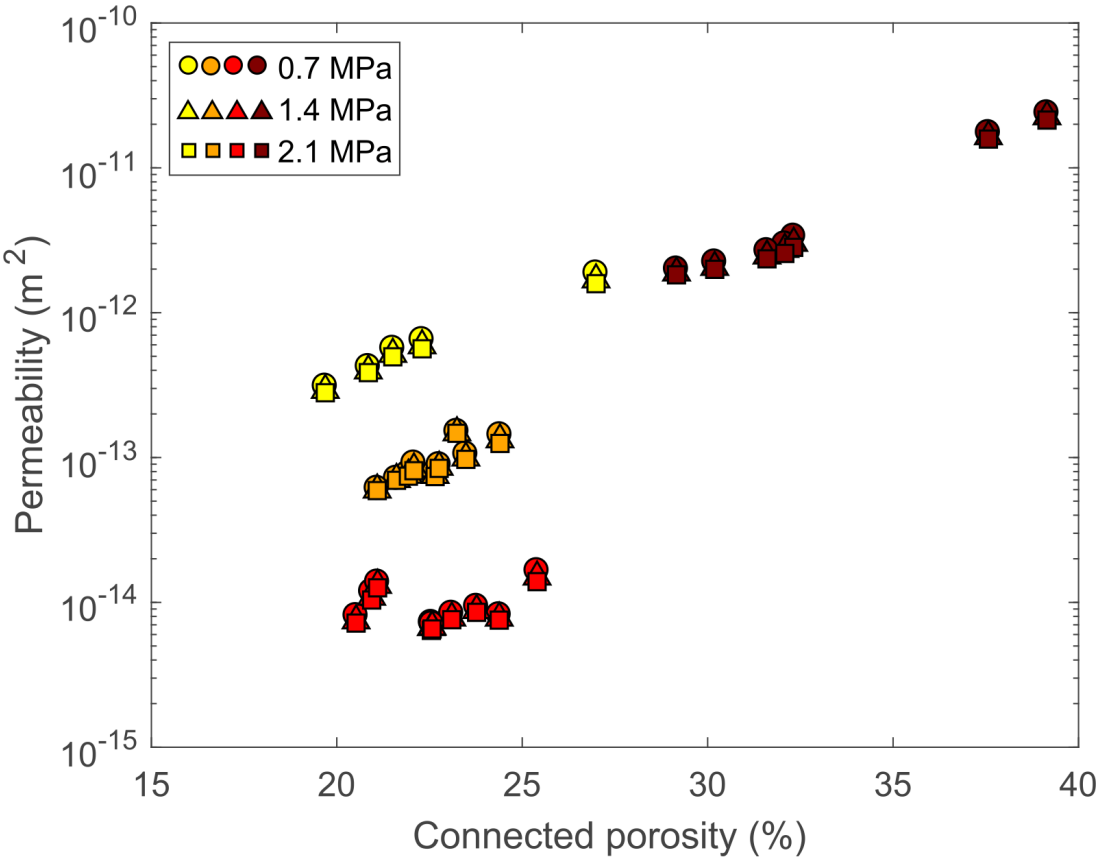

Figure C.4: Permeability as a function of connected porosity, shown at confining pressures of 0.7 MPa, 1.4 MPa and 2.1 MPa. The color refers to Phases: Phase 1: yellow; Phase 3: orange; Phase 4: red; Phase 4: mauve.

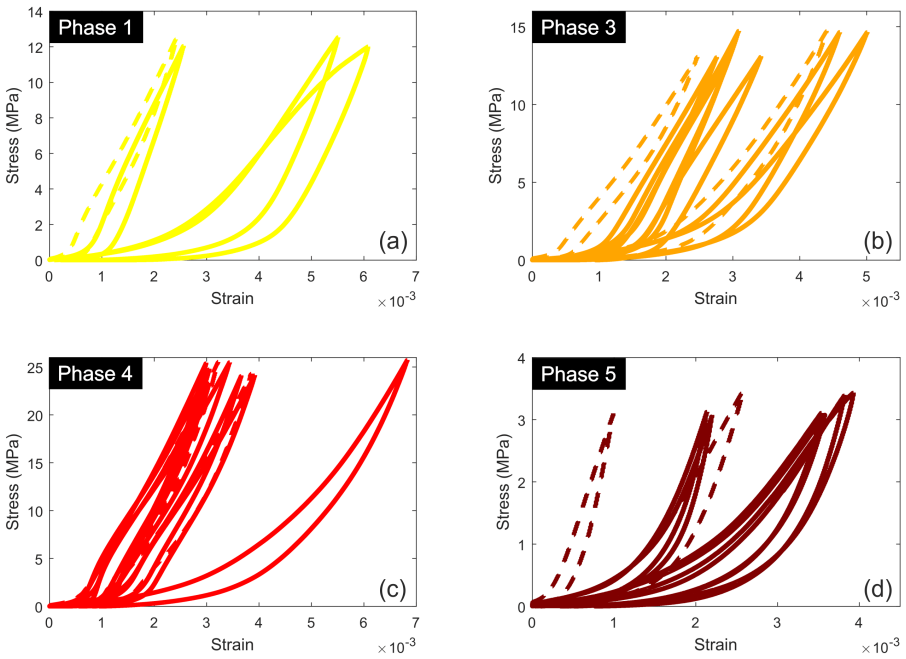

Figure C.5: Stress-strain plots for cyclic loading tests in each phase, where solid lines show tests on 26 mm cores, and dashed lines show tests on 37 mm cores for **(a)** Phase 1, **(b)** Phase 3, **(c)** Phase 4, and **(d)** Phase 5.

Appendix D

Supplementary Material for Chapter 5

D.1 Supplementary Tables

Table D.1: Height/radius relationships for all 'initial condition' domes first presented in Chapter 3.

Conduit diameter (m)	Solidus Pressure (MPa)	Height (m)	Radius (m)	H/R
20	0.4	70	97.5	0.718
20	0.2	68.5	111	0.617
20	0.8	76.5	104	0.736
50	0.4	112	170	0.659

D.2 Supplementary Figures

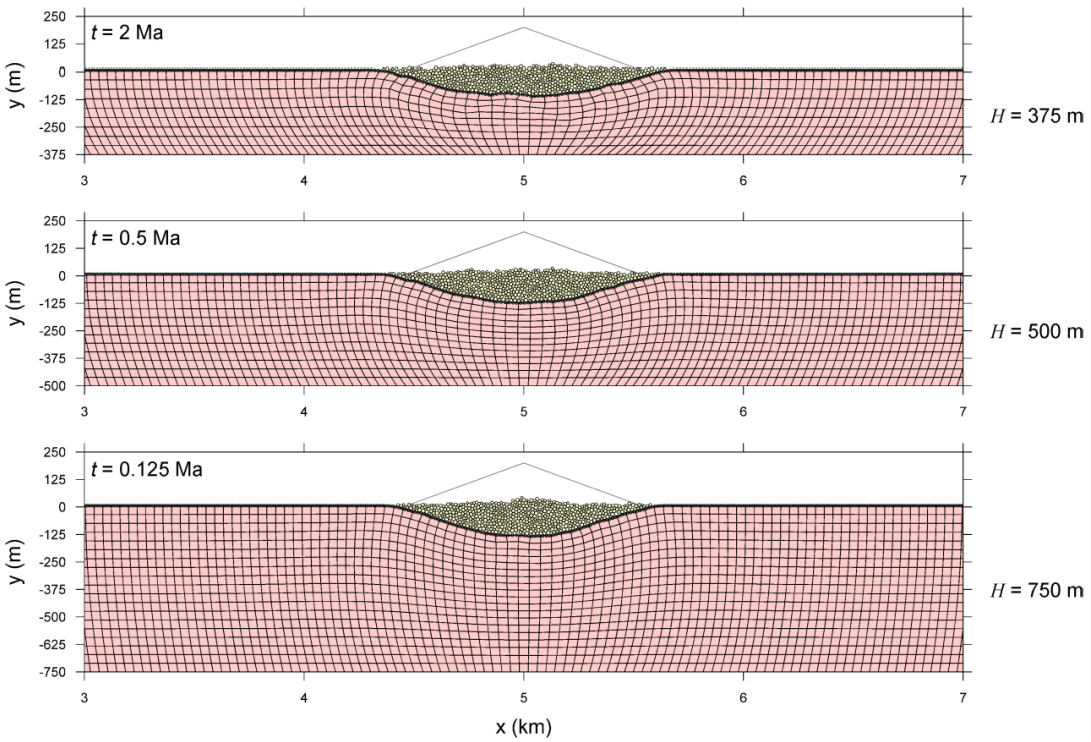

Figure D.1: Results of coupled PFC2D-FLAC simulations, by Martin Schöpfer (unpublished). Thin triangular line is the outline of the particle model prior to substratum creep. t is final creep-time in million years. H is initial substratum thickness.